The ejecta blanket of the Chicxulub impact crater, Yucatán, Mexico:

Petrographic and chemical studies of the K-P section of El Guayal and UNAM boreholes

Dissertation

zur Erlangung des akademischen Grades
doctor rerum naturalium
(Dr. rer. nat.)
im Fach Chemie

eingereicht an der
Mathematisch-Naturwissenschaftlichen Fakultät I
der Humboldt-Universität zu Berlin

von
Dipl.-Min. Tobias Salge
02.03.1970 in Hannover

Präsident der Humboldt-Universität zu Berlin:
Prof. Dr. C. Markschies

Dekan der Mathematisch-Naturwissenschaftlichen Fakultät I:
Prof. Dr. C. Limberg

Gutachter: 1. Prof. Dr. D. Stöffler
2. PD Dr. L. Hecht

Tag der mündlichen Prüfung: 12.01.2007

Nor is there a least of what is small, but there is always a smaller …
But there is also always something greater than what is great …

Anaxagoras (500 BC–428 BC)

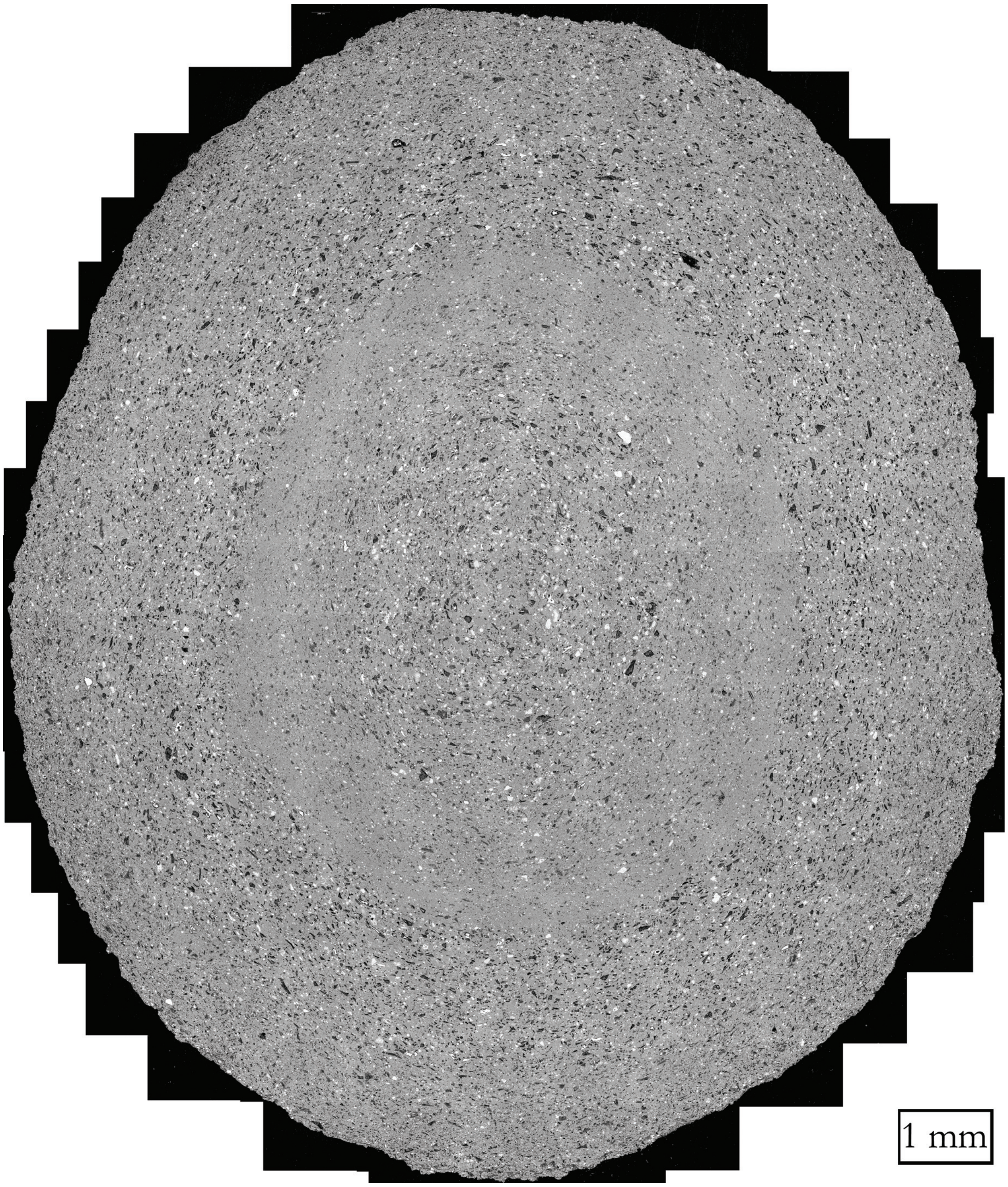

Back scattered electron composite micrograph of accretionary lapillus.

Note the tangential alignment of elongated particles and the concentrically lamination due to grain size sorting.

Kurzfassung

Impaktite des Chicxulub Impaktkraters (D~180 km, ~65 Ma) auf der Yucatán Halbinsel in Mexiko wurden petrographisch und chemisch untersucht, um das Verhalten von Auswurfmassen während des Transport durch die Atmosphäre zu erforschen. Das Zielgestein bestand aus einer ~3 km mächtigen Karbonat-Anhydrit-dominierten sedimentären Abfolge über kristallinem Grundgebirge. Impaktite der UNAM-5 und UNAM-7 Bohrungen nahe des äußeren Kraterrands sowie der K-P Grenze von El Guayal (~520 km SW vom Kraterzentrum) wurden untersucht. In UNAM-5 wurde eine 172 m mächtige suevitische Brekzie zwischen den Teufen 332.0 und 504.0 m angetroffen. Die Impaktite von UNAM-7 bestehen aus einer oberen suevitischen Brekzie (222.2 bis 384.4 m) und einer basalen, polymikten Brekzie mit geringem Silikatschmelzanteil. Letztere beinhaltet Evaporit-Megablöcke und stellt ein Analog zur Bunten Brekzie des Nördlinger Ries dar. Bei El Guayal wurde eine impakt-induzierte Abfolge zwischen Kalksteinen der Oberen Kreide und Mergeln des jüngsten Paläozän abgelagert. Diese besteht aus (1) einer basalen ~40 m mächtigen monomikten Karbonatbrekzie, (2) gefolgt von einer ~10 m mächtigen suevitischen Einheit mit zahlreichen akkretionären Lapilli in den obersten 2,3 m, überlagert von (3) der mehrere cm mächtigen K-P Grenztonschicht. Das Auftreten von Auswurfmassen des Chicxulub-Impakts zusammen mit der PGE-angereicherten Impaktorkomponente im Ton von El Guayal belegt den Zusammenhang der K-P Grenze mit dem Chicxulub-Impakt.

Die Abkühlungsgeschichte der Auswurfmassen ist durch die Gefüge der Karbonatschmelzen angezeigt. In der basalen Brekzie von UNAM-7 wurden Karbonatschmelzen überwiegend im geschmolzenen Zustand abgelagert, wohingegen diese bei El Guayal schnell abgeschreckt wurden. Das zusammenhängende Auftreten von unterschiedlich strukturierten Kalzitkristallen spiegelt Temperaturvariationen während des atmosphärischen Transports wieder. Die Karbonate der basalen Brekzie von UNAM-7 zeigen komplette Aufschmelzung und/ oder Rekristallisation. Die bläschen-führende Kristallisationabfolge eines Anhydritkerns umgeben von Silikatschmelze zeigt die zusammenhängende Aufschmelzung und Zersetzung von Anhydrit bei T~1465°C an. Diese Beobachtungen weisen auf eine ausgeprägte thermische Alteration und Transport bei höheren Temperaturen im Vergleich zur Bunten Brekzie des Nördlinger Ries hin. Bei El Guayal sind größere Variationen der thermischen Alteration durch Rekristallisation im Randbereich von festen Kalzitpartikeln und abgeschreckten Karbonatschmelzpartikeln indiziert. Vermischung von heißer Silikatschmelze mit Kalzit führte zum Zusammenschweißen der unterschiedlichen Komponenten. Hohlräume, welche mit mikrokristallinen Kalzitkristallen assoziiert sind, weisen auf eine komplexe Reaktion inklusive Rekristallisation und Zersetzung von Kalzit hin. In der basalen Brekzie von UNAM-7 ist Zersetzung von Kalzit und anschließende Rückreaktion durch Entgasungsbläschen, welche

mit Einlagerungen von mikrokristallinem Kalzit in plastisch deformiertem Anhydritpartikel assoziiert sind, indiziert. Da vesikuläre Formen der Karbonatschmelzpartikel erhalten sind, ist ein bedeutsamer Anteil der Kalzitmatrix nicht nur durch Kristallisation aus einer Karbonatschmelze entstanden sondern ebenfalls via Rückreaktion. In der oberen suevitischen Brekzie wurden Silkatschmelzpartikel im geschmolzenen Zustand abgelagert und die Alteration mit Meerwasser führte zu einer Anreicherung von Br, Cl, Sr und SO_3. Diese hydrothermale Reaktion weist darauf hin, dass die Kalzitmatrix von UNAM-7 möglicherweise durch exotherme Reaktion von zersetztem Kalzit und Anhydrit (CaO) mit Wasser und anschließender Rückreaktion mit CO_2 entstanden ist. Diese Reaktion sowie die Impaktschmelzen lieferten die thermische Energie für die Kristallisation von euhedralen Anhydrit in der Matrix von sulphat-reichen Fluiden bei $T>350°C$.

Die folgenden fünf Stadien können für die Ablagerung und Alteration der Chicxulub Auswurfmassen unterschieden werden: (1) Impakt-induzierte seismische Aktivität führte zum Kollaps des Randbereichs der Yuacatán-Platform und proximalen Ablagerung im Schelfbereich. In der Hochdruckzone zwischen Impaktor und sedimentären Zielgestein wurden Zersetzungsprodukte (CaO, CO_2, SO_X) in die Atmosphäre beschleunigt. Ein heißer Gasstrom ist durch explosiv verdampftes Wasser des Zielgestein und der schnellen Rückreaktion von CaO mit CO_2 zu Kalzit entstanden. (2) Karbonatschmelzen von intermediären Lithologien wurden zusammen mit Anhydrit- und Karbonat-Megablöcken ausgeworfen und initiierten einen lateral ausbreitenden „Ejektavorhang“. Dabei induzierte die Rückreaktion zu Kalzit einen Transport bei hohen Temperaturen. Zusätzliche Entstehung von Wasserdampf veränderte einen anfangs ballistischen zu einem strömungsähnlichen Transport. (3) Nach mehreren 10’er min kollabierte die turbulente, expandierende Ejektionswolke, wobei der zurückfallende Suevit vom Impaktormaterial, das in die Stratosphäre verteilt wurde, fraktioniert wurde. Kombination von heißer Silikatschmelze mit Karbonaten initiierte einen gas-angetriebenen, lateralen basalen Strom (T~550–1100°C). In einer darüberliegenden, moderat temperierten (T~100°C), turbulenten Aschewolke kondensierte Wasserdampf und durch Akkretion von Asche entstanden akkretionäre Lapilli. (4) Die Impaktorkomponente wurde mit dem feinsten Auswurfsmaterial vermutlich für Wochen bis Jahre im K-P Grenzton von El Guayal abgelagert. (5) Der andauernde Transport von Auswurfmassen in der heißen Ejektionswolke induzierte Alterationsprozesse in den abgelagerten Impaktiten. Es kann geschlussfolgert werden, dass Aggregation die Anzahl von Aschepartikeln aus der Atmosphäre und möglicherweise die Dauer der globalen Verdunkelung reduzierte. Ein gewisser Anteil des CO_2 hat zurückreagiert, währenddessen SO_X Gase vollständig in die Atmosphäre eingetragen wurden. Diese Beobachtungen inklusive das häufige Auftreten von Karbonatschmelzen unterstützen, dass der freigesetzte Anteil von CO_2 in die Atmosphäre in der Vergangenheit überbewertet wurde.

Abstract

Impactites from the Chicxulub impact crater (D~180 km, ~65 Ma) on the Yucatan peninsula, Mexico, were studied petrographically and chemically to investigate the compositional evolution of ejecta during transit through the atmosphere. The target lithology is a ~3 km thick carbonate-anhydrite-dominated sedimentary sequence on top of a crystalline silicate basement. Three different sites were studied including impactites from the UNAM-5 and UNAM-7 boreholes near the outer crater rim and the K-P site of El Guayal (~520 km SW of the crater centre). At the UNAM-5, a 172 m thick suevitic breccia was encountered between 332.0 and 504.0 m depths. At UNAM-7, the sequence of impactites consists of a suevitic breccia (222.2 to 348.4 m) on top of a polymict silicate melt-poor breccia. The latter is intercalated with evaporite megablocks and represents an analogue to the Bunte breccia of the Nördlinger Ries crater. At El Guayal, an impact-related sequence was emplaced between Upper Cretaceous limestones and earliest Palaeocene marls. It consists of (1) a basal ~40 m thick monomict carbonate megabreccia, (2) followed by an ~10 m thick suevitic unit, where an upper ~2.3 m subunit contains at its basis abundant accretionary lapilli, and (3) on top a several cm thick clay layer. In the clay of El Guayal, the presence of Chicxulub impact ejecta together with the PGE-enriched impactor component links the K-P boundary with the Chicxulub impact.

The cooling history of the impact ejecta is recorded by the texture of the carbonate melts. In the polymict silicate melt-poor breccia of UNAM-7, carbonate melts were deposited mainly in liquid state, whereas at El Guayal carbonate melts were rapidly quenched. The cogenetic association of carbonate melts with variably textured calcite crystals displays temperature variations during transport through the atmosphere. The carbonates in the polymict silicate melt-poor breccia of UNAM-7 show complete melting and/ or recrystallisation. A vesicle-bearing crystallisation sequence at an anhydrite core coated with silicate melt indicates coherent melting and decomposition of anhydrite at T~1465°C. These observations indicate a pronounced thermal alteration and transport in the ejecta curtain with higher temperatures than the Bunte breccia from the Nördlinger Ries crater. At El Guayal, larger variations of thermal alteration are recorded by recrystallisation at the rim of solid calcite particles and quenched carbonate melt particles. Intermixing of hot silicate melt with calcite resulted in annealing of the different components. Degassing voids associated with microcrystalline calcite crystals in silicate melt indicate a complex annealing reaction including calcite recrystallisation and decomposition. In the polymict silicate melt-poor breccia of UNAM-7, calcite decomposition and subsequent back-reaction is indicated by degassing vesicles associated with intercalations of microcrystalline calcite into plastically deformed anhydrite particles. There, a significant amount of the calcite matrix formed by similar processes and not

solely by crystallisation from a carbonate melt as indicated by the preservation of vesicular shapes of carbonate melt particles. In the overlying suevitic breccia, silicate melt particles were deposited in liquid state and alteration due to reaction with seawater caused enrichment in Br, Cl, Sr and SO_3. This hydrothermal alteration suggests that the calcite matrix at UNAM-7 formed by an exothermic reaction of decomposed calcite and anhydrite (CaO) with water and subsequent back-reaction with CO_2. This reaction and impact melts provided the thermal energy for the crystallisation of euhedral anhydrite in the matrix from sulphate-rich fluids at $T>350°C$.

The following five stages can be distinguished for the deposition and alteration of the Chicxulub ejecta blanket: (1) Impact-induced seismic activity resulted to the collapse of the Yucatan platform and proximal deposition of local material near the shelf region. In the high-pressure zone between impactor and sedimentary target, jetting accelerated decomposition products (CaO, CO_2, SO_X) in the atmosphere. A hot vapour flow was initiated by target water explosively vaporised and a prolonged energy release during fast-back-reaction of CaO with CO_2 to calcite. (2) Carbonate melts from intermediate target lithologies were excavated with anhydrite and carbonate megablocks and initiated a lateral extending ejecta curtain. Thereby, calcite reformation induced a transport at elevated temperatures. Additional steam generation changed an initially ballistic transport to a flow-like transport. (3) After some 10's of min, the turbulent expanding ejecta plume partially collapsed separating the falling back suevite from impactor material that had been lifted into the stratosphere. Combination of hot silicate melt with carbonates initiated a gas-driven basal flow (T~550–1100°C). In an upper moderately tempered (T~100°C), turbulent ash cloud steam condensed and accretion of ash-sized material formed accretionary lapilli. (4) The impactor component was deposited with the finest ejecta in the K-P clay of El Guayal presumably for weeks to years. (5) The prolonged transport of ejecta in the hot ejecta plume induced the alteration processes observed in the ejecta deposits. It can be concluded that aggregation reduced the amount of ash from the atmosphere and possibly the duration of global darkening. A certain amount of CO_2 has back-reacted to calcite, whereas SO_X gases were completely liberated into the atmosphere. These observations including the abundant presence of carbonate melts support that the amount of CO_2 released to the atmosphere during the Chicxulub impact was overestimated previously.

Table of contents

APPENDIX

List of figures

List of tables

1 Introduction

1.1 Scientific issue and aims of investigation

Impact cratering is a fundamental process in the solar system as documented by the ubiquitous presence of impact craters on planets, moons and satellites. The accretionary history of planetary bodies, and the Moon's origin by collision of the mars-sized planet (e.g. Stevenson, 1987) Theia with the proto-earth 4.52 Ga ago shows the strong influence of impact cratering on Earth's history. The frequency of large scale impacts decreased drastically after the late heavy bombardment between ~3.8 to 4.0 Ga (Grieve 1987; Stöffler & Ryder 2001; Gomes et al. 2005). However, in 1994 large fragments of the disrupted Shoemaker-Levy comet impacted on the planet Jupiter and spectacularly demonstrated that large scale impacts events occur in the solar system even nowadays. Large scale impact cratering can interfere with the evolution of life on the Earth causing mass extinctions by introducing a massive amount of energy in a short time interval to the biosphere (Alvarez et al. 1980). These perspectives have lead to a paradigmatic change of the theory of geoscience from gradualism to catastrophism.

The Chicxulub impact structure is one of the best preserved impact craters on Earth. The target rock of the Chicxulub impact was a layered continental crust with (1) an upper ~3 km thick sedimentary unit of the Yucatán platform, representing a volatile-rich target sequence and (2) the underlying Pan African crystalline silicate basement (Lopez-Ramos 1975; Krogh et al. 1993; Morgan et al. 1997). Current models show that the effects of global darkening by dust particles were less severe than previously thought (Pierazzo et al. 1998). The key role is an environmental change caused by the release of climatically active gases due to the vaporisation of carbonates and sulphates. The SO_X gases cause a short lasting cooling, whereas the CO_2 leads to a long-term global warming (Pierazzo et al. 1998).

On a global scale, ~70 % of the currently known 172 impact craters were targeting sedimentary rocks (Osinski et al. 2003a). However, the influence of sedimentary target rock to the impact process is poorly understood. A better understanding of the behaviour of carbonates and sulphates upon hypervelocity impact and their interaction with the ejecta plume is needed to address the consequences for the global ecosystem (e.g. Ivanov et al. 1996; Pierazzo et al. 1998, 2003).

It is widely accepted that the Chicxulub impact structure on the Yucatán peninsula coincides with the mass extinction observed at the Cretaceous-Palaeogene (K-P) boundary (Hildebrandt et al. 1991; Swisher et al. 1992). The K-P boundary is traditionally named the K/T boundary, but the term "Tertiary" was abandoned during the early 90's by the International Stratigraphic Commission. Therefore, this term is no longer stated in the geologic timescale and replaced by the term "Palaeogene". Based on interpretations of the Yaxcopoil-1 (Yax-1) drill core (Fig. 1-1) –drilled in 2001–2002 in the southern sector of the crater at ~62 km radial distance from the approximate crater centre at Chicxulub Puerto– one working group (Keller et al. 2004) infers that the impact event took place at 300 ka before the K-P boundary. The main arguments presented by this group are that (1) no extraterrestrial component is observed in or above the impactites and (2) planktic foraminifera of latest Cretaceous age are observed in a 50 cm interval on top of the impact breccia interpreted to be deposited in a normal undisturbed marine environment. However, this is a unique view which is not shared by other researchers who were able to demonstrate that the K-P boundary is directly linked to the Chicxulub impact (Arz et al. 2004; Smit et al. 2004; Arenillas et al. 2006).

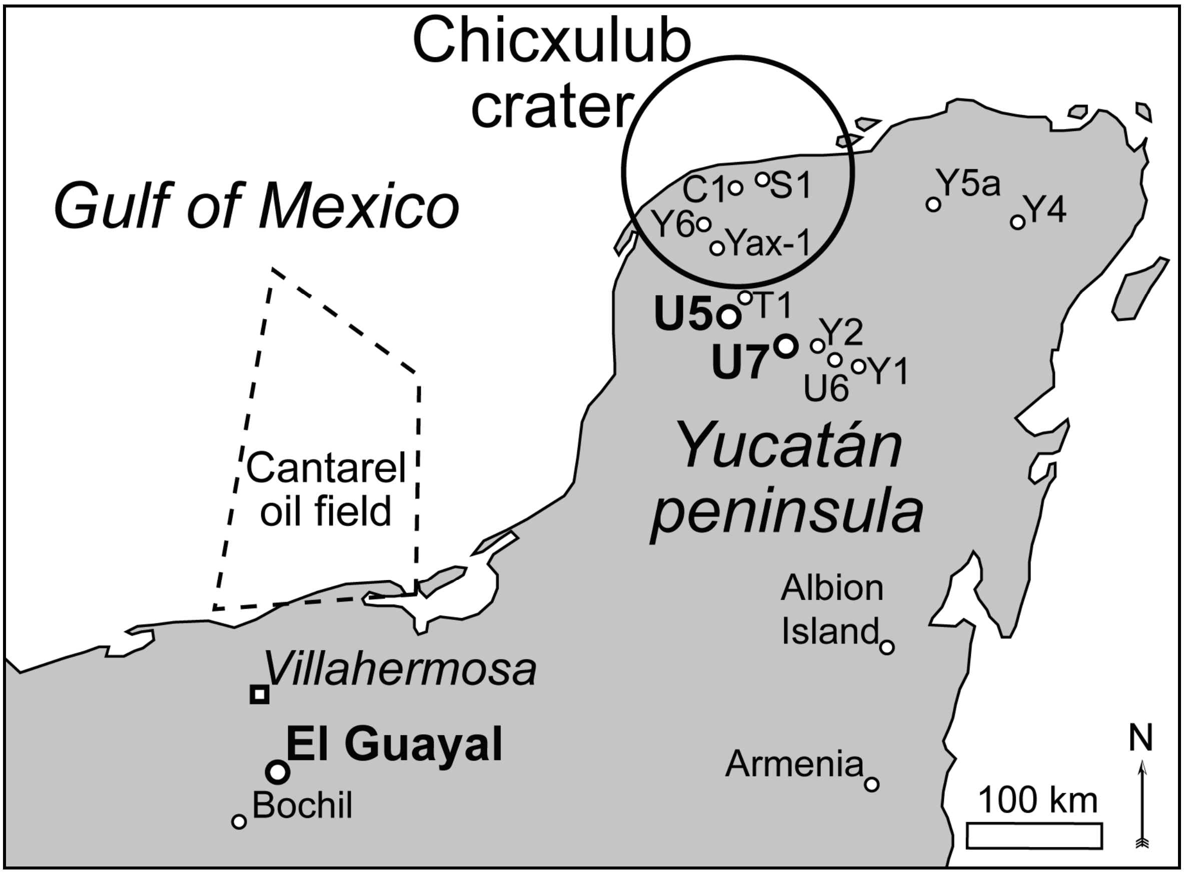

Figure 1-1 Map of the Yucatán peninsula showing the outer crater ring with (1) drill sites within the crater Chicxulub-1 (C1), Sacapuc-1 (S1), Yucatán-6 (Y6), Yaxcopoil-1 (Yax-1), outside the crater Ticul-1 (T1), Yucatán-1 (Y1), Yucatán-2 (Y2), Yucatán-4 (Y4), Yucatán-5a (Y5a), UNAM-5 (U5), UNAM-6 (U6) and UNAM-7 (U7), (2) subaerial exposed proximal ejecta sites of Albion Island and Armenia, and (3) K-P sites of El Guayal, Bochil and the with the K-P boundary associated Cantarel oil field.

The aim of this investigation is to obtain a better understanding on the ejecta distribution and behaviour of the different target lithologies upon hypervelocity impact. A major interest is the response of the sedimentary target within the ejecta plume since these processes (e.g. melting, decomposition, back-reaction of carbonates and sulphates) are so far poorly understood. Therefore, a detailed study on impactites of the marine K-P site of El Guayal ~520 km SW of the crater centre (Fig. 1-1) has been carried out. El Guayal is an ideal candidate for studying the complete deposition of impact debris. This section is a continuous impact sequence with a complete depositional succession of impact related material (Sigurdsson et al. 1995; Griscom 1999; Grajales-Nishimura et al. 2000, Arenillas et al. 2006). The occurrence of unique accretionary lapilli (Grajales-Nishimura et al. 1996, Griscom 1999) is an outstanding feature. A petrographic study on the ejecta components has been carried out with specific focus on carbonate microtextures in order to identify possible sedimentary impact debris. Additionally, a combined chemical study of this sequence contributes to the recent debate if Chicxulub is definitely linked with the global K-P boundary. Furthermore, a comparison of the distally deposited impactites of El Guayal with selected samples of the UNAM borehole near the crater rim will help to improve the current model of ejecta plume formation.

1.2 Basic principles of impact cratering

In general, the following approaches have been used to better understand the complex impact cratering process: (1) Field studies on Earth especially at the Nördlinger Ries impact structure [see Kring (2005) for summary and comparison with the Chicxulub impact structure], (2) remote sensing of craters on Moon, Mars, Mercury and Venus, (3) impact cratering experiments (e.g. Stöffler et al. 1975) and (4) numerical simulations (e.g. Ivanov et al. 1996, Pierazzo & Melosh 2000).

The process of hypervelocity impact of a projectile on a target can be divided into the following three major phases (Melosh 1989). (1) Contact and compression stage: The projectile is decelerated and compressed. Target material is accelerated and strongly compressed resulting in shock waves of several 100 GPa in the zone of first contact. This transformation of kinetic energy results in vaporisation and melting of the impactor and the target rock during decompression from the shocked state. The duration of this stage is much less than one second for most projectiles. (2) Excavation stage (Fig. 1-2, upper image): The shock-weakened target sets into motion initiating an excavation flow. Ejecta are launched on ballistic trajectories out of the crater. Several seconds to minutes upon impact a bowl-shaped transient cavity is formed. (3) Modification stage (Fig. 1-2, lower image): In small craters loose debris is sliding into the crater from the walls. For larger craters the unstable transient cavity collapses. Depending on the initial conditions of the impact event the final complex crater displays a central uplift, a peak-ring or even multi-peak-ring structure. The subject of this work is to derive information about the excavation stage and the formation of the ejecta plume at the Chicxulub impact site from the study of geological sections of the Chicxulub ejecta blanket.

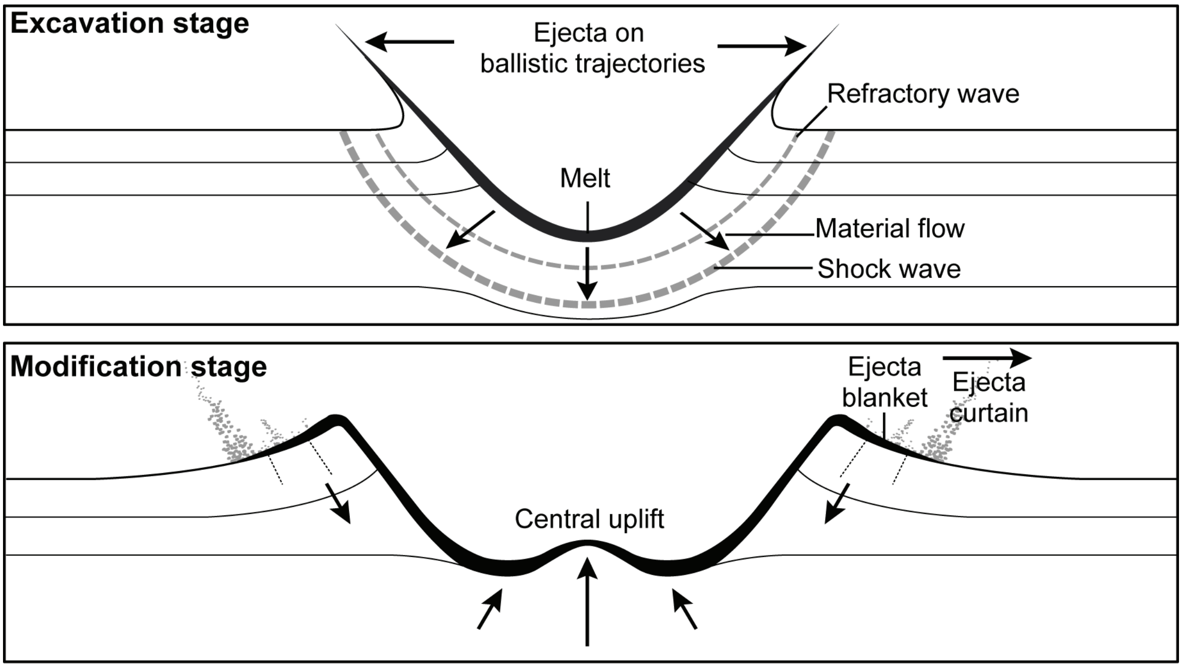

Figure 1-2 Schematic illustration of the excavation and modification stage during impact cratering. Modified after French et al. (1998, Fig. 3.10)

On Earth, the well studied 14–15 Ma old Nördlinger Ries impact structure has an estimated final crater diameter of 24–26 km and a transient cavity of 12–16 km. Its continuous ejecta blanket is named Bunte breccia (Hörz et al. 1983). It is composed of primary crater ejecta and material of the upper lithologies that was reworked by ground surge and secondary cratering transport processes. Due to comparatively low shock pressures and emplacement at ambient temperatures no melt particles or highly shocked minerals are expected in the Bunte breccia. The maximum extension of the continuous ejecta blanket is ~40 km from the crater centre (Engelhardt 1990). The suevite unit (Stöffler & Grieve 1996) is an allochthonous melt-bearing polymict breccia with shocked target rock deposited above the Bunte breccia. It contains shocked particles with solid, molten and condensed material from lower target lithologies. Silicate melt fragments in the suevite have aerodynamically formed shapes (Hörz 1965) indicating a transport through the atmosphere from a highly energetic plume (Fig. 1-3). Crater suevites are termed fall-back suevite and those outside the crater extending up to ~10 km behind the final crater rim are referred to as fall-out suevite. This succession displays an inverse stratigraphy, as the lower Bunte breccia is composed of displaced upper sedimentary target rock, while the suevite contains abundant silicate melt particles excavated from lower target lithologies.

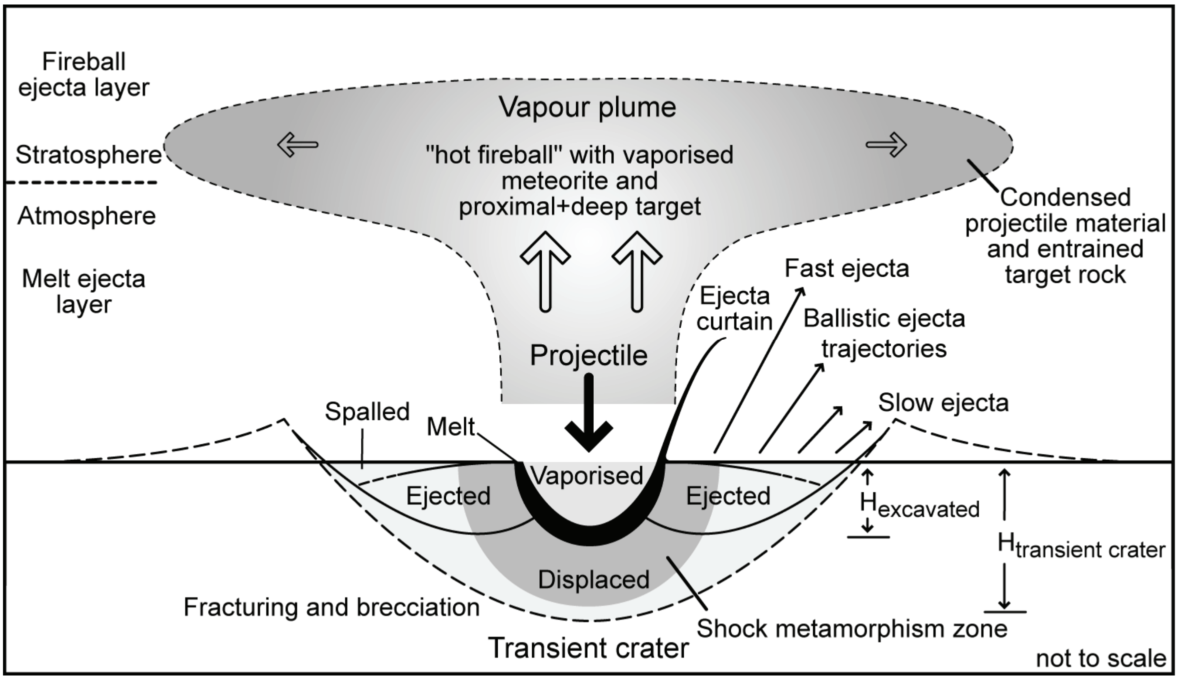

Figure 1-3 Cross section through the transient crater showing the discreet zones from where the shock-metamorphosed materials are derived, the ballistically emplaced ejecta curtain and the formation of the vapour plume. Modified after French et al. (1998, Fig 3.5).

Observations from impact craters on other planets and the Moon reveal insights which are important for interpreting the ejecta blanket of terrestrial impact craters. Studies of impact crater deposits on the Moon predict a ballistically emplaced, low energy ejecta curtain (Oberbeck 1975). Images of surface structures on Mars and Venus show that the continuous ejecta blanket is spreading much farther compared to the continuous ejecta blanket at the Ries crater. Some ejecta blankets on the terrestrial planets have been deposited as multiple lobes as seen on rampart craters indicating a more complex depositional system than expected from pure ballistic emplacement. Such behaviour may be explained by the presence of water or ice (e.g. Carr et al. 1977; Wohletz & Sheridan 1983; Reiss et al. 2005) or by atmospheric interactions (e.g. Schultz 1992; Barnouin-Jha & Schultz 1996, 1998).

1.3 Major characteristics of the Chicxulub impact structure and its ejecta deposits

1.3.1 The Chicxulub impact structure

The Chicxulub impact structure has a diameter of ~180 km and represents a peak-ring or multi-peak-ring impact basin (Fig. 1-4) formed by a projectile with a diameter of ~10–14 km (Hildebrand et al. 1991; Swisher et al. 1992; Sharpton et al. 1993; Ivanov et al. 1996; Melosh 2001; Morgan et al. 2002; Stöffler et al. 2004). The present structure has been formed by the collapse of the transient cavity of ~100 km diameter and ~30 km depth with excavation depths of ~15 km (e.g. Ivanov et al. 1996; Pierazzo et al. 1998; Pierazzo & Melosh 1999; Morgan et al. 1997, 2000).

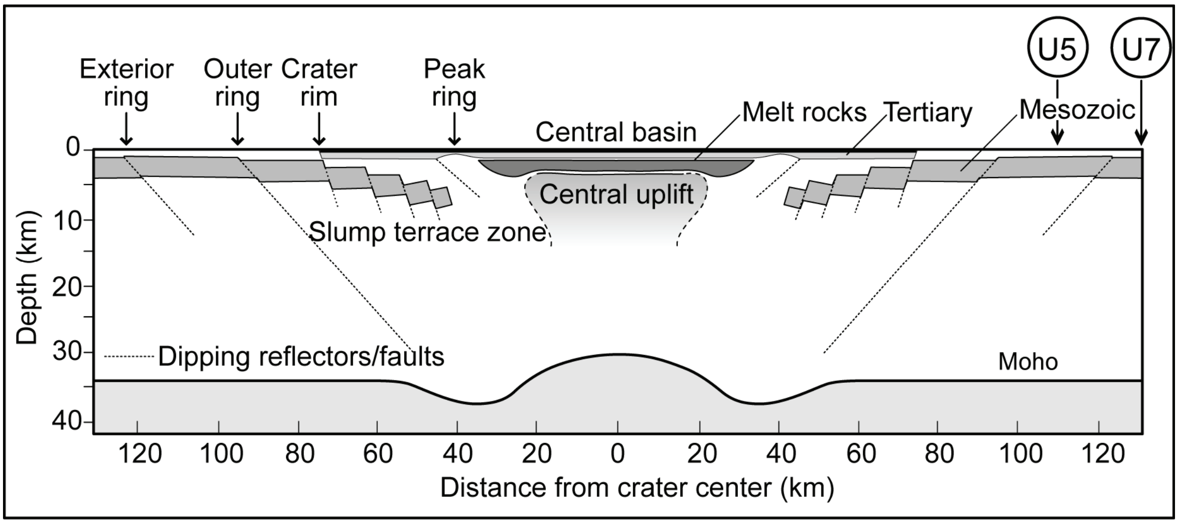

Figure 1-4 Schematic cross-section of the Chicxulub impact crater morphology with the location of the UNAM-5 (U5) and UNAM-7 (U7) boreholes. Modified after Melosh (2001).

The impactites of the Chicxulub impact structure have been sampled by several boreholes (Fig. 1-1) in and around the crater by Petroleos Mexicanos (PEMEX) and the Universidad Nacional Autónoma de México (UNAM) near the crater rim. Between 2001 and 2002, the Yax-1 borehole, which was financed by the International Continental Drilling Program (ICDP), the Chicxulub Scientific Drilling Project (CSDP) and UNAM, has been specifically drilled to study the impact crater.

Two petroleum exploration wells (Chicxulub-1 and Sacapuc-1) are within the transient crater. One petroleum exploration well (Yucatán-6, Y6) and one borehole (Yax-1) are located between an uplifted peak ring and the final crater rim. The region outside the final crater has been drilled by five petroleum exploration wells (Ticul-1, Yucatán-2, Yucatán-5a, Yucatán-1, and Yucatán-4). The three shallow boreholes (UNAM-5, UNAM-6, UNAM-7) were drilled to specific study the continuous ejecta blanket near the crater rim.

A coherent impact melt layer of unknown thickness is located in the crater and topped by a polymict suevite breccia with altered impact melt fragments (e.g. Kring 2005). Those polymict suevite breccias have been described in the Y6 borehole (e.g. Kring et al. 1991; Hildebrand et al. 1991; Sharpton et al. 1996; Claeys et al. 2003) and in the Yax-1 borehole (e.g. Dressler et al. 2004; Hecht et al. 2004; Kring et al. 2004; Stöffler et al. 2004; Tuchscherer et al. 2004a). The suevite is stratified showing variations with respect to the texture, grain size and composition. Additionally, suevitic dikes have been observed (Wittmann et al. 2004) indicating that not all suevites are necessarily transported aerodynamically. Thus, the petrographic term suevite (proximal impactite comprising an allochthonous breccia with shocked target rocks and cogenetic melt particles; Stöffler & Grieve 1996) is better used without the implication of a transport mechanism. Compared to the Nördlinger Ries impactites, the origin and emplacement of the Chicxulub impactites is more complicated as the later event released a substantially larger amount of energy.

1.3.2 Drill core sections within the Chicxulub ejecta blanket (UNAM drilling project)

Between 1994 and 1995 the UNAM drilled eight shallow wells between 63.1 m and 702.4 m depth in and around the crater (Urrutia-Fucugauchi et al. 1996a, b). Each hole was fully cored, recovering a total of 2.62 km of rock with a recuperation rate of 98 %. Of the eight boreholes only UNAM-5, UNAM-6 and UNAM-7 encountered the Chicxulub impactites. The others sampled background Cenozoic strata but are still useful to constrain variation in thickness of the Cenozoic crater fill.

UNAM-5 is located close to the village of Santa Elena at ~3 km in the direction of Muna. This corresponds to a distance of ~105 km from the crater centre (Puerto Chicxulub). UNAM-7 is located at ~2.5 km from downtown Tekax to the direction of Ticum, and ~126 km from the crater centre. UNAM-6 is located ~3 km from the village of Peto in the direction of Dziuche, ~151 km from the crater centre. UNAM-5 is located near the crater rim directly on the outside flank of the outer ring visible of the seismic data (Morgan & Warner 1999). All three boreholes are outside the crater and encountered thick sequences of polymict breccia with various lithological compositions (Fig. 1-5). These three wells provide a cross

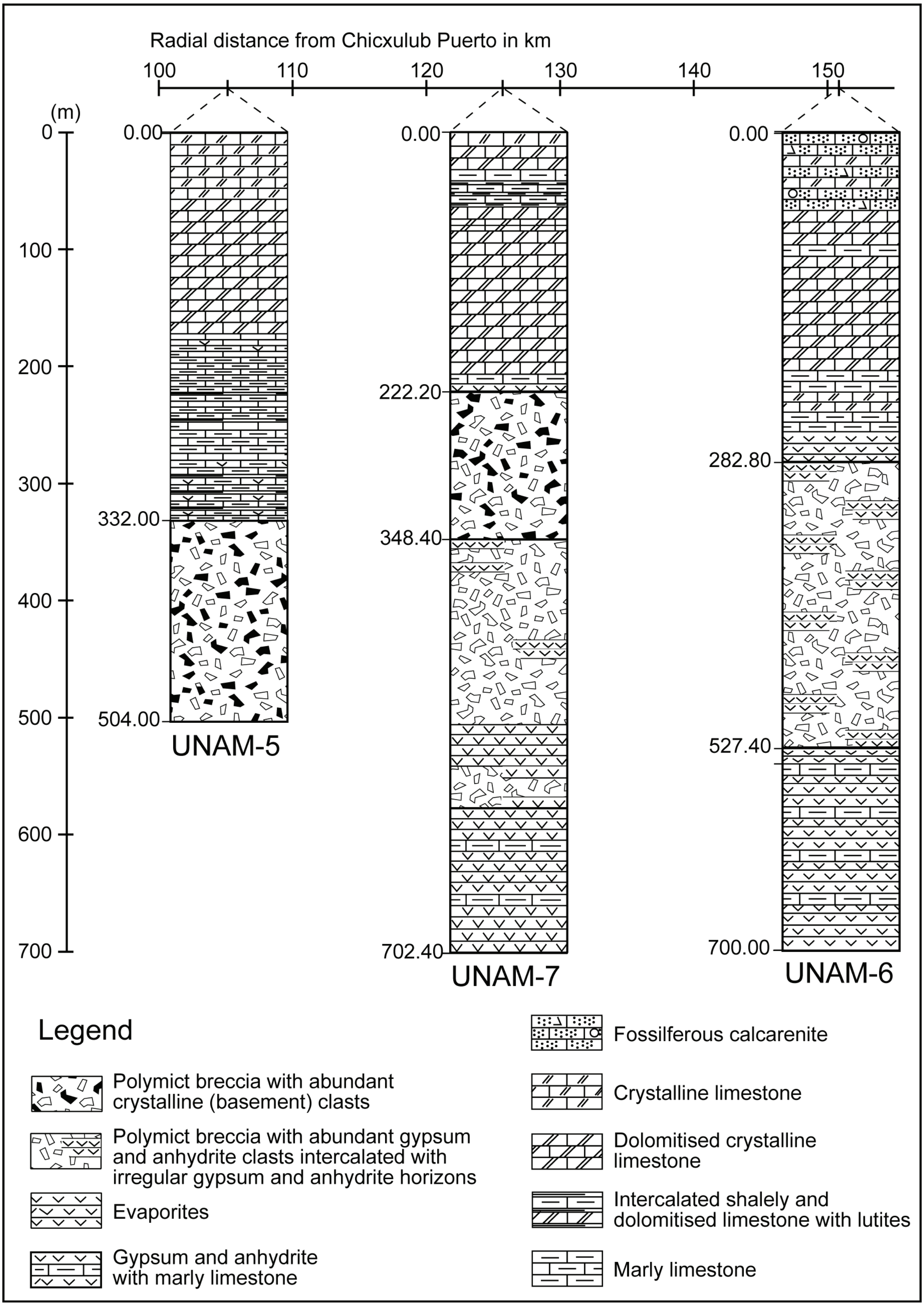

Figure 1-5 Stratigraphy of the UNAM boreholes which encountered the Chicxulub ejecta blanket (modified after Urrutia-Fucugauchi et al. 1996a, b).

section of ejecta blanket thickness and lithology from the crater rim to the seismic disturbance interpreted as a potential exterior ring by Morgan & Warner (1999).

UNAM-6, the most distal borehole, encountered an evaporite-rich polymict breccia that shows irregularly intercalated gypsum and anhydrite horizons between 282.8 to 527.4 m (Urrutia-Fucugauchi 1996a). UNAM-6 bottomed out in evaporite layers interpreted to be representative of the Mesozoic pre-impact target rock. However, it cannot be excluded that these stratified layers may represent displaced large blocks. In the UNAM-5 core at a depth from 332.0 m to 504.0 m and at UNAM-7 from 222.2 to 348.4 m the polymict breccia contains highly shocked crystalline (basement) clasts and abundant silicate melt particles. This unit is comparable to a suevite (Sharpton et al. 1999): In the suevitic breccia of UNAM-5 the silicate component averages ~60 wt.% and varies at UNAM-7 between 25–43 wt.%. In the UNAM-7 borehole at 348.4 m this suevite overlies an evaporite-rich polymict breccia, where the silicate component drops to 3–4 wt.%. This evaporite-rich breccia is intercalated with evaporite horizons (Urrutia-Fucugauchi et al. 1996b; Sharpton et al. 1999; Schönian et al. 2003, 2006) and is comparable to the polymict breccia of UNAM-6. The succession of the UNAM-7 drill core is similar to the inverse stratigraphy observed at the Nördlinger Ries crater (Urrutia-Fucugauchi et al. 1996b), where silicate melt-rich suevite is deposited above the silicate melt lacking Bunte breccia. Sharpton et al. (1999) noted that the preservation of this boundary, the high content of primary ejecta and preservation of ejecta as 60 m thick megaclasts are in contrast with ejecta characteristics predicted by pure ballistic sedimentation. Those features indicate that these deposits have possibly been emplaced as flow deposits as highly heated masses of gas-charged debris transported more or less horizontally (Sharpton et al. 1999).

1.3.3 The Cretaceous-Palaeogene (K-P) boundary

The K-P boundary is correlated worldwide using evidence such as impact products like shocked minerals, microspherules, an anomaly of the platinum group elements (PGE), and Ni-rich spinels (Fig. 1-6). A total of 101 from all 345 known K-P boundary sites contain impact related products (Claeys et al. 2002). The Global Standard Stratotype Section and Point (GSSP) for the K-P boundary is located in El Kef, Tunisia. According to Remane et al. (1998) the K-P site El Kef has the most expanded and continuous sedimentation record worldwide. It consists of a 50–60 cm thick clay layer with a 2–4 mm thick red clay layer at the base which contains impact related products.

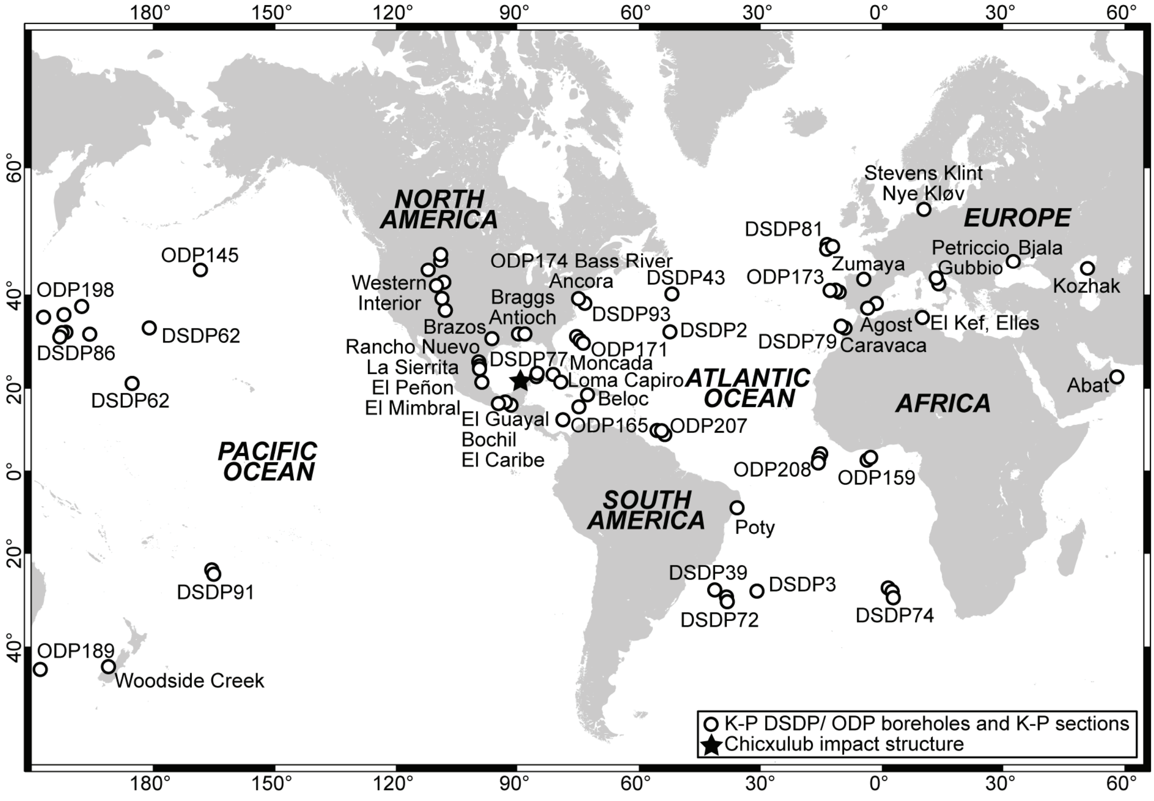

Figure 1-6 Overview of Deep Sea Drilling Project (DSDP) and Ocean Drilling Program (ODP) boreholes and outcrops on land that include impact debris at the K-P boundary (modified after Schulte & Kontny 2005).

On a global scale, the distal ejecta occur in a several millimetre thick layer and extend to a centimetre thick layer at 2500–4000 km from the Chicxulub crater (Smit 1999). At the Western Interior (New Mexico, Colorado, Wyoming, Montana) many terrestrial K-P sections at 2000–4000 km away from Chicxulub show a dual-layer stratigraphy (Bohor et al. 1984; Bohor et al. 1987; Izett 1990): There, the impact layers have a maximum thickness of 2 cm and consist of a lower spherule layer and a thin upper layer; the latter is termed the fireball layer due to the enrichment in PGE. According to Smit (1999) the deposition of the distal sites in the Western Interior happened almost simultaneous due to the amalgamation of those two separate layers and *"not even a single season of fallen leaves separates the (spherule and fireball) layers"*. Thus, this dual-layer stratigraphy present in the Western Interior has been explained by the much faster arrival of low energy ejecta on ballistic trajectories forming the lower layer and the longer deposition time of high energy ejecta expanding turbulently above the atmosphere to form the upper fireball layer (Kring & Durda 2002). A similar scenario has been proposed for marine K-P sites deposited in shelf regions of the North American continent at the Gulf of Mexico <800 km from Chicxulub (Fig. 1-7). There, the multiple impact layers are divided by a sandstone complex from the earliest Palaeocene sediments. This sandstone complex has been interpreted as tsunami deposits (Smit et al. 1996) deposited within several days above the ejecta bearing layer and below the PGE-enriched units. Contrary, Keller et al. (2003) argued that multiple spherule layers in NE Mexico indicate multiple impact events. However, Schulte et al. (2003) have documented that multiple spherule layers in NE Mexico are produced by subsequent remolding, reworking, and redeposition.

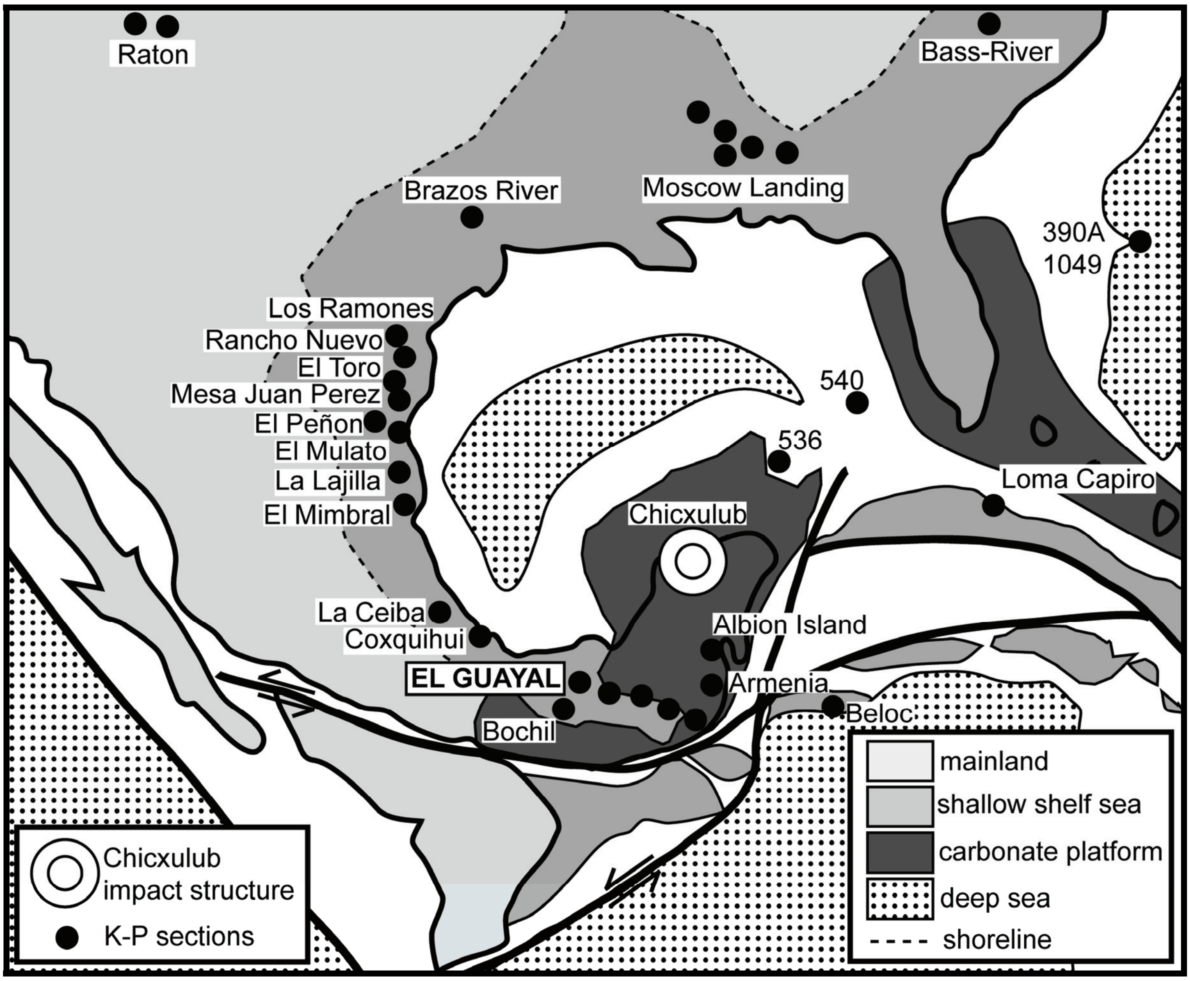

Figure 1-7 Palaeogeographic reconstruction at Late Cretaceous of the Gulf of Mexico showing K-P sites (with names) and DSDP-ODP sites (as numbers). Redrawn after Smit (1999).

In the vicinity of the crater, close to the energy source, the deposition of ejecta is complicated by accompanying and subsequent perturbations of the sea floor. This is documented in the basinal Gulf of Mexico and Caribbean Sea by several 10's of metres thick sedimentary gravity flows –most likely triggered by platform collapse– which are associated with ejecta-bearing deposits (Alvarez et al. 1992; Bralower et al. 1998; Grajales-Nishimura et al. 2000; Takayama et al. 2000; Kiyokawa et al. 2002; Alegret et al. 2005). At the Deep Sea Drilling Project (DSDP) sites 536 and 540 (Fig. 1-7), there is a succession of (1) a 45 m thick submarine landslide deposit, (2) followed by a >2.5m thick ejecta-bearing reworked unit and (3) topped by a 50 cm interval of calcareous mudstone with an Ir anomaly that was deposited above Cretaceous limestone and underlies Tertiary sediments (Alvarez et al. 1992). Alvarez et al. (1992) suggested that these deposits are evidence for a K-P age for the nearby Chicxulub impact crater.

On the southern Yucatán peninsula, the Chicxulub ejecta blanket has been identified at sites 280 to 470 km from the crater centre (e.g. Albion Island and Armenia, Fig. 1-1 and Fig. 1-7) mainly by the presence of shocked quartz particles (Pope et al. 2005; Kenkmann & Schönian 2006). Those K-P sections give useful insight on the early stage of ejecta emplacement. However, due to rapid weathering and erosion no PGE-enriched impactor component has been identified.

Since the drilling of the Yax-1 borehole, it is a matter of debate if the Chicxulub impact structure is linked with the K-P boundary. On top of the crater suevites a ~50 cm thick sandstone interval is interpreted by Keller et al. (2004) as undisturbed marine sedimentation. Those authors interpreted foraminifera in this interval to be of Late Cretaceous age and, thus, suggested predating the Chicxulub impact event at 300 ka before the K-P boundary. Contrary, Arz et al. (2004) and Smit et al. (2004) interpreted this crossbedded unit to be reworked and concluded that those sediments represent the uppermost part of the initial crater infill deposited during the last phases of the catastrophic event.

Finally, the controversy, if Chicxulub is linked with the K-P boundary, mainly originates due to differing interpretations, if the deposition at K-P sites in the Gulf of Mexico and at the Yax-1 bore hole happened in an undisturbed environment, or if those deposits are reworked during or after the Chicxulub impact.

1.3.4 The K-P boundary sequence of El Guayal

The K-P boundary section of El Guayal (17°32´6.15´´N, 92°36´15.1´´W; Grajales-Nishimura et al. 2000) is located at ~520 km southwest from the centre of the Chicxulub impact structure (Fig. 1-1). El Guayal is located ~60 km south-south-east from Villahermosa, Tabasco, Mexico. Palaeogeographic reconstructions show that this area represented the shelf region of the Yucatán peninsula (Fig. 1-7). The riverbanks of El Guayal expose a K-P section of ~100 m thickness and can be divided into four lithostratigraphic units (Grajales-Nishimura et al. 2000; Fig. 1-8):

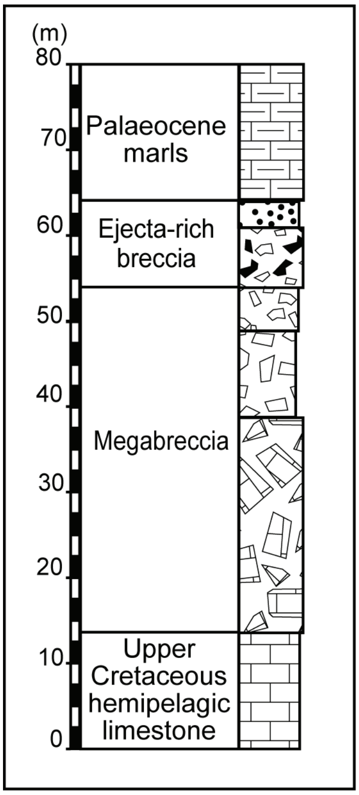

Figure 1-8 Stratigraphic column of the K-P boundary sequence of El Guayal. Modified after Grajales-Nishimura et al. (2000).

The basal unit consists of ~14 m of hemipelagic grey limestone beds containing biomicrite with planctonic foraminifera *(Trinitella scotti, Racemiguembelina fructicosa, Contusotruncana contusa)* of middle to late Maastrichtian age. The uppermost Cretaceous is not present, and most likely was eroded during deposition of a ~40 m thick chaotic coarse calcareous megabreccia. This megabreccia has large limestone blocks (up to 2 m diameter) at the base and is progressively fining upward. It contains mainly blocks of platform carbonates with rudists and coral fragments. In the breccia matrix fossils of middle to late Maastrichtian age *(Contusotruncana contusa, Racemiguembelina fructicosa)* have been found.

An ~11 m thick, fining upward unit marks the first occurrence of impact related material from the Chicxulub crater. At the base, a microbreccia contains centimetre sized limestone fragments, sub-millimetre sized shocked quartz and altered basement clasts. It is followed by a succession of medium to fine grained loose calcareous sandstone and siltstone beds with accretionary lapilli at the base (Grajales-Nishimura et al. 1996; Griscom et al. 1999). This is covered by a 1–2 cm thick brown to yellowish layer of fine clay. The upper unit consists of calcareous shales with laminated micritic limestone beds at the base. Here, the lowermost Danian *H. holmdelensis* subzone (=Biozone P0) was identified just above the Chicxulub impactites proving that such bed is chronostratigraphically equivalent to the K-P boundary (Arenillas et al. 2006).

Grajales-Nishimura et al. (2000) correlated the stratigraphic succession of El Guayal with the K-P boundary sequence of Bochil located ~53 km southwest of El Guayal and with the offshore Cantarel oil fields ~250 km north of El Guayal (Fig. 1-1). Those oil-producing units at the western Campeche marine platform had a daily production of 1.3 million barrels in the year 2000 (~3 % of the world's production) and are probably the most important oil-field related to an impact event. Whereas a ~300 m thick dolomitic carbonate breccia is the oil-producing reservoir facies, the overlying ~30 m thick reworked ejecta and breccia lenses represent the sealing facies. At Bochil, a succession of >60 m thick megabreccia and ~5 m thick ejecta-bearing breccia is comparable to those of El Guayal. At Bochil, the top of the sequence is marked by clay laminae where a 1.5 ppb Ir anomaly was detected (Montanari et al. 1994).

Current depositional models for El Guayal

Depositional models of Sigurdson et al. (1995) and Grajales-Nishimura et al. (2000) for the K-P boundary site of El Guayal do not distinguish between a ballistic ejection of ejecta material and deposition of impact debris in a turbulent ejecta plume. Based on early work on trace elements in clay minerals, Sigurdsson et al. (1995) suggested that the clay minerals of the ejecta-bearing units at El Guayal represent altered impact melt. In particular, the Ni enrichment in the upper clay layer suggests an extra-terrestrial component and the modal abundance of altered impact melt increases towards the upper clay layer. Sigurdsson et al. (1995) interpreted the deposits as a mixture of locally slumped material and primary and secondary crater ejecta from a ballistically emplaced carbonate-dominated ejecta curtain. This deposition was accompanied and followed by ballistically transported impact glass spherules. Griscom (1999) developed a more detailed depositional model: (1) Primary and secondary crater ejecta teared up the sea floor and created the 40 m thick megabreccia in ~10 min, (2) earthquakes from the shockwaves triggered mass flows which transported and deposited sand from near-shore sands, (3) accretionary lapilli from the ejecta plume settled through the water column, (4) tsunami waves deposited fine sand for many hours and (5) dust from the expanding plume fell out of the stratosphere for a period of weeks. Grajales-Nishimura et al. (2000) agreed with Griscom (1999) that the upper part of the ejecta-bearing unit at El Guayal was reworked by tsunami waves which were reflected back and forth across the Gulf of Mexico palaeogeography. However, Grajales-Nishimura et al. (2000) documented that the basal megabreccia represents the collapse of the Yucatán carbonate platform margin as a consequence of impact-induced seismic shacking. Thus, the megabreccia was deposited by sedimentary gravity flows prior to the arrival of ballistic ejecta at the depositional site.

2 Samples and analytical methods

2.1 Optical microscopy

El Guayal samples

The El Guayal samples have been collected by P. Claeys during field trips in 1998 and 1999. The locations of the 42 samples within the stratigraphic context are shown in Fig. 2-1. Five samples of the megabreccia have been cut and polished for macroscopic studies. Petrographic examinations were carried out on one thick section 19x6 cm in size of the lowermost megabreccia on sample G0, and on 45 thin sections on bulk rock samples of the Ir- and G-series from the uppermost megabreccia, microbreccia, accretionary lapilli unit and clay unit as well as on individual accretionary lapilli and particles from the accretionary lapilli unit (Tab. 2-1).

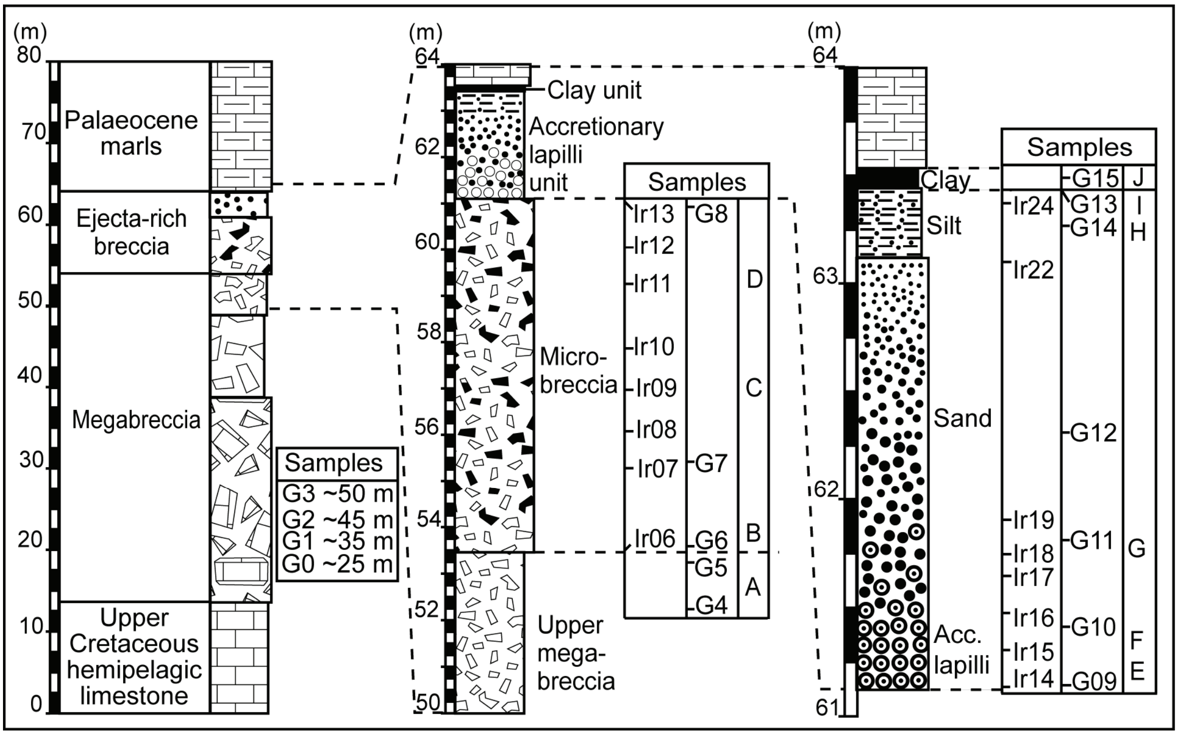

Figure 2-1 Stratigraphic column and sample location of the K-P boundary sequence of El Guayal. Left column as in Fig. 1-8 (modified after Grajales-Nishimura et al. 2000). Middle column magnified figure of the ejecta-rich breccia and its subdivisions proposed in this study. Right column magnified figure of the accretionary lapilli unit and clay unit (Acc. lapilli: accretionary lapilli).

For a general overview, 14 thin sections of the Ir-sample series have been photographed with a binocular. Four individual pictures were needed for a composite picture of one thin section. Crossed polarisers were chosen as the altered silicate melt particles are better recognised than in plane polarised light. All thin sections were examined by optical microscopy. Immersion oil was used for images with objectives 50x and 100x for optimal resolution.

Table 2-1 Number of thin sections of the different units present at El Guayal. See Fig. 2-1 for detailed stratigraphic sample location.

Unit	No. of thin sections	Details
Uppermost megabreccia	2	
Microbreccia	13	
Accretionary lapilli unit	29	a) Lower accretionary lapilli unit: 20 (6 of bulk rock, 8 of individual accretionary lapilli, 6 of individual particles) b) Middle to upper accretionary lapilli unit: 7 c) Transition zone uppermost accretionary lapilli unit to clay unit: 2
Clay unit	1	

Table 2-2 UNAM drill core sample list.

Well	Sample No.	Depth (m)	Box	Diameter	Length (cm)	Quantity
UNAM-5	1	357.40 - 357.50	107	BQ	5	half
	2	409.77 - 409.82	125	BQ	5	half
	3	464.78 - 464.88	143	BQ	10	half
	4	480.37 - 480.42	148	BQ	5	half
	5	500.55 - 500.60	155	BQ	5	half
UNAM-7	1	267.40 - 267.50	97	NQ	10	quarter
	2	307.85 - 307.95	111	NQ	10	quarter
	3	381.40 - 381.50	135	NQ	10	quarter

BQ: 3.65 cm, NQ: 4.76 cm

UNAM borehole samples

The studied samples are shown in Tab. 2-2. All of the five samples of UNAM-5 belong to a polymict breccia with abundant crystalline (basement) clasts (Fig. 2-2). At UNAM-7, the upper two samples (UNAM-7-267.40, UNAM-7-307.85) are also derived from a polymict breccia with abundant crystalline (basement) clasts. The lower sample UNAM-7-381.40 belongs to the unit of polymict breccia with abundant evaporite clasts which is intercalated with evaporite horizons. Those samples were studied macroscopically and photomicrographs were taken using a binocular. Detailed petrographic examinations were carried out on one thin section of sample UNAM-7-381.40.

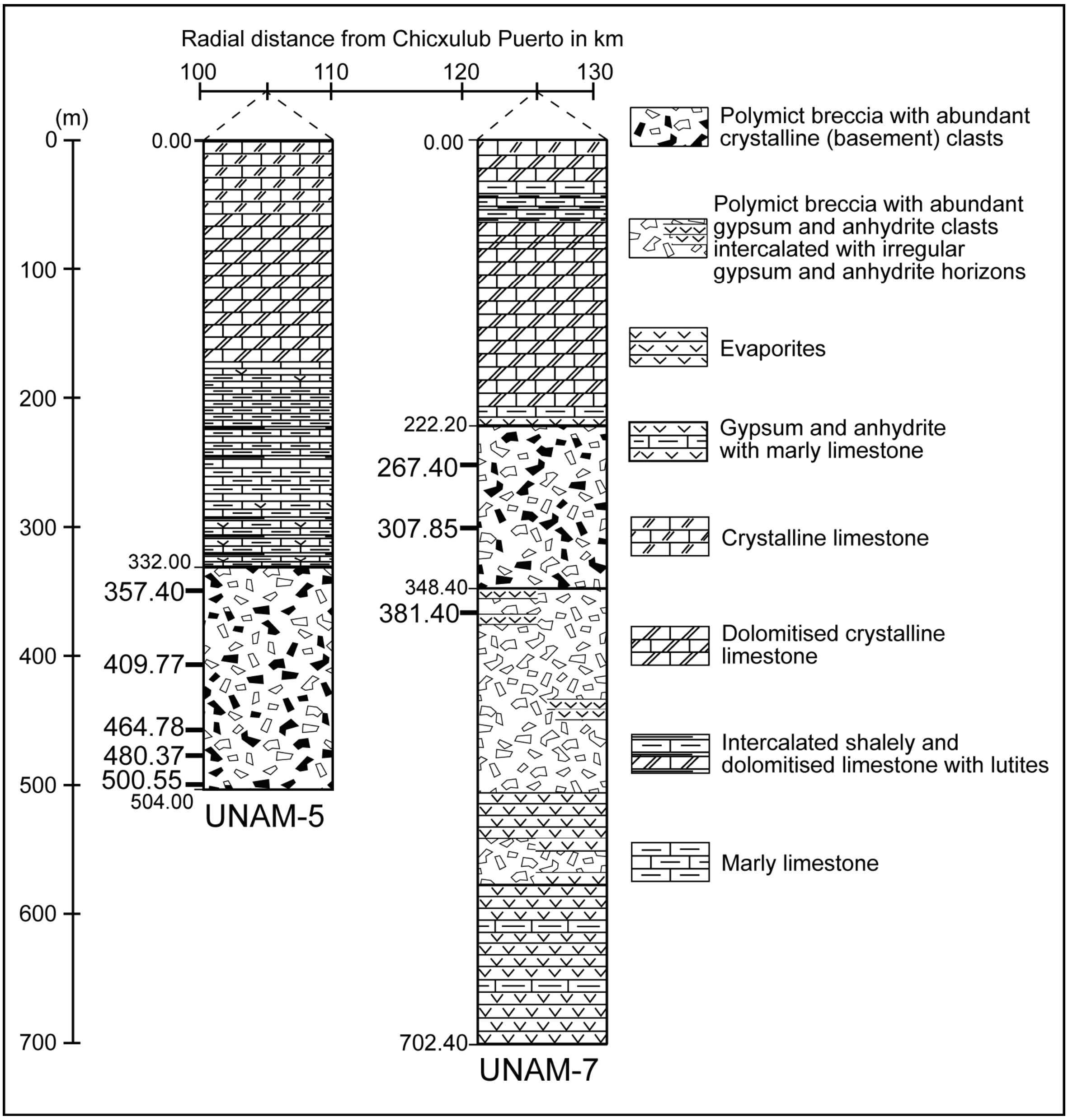

Figure 2-2 Stratigraphic column of the UNAM-5 and UNAM-7 boreholes (modified after Urrutia-Fucugauchi et al. 1996a, b) showing the location of the studied samples.

2.2 Scanning electron microscopy

Selected areas of the thin sections were chosen for scanning electron microscopy (SEM) studies using a JEOL JSM-6300 instrument with a RÖNTEC X-ray energy dispersive analytical system. To enable navigation and assist in the choice of areas to be analysed, composite SEM images of two accretionary lapilli were prepared in BSE mode. One map consists of 149 individual images each of a resolution of 640 x 480 pixels (Fig. A3-5). The printout on A0 sized paper represents a 74.5x magnification. The second lapillus consists of 155 pictures each with a resolution of 1024 x 768 pixels. The higher resolution allowed the printout on two A0 posters representing 155x magnification. Furthermore, a third lapillus composite picture has been prepared using 76 pictures from reflected light microscopy.

2.3 Electron microprobe analyses

Quantitative analyses of silicate melt particles, feldspars, quartz and carbonates were acquired using a JEOL JXA-8800 electron microprobe (EMP). The analyses were performed on the manual modus which allows a better control of the measured position. Analyses were calibrated using certified reference standards for electron microprobe analyses of the United States National Museum (Jarosewich et al. 1980, 1987) and Astimex Scientific Limited, MINM25-53.

For silicate minerals an acceleration potential of 15 kV, a beam current of 15 nA with an electron beam diameter of 3 µm, and for small grains beam sizes of 1 µm, were used. Accumulation time was 20 s on the peak and 10 s on the background. To minimize loss of the volatile elements, Na and K were analysed first. Carbonate analyses were performed at 10 kV, 10 nA, and using a beam diameter of 10 µm and accumulation of 10 s for the peak and 5 s for the background. The carbonate analyses have been recalculated to a 100 % total after the amount of CO_3^{2-} corresponding to the measured Ca, Mg and Fe was calculated. This approach was chosen in order to avoid the automatic procedure of the EMP which assumes a CO_3^{2-} anion for all cations, including Si and Al, which is certainly wrong.

Detection limits for all elements were determined from a large number of standard analyses: 105 on basaltic glass, 101 on tektite glass, 49 on microcline, 53 on plagioclase and 31 on anorthoclase. In Tab. A2-3 the detection limit is equivalent 3 times the background variation. For the detection limit, the average background for both peak sides has been determined and subsequently the standard deviation of standard analyses calculated. The highest detection limit for each element of all measured standards is the assumed detection limit. For mean values, the detection limit has been applied, when the majority of the single analyses for each element were below the detection limit. In the case that the majority or equal number of analyses were above the detection limit, the values above the detection limit were used to estimate the mean value.

In order to control the stability of the EMP calibration, certified reference standards were measured after each 10 measurements. Tab. A2-4 compares the provided certified standard composition with measured standard analyses.

Table 2-3 Sets of international standards used for EMP calibration.

Standard	Element
Plagioclase (Labradorite), Lake Country, OR, USNM 115900	SiO_2, Al_2O_3, CaO, Na_2O
Ilmenite, Ilment. Mtns., Miask, USSR, USNM 96189	TiO_2, FeO, MnO
Microcline, location unknown, USNM 143966	K_2O
Kaersutite, Astimex Scientific Ltd., MINM25-53	TiO_2
Calcite, Astimex Scientific Ltd., MINM25-53	CaO
Chromium augite, Black Rock Summit Flow, Nye County, Nevada, NMNH 164905	SiO_2, MgO
Dolomite, Astimex Scientific Ltd., MINM25-53	MgO

2.4 Cathodoluminescence studies

Cathodoluminescence (CL) microscopy was carried out on selected thin sections. Cathodoluminescence in carbonates is an ideal tool to discriminate different carbonate generations. Its intensity is dependent on the counterbalance of activators like Mn^{2+} or rare earth elements and quenchers like $Fe^{2+/3+}$, Ni^{2+} and Co^{2+}. Mn^{2+}-activated luminescence has a yellow to orange/ red colour (Machel et al. 1991). Already 10–20 µg/g of Mn^{2+} leads to a detectable luminescence, if the total Fe is <150 µg/g (Machel et al. 1991; Neuser et al. 1996). A hot cathodoluminoscope LUMIC HC3-LM system was operated at 14 kV and 0.08–0.25 mA. A KAPPA Image Base DX 20 HC thermoelectronically cooled camera was used to obtain the low-intensity CL images.

2.5 Chemical analyses

For bulk rock analyses samples were grinded using a metal mortar for a first series. For a second series a corundum mortar has been used to exclude contamination by metal during grinding.

Major and trace elements were determined by X-ray fluorescence spectroscopy (XRF) with a SIEMENS SRS-3000 on glass tablets (Schmitt et al. 2004). PGE concentrations were measured by R. Tagle at the GeoForschungsZentrum (GFZ) Potsdam using an inductively coupled plasma mass spectrometer (ICP-MS) following nickel sulphide fire assay pre-concentration and separation steps (Tagle et al. 2004).

Additional trace element analysis has been performed with a benchtop total reflection X-ray fluorescence (TXRF) spectrometer RÖNTEC PicoTax (now BRUKER AXS S2 PicoFox). Basic principles of this method are explained by Klockenkämpfer (1997); detailed technical specifications of this spectrometer are given by Stosnach (2005). A small quantity (some mg) of solid bulk rock powder of the El Guayal samples has been transferred on an acrylic glass sample carrier. Fe_2O_3 data of XRF analyses has been used as an internal standard. For comparison two analyses of one altered silicate melt particle from sample UNAM-7-307.85 were carried out. For the UNAM samples no XRF data were available for internal standardisation. Thus, a liquid internal standard (100 µl Ga standard solution, Merck 1g/l) was added to 1.5 ml of an organic detergent (1% aqueous Triton X100$^{©}$) with 21 respectively 33 mg solid sample material. After homogenisation 10 µl of the suspension has been first vaporised and then measured on an acrylic glass sample carrier. Measurement time for all of the samples was 10 minutes per sample. TXRF analyses show that the concentration of light elements ($Z<19$) are systematically underestimated due to matrix (absorption) effects (Klockenkämpfer 1997) when compared with XRF analyses. Hence, these data allow only semiquantitative interpretations.

2.6 Modal composition calculations

XRF bulk rock and EMP phase composition were used to calculate the proportion of given phases. Modelling of the modal composition for 12 samples have been done using the mean value of (1) the constrained mixing model of Le Maitre (1979) and (2) the method of the least square (Davis 1973) using an excel spreadsheet. For the lower accretionary lapilli unit, where individual accretionary lapilli are common, individual calculations for each accretionary lapilli and the host rock have been carried out. Several calculations with different phase combinations were carried out for each sample. These calculations with negative phase proportions were rejected. In order to control the accuracy of the result the bulk rock concentration of each element was calculated (see Tab. 3-9 for examples). The deviation of each element from the control composition with the reference composition is used to calculate the cumulative error for the calculation. Results with lowest cumulative error were assumed to be the most accurate phase combination. In the case of a large deviation of one or more elements, additional proposed phases were added to minimise the deviation for these elements and the resulting cumulative error (Tab. 3-9).

3 Results

3.1 Stratigraphy, lithology and petrography of the El Guayal section

On top of the ~14 m thick Upper Cretaceous hemipelagic limestone an impact induced breccia succession is exposed and underlies Palaeocene marls (Fig. 2-1, left stratigraphic column). In this section the four subdivisions of this unit (megabreccia, microbreccia, accretionary lapilli unit, clay unit; Fig. 2-1, middle stratigraphic column) are described. Here and in the following chapters, the terms sparite and micrite or sparitic and micritic calcite are used to describe the size of calcite crystals in clasts, particles or pore fillings, and the term microcrystalline calcite is used to describe crystal size larger than those at micritic calcite.

Megabreccia

On top of Upper Cretaceous limestone lies a ~40 m thick, clast-supported, monomict carbonate megabreccia (Fig. 2-1, left column). It contains angular to subrounded carbonate fragments in a matrix of carbonate mud with isolated foraminifera and shell fragments. It is jointed and some fragments show stylolites of high amplitudes indicative for pressure dissolution under deep burial conditions. At sample G2 (Fig. 3-1A), the following carbonate microfacies have been identified with a binocular: foraminifera grainstone; intraclastic foraminifera-bearing wackestone; fine detritic packstone; pack- to grainstone with foraminifera, ostracodes and gastropods; biogenous pack- to grain- to rudstone with foraminifera, corals, shell fragments and bryozoan clasts; slight laminated mudstone; mud- to wackestone with small components; foraminifera bearing wackestone; biogenic clasts like Cretaceous rudist bivalves (Hippurites, Radiolitidae). The available samples of the lower megabreccia show clast sizes larger than the sample size and blocks of up to 2 m diameter have been reported (Grajales-Nishimura et al. 2000). At stratigraphic level of ~50 m a maximum clast size of >5 cm is observed. The overlying ~3.5 m thick subunit shows a reduction in clast size from ~1 cm with rare 2 cm sized clasts at the basis towards 5 mm with some clasts of 1 cm at the top. Microscopic studies of the uppermost megabreccia show that silicate melt particles are absent in the megabreccia. Dolomite is common and silification of calcite is not observed.

Microbreccia

The megabreccia is grading into a ~7.5 m thick polymict carbonate microbreccia. The grey clastic microbreccia is fining upward with clast sizes from <5 mm (rarely 2 cm) at the base to

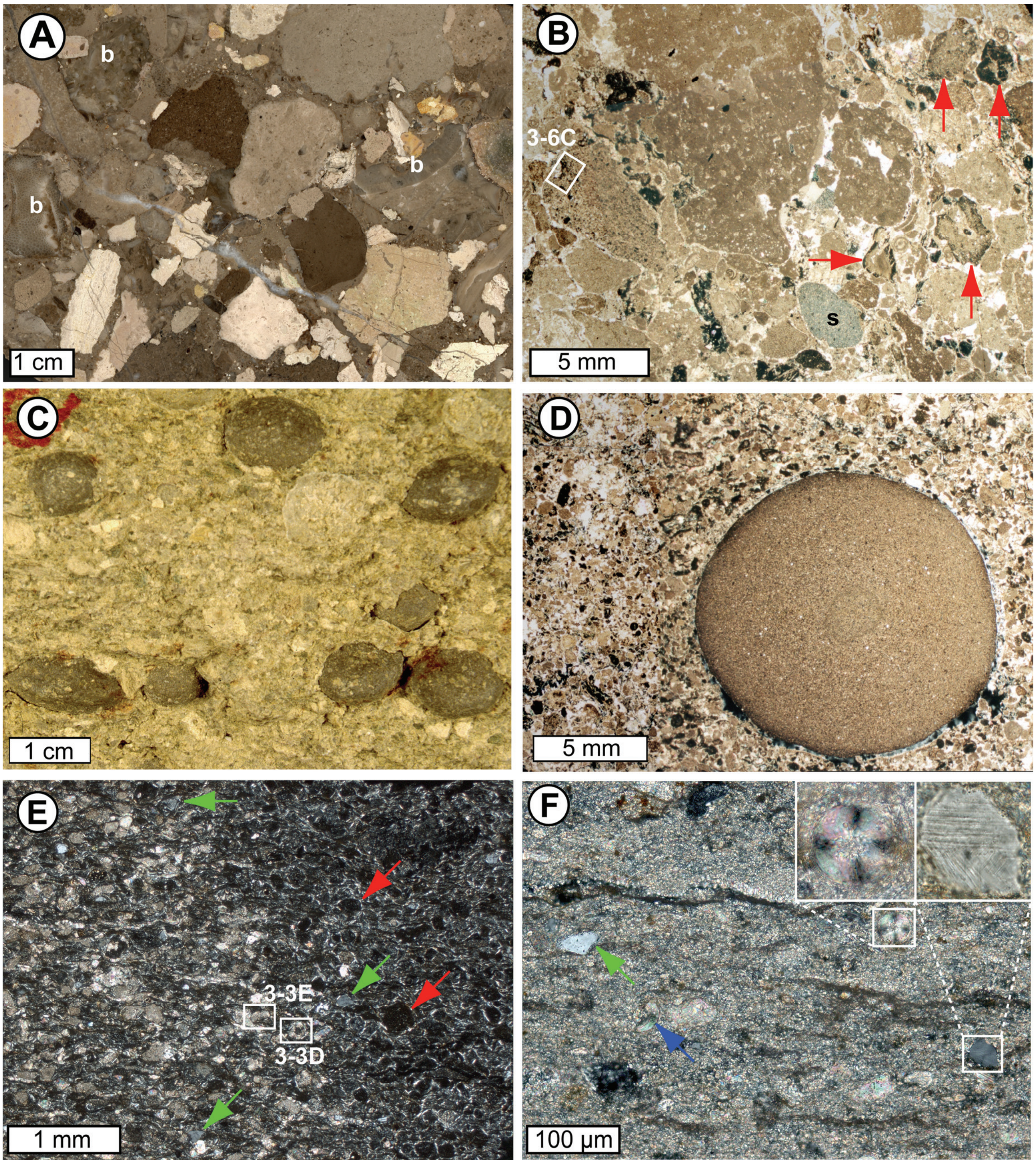

Figure 3-1 Unit overview of the K-P site of El Guayal. **(A)** Polished hand specimen of the upper megabreccia. b: biogen (sample G02). **(B)** Binocular composite image (XPL) from the microbreccia showing altered silicate melt particles (black), micritic calcite clasts (brown) and sparitic calcite (bright) in between clasts. s: silicified calcite; arrows: carbonate particles with rims of silicate melt (sample Ir07B) (see A1-3). **(C)** Hand specimen of lower accretionary lapilli unit with abundant accretionary lapilli. **(D)** Binocular composite image (XPL) from the lower accretionary lapilli unit with accretionary lapillus, micritic (brown) and sparitic (bright) calcite and altered silicate melt (dark) (sample Ir15B). **(E)** Micrograph (XPL) of the uppermost accretionary lapilli unit where altered silicate melt (dark) is the major component of the matrix. Left side: Towards accretionary lapilli unit, where almost all calcite particles (bright to brown) are microcrystalline. Right side: Towards clay unit, where calcite is almost absent. Red arrows: clastic silicate melt particles; green arrows: quartz particles (sample G13-2). **(F)** Micrograph (XPL) of the clay unit showing marly matrix with microcrystalline calcite. Magnifications show spherulitic calcite spheroid (left, XPL) and shocked quartz particle (right, PPL) with multiple sets of planar deformation features (PDFs). Green arrow: quartz particle; blue arrow: spherulitic carbonate fragment. (sample G15). XPL: cross polarised light; PPL: plane polarised light.

<2 mm (rarely 5 mm) at the top. Altered silicate melt (see section 3.3) is observed in the hand specimen as greenish particles. Thin section studies show that the pore space of the clast-supported breccia is filled with secondary sparitic calcite (Fig. 3-1B). While crystalline (basement) particles are not observed, melt particles are abundant and often associated with carbonates (see sections 3.2 and 3.3). Quartz and feldspar grains show shock metamorphism features like planar deformation features (PDFs, commonly decorated), an undulatory extinction and association with vesicle-rich areas. Shocked quartz and feldspar particles are often embedded into altered silicate melt particles. Unusual spherulitic textured calcite particles are associated with microcrystalline calcite (see section 3.2). Micritic carbonate clasts often contain well preserved microfossils. Foraminifera, sometimes broken, occur as isolated particles. Micritic calcite particles show a schlieren-like silification beginning from the outer grain boundaries. Former calcite clasts are replaced by silica, but some contain remnant areas of calcite at the centre. While most of the former micrite clasts show various degrees of silification, sparite is usually less silicified. However, silification of sparite seems to be more pronounced near altered silicate melt particles.

Accretionary lapilli unit

Above the microbreccia at a stratigraphic level of ~61 m the ~2.3 m thick accretionary lapilli unit shows a fining upward trend (Fig. 2-1, right stratigraphic column). The lower accretionary lapilli unit is a ~40 cm thick distinct clastic bed and contains abundant extraordinary accretionary lapilli (Fig. 3-1C). These (see section 3.4) are up to 1.5 cm in diameter, rounded, slightly elongated and flattened towards the bedding plane. Average dimensions of a set of 24 lapilli are 1.3x1.1x0.8 cm (s.d.=0.19, 0.14, and 0.16) with an average aspect ratio of 0.59 (s.d.=0.13) (Burns et al. 2003). Broken accretionary lapilli are absent. Next to accretionary lapilli, there are subrounded grey particles with cores of calcite up to 2 cm in size. The base of the accretionary lapilli unit is coarser and less well sorted compared to the underlying microbreccia. Angular carbonate clasts up to 5 cm and melt particles >2 cm are observed, but most of the clasts and particles are <2 mm in size. The middle accretionary lapilli subunit is ~1.6 m thick. Those beds are well sorted with particle sizes of <2 mm and poor in accretionary lapilli. The laminated upper accretionary lapilli subunit is ~30 cm thick, silt-sized and topped by a ~5 cm thick yellowish clay unit. The accretionary lapilli unit can be readily distinguished from the underlying microbreccia by its yellowish colour caused by increased staining of iron hydroxides/ oxides due to the alteration of impact melt as indicated by rust-like areas in the hand specimens. Thin section studies show that the accretionary lapilli unit

(Fig. 3-1D) consists of components comparable to those of the underlying microbreccia. However, in the accretionary lapilli unit the amount of altered silicate impact melt is higher. Calcite appears more often as spherulitic or microcrystalline particles than in the underlying microbreccia. The combination of altered silicate melt with carbonates within the same particle (see sections 3.2 and 3.3) is more often observed. Additionally, silification of calcite is more pronounced.

Thin section studies indicate that flow-textured altered silicate melt becomes the main component of the matrix within the laminated silt beds near the overlying clay unit. Embedded microcrystalline or spherulitic calcite particles and melt particles have a size <150 µm (Fig. 3-1E, left side). At the uppermost accretionary lapilli unit, near the contact with the clay unit, a distinct boundary is observed at crossed polarisers (XPL) which is caused by an abrupt decrease of calcite (Fig. 3-1E, right side).

Clay unit

The transition of the accretionary lapilli unit towards the clay unit (Fig. 3-1F) is marked by a sudden change of the main matrix component from altered silicate melt to a fine-grained marly matrix. Silicate melt particles are not observed, but the mainly microcrystalline calcite matrix display darker cloud-like schlieren. Spherulitic calcite fragments and spheroids are observed. Compared to the underlying beds, the clay unit has a significant higher amount of quartz. Undulatory extinction or planar fractures are common and, compared to the mainly decorated PDF's in shocked quartz particles of the underlying beds, the PDFs of quartz particles in the clay unit are well preserved.

Overall, the units of the El Guayal section represent a stepwise fining upward succession. The ejecta-rich microbreccia, accretionary lapilli unit and the clay unit contain similar components and can be distinguished by the different abundance of (1) a sedimentary endmember of major calcite with rare dolomite (sulphates are not observed) and (2) a silicate endmember of mostly altered melt and some shocked minerals. Therefore, it is inferred that the ejecta-rich units and the megabreccia were deposited in between undisturbed sediments and represent one coherent succession related to the Chicxulub impact event. Both, the silicate and carbonate endmember show differences with respect to their abundance, texture and interaction with each other. While microcrystalline and spherulitic textured calcite particles are only rarely observed in the very uppermost megabreccia, they occur often in the microbreccia and are abundant in the accretionary lapilli unit. This behaviour is comparable to the abundance of altered silicate melt which is not observed in the megabreccia but significantly increases from the lower microbreccia towards the uppermost accretionary lapilli unit. Furthermore, the combination of altered silicate melt and carbonates is more pronounced in the accretionary lapilli unit than in the microbreccia. The following two sections focus on the detailed petrographic description of carbonate and silicate melt particles and their textural relationships.

3.2 Petrography and classification of calcite particles

This section describes the unusually textured calcite particles in the ejecta-bearing units and their relationship to altered silicate melt at some representative examples. The microscopic observations are summarised in Tab. 3-1.

Spherulitic textured calcite particles show radiating crystal growth which often results in feathery-like extinction under crossed polarisers. The spherulitic areas in particles are often associated with needle-like textured areas. A grading into microcrystalline calcite or coarse, elongated, euhedral calcite is observed (Fig. 3-2A). Furthermore, fine-grained, dark micritic areas are observed within spherulitic textured calcite particles. Compared to (fossil-bearing) micrite clasts, these micritic textured areas, show locally a slight increase in grain size and individual crystals can be identified by optical microscopy. Thus, micritic areas and also micritic particles with a (locally) increased grain-size will be termed micrite-like calcite.

In the uppermost megabreccia near the microbreccia minor spherulitic particles have been observed as angular fragments commonly several mm in size (Fig. 3-2B) or as spherulitic areas in the rim of micritic calcite clasts. In the ejecta-rich microbreccia and in the accretionary lapilli unit, particles or accumulations of feathery- to needle-like textured areas are more abundant. In some cases feathery-like textured calcite particles appear as rounded elongated particles with a maximum size of ≤2 mm (Fig. 3-2C). Additionally, calcite spheroids ≤250 µm in size have a spherulitic texture (Figs. 3-2D and E).

In plane polarised light, the spherulitic textured calcite particles show a reduced transparency due to the presence of <1−3 µm sized vesicles, which is not observed at secondary sparitic calcite present in veins and between clasts (Fig. 3-2C, white arrows). Fig. 3-2E is the close up from the upper left corner of the spherulitic textured calcite spheroid shown in Fig. 3-2C. Radially arranged needle-like calcite crystals (green arrow) emerge from the centre. There,

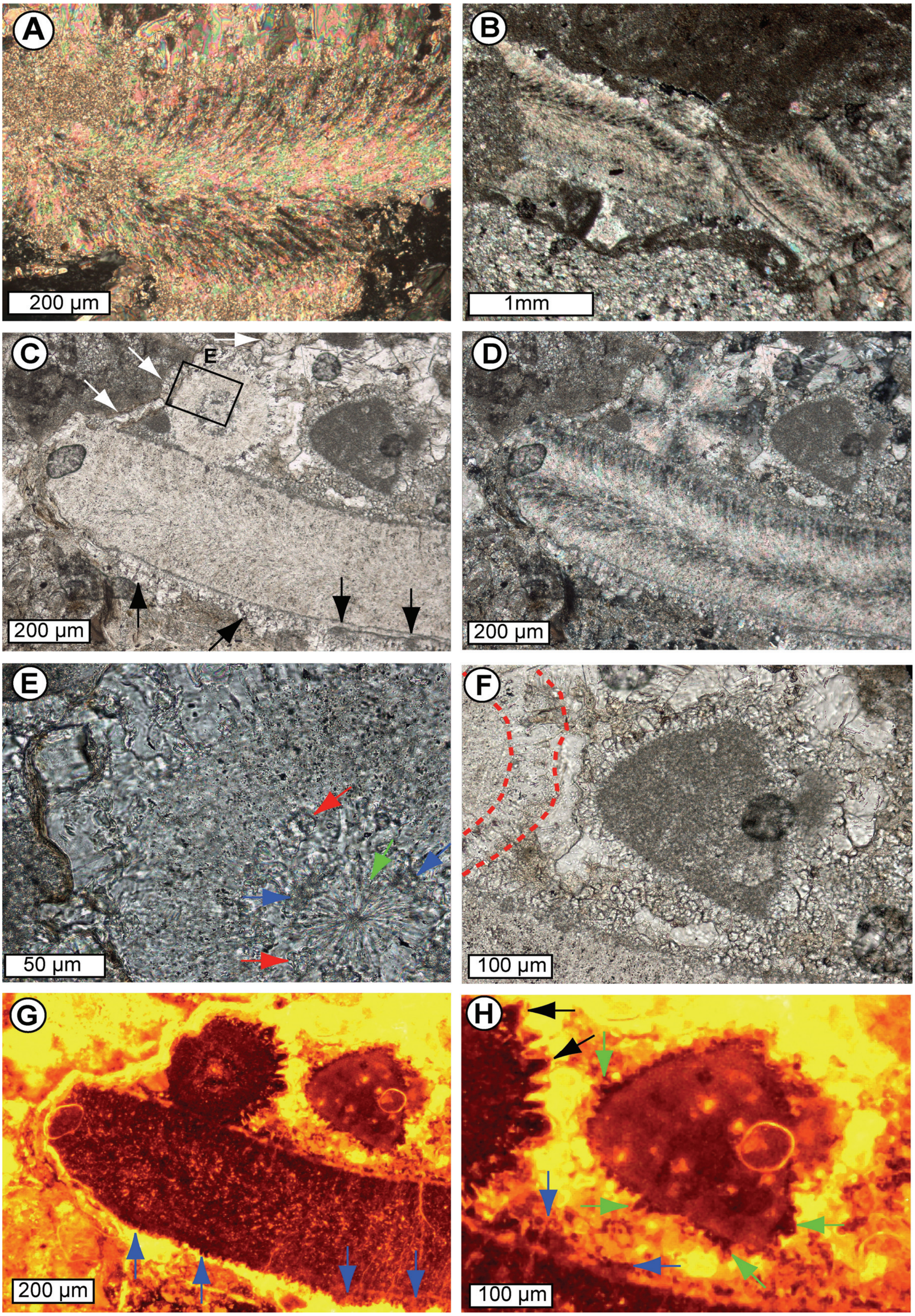

Figure 3-2 Micrographs of spherulitic calcite particles associated with microcrystalline to micrite-like calcite areas. (A, B, D): XPL, (C, E, F): PPL, (G, H): CL. **(A)** Sample G10 (lower accretionary lapilli unit). **(B)** Sample G05 (uppermost megabreccia). **(C-H)** Sample Ir07B (lower microbreccia). XPL: cross polarised light; PPL: plane polarised light; CL: cathodoluminescence. Explanations see text.

accumulations of micrite-like calcite crystals (blue arrows) are present. Between the central sphere and the outer vesicle-rich rim, there are, compared to the micrite-like crystals, some larger microcrystalline calcite crystals (red arrows). At the outermost rim (red dashed lines at Fig. 3-2F), there are coarse euhedral to subhedral, elongated, radially arranged crystals with a maximum size of 65x20 µm which are similar to sparitic calcite free of vesicles. These features follow the spherulitic (cross-like) extinction observed in the whole spheroid (Fig. 3-2D). Similar but smaller, elongated, radially arranged calcite crystals, microcrystalline calcite crystals (up to 10 µm size) and much finer micrite-like areas are often present at the rim of unbroken feathery textured calcite particles (Fig. 3-2C, black arrows) and also at the micrite-like particle of Fig. 3-2F.

In order to classify the different calcite generations cathodoluminescence studies have been carried out on several calcite particles. Secondary sparitic calcite, which is present in between clasts, has a bright luminescence of yellow colour (Fig. 3-2G) as well as most of the micritic calcite clasts. The latter often show a reduced luminescence of bright orange colours at their rim. SEM studies revealed that this is caused by silification of carbonate. The spherulitic calcite particles and spheroids show no or only reduced luminescence of dark red to dull brown colours. Furthermore, the radial sparitic calcite crystals around the spherulitic textured calcite spheroids exhibit radially arranged non-luminescent spikes (Fig. 3-2H, black arrows). Their outer crystal margin shows bright yellow luminescence and cannot be distinguished from the secondary sparitic calcite. A similar behaviour in luminescence is observed at the rim of the larger elongated, spherulitic particle (Figs. 3-2G and H, blue arrows), where the rims display euhedral, radially arranged crystals and more often microcrystalline to micrite-like calcite. Additionally, similar non-luminescent radial spikes with bright luminescent margins occur at the microcrystalline calcite rim around the micrite-like calcite particle (Fig. 3-2H, green arrows). This micrite-like particle emits a reduced, heterogeneous luminescence of brick brown to orange colours with lower intensities at locally larger crystal sizes.

The feathery texture is generally not observed at calcite particles associated with altered silicate melt. Though, some calcite particles that are embedded in silicate melt display a needle-like texture. The bright central calcite of Fig. 3-3A is composed of radially arranged blocky aggregates which have a cauliflower-like morphology. In between those vesicle-rich aggregates, there are darker micrite-like to microcrystalline calcite areas. The outer particle rim consists of silicate melt with a partially angular, partially rounded morphology (Fig. 3-3B). In the close-up (Fig. 3-3C) a needle-like texture within the cauliflower shaped calcite aggregates can be

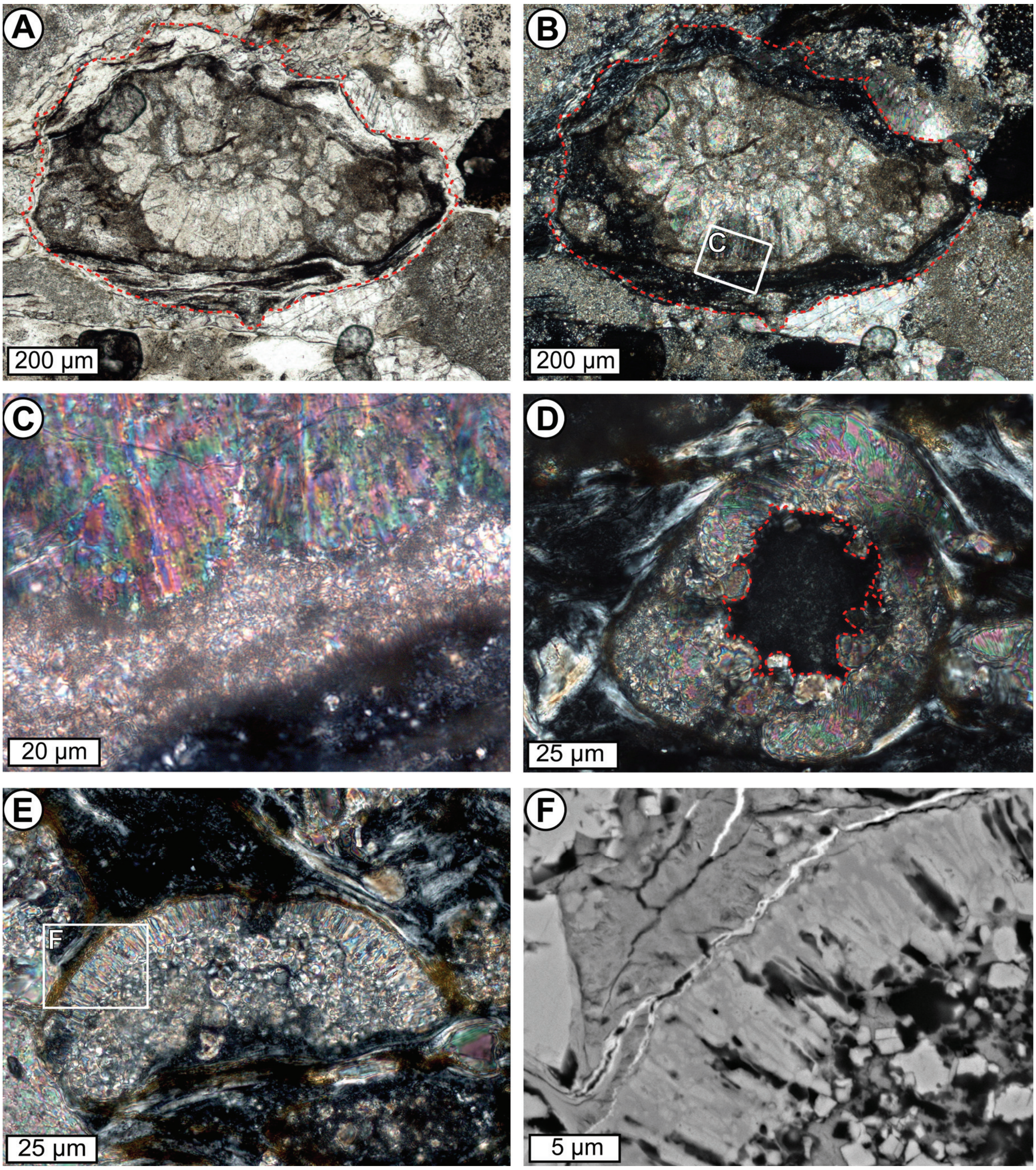

Figure 3-3 Micrographs of spherulitic, needle-like textured calcite particles associated with microcrystalline calcite and altered silicate melt (black in XPL). (A): PPL, (B-E): XPL, (F): BSE. **(A-B)** Calcite aggregate embedded in silicate melt (sample Ir11, upper microbreccia). **(C)** Close up of (B). **(D)** Microcrystalline to spherulitic calcite spheroid mantling vesicular silicate melt particle (sample G13, uppermost accretionary lapilli unit. (see Fig. 3-1E). **(E)** Calcite spheroid fragment with former core of microcrystalline calcite and radially arranged needle-like textured calcite rim (sample G13, uppermost accretionary lapilli unit, see Fig. 3-1E). **(F)** BSE micrograph showing close up of (E). Bright: calcite; black: voids which are pseudomorph of calcite; grey: altered silicate melt in core and as matrix; grey schlieren in particle rim: silica replacing calcite. PPL: plane polarised light; XPL: cross polarised light; BSE: backscattered electron.

Table 3-1 Characteristics of calcite textures.

	Spherulitic	Needle-like	Micrite-like	Microcrystalline
Description	A) Elongated particles, angular fragments or aggregates with feathery-like texture B) Spheroids with spherulitic texture <250 μm in size	Blocky, radially arranged aggregates with "cauliflower" morphology; At the rim of particles	Rounded particles Associated with spherulitic, needle-like and microcrystalline particles (see combination with different calcite textures)	Associated with spherulitic, needle-like and micrite-like particles (see combination with different calcite textures)
Occurrence	A) Rare but present in uppermost MB; Often in μB and ALU; Some in CU B) None in uppermost MB; Some in μB and ALU; Rare but present in CU	None in uppermost MB; Often in μB and ALU; Some in CU	None in MB; Often in μB and ALU; None in CU	None in MB, Often in μB and ALU, Most particles in upper ALU; As major component of marly matrix in CU
Vesicles	Sub-μm to <3 μm	Sub-μm to <3 μm	None	None
Combination with silicate melt	A) Not observed B) As (vesicular) core of 40 μm sized spheroids in CU, upper ALU and within accretionary lapilli (see section 3.4)	As rim of particles; As core of spheroids.	Observed, see section 3.3 (melt particle type 2)	Observed, see section 3.3 (melt particle type 2)
Combination with different calcite textures	A) Euhedral, elongated, radial, sparitic crystals and microcrystalline to micrite-like areas at rim of unbroken elongated particles B) Gradings to needle-like and microcrystalline texture	Micrite-like to microcrystalline in between and around blocky aggregates; Microcrystalline rim at contact with silicate melt rim	Heterogeneous areas with grain size increase towards microcrystalline Rims with crystals which are partially elongated, radially arranged or microcrystalline	Associated with spherulitic, needle-like and micrite-like textures (see left)
Cathodo-luminescence	Non-luminescent dark red to dull brown Radially, elongated sparitic and microcrystalline rims are non-luminescent (dark red to dull brown) near non-luminescent spherulitic calcite and luminescent (yellow) towards the outer crystal margin Micrite-like areas at rim are low luminescent (dark red to brick brown)	Variably luminescent (orange to yellow)	Reduced varying luminescence (red to orange); Lower intensities at enlarged crystals Microcrystalline rims are non-luminescent (dark red to dull brown) near micrite-like particles and luminescent (yellow) towards the outer rim; (compare with spherulitic CL)	Non-luminescent with spherulitic spheroids Partially luminescent at rim of spherulitic and micrite-like particles (see left)

MB: megabreccia; μB: microbreccia; ALU: accretionary lapilli unit; CU: clay unit.

observed. Between this area and the altered silicate melt is a 15–40 µm thick layer of microcrystalline to micrite-like calcite. Cathodoluminescence studies of the embedded calcite show at the different textured areas a similar luminescence of orange to yellow colour which is difficult to distinguish from many micritic clasts.

The amount of microcrystalline calcite particles is much higher in the accretionary lapilli unit compared to the underlying microbreccia. In the upper accretionary lapilli unit (Fig. 3-1E, left side) all of the calcite particles are microcrystalline. There, some spheroids show a centre of altered vesicular silicate melt which is mantled by curved, radiating to microcrystalline calcite crystals (Fig. 3-3D). SEM studies reveal the presence of voids which are pseudomorphs of calcite in the silicate melt at the contact to the calcite. The former core of the other spheroid fragment (Fig. 3-3E) consists of microcrystalline calcite and the radiating needle-like rim hosts similar voids. At the partially silicified rim those voids follow the direction of the radiating calcite crystals (Fig. 3-3F). In the former core of the spheroid fragment the voids are associated with microcrystalline calcite embedded in silicate melt.

3.3 Properties and classification of silicate melt particles

This section focuses on silicate melt particles, which are metastable glasses altered to clay minerals, with a well preserved morphology. Rare unaltered impact glass particles were separated by hand picking after treating the whole rock sample with diluted hydrochloric acid. In plane polarised light, the altered silicate melt particles have a brownish colour of different intensity due to the oxidation of iron oxides/ hydroxides. The following types of altered silicate melt particles have been classified according to the absence (melt particle type 1) or presence (melt particle type 2) of microcrystalline calcite associated with small sized voids. The characteristics of the different types of melt particles are summarised in Tab. 3-2.

Melt particles type 1 appear as subrounded to angular or dented bodies often with vesicular morphology (Fig. 3-4A). Characteristic for melt particles type 1 is a flow texture. SEM studies show a schlieren-like internal flow texture including oval areas with round or parallel fractures that follow the flow direction (Fig. 3-4B). This is possibly caused by the collapse of large vesicles, as the beginning vesicle collapse can be observed in the angular type of melt particles (Fig. 3-4A). Most of the silicate melt particles appear as elongated flattened particles and as thin, non-vesicular lumps. Rarely cuspate- or Y-shaped bubble-wall shard fragments with thin walls are observed (Fig. 3-4C, arrows). Small, closed vesicles within melt particle type 1 are

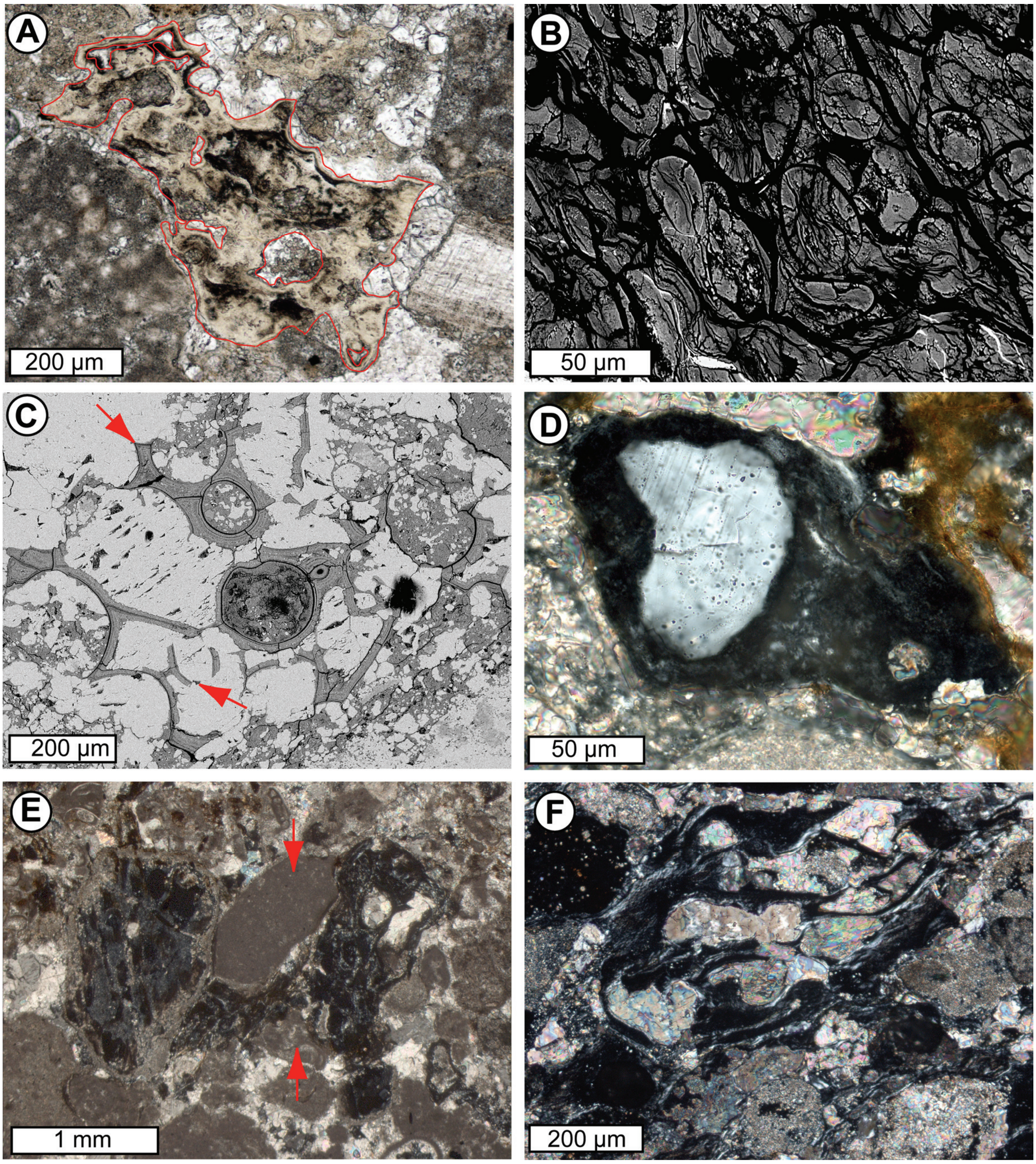

Figure 3-4 Micrographs of silicate melt particles type 1 (altered to clay minerals). (A): PPL, (B, C): BSE, (D, E, F): XPL. **(A)** Vesicular melt particle (sample Ir09, middle microbreccia). **(B)** Typical flow texture with oval areas and planar fractures towards flow direction. (sample Ir18, lower accretionary lapilli unit). **(C)** Bubble wall shards (dark grey, arrows) filled with sparitic calcite (bright) (sample Ir07B, lower microbreccia). **(D)** Melt particle with quartz showing multiple (decorated) PDFs (sample Ir09, middle microbreccia). **(E)** Melt particle partially enveloping micritic calcite clasts (red arrows) (sample G09, lowermost accretionary lapilli unit). **(F)** Melt particle with deformed vesicles filled with secondary sparitic calcite (sample Ir11, upper microbreccia). PPL: plane polarised light; XPL: cross polarised light; BSE: backscattered electron.

rare and their size does not exceed 1 µm. Quartz grains up to 35 µm in size have been identified within these melt particles and some show (mostly decorated) PDFs (Fig. 3-4D). Micritic calcite clasts are partially enveloped by the flow-textured melt particles type 1 (Fig. 3-4E, arrows). Secondary sparitic calcite is present in vesicles and thin-walled particles. In some cases, elongated silicate melt particles contain calcite with sharp curved menisci and cusps (Fig. 3-4F). However, neither a special texture nor inclusions as those present in the spherulitic calcite particles are present. Additionally, cathodoluminescence studies show a bright luminescence of yellow colour similar to (pore filling) sparitic calcite.

Melt particles type 2a are angular, dented to slightly rounded sometimes vesicular. The altered silicate melt generally contains varying amounts of microcrystalline calcite (Fig. 3-5A, arrows). Additionally, voids ranging in size from <1 µm up to 30 µm are larger and more abundant than in melt particle type 1 (Fig. 3-5B). The amount of such voids and microcrystalline calcite varies for different particles and sometimes also within one particle. Areas of angular silicate melt which lack voids and microcrystalline calcite are observed. Additionally, angular zircon particles are present in some type 2a melt particles.

Melt particles type 2b include particles with irregularly shaped areas of silicate melt and calcite. A different extinction is observed at polycrystalline subareas with <1–10 µm sized crystals (Figs. 3-5C and D). A reduced transparency of calcite is caused by vesicles. Within such particles the silicate melt is present as thin coatings around and interstitial between individual calcite subareas. It is oriented as rounded areas (Fig. 3-5C) of 25−200 µm in size or as layered elongated intercalations into the calcite particles (Fig. 3-5D). Quartz grains (arrows in Figs. 3-5C and D) up to 125 µm in size with (decorated) PDFs (Fig. 3-5E) occur often within melt particle type 2b near their rim. Apatite and locally minor rutile and framboidal iron sulphides are observed in melt particle type 2b. Furthermore, there are some occurrences of chalcopyrite exhibiting an inner rim of iron titanium sulphide and an outer rim of iron sulphide.

Transitions regarding the abundance of silicate melt, microcrystalline calcite and voids are observed between melt particles type 1 and melt particles type 2 (see A1-4). Often particles contain a micrite-like calcite dominated centre and show a gradual increase of silicate melt towards the rim. Some particle centres are micritic calcite with microfossils (Fig. 3-5F). The rim in those cases resembles melt particle type 1 with locally developed vesicular texture.

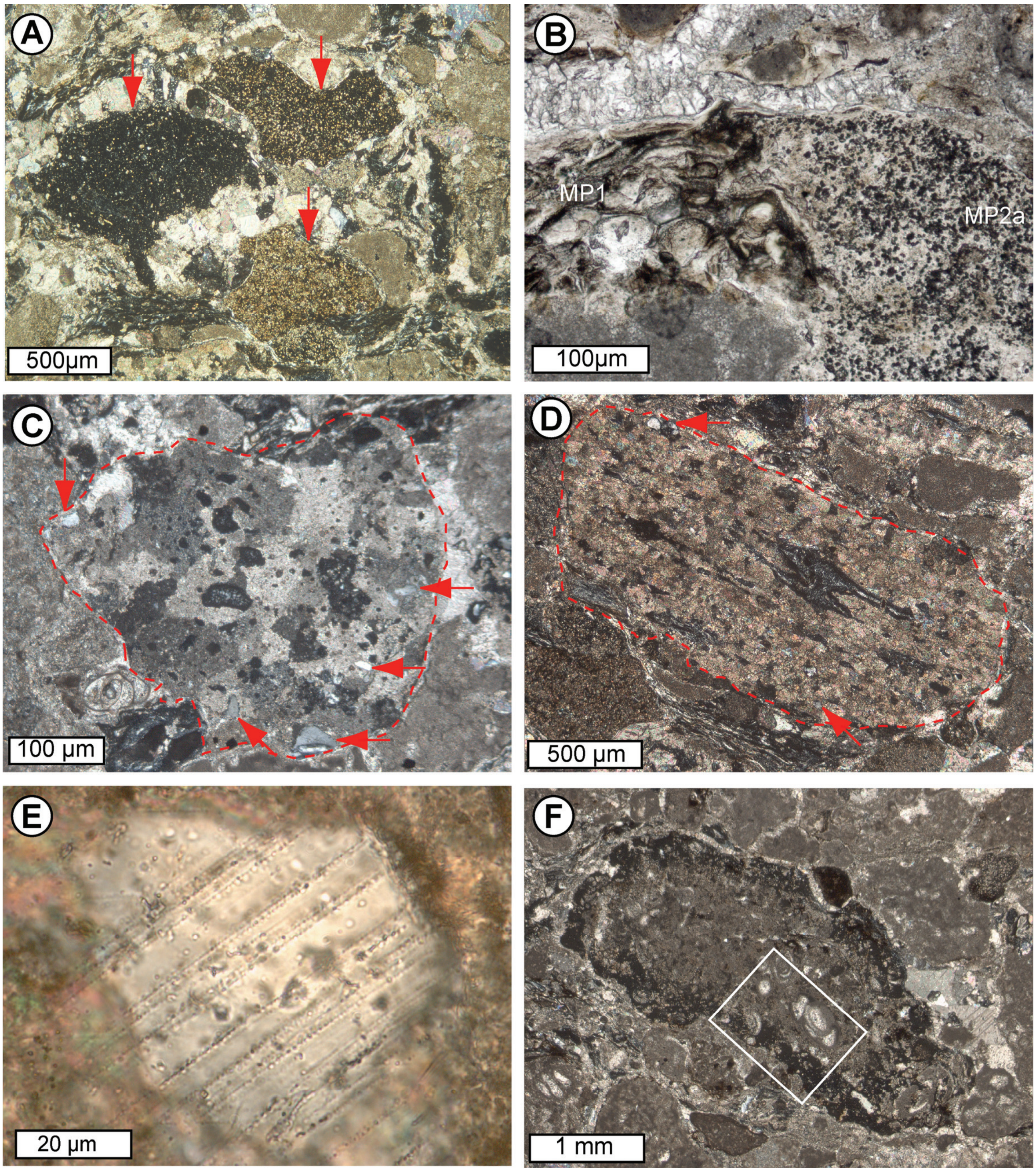

Figure 3-5 Micrographs of silicate melt particles type 2 (altered to clay minerals). (A, C, D, E, F): XPL, (B): PPL. **(A)** Overview showing the varying abundance of microcrystalline calcite in three different melt particles type 2a (arrows) (sample Ir18, lower accretionary lapilli unit). **(B)** Right side: Void-rich melt particle type 2a (MP2a); left side: flow textured melt particle type 1 (MP1) (sample Ir07A, lower microbreccia). **(C)** Melt particle type 2b with (different extinct) polycrystalline calcite subareas, round areas of silicate melt and quartz particles at rim (arrows) (sample Ir07A, lower microbreccia). **(D)** Melt particle type 2b of (different extinct) polycrystalline calcite subareas with elongated layered silicate melt intercalations and quartz particles at rim (arrows) (sample Ir18, lower accretionary lapilli unit). **(E)** Quartz particle of melt particle type 2b showing decorated PDFs (sample Ir10, middle microbreccia). **(F)** Fossil-bearing micritic calcite particle mantled by silicate melt (sample Ir08, middle microbreccia). XPL: cross polarised light; PPL: plane polarised light.

Silicate melt is further accumulated at indentions of larger carbonate particles (Fig. 3-1B, rectangle). The varieties of microcrystalline calcite in the transition zone resemble those observed at individual melt particles as shown in Fig. 3-5A. Where the centre resembles melt particle type 2b the size of polycrystalline calcite subareas is decreasing near the contact to the silicate melt grading into melt particle type 2a with microcrystalline calcite embedded in silicate melt.

Table 3-2 Characteristics of silicate melt particle type 1 and 2.

	Melt particle type 1	**Melt particle type 2a**	**Melt particle transition type 1/type 2**		**Melt particle type 2b**
			Rim	Centre	
Silicate melt appearance	Vesicular, angular morphology; Flow texture with collapsed vesicles; Bubble-wall shards	Angular to rounded	Abundant; Similar to melt particle type 1	Rare	Thin rims; Rounded areas; Layered elongated intercalations
Calcite	Sparitic as vesicle fillings	Microcrystalline; Variable amounts	Rare; Micro-crystalline	Abundant; Microcrystalline glomeroblastic to (fossil-bearing) micrite	Abundant; Polycrystalline subareas showing a different extinction composed of <1–10 μm grains
Voids	Not present	Variable amounts; <1–30μm; Pseudo-morphs of calcite; Associated with microcrystalline calcite	Abundant; Smaller; Pseudo-morphs of calcite Absent when similar to melt particle typ 1	Less abundant; Larger; Pseudo-morphs of calcite; Around subhedral microcrystalline calcite	Less ambundant; <1–30μm; Pseudomorphs of calcite
Shocked minerals	Some	Rare	Rare	Rare	Often at rim

Detailed microscopic observations reveal that the calcite/ silicate melt transition represents a replacement of calcite by silicate melt. This is indicated by intercalations of void-rich silicate melt into calcite. It is notable that fossils appear to be resistant to this replacement and the amount of voids in silicate melt is pronounced near the calcite contact (Figs. 3-6A and B, arrows). Fig. 3-6C is the close-up of Fig. 3-1B, where the silicate melt is accumulated in an indention of a melt particle type 2b. SEM analyses show that the microcrystalline calcite in the silicate melt is associated with voids (Fig. 3-6D). At the silicate melt-dominated rim of the particle, the void/ calcite ratio is high, and decreasing towards the calcite-rich centre. In the centre and transition zone, the voids are generally associated with calcite, often located as a thin layer in between the calcite crystals and the silicate melt. SEM studies reveal that the voids are pseudomorphs of calcite (Fig. 3-6E). Thereby, calcite crystals embedded in silicate melt

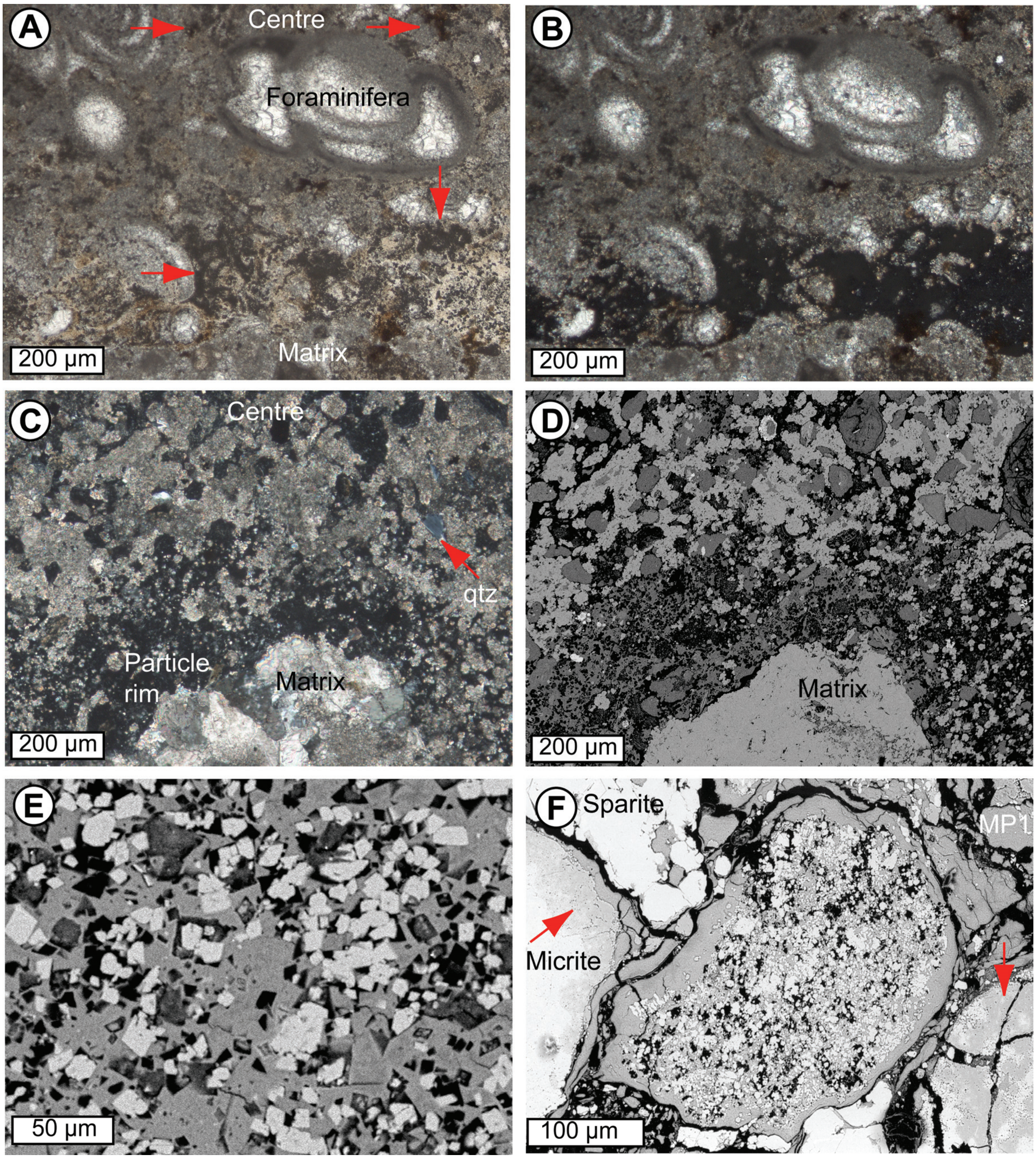

Figure 3-6 Micrographs of the transition zone of silicate melt coatings (altered to clay minerals) around calcite at melt particles type 2. (A): PPL, (B, C): XPL, (D–F): BSE (bright: calcite, grey: silicate melt, black: voids). **(A, B)** Close up of Fig. 3-5F showing replacement of carbonate by silicate melt. Voids in silicate melt (arrows) are pronounced near calcite contact (sample Ir08, middle microbreccia). **(C, D)** Close up of particle from rectangle at Fig. 3-1B showing zonation regarding abundance of microcrystalline calcite, silicate melt and associated voids. Qtz: quartz (sample Ir07B, lower microbreccia). **(E)** Example of melt particle type 2 texture showing voids in silicate melt, which are pseudomorphs of calcite, and associated with euhedral to subhedral calcite (sample Ir07B, lower microbreccia). **(F)** Melt particle type 2a with abundant microcrystalline calcite in silicate melt, voids and a rim of melt particle type 1 (MP1); Arrows: Micritic calcite particles showing silification at the rim (sample Ir15A, lowermost accretionary lapilli unit). PPL: plane polarised light; XPL: cross polarised light; BSE: backscattered electron.

are in most cases euhedral, though subhedral calcite is observed in the centre of larger voids. Subsequent calcite dissolution during preparation can be excluded as the voids contain glue with which the sample was saturated before cutting.

In the accretionary lapilli unit many, especially smaller particles with a very high content of microcrystalline calcite are sometimes difficult to distinguish microscopically from micritic calcite. However, SEM studies reveal that these particles represent melt particle type 2 as they are composed of microcrystalline calcite crystals and voids in altered silicate melt and rimmed by a ~2-10 μm thick layer of melt particle type 1 (Fig. 3-6F). At the uppermost accretionary lapilli unit near the contact to the clay unit (where microcrystalline calcite particles are absent), also the melt particles type 2 (<150 μm in size) do not contain any microcrystalline calcite (Fig. 3-1E, red arrows) but only voids which are pseudomorphs of calcite. There, the silicate melt matrix is similar to the flow-textured melt particle type 1.

3.4 Petrography and chemistry of accretionary lapilli

Within the accretionary lapilli unit, the accretionary lapilli are particularly abundant in a distinct basal ~40 cm thick bed. In contrast, within the middle accretionary lapilli unit, at one metre above the base from the basal accretionary lapilli unit, only one single lapillus was identified. Here, the petrography and texture of those extraordinary spheroids is examined. This is followed by petrographic observations and chemical results on accreted calcite particles and accreted feldspar particles.

3.4.1 Petrography and texture of accretionary lapilli

The internal texture of the accretionary lapilli and the shape of accreted particles are well preserved. The ash sized particles are dispersed in a matrix of diagenetic microcrystalline silica. Most of the accreted particles have grain sizes between ~10–100 μm and many are less than 1 μm in size. The maximum grain size is ~150 μm with rare larger particles up to 300 μm. The internal structure of the accretionary lapilli can be investigated best by reflected light microscopy. Broken hand specimens show concentric structures with up to two continuous concentric laminations of ~1 mm thickness (Fig. 3-7A). Reflected light microscopy and SEM studies show that those laminations correspond to a decrease in particle size. Within the core,

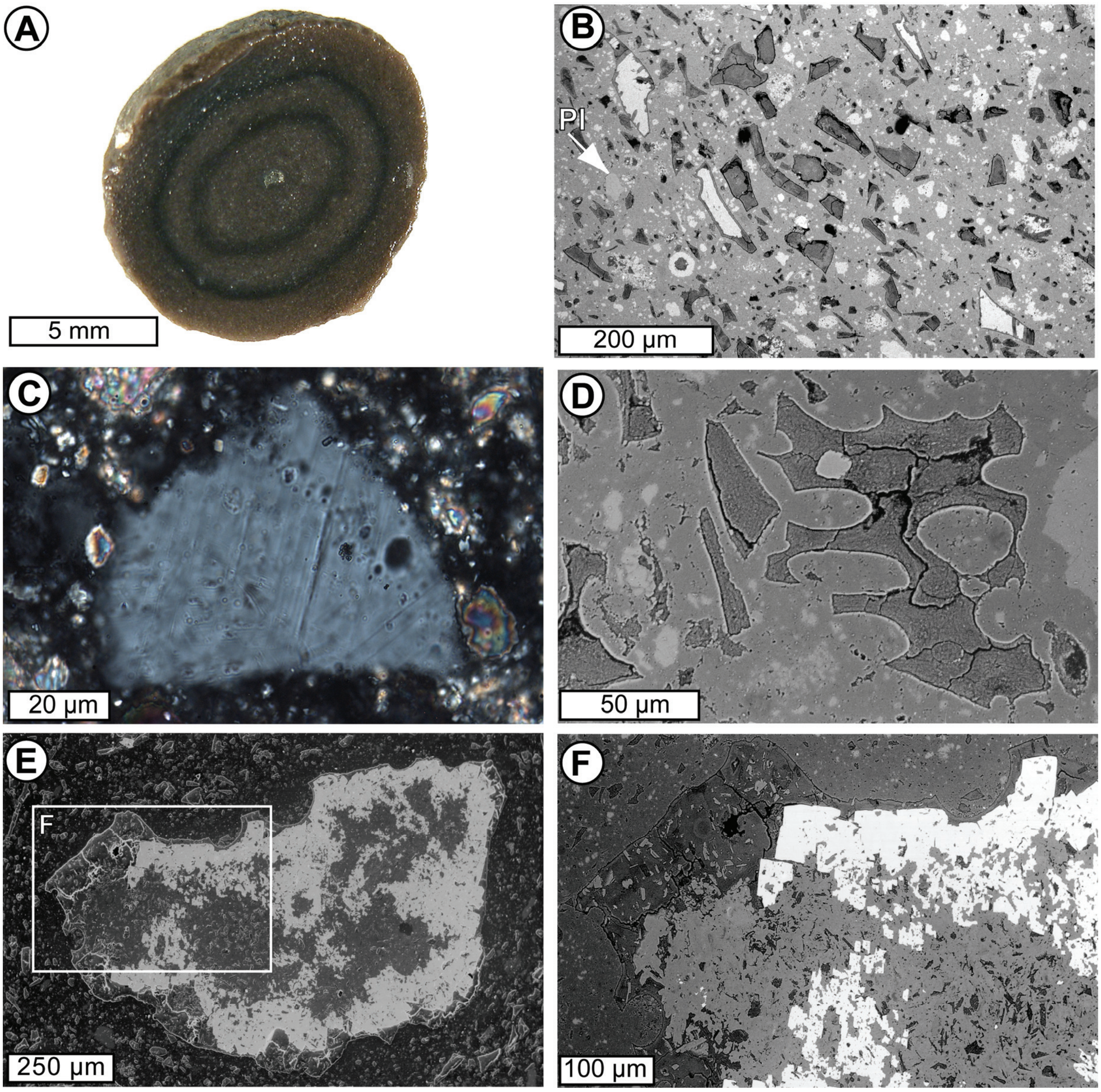

Figure 3-7 The structure of accretionary lapilli and accreted particles. **(A)** Broken lapillus with multiple concentric laminations and a nucleus. **(B)** BSE micrograph showing tangentially accreted ash-size particles dispersed in a matrix of silica. Bright: calcite; dark: altered silicate melt fragments; grey with arrow: rare plagioclase (Pl). **(C)** Micrograph (XPL) of quartz with multiple sets of planar deformation features (PDFs). **(D)** BSE micrograph of silicate melt particle with bubble-wall shard morphology next to angular vesicle-free fragments. **(E)** SEM micrograph of nucleus 1.1x0.6 mm in size with vesicular morphology. Note the several layers of tangential aligned particles and grain size reduction in the vicinity of nucleus. **(F)** BSE micrograph of close up of (E). Dark grey: altered silicate melt; bright: pyrite as dominant phase at the rim; grey: K-feldspar areas within melt particle and as euhedral laths together with plagioclase laths at rim. Note the laths-shaped clay minerals embedded in K-feldspar e.g. in lower right corner. BSE: back scattered electron; XPL: cross polarised light; SEM: scanning electron microscope.

particles are more randomly distributed than towards the edges, where elongated particles are aligned tangential to the lapilli rim (Fig. 3-7B). Near the rim, the particles decrease in size but are still larger than those in the concentric laminations. Modal composition calculations (section 3.7) indicate a modal content of 19 % clay minerals from altered silicate melt, 11 % calcite and 6 % dolomite. The silica matrix together with some quartz clasts showing (decorated) PDFs (Fig. 3-7C) make up 64 %. Trace amounts of feldspar, apatite, titanite, ore minerals and mica (locally intergrown with rutile) were observed by SEM.

Most of silicate melt particles have an angular, cuspate, vesicle-free texture (Fig. 3-7B), but some vesicular examples have also been observed (Fig. 3-7D). Rarely, silicate melt particles contain primary plagioclase laths which in some cases are aligned defining a fluidal texture. In the centre of some accretionary lapilli, there are unusual nuclei (Figs. 3-7A and E) of vesiculated silicate melt particles up to 1 mm in size. The particle size in the immediate vicinity of those nuclei is smaller than in regions farther away from the nuclei. In the rim of nuclei, euhedral K-feldspar and plagioclase laths are observed in silicate melt, whereby larger K-feldspar areas with rare subhedral plagioclase are present in the centre (Fig. 3-7F). At the latter small grains of chalcopyrite and sphalerite with calcite areas have been identified. Overgrowth of iron sulphide is observed at the rim (Fig. 3-7F).

Calcite is often affected by silification. The larger calcite particles show a schlieren-like replacement by the silica matrix beginning at their former outlines (Fig. 3-8A). This silification of calcite is similar to that observed at calcite clasts of the bulk rock. Many individual calcite particles of <1−20 µm in size in the silica matrix have a schlieren-like amoeboid shape. These calcites are most likely remnants of larger particles subsequently replaced by silica. Calcite is often observed as vesicle infillings in melt particles. These have a sleek or smooth surface sometimes with fractures which occasionally resemble crystal shapes similar to secondary sparitic calcite. In some cases, intergrowths of euhedral potassium feldspar are observed in these calcites preferentially around and altered silicate melt and near small voids (Fig. 3-8B). Some former silicate melt particles are completely replaced by potassium feldspar and show clay minerals which are pseudomorphs of a former laths-shaped phase (Fig. 3-8C, Fig. 3-7F). Similar "laths-shaped clay minerals" are radially arranged at the former boundary of the altered melt particles (Fig. 3-8D).

Dolomite is difficult to distinguish from the silica matrix in the BSE mode of the SEM due to their similar brightness. However, two different modifications of dolomites have been

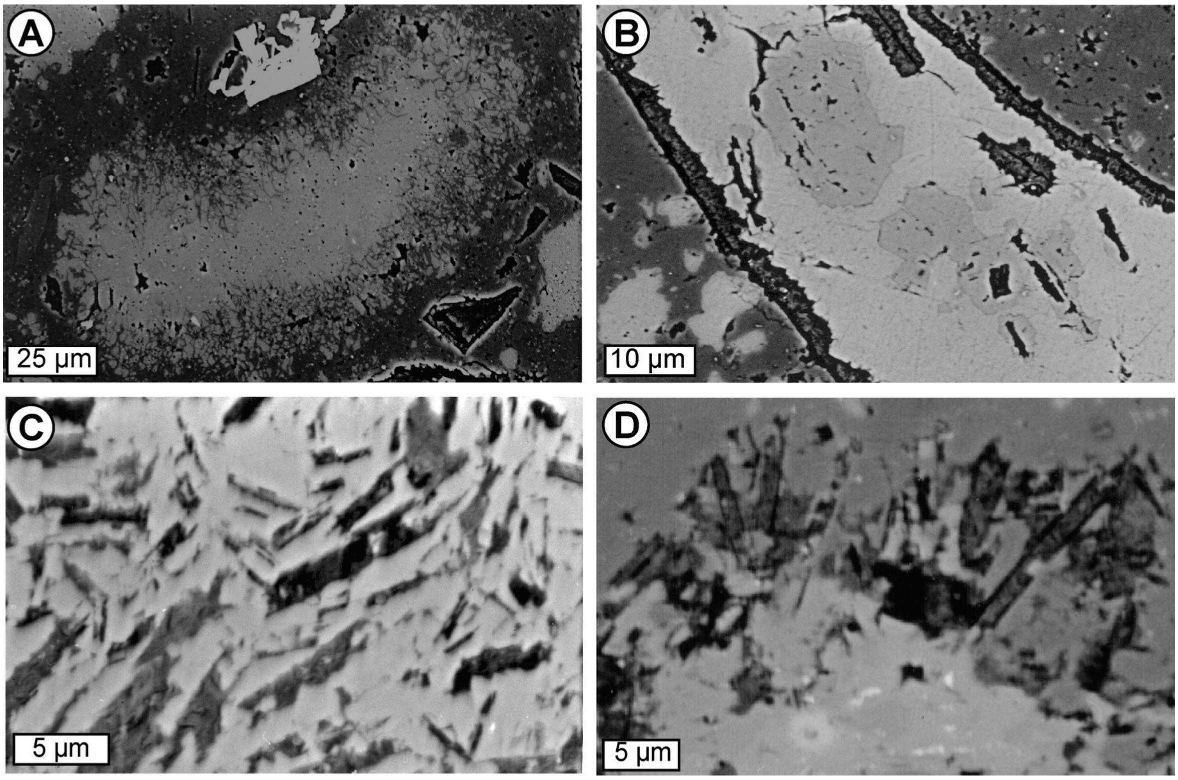

Figure 3-8 BSE micrographs showing alteration processes in accretionary lapilli. **(A)** Calcite area with schlieren-like replacement by silica. **(B)** Altered silicate melt particle (thin, dark grey rim) with vesicle filling of sparitic calcite (bright) associated with potassium feldspar intergrowths (light grey). (**C)** Clay minerals which are pseudomorphs of a former lath-shaped phase (dark grey) within by K-feldspar replaced melt particle. **(D)** Heavily altered silcate melt particle (replaced by potassium feldspar) with similar "lath-shaped clay minerals" of (C) which are radial orientated at the former particle rim. BSE: back scattered electron.

identified. EMP chemical composition analysis show that dolomite with a darker colour in BSE mode contains 31.1 ± 0.8 wt.% CaO and 21.2 ± 0.7 MgO which is the common dolomite composition. A second dolomite type is Ca-rich and Mg-poor and slightly brighter in the BSE. This type contains 34.3 ± 1.0 wt.% CaO and 18.3 ± 1.1 wt.% MgO. Both dolomite types can occur together and in most cases there are overgrowths of the Ca-rich type. The latter is often euhedral to subhedral with a tabular shape. In some cases, it contains calcite areas similar in shape to the amoeboid calcite in the silica matrix or overgrowths of calcite at their euhedral to subhedral rim.

3.4.2 Petrography and chemistry of accreted calcite particles

Calcite spheroids commonly have a core of silicate melt. Optical microscopy with crossed polarisers shows that these calcite spheroids are ~ 50 µm in size and have a spherulitic extinction (Fig. 3-9A). Similar spherulitic spheroids occur (without altered silicate melt core)

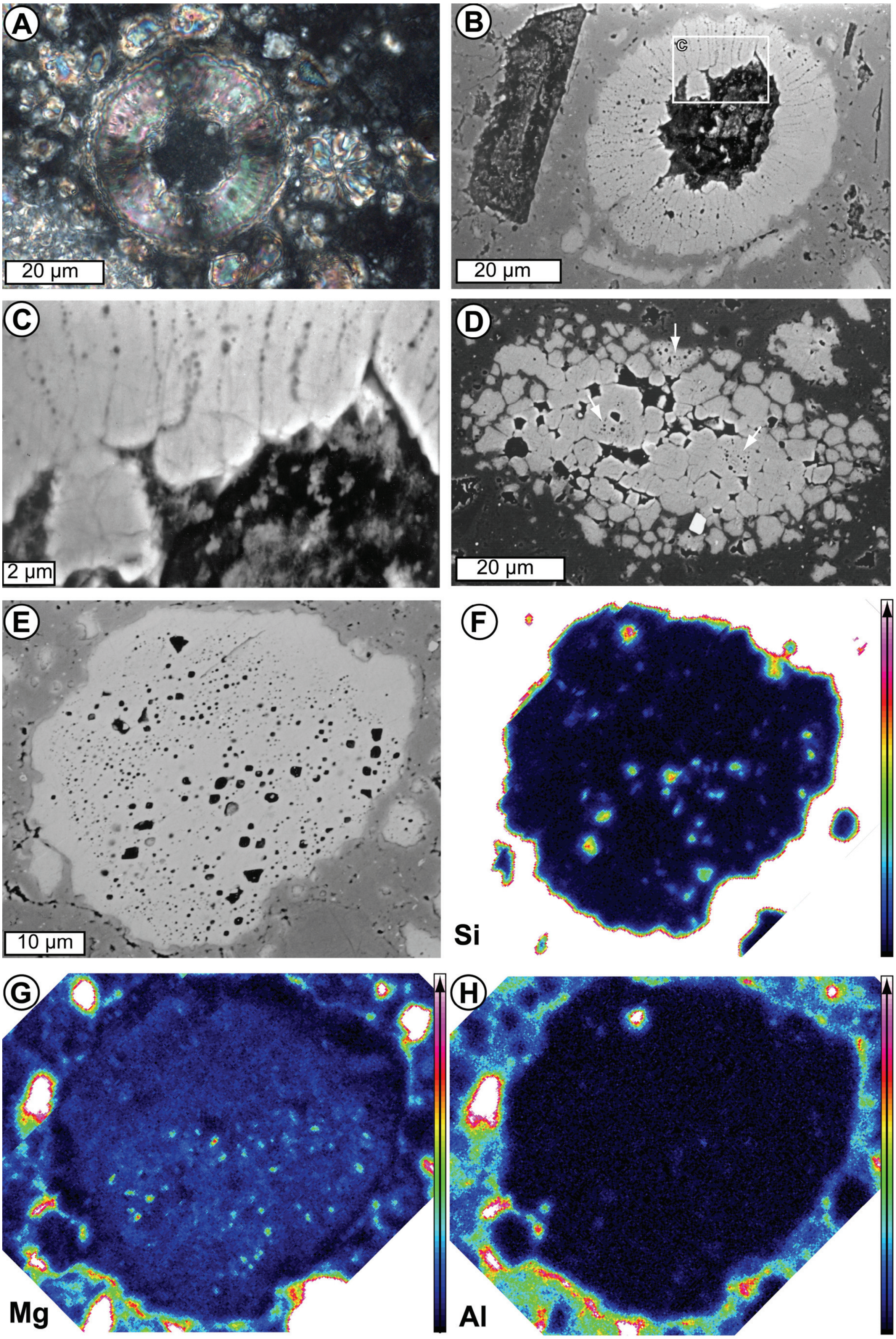

Figure 3-9 Figure caption on next page.

in the microbreccia (Fig. 3-2D) and in the clay unit (Fig. 3-1F), whereas spheroids with a core occur in the upper accretionary lapilli unit (Fig. 3-3D). At the accreted spheroids, a cauliflower-like morphology of calcite is observed at the contact with the silicate melt core, which is similar to calcite aggregates which are coated with altered silicate melt (Fig. 3-3C).

Calcite aggregates with areas ~10 µm in size contain sub-µm sized spherical inclusions (Fig. 3-9D, arrows). At the (partially silicified) rim, they are associated with microcrystalline, glomeroblastic textured calcite with interstitial silicate melt. Similar spherical inclusions in calcite particles are <1−2 µm in size (Fig. 3-9E) and difficult to observe in the BSE mode. Element mapping obtained by EMP analyses show that these spherical inclusions mainly correspond to an increase of SiO_2, MgO and Al_2O_3 (Figs. 3-9F–H). Some angular voids at the particle rim display enrichment of SiO_2 and Al_2O_3 and are, compared to the spherical inclusions, are less enriched in MgO. EMP analyses indicate that also calcite particles lacking inclusions have elevated SiO_2, Al_2O_3, MgO and FeO contents (Tab. 3-3).

Table 3-3 Composition of selected calcite particles within accretionary lapilli.

Sample	Particle 1	s (± wt.%)	Particle 2	s (± wt.%)	Particle 3	s (± wt.%)
N	4		3		5	
SiO_2	1.17	0.45	1.12	0.22	1.15	0.42
Al_2O_3	0.54	0.16	0.57	0.08	0.64	0.21
FeO	0.26	0.05	0.28	0.05	0.29	0.02
MgO	0.85	0.04	0.96	0.07	0.97	0.10
MnO	<0.09	-	<0.09	-	<0.09	-
CaO	52.4	0.8	52.2	0.48	52.1	0.91
CO_2	44.8	0.17	44.8	0.05	44.8	0.22
Total	100.0		100.0		100.0	

N: number of analyses

Figure 3-9 Combinations of calcite with silicate melt (altered to clay minerals) at accreted particles. **(A)** Micrograph (XPL) of spherulitic calcite spheroid enclosing altered silicate melt particle. **(B)** BSE micrograph of similar spherulitic calcite spheroid. **(C)** Close-up of (B). **(D)** BSE micrograph of glomeroblastic textured calcite particle with inclusions-rich areas (arrows) and interstitial altered silicate melt (black). Note the pervasive replacement of silica at the rim. **(E)** Calcite particle with spherical inclusions sub-µm to 2 µm in size. **(F-H)** Element mappings for Si, Mg and Al of (E). XPL: cross polarised light; BSE: back scattered electron.

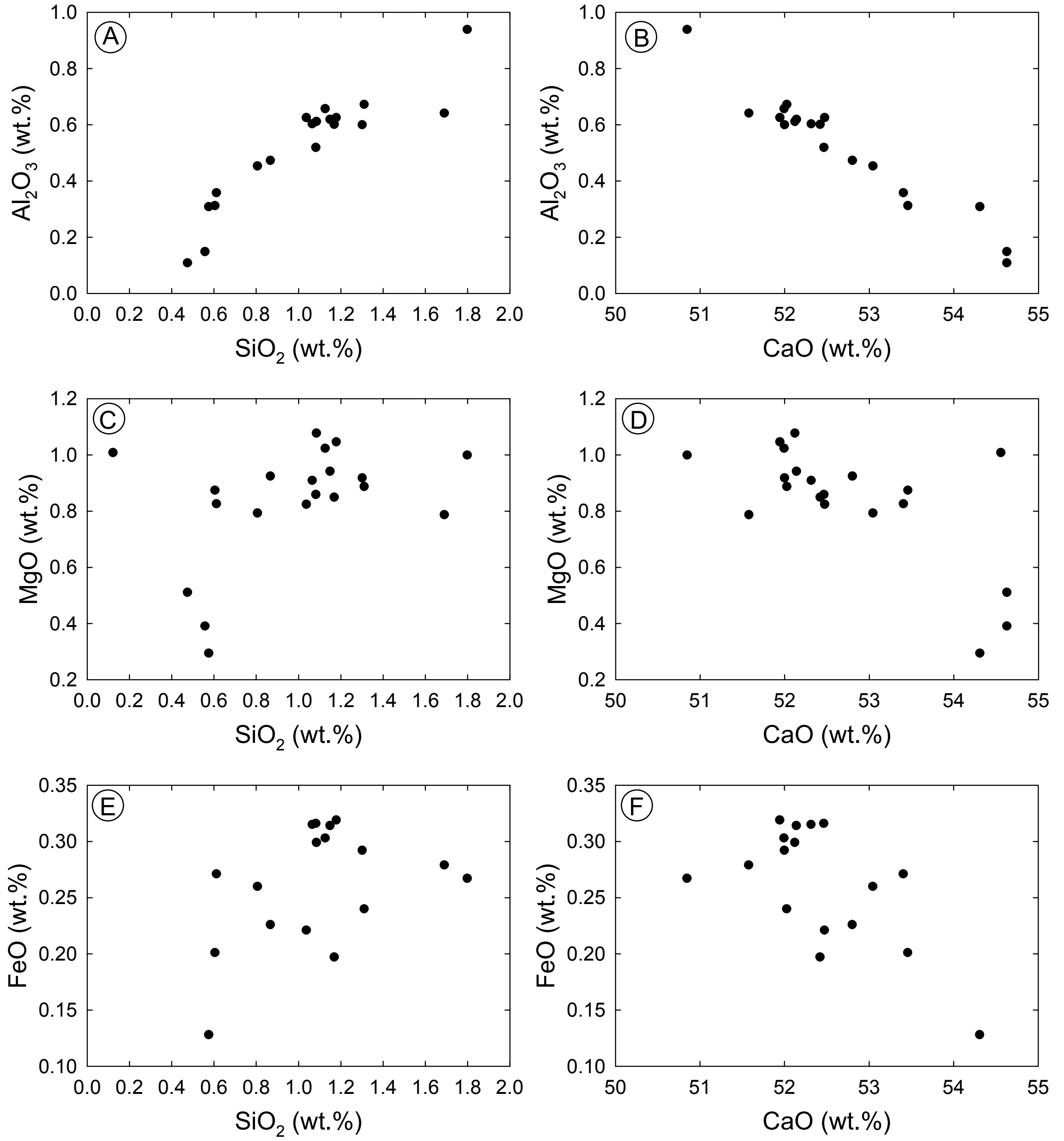

Figure 3-10 SiO_2 (left column) and CaO (right column) correlations with Al_2O_3 **(A, B)**, MgO **(C, D)** and FeO **(E, F)** for selected compositions of calcite particles within accretionary lapilli.

The element correlation diagrams for selected calcite particles (Fig. 3-10) show a positive correlation of Al_2O_3 with SiO_2 with an inclination of ~0.5 and no correlations for MgO and FeO. The element correlation with CaO shows a negative correlation for Al_2O_3 and no correlation for MgO. FeO shows a negative correlation with CaO, however, strong variations for FeO occur at intermediate CaO values.

Cathodoluminescence studies have been carried out on one lapillus with fractures which were subsequently filled with secondary sparitic calcite (Fig. 3-11C). The secondary sparitic calcite in these veins as well as calcite embedded within larger vesicles of silicate melt shards have a bright yellow to orange luminescence (No. 1 in Fig. 3-11D). The spherulitic calcite spheroid (Fig. 3-9A) with a core of altered silicate melt shows no luminescence (No. 3 in Fig. 3-11D). Individual calcite areas in the silica matrix show a nonuniform behaviour: Some areas show a bright yellow luminescence, while others do not display a luminescence. A similar indifferent behaviour is observed for dolomite. Additionally, some euhedral dolomites show no luminescence but enclose brightly luminescent amoeboid calcite areas.

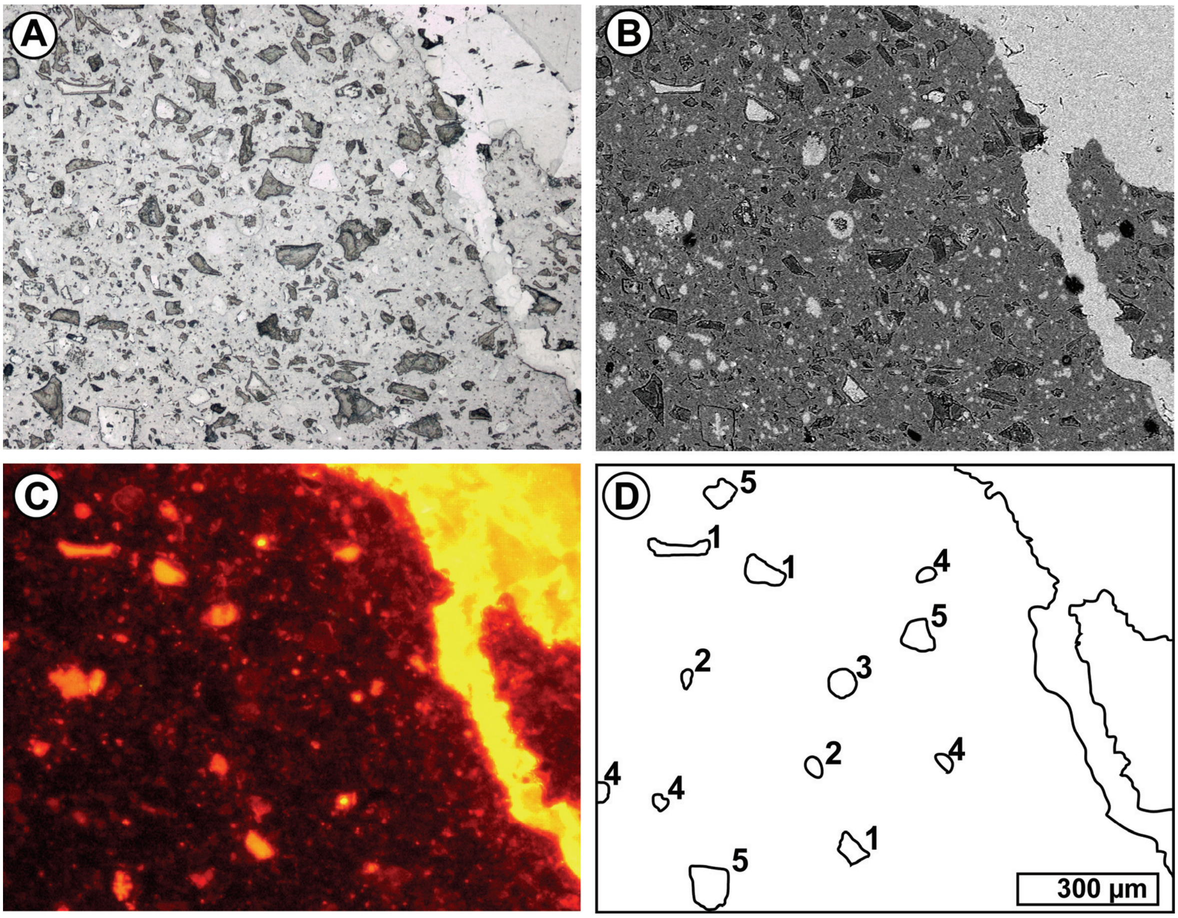

Figure 3-11 Micrographs of an accretionary lapillus with secondary sparitic vein. **(A)** Reflected light. **(B)** SEM. **(C)** CL. **(D)** Sketch of selected areas. 1: luminescent calcite as vesicle fillings of altered silicate melt particles; 2: individual luminescent calcite areas; 3: spherulitic calcite spheroid with core of altered silicate melt (Fig. 3-9A) with missing luminescence; 4: individual calcite areas without luminescence; 5: euhedral dolomite with missing luminescence. Dolomite grain is enclosing luminescent, amoeboid calcite at lower left margin. Scale of (D) is valid for all micrographs. SEM: scanning electron micrograph; CL: cathodoluminescence.

3.4.3 Petrography and chemistry of accreted feldspar particles

Feldspars are rare in the accretionary lapilli but the observed PDFs or undulatory extinction are evidences of shock metamorphism. The SEM in BSE mode of those particles displays compositional variations. EMP analysis of the different feldspar phases is difficult due to their

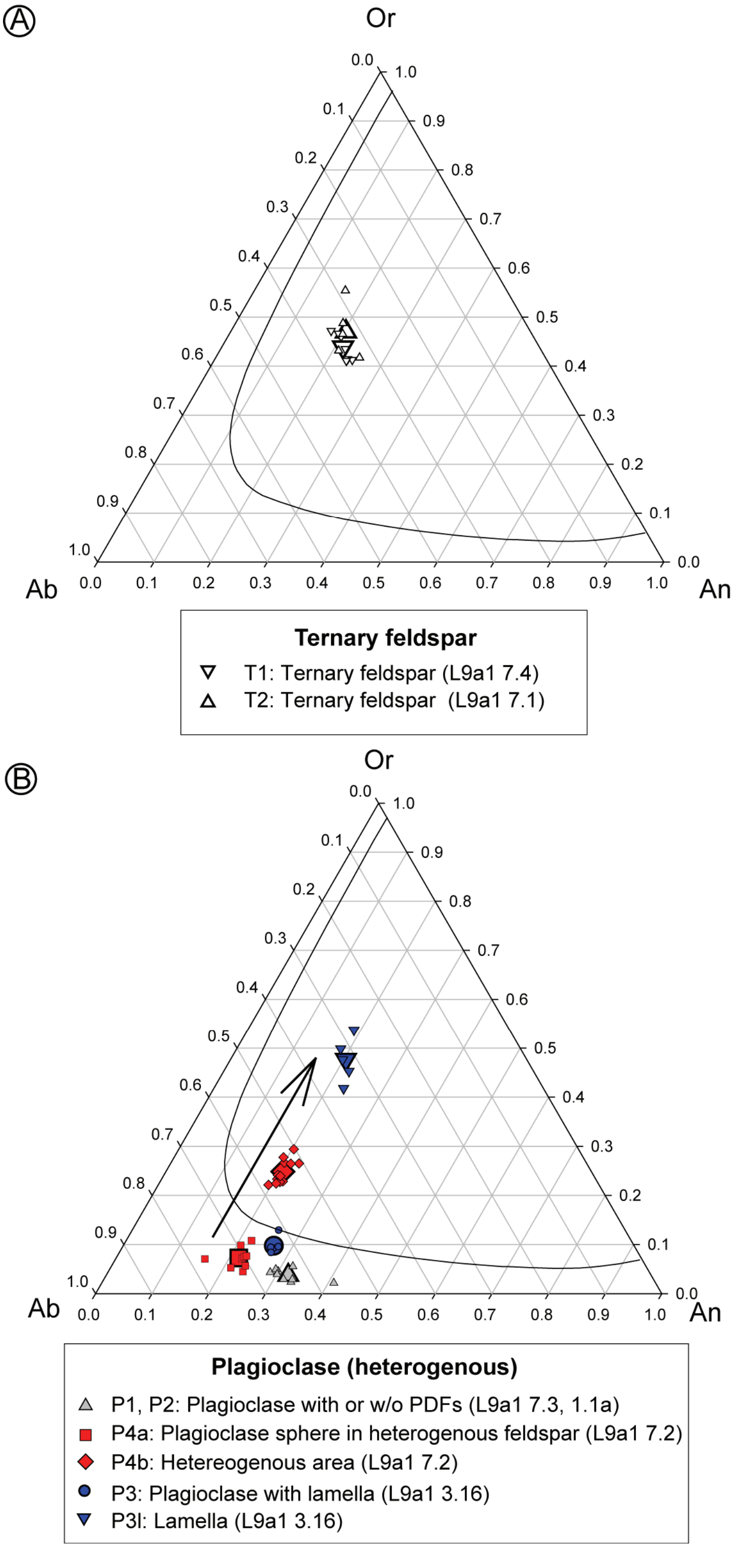

Figure 3-12 Compositions of ternary feldspar and plagioclase particles within accretionary lapilli. **(A)** Two ternary feldspar particles. **(B)** Four plagioclase particles (two homogenous composed plagioclase particles; one associated with K-rich and Na-poor area, Fig. 3-13B; one with K-rich and Na-poor lamella, Fig. 3-13C). Large symbols represent mean values of single analyses (small symbols). Arrow shows compositional trend towards a higher potassium and lower sodium content. Sample numbers are given in parentheses. Isotherm at 900°C, 0.5 kbar after Deer et al. (1992).

small size and, therefore in some cases only qualitative compositional trends can be recognised.

Fig. 3-12A shows the composition of feldspars in the ternary system $NaAlSi_3O_8$ (albite, Ab)–$KAlSi_3O_8$ (orthoclase, Or)–$CaAl_2Si_2O_8$ (anorthite, An). The compositions of feldspar particles (T1 and T2) plot in the immiscibility gap which is marked with the isotherm at 900°C and 0.5 kbar. Phase separation is below the resolution of the optical microscope. However, compositional differences are indicated by sets of parallel and crosscutting microstructures in the sub-µm scale recognisable in the BSE mode of the SEM at high contrast with high magnification. These observations including the elevated values for FeO, MgO and TiO_2 (Tab. 3-4) indicate that the ternary feldspars have formed at high temperatures and were rapidly quenched with no time for chemical equilibration. Some of the ternary feldspars show overgrowths of calcite and grains of pyrite of ~2 µm in size. Other feldspar particles have an angular to dented morphology with exsolution lamellae of $BaSO_4$ (Fig. 3-13A) and inclusions <1 µm in size.

Table 3-4 Ternary composition of two feldspar particles in accretionary lapilli.

Particle No. N	L9a1 7.4 7	s (± wt.%)	L9a1 7.1 5	s (± wt.%)
SiO_2	63.5	1.3	62.2	0.9
TiO2	0.15	0.05	0.20	0.06
Al_2O_3	20.2	0.7	20.1	0.3
MgO	0.34	0.34	0.23	0.05
FeO	1.01	0.24	1.09	0.27
MnO	<0.08	-	<0.08	-
CaO	3.92	0.49	4.05	0.77
K_2O	6.74	0.54	7.87	0.83
Na_2O	3.50	0.21	3.58	0.30
Total	99.3	1.1	99.3	0.6
Ab	0.35		0.33	
An	0.21		0.20	
Or	0.44		0.47	

N: number of analyses

Other feldspar particles (Fig. 3-13B) have a partially euhedral, partially resorbed morphology together with overgrowths of calcite and contain inclusions. Two areas of different composition have been identified in this feldspar particle. The smaller partially round area is of plagioclase composition (Fig. 3-13B, dashed line). The larger area has a patchy appearance due to the presence of two phases. EMP analyses show that the composition of these mixed phases have a higher potassium and lower sodium content than the associated area having the composition of plagioclase (P4a and P4b in Fig. 3-12B). A similar relationship is observed for plagioclase particles with thin lamellae which are embedded in silicate melt shards (Fig. 3-13C). The lamellae (P3l at Fig. 3-12B) show enrichment in potassium and depletion in sodium compared to the associated plagioclase particle (P3 at Fig. 3-12B).

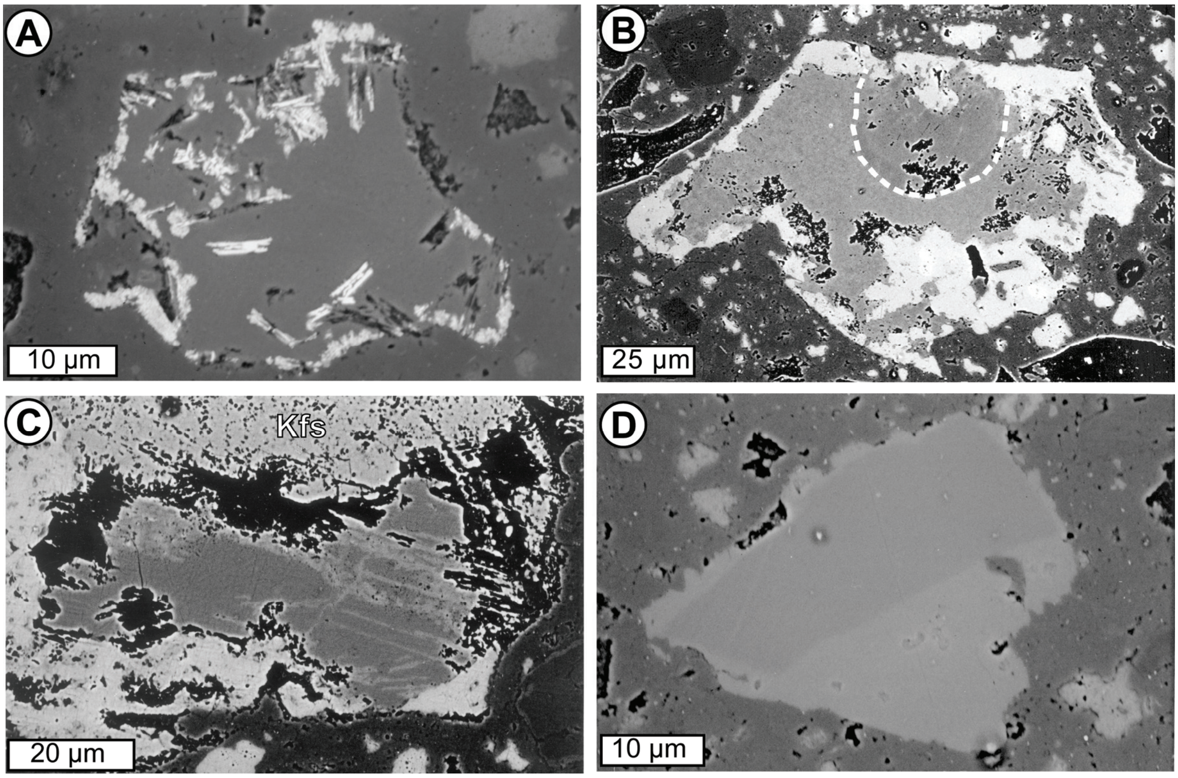

Figure 3-13 BSE micrographs of heterogeneous composed feldspar particles in accretionary lapilli. **(A)** Feldspar with ternary composition and needle-like exsolution lamella of $BaSO_4$ (L9a1 7.4, T1). **(B)** Feldspar (L9a1 7.2) with plagioclase area (round dark grey within dashed line, P4a) and larger, heterogeneous composed area (P4b). Note the inclusions of altered silicate melt (black), overgrowths of calcite at the rim (bright) and partially euhedral (upper margin), partially resorbed (lower margin) particle rim. **(C)** Plagioclase grain in altered silicate melt particle (L9a1 3.16, P3) showing planar K-rich lamella (P3l). Other phases are inclusion-rich potassium feldspar (Kfs; light grey at upper margin), calcite (bright) and altered silicate melt (black). **(D)** Potassium–sodium feldspar with rim of potassium feldspar (L9a1 4-3, A1). Sample numbers and classification numbers corresponding to Fig. 3-12 and Fig. 3-14 are given in parentheses. BSE: back scattered electron.

Potassium–sodium feldspars are often associated with potassium feldspar either as lamellae or rims (Fig. 3-13D). The potassium feldspar composition is close to the pure potassium endmember (Fig. 3-14A). Figs. 3-15A–D show a potassium–sodium feldspar particle with a heterogeneous composition displaying PDFs, undulatory extinction (Fig. 3-15B) and vesicles. The Fe element mapping (Fig. 3-15E) reveals that altered silicate melt is located around and

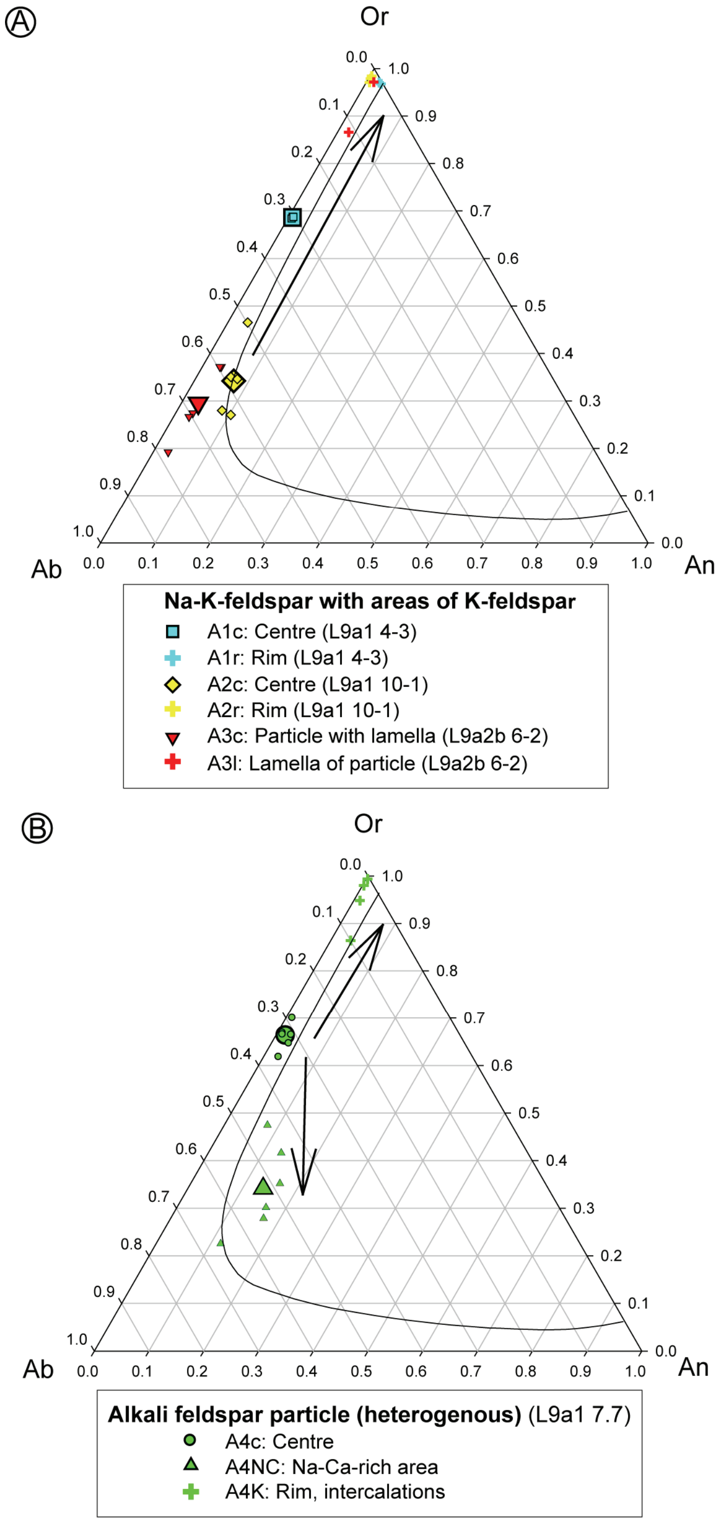

Figure 3-14 Compositions of alkali feldspar particles within accretionary lapilli. **(A)** Three potassium–sodium feldspar particles (two with potassium-feldspar rims, one with potassium-feldspar lamella). Arrow shows compositional trend towards higher potassium and lower sodium content. **(B)** One potassium–sodium feldspar particle with potassium-feldspar areas associated with Na/Ca-rich areas. Arrows show compositional trends towards higher potassium, lower sodium and higher calcium, lower potassium content. Large symbols represent mean values of single analyses (small symbols). Sample numbers are given in parentheses. Isotherm at 900°C, 0.5 kbar after Deer et al. (1992).

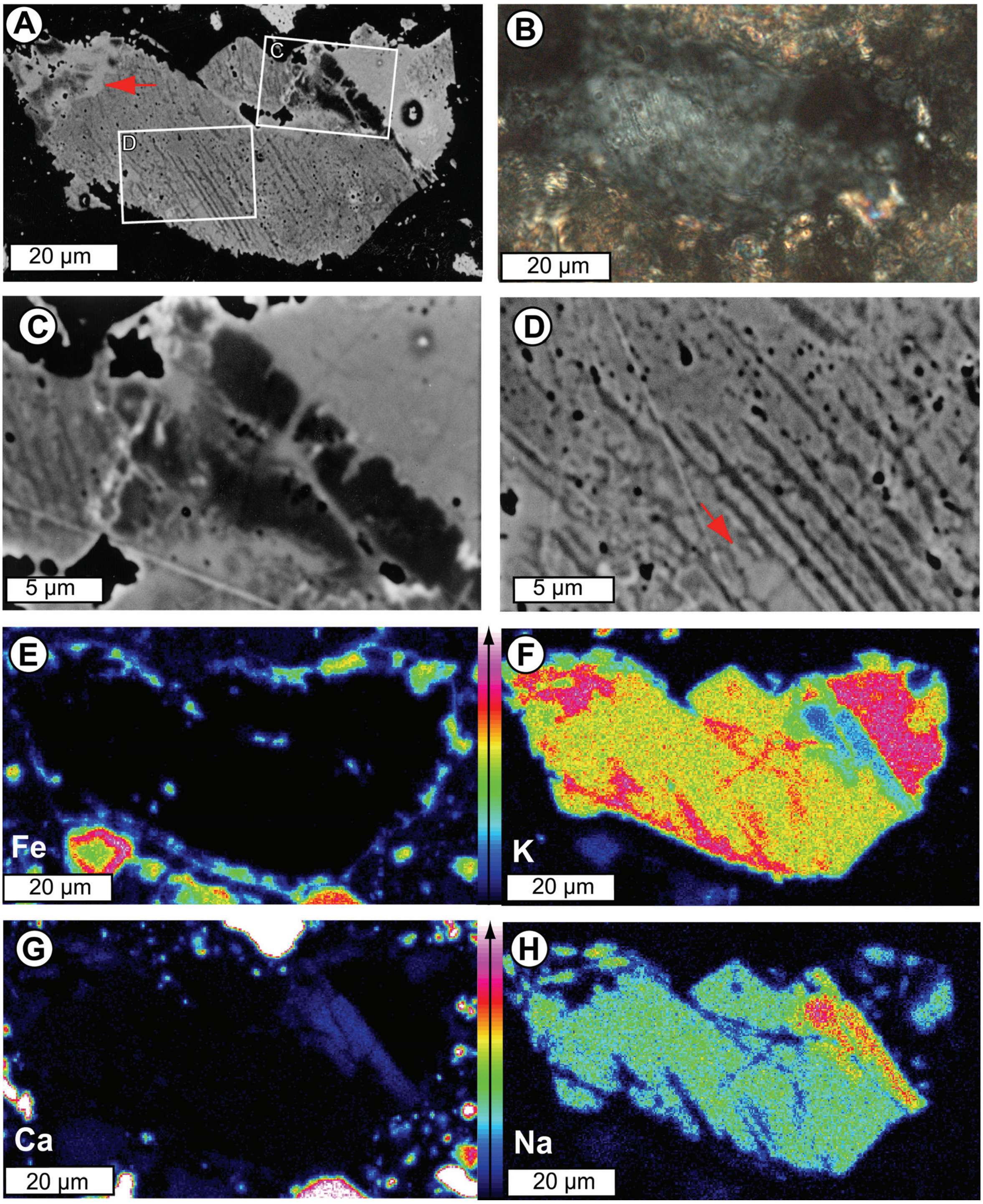

Figure 3-15 Heterogeneous composed alkali feldspar particle within accretionary lapillus. **(A)** BSE micrograph. Spot right of rectangle (C) is an artefact due to contamination. **(B)** Same section of (A) in XPL showing undulatory extinction and PDFs. **(C, D)** Close-up of (A). **(E–H)** Element mappings (K, Ca, Na) of same section of (A,B). Red arrows in (A, D) mark K-feldspar areas (light grey) as intercalations and rims associated with different composed areas (dark to medium grey). BSE: back scattered electron; XPL: cross polarised light.

intercalating into the particle, which is confirmed by EDX analyses and reddish, iron stained areas observed with optical microscopy. In BSE mode, there are light grey potassium-rich areas, which occur preferentially near the altered silicate melt forming a flow texture or intercalations (arrows in Figs. 3-15A and D; compare with element mapping at Fig. 3-15F). The potassium-rich areas are often associated with areas which appear darker in BSE mode (Figs. 3-15A and C). EMP analyses (Fig. 3-14D) show a composition close to the pure potassium-rich composition of the first, whereas the latter show an increase of sodium, a slight increase of calcium and a decrease of potassium (Figs. 3-15F–H). The planar lamellae (Fig. 3-15D) are too small to be analysed with the EMP or SEM, but they show a darker colour range in BSE mode similar to the sodium and calcium rich areas identified.

3.5 Chemistry of silicate melt particles

A total of 35 melt particles from the bulk rock have been measured with 260 individual EMP analyses in order to characterise their compositional variations. Furthermore, there are 60 individual EMP analyses of 8 accreted melt particles, and 22 individual analyses of 5 clay minerals which are pseudomorphs of a former laths-shaped phase (Tab. 3-5):

Table 3-5 Number of melt particles and analyses in bulk rock and accretionary lapilli and those of laths-shaped clay minerals in accretionary lapilli.

	No. of particles	No. of analyses
BULK ROCK		
Melt particle type 1	15	92
Melt particle type 2a	16	124
Melt particle type 2b	4	44
ACCRETIONARY LAPILLI		
Melt particle	8	60
Laths-shaped clay minerals	5	22
Total	48	342

Fig. 3-16 and Fig. 3-17 show Harker diagrams of major element correlations with SiO_2 for melt particles (data renormalised to 100 wt.% anhydrous). The clay mineral compositions of bulk rock melt particles (melt particle type 1 at left and melt particle type 2 at middle column) are compared with melt particles and laths-shaped clay minerals of accretionary lapilli (right column).

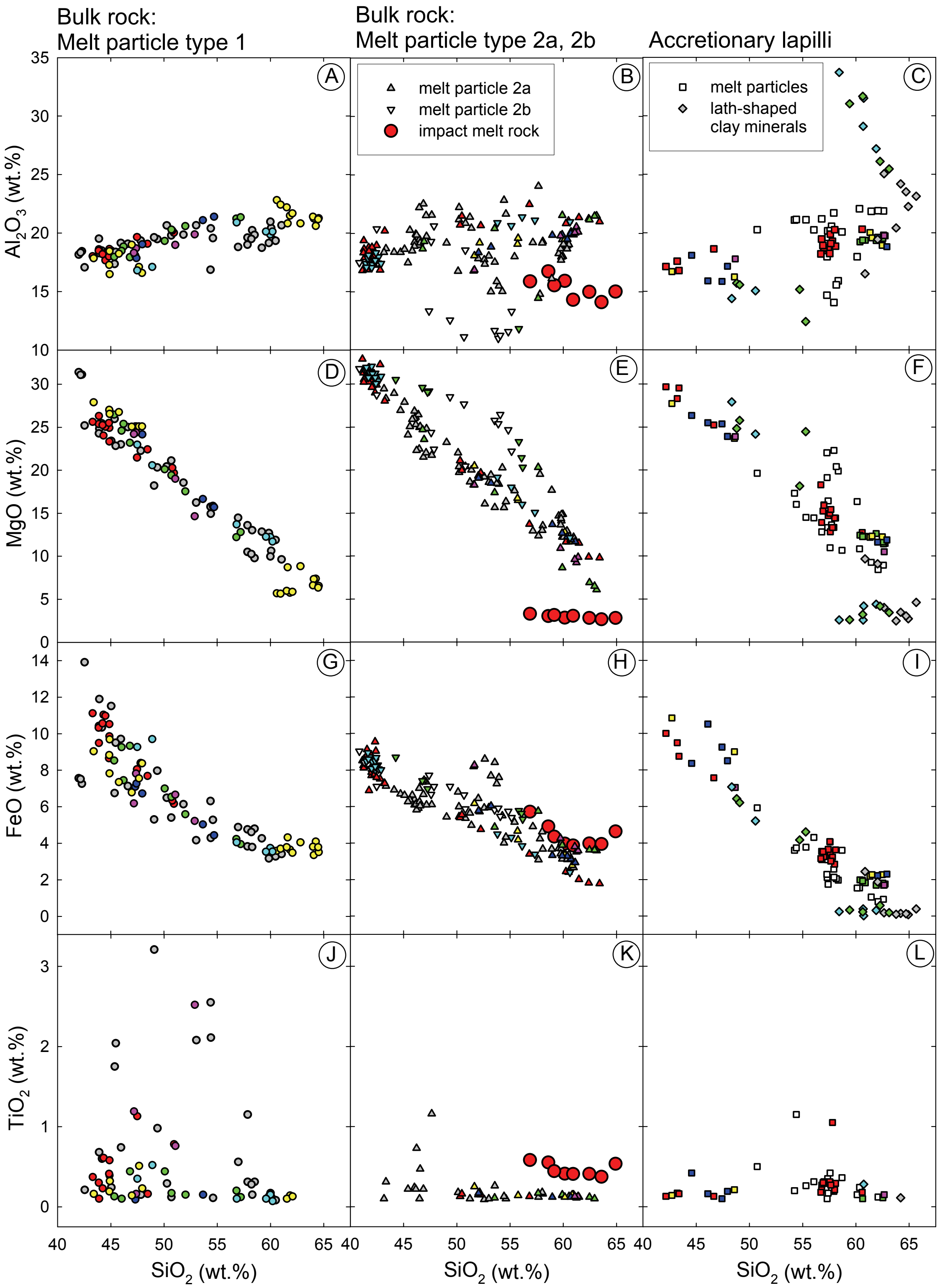

Figure 3-16 Harker diagrams for Al_2O_3, MgO and FeO and TiO_2 for bulk rock melt particles (melt particle type1: left column; melt particle type 2a and 2b: middle column) in comparison with melt particles and "laths-shaped clay minerals" of accretionary lapilli (right column). Grey and white data points represent compositions of different particles with homogeneous composition. Data points with similar colour are heterogeneous compositions within the same particle. Impact melt rock composition of Y6 and C1 (Schuraytz et al. 1994) is added in middle column for comparison. The data are renormalised to a total of 100 wt.% anhydrous.

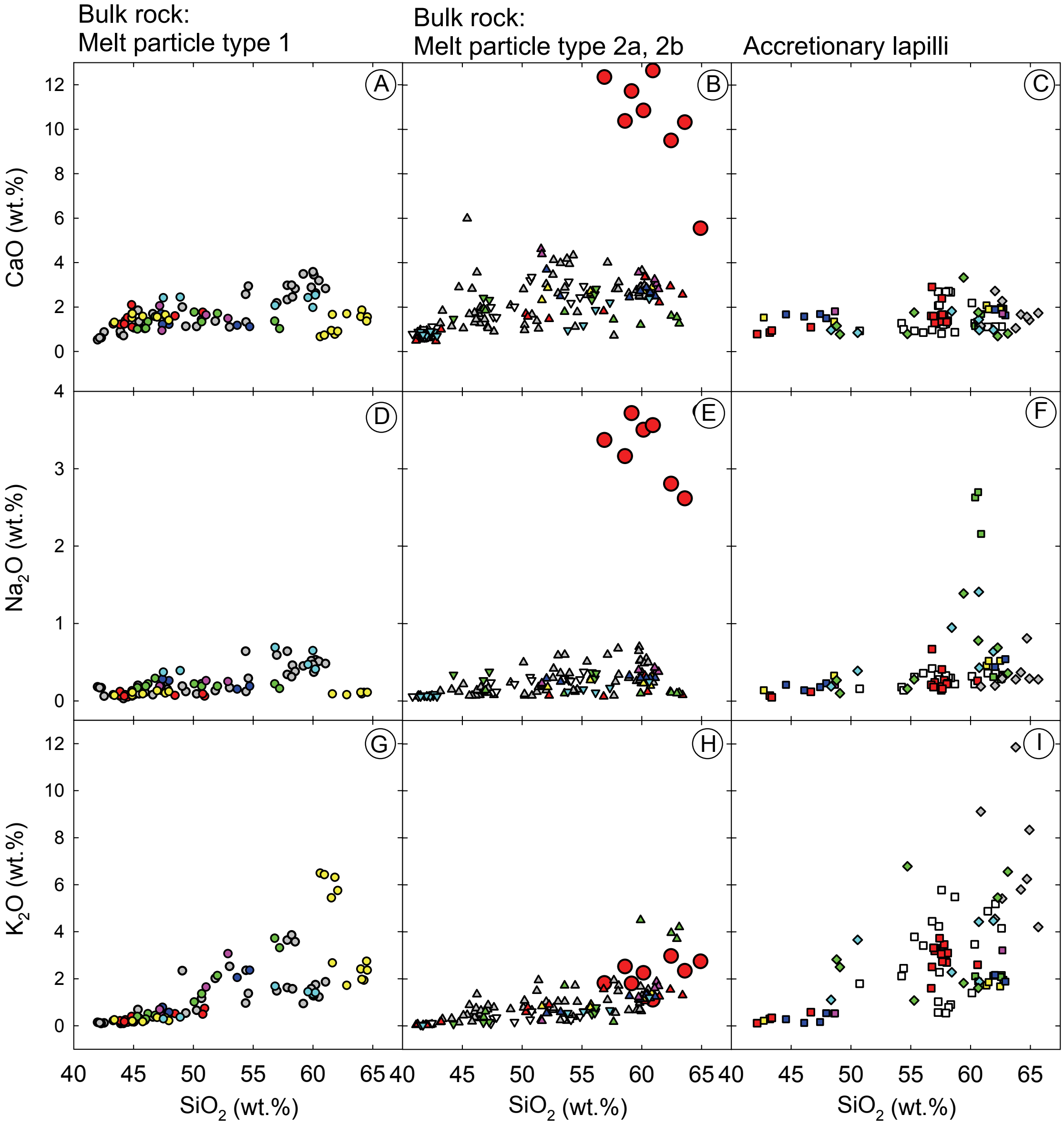

Figure 3-17 Harker diagrams for CaO, Na_2O and K_2O for bulk rock melt particles (melt particle type 1: left column; melt particle type 2a and 2b: middle column) in comparison with melt particles and "laths-shaped clay minerals" of accretionary lapilli (right column). Grey and white data points represent compositions of different particles with homogeneous composition. Data points with similar colour are heterogeneous compositions within the same particle. Impact melt rock composition of Y6 and C1 (Schuraytz et al. 1994) is added in middle column for comparison. The data are renormalised to a total of 100 wt.% anhydrous. Symbols are same as in Fig. 3-16.

Different measurements of one particle are shown by the same colour in the Harker diagram to illustrate the chemical heterogeneities within the same particle. The silicate melt particles of the bulk rock and those of accretionary lapilli generally show a decrease in Al_2O_3 (Figs. 3-16A–C), CaO (Figs. 3-17A–C), Na_2O (Figs. 3-17D–F) and K_2O (Figs. 3-17G–I) with decreasing SiO_2, whereas MgO (Figs. 3-16D–F), FeO (Figs. 3-16G–I) show increasing concentrations. Melt particle type 1 shows variations towards higher values for TiO_2 especially for intermediate to lower SiO_2 values (Fig. 3-17J).

Ternary diagrams of SiO_2, Al_2O_3 and MgO + FeO show that melt particle type 1 (Fig. 3-18A), melt particle type 2a (Fig. 3-18B), melt particle type 2b (Fig. 3-18C) and the melt particles of the accretionary lapilli (Fig. 3-5D) show variations between two extreme compositions: (1) The SiO_2-rich compositions plot near the montmorillonite field (Fig. 3-18, centre); (2) the SiO_2-poor compositions near the vermiculite field, but some compositions extend towards the chlorite field. For melt particle type 2b only a few data points show a shift from the vermiculite field towards the saponite field. Some of the “laths-shaped clay minerals” in the accretionary lapilli are shifted from the montmorillonite towards the illite/ kaolinite field.

For the bulk rock and accretionary lapilli the average melt particle composition of the two extreme compositions was obtained by selecting the analyses according to their SiO_2 content (Tab. 3-6). The compositions clearly show that the montmorillonite/ illite type has high SiO_2, Al_2O_3, CaO, K_2O, Na_2O with low FeO, MgO values and the vermiculite/ chlorite type low SiO_2, Al_2O_3, CaO, Na_2O, K_2O with high FeO, MgO values.

Optical microscopic studies show that the heterogeneities as indicated by brownish stained areas of iron hydroxide/ oxides are visible at plane polarised light. They mostly occur at the rim of melt particles in the bulk rock and the accretionary lapilli. Fig. 3-19A shows a layer of melt particle type 1 rimming an accretionary lapillus. Close to the larger angular melt particles the coexisting sparitic calcite is preferentially replaced by silica (Figs. 3-19A–C). In the BSE mode, the darker areas of the melt particle correspond to the montmorillonite/ illite and the bright areas to the vermiculite/ chlorite type. The vermiculite/ chlorite type preferentially occurs at the rim. It is associated with fractures and near triple junction fractures (Fig. 3-19A, arrow) and appears as smaller spot-like intergrowths. Most of the elements are uniformly distributed within the two different areas. However, K_2O locally shows higher concentrations within the montmorillonite/ illite areas (Fig. 3-19F; >5 wt.% K_2O, EMP analyses documented in Tab. 3-6, Ir15aK). Furthermore, small spot-like enrichments of Ti are observed at the transition zone of those two areas (Fig. 3-19H). These could represent intergrowths of rutile and may explain some of the Ti variations observed at EMP analyses (Fig. 3-16J).

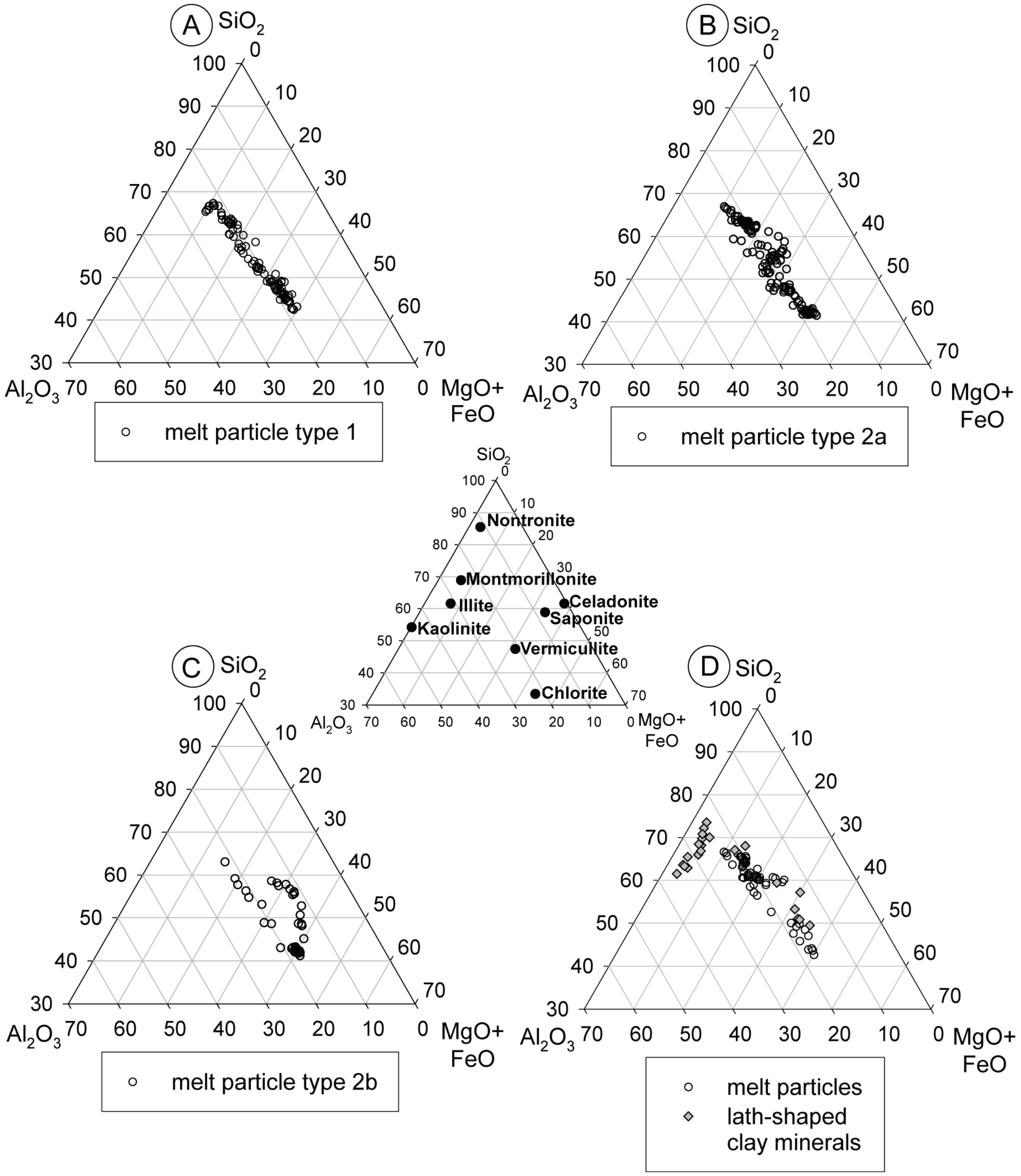

Figure 3-18 Ternary diagrams for bulk rock melt particles **(A)** melt particle type 1, **(B)** melt particle type 2a, **(C)** melt particle type 2b and **(D)** melt particles and lath-shaped clay minerals in accretionary lapilli. Figure in centre are reference compositions after Newsom & Nelson (2004).

Table 3-6 Extreme compositions of melt particles (altered to clay minerals) of the bulk rock compared with those of accretionary lapilli (upper table). Lower table show heterogeneous composed areas within melt particle of Fig. 3-19.

Type	Montmorillonite/ illite type						Vermicullite/ chlorite type					
Sample	Bulk rock			Accretionary lapilli			Bulk rock			Accretionary lapilli		
	$SiO_2 > 52$ wt.%			$SiO_2 > 50$ wt.%			$SiO_2 < 37$ wt.%			$SiO_2 < 41$ wt.%		
N	36			23			75			10		
SiO_2	53.4	±	0.9	52.5	±	1.3	35.5	±	0.8	38.3	±	1.9
TiO_2	0.10	±	0.07	0.28	±	0.21	<0.09			0.16	±	0.08
Al_2O_3	17.7	±	1.1	17.0	±	0.8	15.1	±	0.7	14.4	±	1.0
FeO	3.13	±	0.74	2.45	±	0.75	7.18	±	0.93	7.81	±	0.82
MnO	<0.08			<0.08			<0.08			<0.08		
MgO	9.3	±	2.6	12.0	±	1.9	24.2	±	3.5	22.5	±	2.0
CaO	2.21	±	0.69	1.56	±	0.35	0.77	±	0.30	1.10	±	0.28
Na_2O	0.27	±	0.16	0.28	±	0.13	<0.06			0.15	±	0.07
K_2O	1.90	±	1.23	2.23	±	0.66	0.13	±	0.11	0.27	±	0.15
Total	87.9	±	2.4	88.2	±	3.4	82.9	±	3.6	84.7	±	1.7

	Heterogeneous melt particle								
Sample	Ir15aH			Ir15aK			Ir15aL		
N	7			5			8		
SiO_2	51.5	±	1.2	52.0	±	1.2	39.9	±	1.3
TiO_2	<0.09			<0.09			0.22	±	0.12
Al_2O_3	17.0	±	0.5	18.7	±	0.6	15.4	±	0.8
FeO	3.11	±	0.29	3.08	±	0.05	7.13	±	0.90
MnO	<0.08			<0.08			<0.08		
MgO	5.99	±	0.89	4.90	±	0.13	22.9	±	1.0
CaO	1.30	±	0.15	0.68	±	0.10	1.35	±	0.13
Na_2O	0.08	±	0.01	<0.06			0.09	±	0.02
K_2O	1.82	±	0.31	5.16	±	0.43	0.20	±	0.06
Total	80.8	±	2.1	84.6	±	1.8	87.1	±	1.2

Ir15aH: Composition with high SiO_2, K_2O and low FeO, MgO values (montmorillonite/ illite type); Ir15aK: Composition of montmorillonite/ illite type with high K_2O values; Ir15aL: Composition with low SiO_2, K_2O and high FeO, MgO values (vermicullite/ chlorite type).

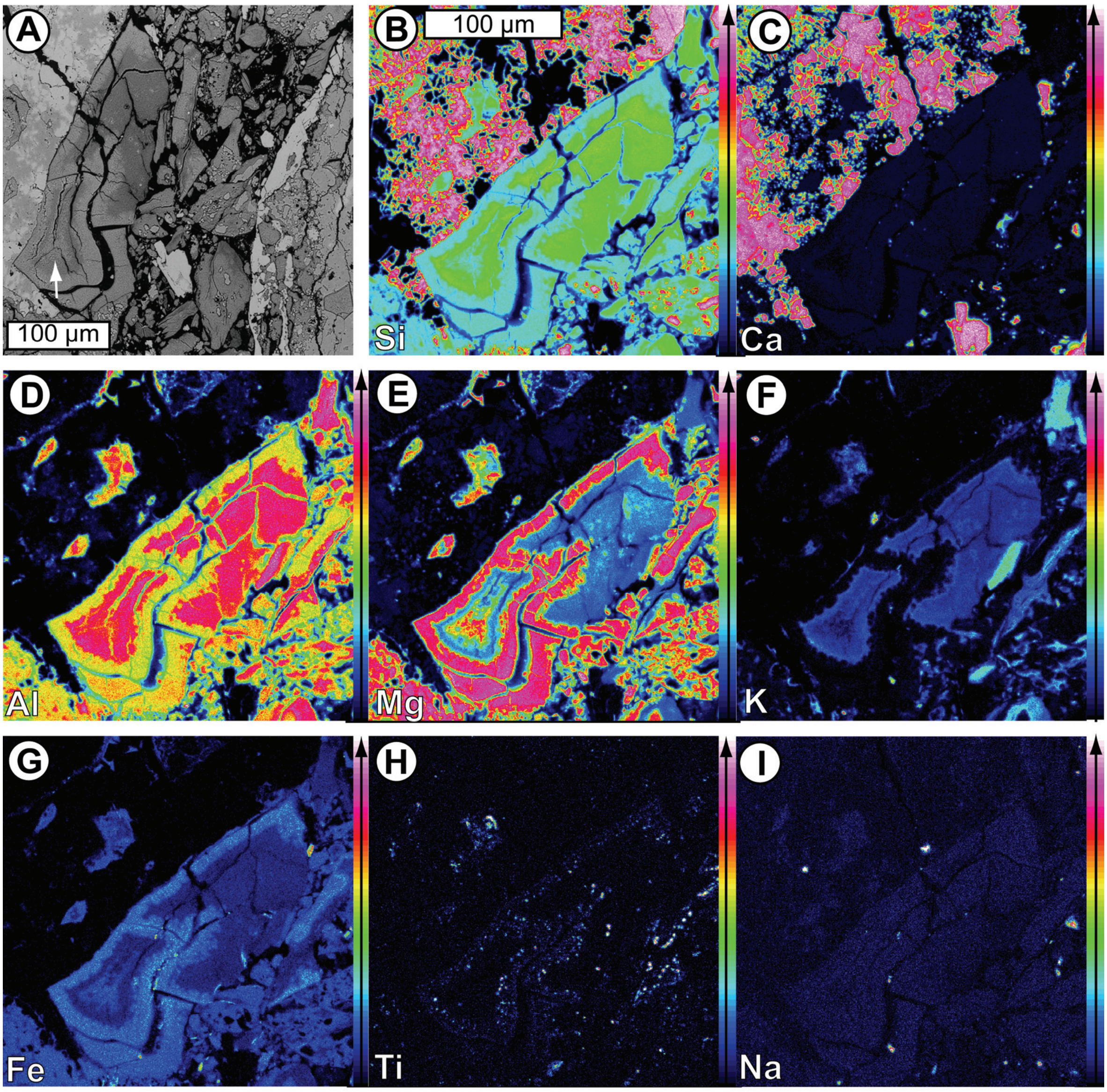

Figure 3-19 Elemental mapping of heterogeneous altered silicate melt particle. **(A)** BSE image of heterogeneous altered melt particles around accretionary lapillus (right). Note the occurrence of vermiculite/ chlorite type of clay mineral at rim of melt particles and the spot-like intergrowths near fracture surfaces (arrow). **(B−I)** EMP elemental map of the angular melt particle of (A).

3.6 Bulk rock and accretionary lapilli chemistry

Fig. 3-20 and Fig. 3-21 show Harker diagrams for major (TiO_2, Al_2O_3, Fe_2O_3, CaO, MgO, MnO, K_2O, P_2O_5) and trace element (Ba, Sr, V, Zr) concentrations plotted versus SiO_2 of mean bulk rock compositions. Na_2O is excluded as only samples of the clay unit show values around 0.09 ± 0.03 wt.%, while most other values are near or below the detection limit of 0.02 wt.%. The data normalisation to totals of 100 wt% has not been carried out as the totals including the loss of ignition range from 99.5 to 100.1 wt.%. A positive correlation with SiO_2 can be observed for Al_2O_3 (Fig. 3-20A), Fe_2O_3 (Fig. 3-20C), K_2O (Figs. 3-20E and F), TiO_2 (Fig. 3-21C), Cr (Fig. 3-21E), V (Fig. 3-21F), Zr (Fig. 3-21D), whereas a negative correlation is present for CaO (Fig. 3-20B) and Sr (Fig. 3-21B). Due to the higher abundance of quartz clasts in the clay unit and the silica matrix in the accretionary lapilli, most element concentrations of those samples are shifted towards a SiO_2-richer composition. In the megabreccia, the Ba values (Fig. 3-21A) are near or slightly above the detection limit of 30 μg/g. The lower accretionary lapilli unit shows a 5 times higher Ba content (145 ± 12 μg/g) compared to the underlying microbreccia. Towards the clay unit, a positive correlation of Ba with SiO_2 is observed. Compared to the host rock, the accretionary lapilli are enriched in SiO_2 and depleted in CaO. This is caused by the dominating presence of silica in the matrix of the accretionary lapilli. Immobile elements like TiO_2, Zr, Cr and V are of similar abundance in the accretionary lapilli as in the host rock. In the clay unit, siderophile elements like Ni, V and Cr are enriched compared to the underlying units.

Fig. 3-22 show selected trace element concentrations obtained by TXRF (Ti, V, Cr, Co, Pb, Cu, Zn, Rb, Ni) in relation to the stratigraphic level of the samples. All of those elements show a similar behaviour: The element concentrations either remain constant or slightly increase in the lower megabreccia to the upper microbreccia. In the accretionary lapilli bearing unit, the accretionary lapilli have lower concentrations compared to their host rock, which can be explained by the large proportion of secondary silica matrix in the accretionary lapilli. At the transition from the upper accretionary lapilli unit towards the clay unit a strong but varying increase of the trace elements concentration is observed. In the clay unit Ni, Cu, Zn and Rb show their highest values. The measured Co concentration in the uppermost microbreccia (G8) is very high compared to the other measured samples. However, this excursion may be an artefact due to a nugget effect (due to a sample size of some mg). Additionally, at the upper accretionary lapilli unit in sample G14-2 high concentrations were measured for all trace elements. This might be due to an inhomogeneously composed sample with a high proportion of (possibly molten) feldspar which would be consistent with the elevated value for Ba (480 μg/g).

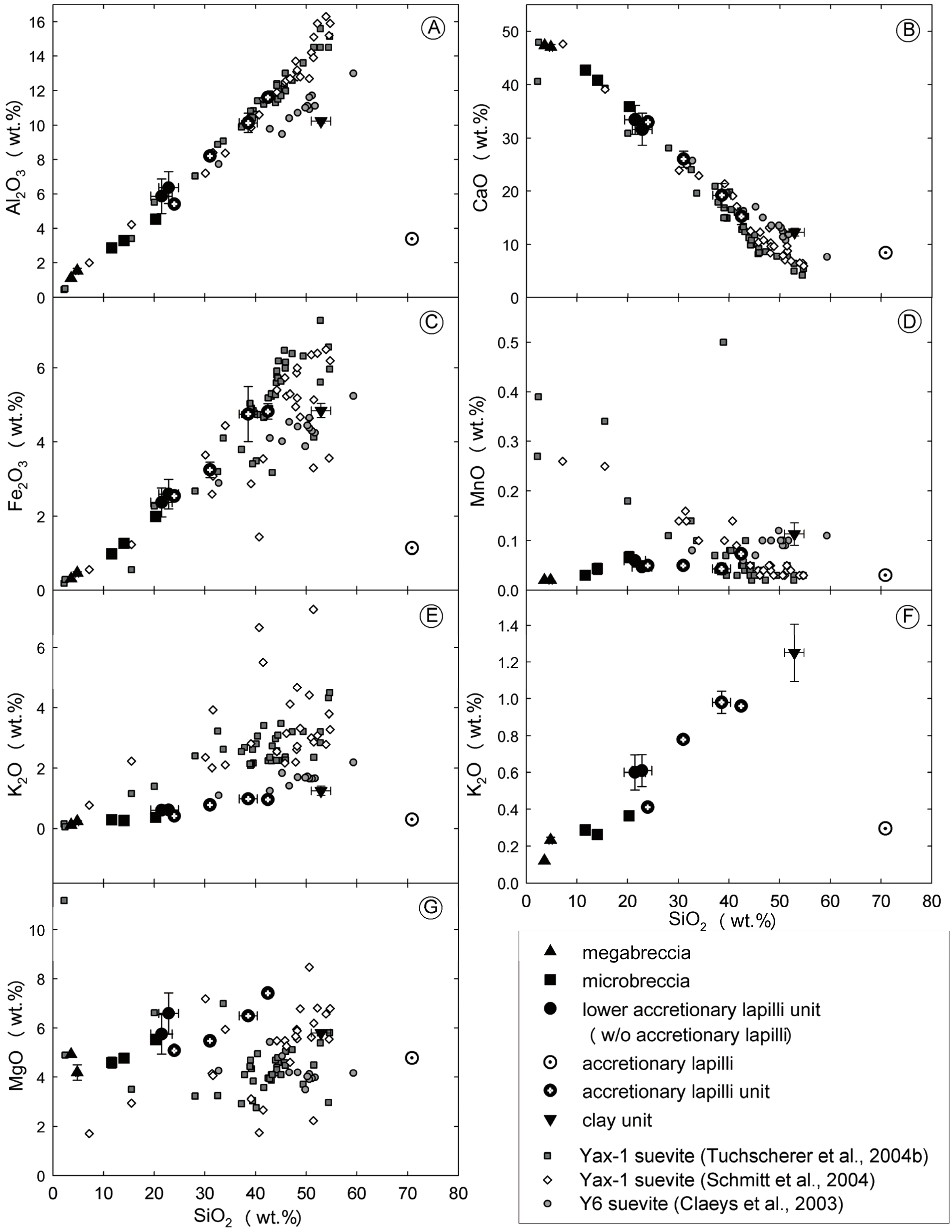

Figure 3-20 Harker diagrams of mean values for major and minor elements of El Guayal bulk rock and accretionary lapilli compared with Y6 suevite (Claeys et al. 2003) and Yax-1 suevite (Schmitt et al. 2004; Tuchscherer et al. 2004b) of the Chicxulub impact structure.

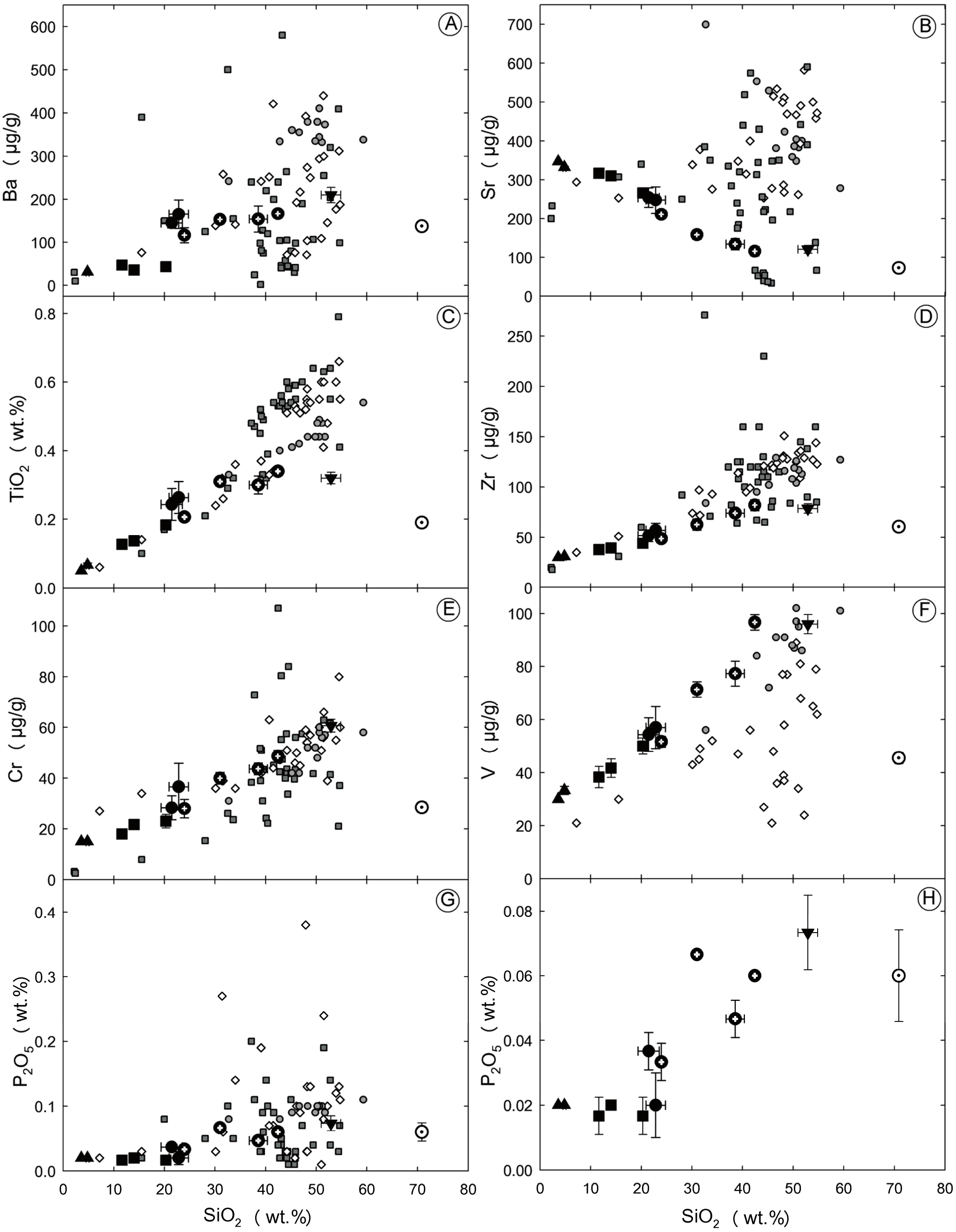

Figure 3-21 Harker diagrams of mean values for minor and trace elements of El Guayal bulk rock and accretionary lapilli compared with Y6 suevite (Claeys et al. 2003) and Yax-1 suevite (Schmitt et al. 2004; Tuchscherer et al. 2004b) of the Chicxulub impact structure. The symbols are as in Fig. 3-20. For a better view following samples of the Chicxulub impact structure have been excluded due to unusual high element concentrations: Yax-1-852.80 (Ba, Sr); Yax-1-895.00 (V); Yax-1-808.30 (Zr) and Yax-1851.20 (P_2O_5).

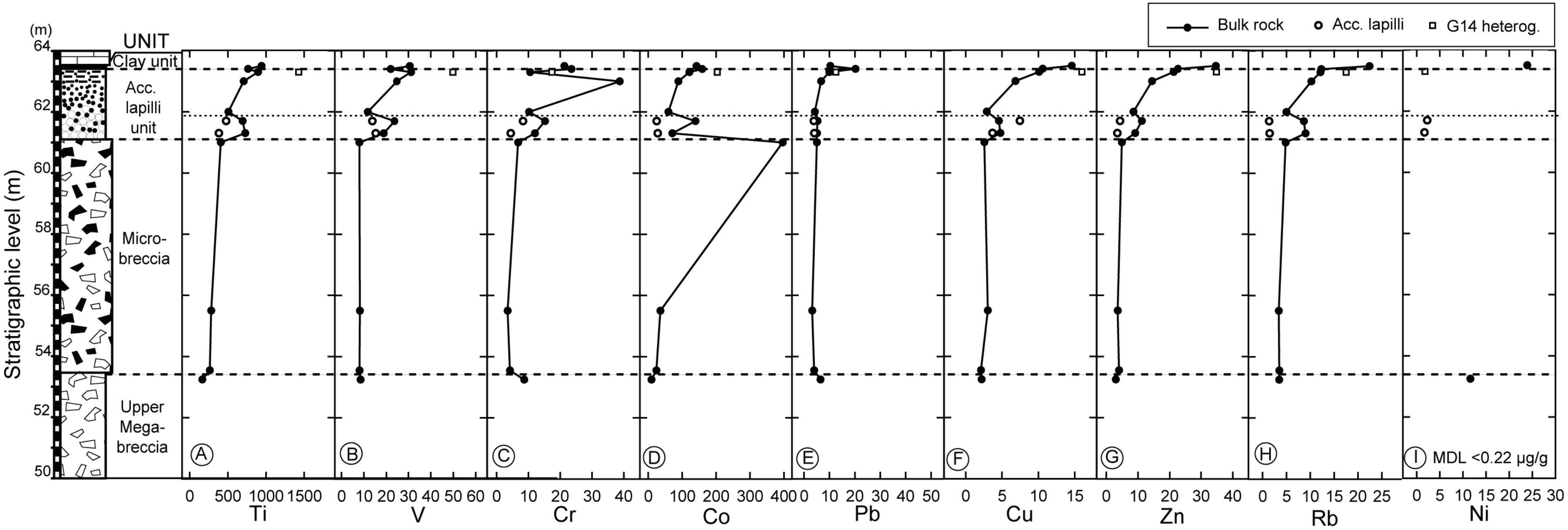

Figure 3-22 TXRF trace element composition (µg/g) of El Guayal as a function of stratigraphic level (stratigraphic column corresponds to the middle stratigraphic column of Fig. 2-1). Dashed line marks different units of megabreccia, microbreccia, accretionary lapilli unit and clay unit; dotted line shows the lower accretionary lapilli unit, where accretionary lapilli (void circles) and the lapilli surrounding rock has been analysed independently. G14 heterog.: inhomogeneous analysis; MDL: method detection limit.

Table 3-7 PGE and Au composition (ng/g) of the PGE-enriched clay unit, accretionary lapilli and their surrounding matrix (bulk rock of lowermost accretionary lapilli unit without accretionary lapilli) (Tagle, unpublished data).

Sample	Ir	Ru	Pt	Rh	Pd	Au
Clay unit	0.73	1.47	1.12	0.24	1.70	0.20
Accretionary lapilli	u.l.d.	u.l.d.	0.25	0.02	0.36	0.12
Matrix	u.l.d.	u.l.d.	0.25	u.l.d.	0.15	0.18
Continental crust	0.02	0.21	0.51	0.06	0.52	2.50
d. l.	0.038	0.062	0.043	0.013	0.127	0.089

d.l.: detection limit after Tagle et al. (2004); u.d.l.: under limit of detection. Composition of the continental crust after Wedepohl (1995), Rh values from Peucker-Ehrenbrink & Jahn (2001).

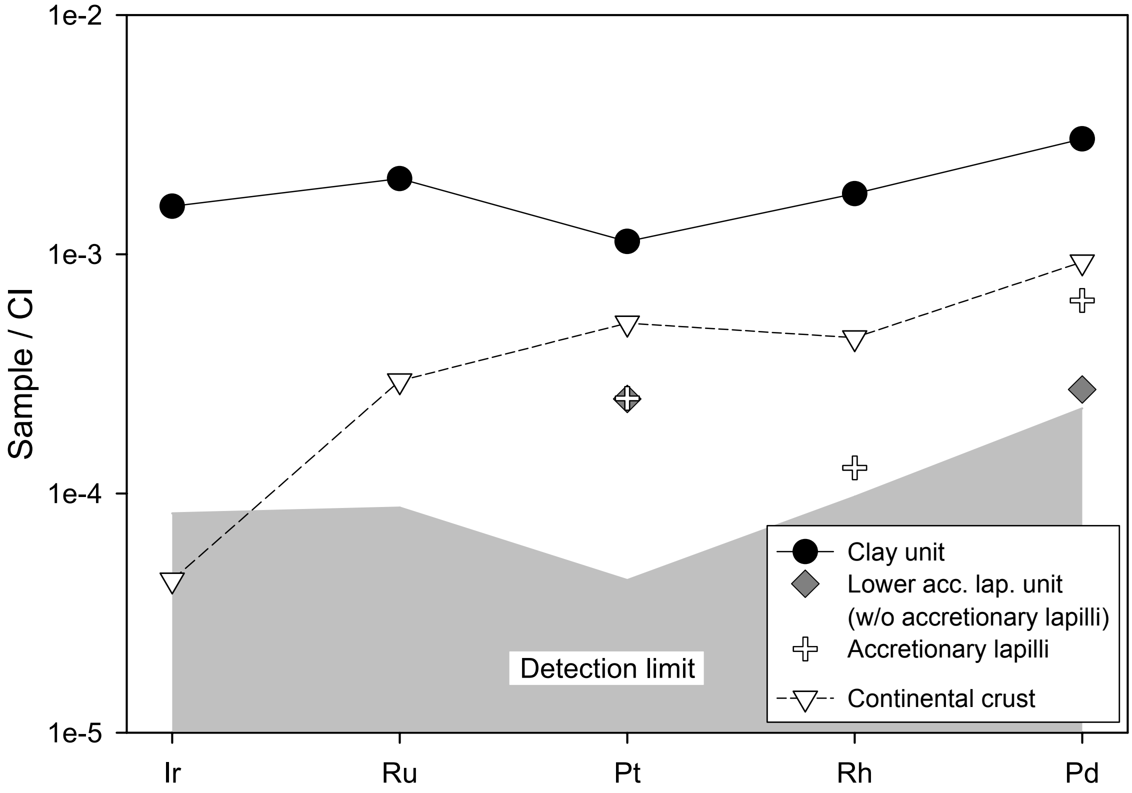

Figure 3-23 CI-normalised PGE concentrations (Tagle, unpublished data) of the clay unit, the accretionary lapilli and their surrounding matrix (bulk rock of lowermost accretionary lapilli unit without accretionary lapilli) compared to the composition of the continental crust (Wedepohl, 1995; Rh values from Peucker-Ehrenbrink & Jahn, 2001). Detection limit (grey) of Tagle et al. (2004). CI composition of Wasson & Kallemeyn (1998).

Analyses of PGE were performed for the accretionary lapilli, their surrounding matrix (bulk rock of lowermost accretionary lapilli unit without accretionary lapilli) and the overlying clay unit (Tab. 3-7). Fig. 3-23 shows that the accretionary lapilli and their surrounding matrix have a pattern similar to the average continental crust with distinct depletion of Ir. Hence, neither the accretionary lapilli nor the matrix is enriched in PGE compared to the average continental crust. Measurements of PGE concentrations of the overlying clay unit resulted in an order of magnitude higher PGE concentrations. Additionally, the relative abundance of the different PGE differs significantly from those of the continental crust. Especially Ir is strongly enriched by two orders of magnitude compared to the average continental crust. Thus, based on the flat pattern of the PGE abundances in the CI normalised diagram, an impactor component is identified in the clay unit.

3.7 Modal composition calculations

The petrographic studies indicate that the impactites of El Guayal contain mainly carbonates (mostly calcite, rarely dolomite), silicate melt particles (altered to clay minerals), quartz and silica. The modal composition has been modelled numerically with the constrained mixing model of Le Maitre (1979) and the method of the least square (Davis 1973). For these calculations, the bulk rock compositions obtained by XRF analyses and phase compositions of mineral by EMP analyses have been used. The results (Fig. 3-24, Tab. 3-8, Tab. A3-1) indicate a two component mixing trend between a carbonate endmember and an altered silicate melt endmember. From the upper megabreccia to the clay unit there is an increase of altered silicate melt (5 to 59 %) and a decrease of carbonates (94 to 13 %). Significant changes in mineralogical composition are correlated with lithological contacts: (1) From the upper megabreccia to the lower microbreccia the proportion of silicate melt increases by 8 % (from 8 to 16 %); (2) within the microbreccia over a range of ~7.5 m an increase of altered silicate melt by 11 % is observed; (3) from the upper microbreccia towards the lower accretionary lapilli unit there is an increase in altered silicate melt by 6 % (from 27 to 33 %). Within the accretionary lapilli unit, the altered silicate melt proportion of 66 % is highest in the upper laminated beds near the clay unit.

The abundance of silica phases increases –similarly to the altered silicate melt– from the upper megabreccia to the lower microbreccia from <1 to 4 %. Within the microbreccia, there is an increase in modal abundance from 4 to 8 %. The silica content in the lower accretionary lapilli unit, which contains abundant accretionary lapilli, is lower compared to the underlying microbreccia and overlying middle accretionary lapilli unit. However, this is an artefact, since the modal content of silica-enriched accretionary lapilli (64 % silica) was calculated independently and was excluded from the calculation for the bulk rock. The silica content does not exceed 9 % within the microbreccia and the accretionary lapilli unit. In the clay unit, a distinct increase by 13 % is observed yielding a total of 22 %.

The upper megabreccia has the highest content of dolomite (15 to 20 %). At the transition from mega- to microbreccia the proportion of calcite does not change significantly. However, the amount of dolomite drops from 15 to 6 %. The lower accretionary lapilli unit shows a dolomite content of 6 to 8 % which is similar to the modal abundance of dolomite in accretionary lapilli. For the upper microbreccia, middle and upper accretionary unit and the clay unit, dolomite was excluded from the calculations. Adding dolomite to the calculations would lead to unrealistic results characterised by high errors and/ or negative values. Thus, according to the calculations dolomite is not present in those units. The role of K-feldspar can be neglected indicated by values <1 %.

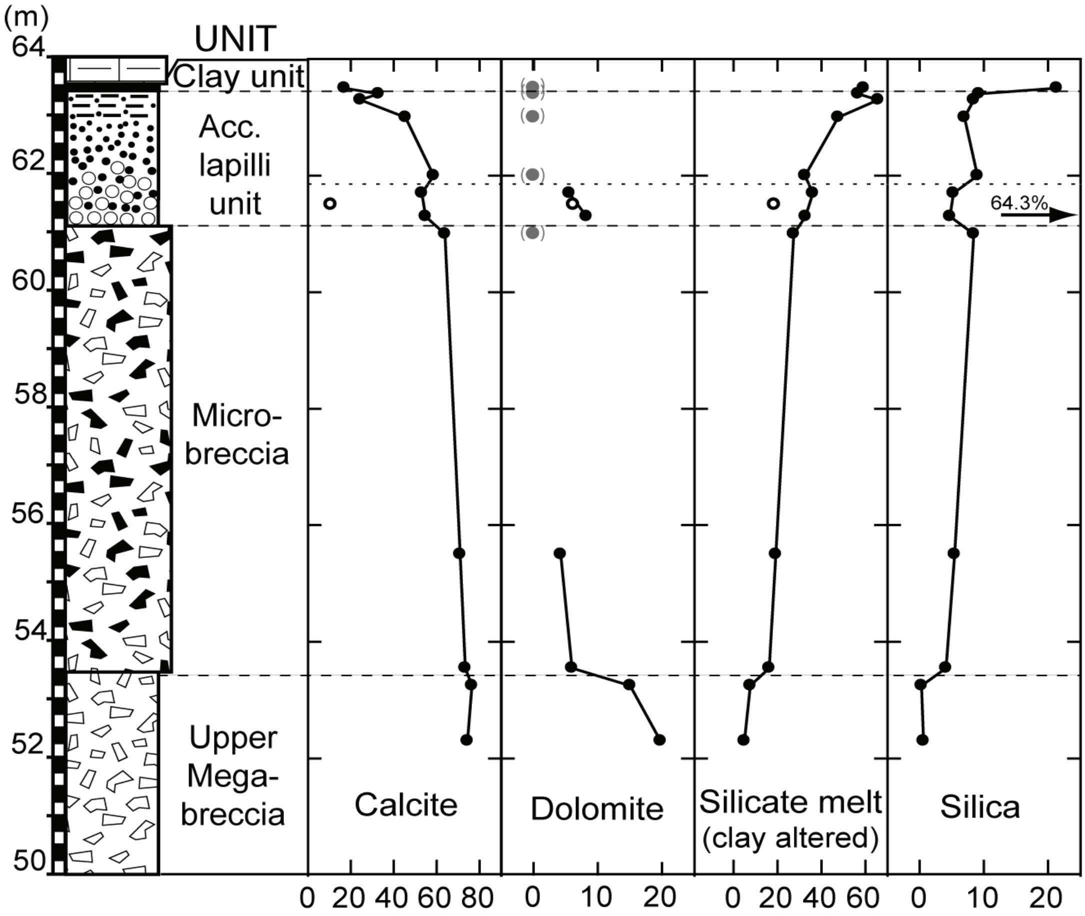

Figure 3-24 Modal content (%) of calcite, dolomite, silicate melt (altered to clay minerals) and silica as a function of stratigraphic level (stratigraphic column corresponds to the middle stratigraphic column of Fig. 2-1). Dashed lines mark different units of megabreccia, microbreccia, accretionary lapilli unit and clay unit. Dotted line shows the lower accretionary lapilli unit, where accretionary lapilli (open circles) and the lapilli surrounding rock has been analysed independently. Grey data points in brackets at dolomite are calculations where dolomite was excluded (see text for explanation). For simplification, the high silica content of accretionary lapilli (64.3 %) has been excluded.

Table 3-8 Results of the calculated modal composition (%) of El Guayal units based on chemical analyses. Extended results are given in Tab. A3-1.

Sample	Unit	Cal	Dol	SM	SiO_2	K-fsp	Hem	Quickl	Total	s (±%)
G04	uMB	74.4	19.7	4.9	0.6	0.5	n.m.	n.m.	100.2	0.2
G05	uMB	76.4	15.0	7.6	0.3	0.7	n.m.	n.m.	100.0	0.2
G06	lμB	73.4	6.0	16.1	4.1	0.8	n.m.	n.m.	100.4	0.3
G07	mμB	70.9	4.2	19.2	5.4	0.6	n.m.	n.m.	100.3	0.3
G08	uμB	63.8	n.m.	27.3	8.4	0.7	n.m.	n.m.	100.3	0.4
G09	lALU	54.8	8.2	32.7	4.7	0.3	n.m.	n.m.	100.8	1.1
G10	lALU	53.1	5.6	36.1	5.3	0.8	n.m.	n.m.	100.8	0.9
G11	mALU	58.6	n.m.	32.5	9.0	n.m.	n.m.	n.m.	100.0	0.8
G12	mALU	45.5	n.m.	47.6	7.0	n.m.	n.m.	n.m.	100.0	1.3
G14	uALU	24.4	n.m.	65.8	8.5	n.m.	2.1	n.m.	100.9	0.8
G13	uALU	32.8	n.m.	56.7	9.3	n.m.	2.3	n.m.	98.8	0.9
G15	CU	12.5	n.m.	58.5	22.1	n.m.	2.7	4.1	99.9	0.3
G09/10L	Lapilli	10.7	6.2	18.5	64.3	0.1	n.m.	n.m.	99.9	0.1

PHASES: Cal: calcite, Dol: dolomite; SM: silicate melt (altered to clay minerals); SiO_2: quartz and silica; K-fsp: K-feldspar; Hem: haematite; Quickl: quicklime. UNITS: MB: megabreccia; μB: microbreccia; ALU: accretionary lapilli unit; CU: clay unit; Lapilli: accretionary lapilli (prefix marks the stratigraphic level. l: lower; m: middle; u: upper). n.m.: not modelled.

Performing calculations only with the five phases –namely the two silicate melt compositions, silica, calcite and dolomite– leads to errors >2 % for the upper accretionary lapilli unit and the clay unit (Tab. A3-1). This error mainly derives from low values for Fe_2O_3 indicated by the (back calculated) bulk rock control composition (Tab. 3-9, calculation 1). Adding the supposed phase haematite to the calculations results in a modal content of 2 to 3 % haematite (Tab. 3-8) and lowers the total error significantly (Tab. 3-9, calculation 2). However, for the clay unit, an error of 2.6 % is observed due underestimation of CaO and overestimation for CO_2 at the (back calculated) bulk rock control composition. Adding the supposed phase quicklime (CaO) to the modal phase calculation could lower the error to 0.3 % with modal content of 4 % CaO (Tab. 3-9, calculation 3).

The modal calculations are in good agreement with the petrographic results with regard to (1) the modal content of silicate melt and calcite, (2) the significant increase of SiO_2 due to quartz particles in the clay unit, and (3) the low modal content of dolomite and K-feldspar.

Table 3-9 Example of calculated modal composition on sample G15 (clay unit) after the constrained mixing model of Le Maitre (1979). Light grey shaded values are elements, where the (back calculated) bulk rock control composition significantly deviates from the measured element composition for this element, which results in a high cumulative error for the calculation (dark grey shaded). Adding supposed phases (calculation 2: haematite; calculation 3: haematite + quicklime) could lower the cumulative error from 3.68 to 2.58 and 0.35 % respectively. Results may slightly differ from Tab. 3-8 and Tab. A2-1 as those values are the mean values of the model of Le Maitre (1979) and the method of least squares (Davis 1973).

Calculation 1

	1	2	3	4			CONTROL			RESULTS	
Phase	SM Mg	SM Si	Cal	Silica		SUM	SUM	s	s^2	Phase	%
	EMPA	EMPA	EMPA	supp.		XRF					
SiO_2	35.46	53.37	0.00	100.00	=	52.90	53.01	-0.11	0.01	SM Mg	5.2
TiO_2	0.08	0.10	0.00	0.00	=	0.32	0.06	0.26	0.07	SM Si	56.6
Al_2O_3	15.09	17.67	0.07	0.00	=	10.23	10.80	-0.56	0.32	Cal	17.2
Fe_2O_3	7.97	3.48	0.09	0.00	=	4.84	2.40	2.44	5.95	Silica	21.1
MnO	0.02	0.01	0.06	0.00	=	0.11	0.02	0.10	0.01	Total	100.1
MgO	24.22	9.27	0.49	0.00	=	5.79	6.60	-0.81	0.65	s	3.68
CaO	0.77	2.21	55.23	0.00	=	12.27	10.80	1.46	2.15		
K_2O	0.08	1.90	0.00	0.00	=	1.25	1.08	0.17	0.03		
Na_2O	0.05	0.27	0.00	0.00	=	0.09	0.16	-0.07	0.00		
CO_2	0.00	0.00	44.07	0.00	=	5.50	7.59	-2.09	4.37		
Total	83.73	88.29	100.00	100.00		93.31	92.52		13.55		

Calculation 2

	1	2	3	4	5			CONTROL			RESULTS	
Phase	SM Mg	SM Si	Cal	Silica	Hem		SUM	SUM	s	s^2	Phase	%
	EMPA	EMPA	EMPA	supp.	supp.		XRF					
SiO_2	35.46	53.37	0.00	100.00	0.00	=	52.90	52.85	0.05	0.003	SM Mg	0.3
TiO_2	0.08	0.10	0.00	0.00	0.00	=	0.32	0.06	0.26	0.07	SM Si	58.6
Al_2O_3	15.09	17.67	0.07	0.00	0.00	=	10.23	10.42	-0.19	0.04	Cal	16.9
Fe_2O_3	7.97	3.48	0.09	0.00	100.00	=	4.84	4.79	0.05	0.003	Silica	21.4
MnO	0.02	0.01	0.06	0.00	0.00	=	0.11	0.02	0.10	0.01	Hem	2.7
MgO	24.22	9.27	0.49	0.00	0.00	=	5.79	5.60	0.19	0.04	Total	99.9
CaO	0.77	2.21	55.23	0.00	0.00	=	12.27	10.62	1.64	2.70	s	2.58
K_2O	0.08	1.90	0.00	0.00	0.00	=	1.25	1.11	0.14	0.02		
Na_2O	0.05	0.27	0.00	0.00	0.00	=	0.09	0.16	-0.07	0.00		
CO_2	0.00	0.00	44.07	0.00	0.00	=	5.50	7.44	-1.94	3.77		
Total	83.73	88.29	100.00	100.00	100.00		93.31	93.08		6.65		

Calculation 3

	1	2	3	4	5	6			CONTROL			RESULTS	
Phase	SM Mg	SM Si	Cal	Silica	Hem	Quickl		SUM	SUM	s	s^2	Phase	%
	EMPA	EMPA	EMPA	supp.	supp.	supp.		XRF					
SiO_2	35.46	53.37	0.00	100.00	0.00	0.00	=	52.90	52.93	-0.03	0.001	SM Mg	2.1
TiO_2	0.08	0.10	0.00	0.00	0.00	0.00	=	0.32	0.06	0.26	0.07	SM Si	56.5
Al_2O_3	15.09	17.67	0.07	0.00	0.00	0.00	=	10.23	10.31	-0.07	0.01	Cal	12.5
Fe_2O_3	7.97	3.48	0.09	0.00	100.00	0.00	=	4.84	4.87	-0.03	0.001	Silica	22.0
MnO	0.02	0.01	0.06	0.00	0.00	0.00	=	0.11	0.01	0.10	0.01	Hem	2.7
MgO	24.22	9.27	0.49	0.00	0.00	0.00	=	5.79	5.81	-0.02	0.0003	Quickl.	4.1
CaO	0.77	2.21	55.23	0.00	0.00	100.00	=	12.27	12.29	-0.03	0.0007	Total	99.9
K_2O	0.08	1.90	0.00	0.00	0.00	0.00	=	1.25	1.07	0.18	0.03	s	0.35
Na_2O	0.05	0.27	0.00	0.00	0.00	0.00	=	0.09	0.15	-0.06	0.004		
CO_2	0.00	0.00	44.07	0.00	0.00	0.00	=	5.50	5.53	-0.03	0.0008		
Total	83.73	88.29	100.00	100.00	100.00	100.00		93.31	93.04		0.12		

SM Mg: MgO-rich, SiO_2-poor altered silicate melt (vermicullite/ chlorite type); SM Si: SiO_2-rich, MgO-poor altered silicate melt (montmorillonite/ illite type); Cal: calcite; Hem: Haematite; Quickl: quicklime; EMPA: phase analyses obtained by EMP; XRF: bulk rock analyses obtained by XRF; supp.: supposed phase; CONTROL: control bulk rock composition (back calculated).

3.8 Comparison of UNAM borehole samples with impactites of El Guayal

To establish a regional context on ejecta distribution and behaviour of the different target lithologies, the distal impactites of El Guayal were compared with selected samples of the UNAM-5 and UNAM-7 boreholes nearby the outer crater rim. In the UNAM-5 core (332.0 m to 504.00 m), a polymict breccia rich in melt particles, clasts of crystalline (basement) and sedimentary rocks is exposed (Fig. 2-2). At UNAM-7, the polymict breccia can be divided into two distinct units. The upper silicate melt bearing part of the polymict breccia (222.2 to 348.4 m) is similar to the impactites of UNAM-5 with respect to the presence of melt particles. However, the average proportion of shocked crystalline particles is much lower, whereas the average modal abundance for melt particles is higher compared to UNAM-5 (Tab. 3-10). At 348.4 m, a sharp transition is observed in the polymict breccia of UNAM-7: The underlying breccia is significantly different to the overlying melt-bearing breccia and shows intercalations of anhydrite megablocks, while the abundance of silicate melt particles strongly decreases (Urrutia-Fucugauchi et al. 1996b; Sharpton et al. 1999; Schönian et al. 2003, 2006). This is in agreement with macroscopic observations on sample UNAM-7-381.40, where the modal content of anhydrite clasts is high, while melt particles are rare (Tab. 3-10).

Table 3-10 Modal abundance (%) of clasts and particles and matrix proportion at UNAM drill cores.

Sample Unit	UNAM-5 silicate melt-rich breccia	UNAM-7 silicate melt-rich breccia	UNAM-7 silicate melt-poor breccia
N	5	2	1
Crystalline	25	2.5	-
Melt particles	10	20	2.5
Anhydrite	10	15	50
Calcite	5	2.5	2.5
Matrix	50	60	45
Total	100	100	100

N: Number of samples

The polymict silicate melt-rich breccia of UNAM-5

While crystalline (basement) clasts are not observed at El Guayal, those are present at UNAM-5. They occur in all of the upper four samples as shocked particles up to 2.5 cm in size (Figs. 3-25A–C), but they are absent in the lowermost sample UNAM-550.55 (Fig. 3-25D). The abundant greenish angular and vesicle-rich silicate melt particles (up to 1 cm in

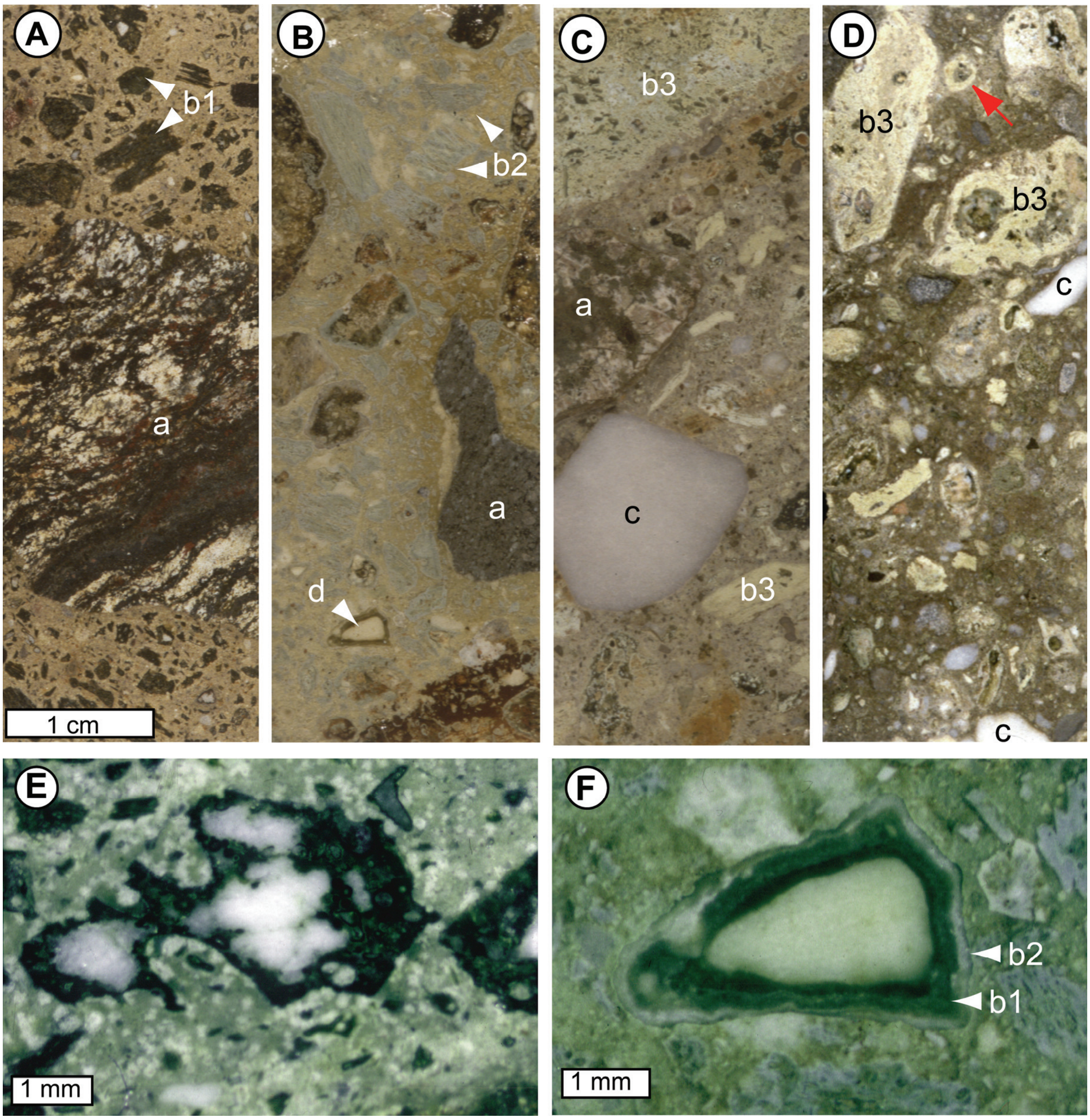

Figure 3-25 The polymict melt-rich breccia of UNAM-5. **(A)** Core sample UNAM-5-357.40. **(B)** Core **s**ample UNAM-5-409.77. **(C)** Core sample UNAM-5-480.37. **(D)** Core sample UNAM-5-500.55; Arrow: Subhedral to rounded pale yellow melt particle with inclusions in centre. Scale of (A) valid for samples at A–D. **(E)** Binocular micrograph of melt particle with core of presumably anhydrite (sample UNAM-5-357.40). **(F)** Binocular micrograph of melt particle with core of presumably calcite and multiple laminated melt rims (sample UNAM-5-409.77). a: crystalline (basement) clast; b: melt particle (b1: greenish; b2: greyish; b3: pale yellow); c: anhydrite; d: carbonate.

size) at the uppermost UNAM-5-357.40 sample represent an analogue to some of the El Guayal melt particles type 1, as they are of similar colour and have a vesicular shard-like morphology. However, melt particles are significantly different in the underlying UNAM lithologies. At sample UNAM-5-409.77 melt particles display a grey colour, and, at UNAM-5-464.78, most of the black to dark green impact melt particles have a bright reaction rim. Melt particles of the lower two samples (UNAM-5-480.37, and UNAM-5-500.55, Figs. 3.25 C and

D) have a pale yellow to white colour. Those melt particles show angular, sometimes subhedral shapes. They often contain inclusions sub-mm to 3 mm in size or cores of the greenish impact melt type. Elongated particles are aligned in the host rock. Larger particles exhibit internal schlieren and their vesiculated surfaces developed reaction rims in contact with the matrix.

Anhydrite, which is lacking at El Guayal, is abundant as rounded clasts (sub-mm up to 1.2 cm) in the lower samples UNAM-5-480.37 and UNAM-5-500.55 (Figs. 3.25C and D). The uppermost sample UNAM-5-357.40 lacks individual anhydrite clasts. However, cores of presumably anhydrite are present in silicate melt particles (Fig. 3-25E). Whereas carbonate clasts are a major component at El Guayal, those are rarely observed at UNAM-5, though the matrix of UNAM-5 contains carbonate as the positive reaction with diluted HCl show. Only at sample UNAM-5-409.87, one rounded carbonate clast (3.5 cm in diameter) with multiple laminations is observed. Similar to the silicate melt rimming around carbonate particles of El Guayal, this sample contains a second carbonate particle as a core with a multiple melt rim (Fig. 3-25F).

The polymict silicate melt-rich breccia of UNAM-7

UNAM-7 is located ~126 km from the crater centre and much farther away from the final crater rim than UNAM-5 (~105 km from the crater centre). The melt particles at sample UNAM-7-267.40 (Fig. 3-26A) and UNAM-7-307.95 are different to those at UNAM-5 and El Guayal. They are brittle and significantly larger with rounded or amoeboid shapes. Larger melt particles show a red to light grey coloured reaction rim in contact with the matrix. Commonly, strong alteration of the brittle impact melt particles is observed. The centre is often less altered and of dark greenish colour. Other melt particles host a black to red core of shocked crystalline (basement) particles. The melt particles have a distinctive light greenish colour sometimes with grey to brown areas (Figs. A1-1A and B). Two different alteration phases can be distinguished in the melt particles under the binocular. Type 1 is greyish coloured and has a firm, compact appearance, while type 2 are greenish, and smaller fine grained particles.

TXRF analyses (Tab. 3-11) revealed enrichments for several elements in type 2 compared to type 1, with 2-3 times higher Cu, Co, Cr, Ni, MnO, Pb, Zn, 4.5 times higher SO_3 and Sr, and 8 times higher CaO content. Additionally, a slight enrichment in Cl, similar values for V, Fe_2O_3, Br and a slight depletion for TiO_2 and K_2O is observed in type 2 with respect to type 1. Comparing those analyses with the impact melt rich transition at the upper accretionary lapilli

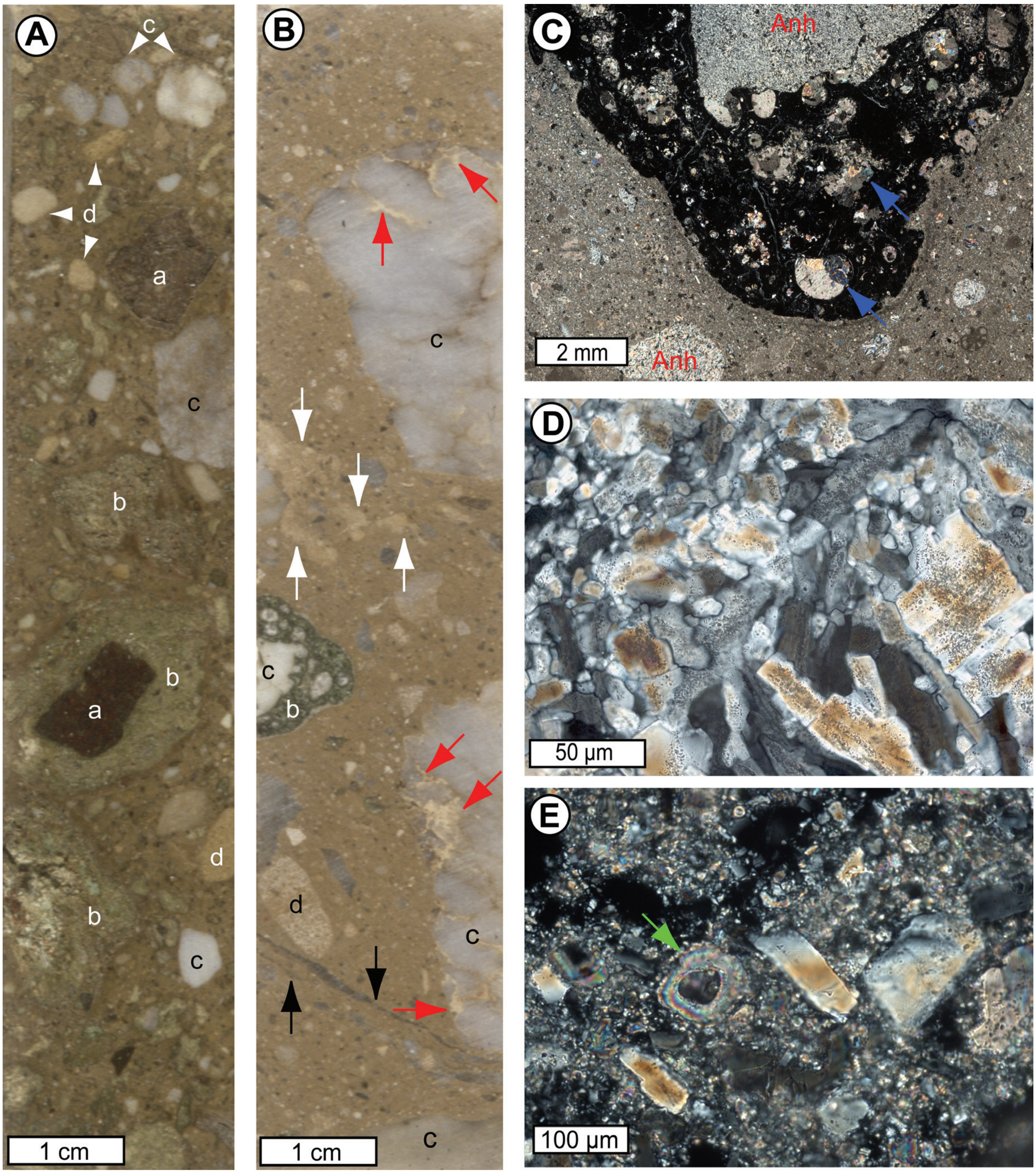

Figure 3-26 The different polymict impact breccias of UNAM-7. **(A)** Core sample of the polymict silicate melt-rich breccia (UNAM-7-267.40). **(B)** Core sample of the polymict silicate melt-poor breccia (UNAM-7-381.40). White arrows: calcite schlieren; black arrows: anhydrite schlieren; red arrows: light brown accumulations and intercalations at anhydrite particles. **(C)** Composite micrograph (XPL) of rare silicate melt particle of sample UNAM-7-381.40 with outer calcite inclusions (arrows) and anhydrite core. Anh: anhydrite **(D)** Micrograph (XPL) of central anhydrite core of (C) with variations in crystal size and vesicles (compare with Figs. A1-2E and F). **(E)** Micrograph (XPL) of matrix of microcrystalline calcite with euhedral anhydrite single crystals (sample UNAM-7-381.40). The subhedral calcite single crystal (arrow) shows a vesicle in centre. a: clast of crystalline (basement) rock; b: altered silicate melt; c: anhydrite particle; d: calcite particle. XPL: cross polarised light.

Table 3-11 TXRF analyses of two alteration phases of one heterogeneous silicate melt particle of sample UNAM-7-307.85 compared with bulk rock analyses of the upper accretionary lapilli unit/ clay unit transition at El Guayal. Major and minor elements are recalculated to wt.%, trace elements are given in µg/g. Concentrations for Si, Al, Mg and Na are not shown as those elements (Z<19) are difficult to measure and underestimated when compared with XRF analysis.

	UNAM-7	UNAM-7	El Guayal	El Guayal	El Guayal
Sample	307.85	307.85	G14-2b	G13-2	G15-2
Comment	Type 1	Type 2	Bulk rock	Bulk rock	Bulk rock
Unit			uALU	uALU	CU
wt.%					
TiO_2	0.27	0.21	0.15	0.13	0.16
Fe_2O_3	6.59	7.21	4.78	5.18	4.95
MnO	0.009	0.021	0.020	0.007	0.031
CaO	2.94	24.2	3.08	4.26	2.96
K_2O	0.40	0.31	0.23	0.23	0.38
SO_3	0.68	3.18	<0.00085	<0.00096	<0.0011
µg/g					
Ba	n.d.	2.83	15	25	345
Br	32	37	0.7	1.5	1.1
Cl	1541	2120	n.d.	n.d.	n.d.
Co	123	277	121	159	142
Cr	201	408	11	24	21
Cu	330	891	10	11	15
Hf	n.d.	n.d.	3	3	3
Ni	47	135	<0.16	<0.18	24
Pb	25	50	10	20	10
Rb	25	2	12	12	22
Sr	751	3376	49	50	68
V	58	60	31	22	31
Yb	n.d.	n.d.	27	43	22
Zn	69	164	21	23	35

Type 1: greyish, firm, compact; Type 2: greenish, fine grained; uALU; upper accretionary lapilli unit; CU: clay unit; n.d.: not detected

unit and clay unit of El Guayal (59–66% altered silicate melt), both of the UNAM altered silicate melt types show a significant enrichment of Cl and SO_3. Additionally, Sr, Br, Cu, Cr are enriched by the factor 10 to 60, while Fe_2O_3, TiO_2 and K_2O show values in the similar range. Ni (only compared to the clay unit), Pb, Zn and Co are of equal concentration in type 1 and or slightly higher (less than 2–5 times) at type 2.

The polymict silicate melt-poor breccia of UNAM-7

Within the silicate melt poor polymict breccia of sample UNAM-7-381.30, a single silicate melt particle (~1mm) has been identified by microscopic studies. This melt particle displays a flow texture and is of similar morphology to most of the melt particles type 1 from El Guayal. At UNAM-7, this and the larger >1 cm sized silicate melt particle (Fig. 3-27B, Figs. A1-2A and B) show a reaction rim in contact with the matrix. Microscopically, the inclusions in this

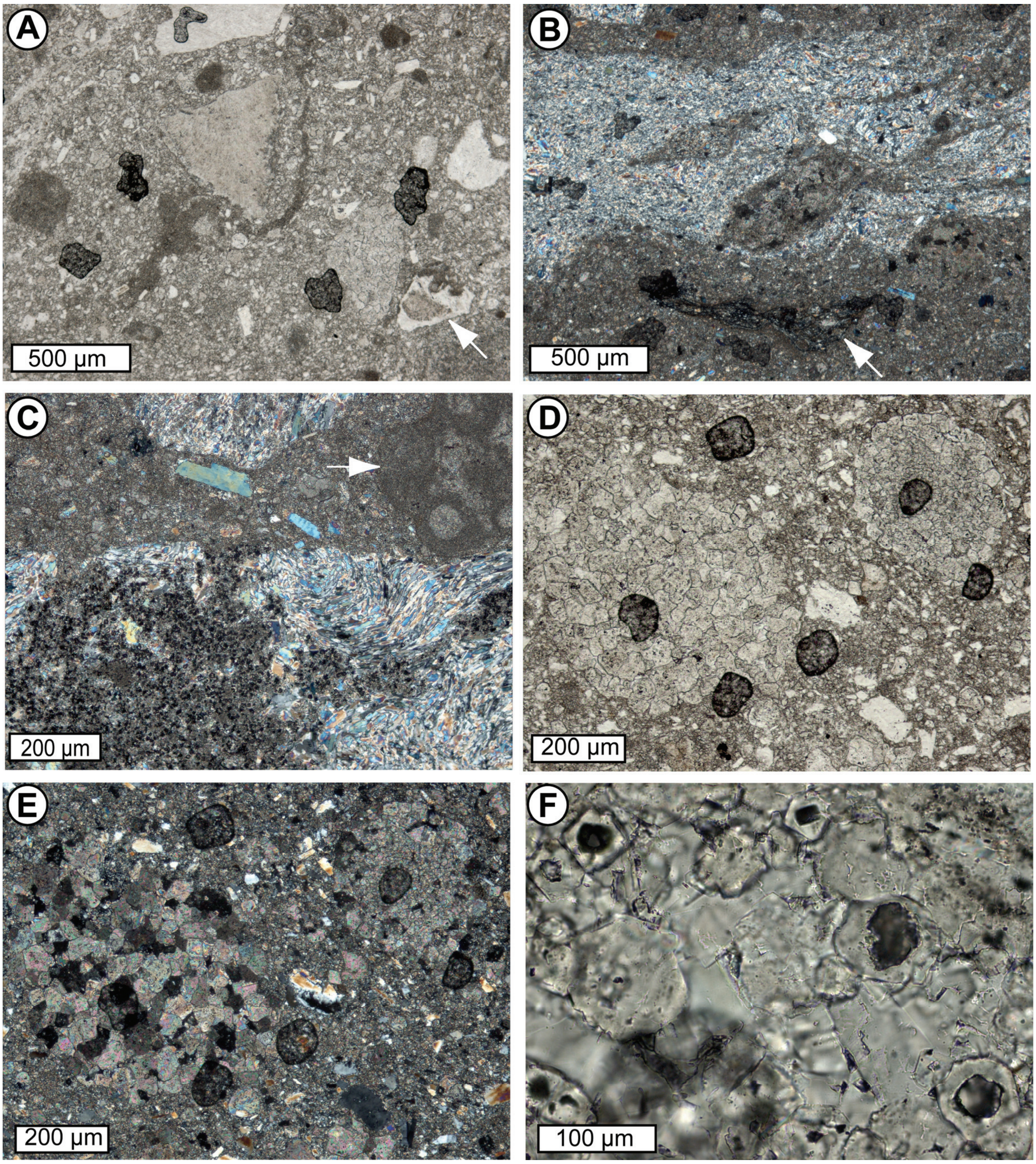

Figure 3-27 Micrographs of sample UNAM-7-3-381.40 (PPL: A, D, F; XPL: B, C, E). **(A)** Flow texture of micrite-like calcite interfering with angular spherulitic (feathery-like) textured calcite particle. Arrow: Angular calcite particle with vesicular morphology and micrite-like core. **(B)** Anhydrite flow texture. Arrow: Rare silicate melt particle similar to flow-textured melt particle type 1 of El Guayal. **(C)** Micrograph of light brown intercalation (microcrystalline calcite with abundant vesicles) into large flow-textured anhydrite particles (Fig. 3-26B, lowermost red arrow; Fig. A1-1F). White arrow: degraded microfossil. **(D, E)** Polygonal to interlobate calcite spheroids. **(F)** Heterogeneous area of 1 cm sized calcite particle (see d in Fig. 3-26B) showing accumulations of euhedral to subhedral single crystals with vesicles similar to (Fig. 3-26E, arrow). Dark bubbles in all micrographs are artefacts from preparation. XPL: cross polarised light; PPL: plane polarised light.

melt particle differ significantly from the sparitic calcite or spherulitic calcite particles embedded in melt particles type 1 of El Guayal. The outer globules and inclusions of the UNAM-7 melt particle (Fig. 3-27C, Figs. A1-2C and D) contain mainly calcite and are in some cases associated with anhydrite. The sparitic calcite crystals display a crystallisation sequence. They are often orientated perpendicular to the contact with the silicate melt with crystal sizes decreasing towards the contact zone. In those cases where the globule thins out, calcite forms a microcrystalline layer at the contact with the silicate melt. In the calcite crystals two sets of planar fractures are developed. The anhydrite crystals within the >5 mm diameter central globule also show a decreasing crystal size from the centre to the silicate melt contact. In the centre, some areas with columnar euhedral to subhedral anhydrite crystals (up to 90x15 µm) contain sub-mm to 2 µm sized vesicles, however, these vesicles are absent near the crystal boundaries (Fig. 3-26D, Figs. A1-2E and F). Contrary, the mainly smaller subhedral to interlobate anhydrite crystals (<10 µm) rarely contain vesicles.

Whereas the impactites of El Guayal are clast supported, the impactites of UNAM-5 and UNAM-7 are composed of a significant amount of fine grained matrix (Tab. 3-10). Microscopic studies at sample UNAM-7-381.40 revealed that the matrix consists mainly of microcrystalline to micrite-like calcite. Subhedral calcite single crystals (up to 100 µm; Fig. 3-26E, arrow) resemble the macroscopic and several mm sized pale white to yellowish particles at UNAM-5-500.55 (Fig. 3-25D, arrow) with respect to their shape and vesicles or inclusions in the centre. Euhedral anhydrite crystals (up to 200 µm) have a tabular morphology (Fig. 3-26E). The matrix is inhomogeneous on a macroscopic and microscopic level. Carbonate (Fig. 3-26B, white arrows; Fig. A1-1E) and also anhydrite (Fig. 3-26B, black arrows; Fig. A1-1D) show schlieren and veins that are several centimetres long. Macroscopically and microscopically, the carbonate (Fig. 3-27A) and anhydrite (Fig. 3-27B) schlieren display flow texture and interfere with calcite particles. The anhydrite crystals are larger than the micrite-like calcite schlieren and show an alignment and reduced crystal sizes towards the matrix. A similar anhydrite flow texture is observed for the ~3 cm sized anhydrite particles (Fig. 3-27C). Inhomogeneous areas are apparent macroscopically as light brown areas (Fig. A1-F) at indenting rims and intercalations of the anhydrite particles (Fig. 3-26B, red arrows). On a microscopic level, the elongated anhydrite crystals are aligned with the microcrystalline to micrite-like calcite intercalations (Fig. 3-27C). Compared to the matrix, the microcrystalline calcite in the intercalations is associated with abundant inclusions (up to 15 µm) but lacks anhydrite microcrystals (Fig. 3-27C).

Feathery-textured, microcrystalline or fossil-bearing calcite particles are abundant at El Guayal, but rare in sample UNAM-7-381.40, where minor angular calcite particles with spherulitic, feathery texture or vesicular shard-like morphology occur (Fig. 3-27A). At sample UNAM-7-381.40, commonly calcite spheroids show variations in textures often with increasing crystal sizes towards the rim. The texture of the calcite spheroids changes from interlobate, glomeroblastic and sometimes micrite-like calcite at the centre towards to larger polygonal crystals (up to 50 µm) at the rim (Figs. 3-27D and E). These calcite spheroids display a reduced transparency attributable to the presence of small vesicles, which is similar to the spherulitic calcite particles of El Guayal. Especially larger carbonate particles have heterogeneous areas with respect to their crystal size and textures resembling those observed at spherulitic to microcrystalline carbonate particles from El Guayal. Those areas at UNAM-7 either show a spherulitic to needle-like or microcrystalline to micrite-like texture. Often, larger polygonal crystals have fewer vesicles at their rim than in their centre. Some areas show accumulations of 15–40 µm sized euhedral to subhedral crystals with 10–20 µm sized central vesicles (Fig. 3-27F) resembling subhedral single crystals in the matrix (Fig. 3-26E, arrow). Many carbonate areas show, similar to micrite-like calcite particles at El Guayal, a slight increase in grain size when compared with micritic calcite, so that their outlines is sometimes difficult to discriminate from the fine grained matrix. A similar increase in grain size is observed when comparing microfossils from El Guayal with degraded microfossils of sample UNAM-7-381.40. The latter are observed as individual foraminifera with blurred outlines (Fig. 3-27C, arrow) or as fossil-rich micritic calcite particles. These micritic calcite particles display similar heterogeneities (like vesicle-rich areas which are associated with a slightly coarser crystal size or spherulitic to needle-like textured areas which are associated with microcrystalline calcite) to those observed on the El Guayal carbonate spheroids.

Cathodoluminescence studies have been carried out on the calcite inclusions within the melt particle, the calcite spheroids and the matrix of sample UNAM-7-381.40. Here, calcite inclusions in the melt particle emit a reduced luminescence of dark grey to red colours (Figs. 3-28A and B) which contrasts to the bright yellow luminescence of homogeneous sparitic calcite in melt particles type 1 at El Guayal. The lowest luminescent areas of the sparitic calcite are often near the contact to the silicate melt and display geometric pattern as interlocked triangles which are perpendicular aligned to the silicate melt contact. Anhydrite crystals are non-luminescent (black) areas in between the calcite crystals and elongated crystals are often oriented perpendicular to the silicate melt contact. Non-luminescent silicate melt intrusions are intercalated in calcite (green arrows) and appear as multiple fingers (yellow arrows). Additionally, thin films of silicate melt are observed in between the calcite crystals (blue arrow).

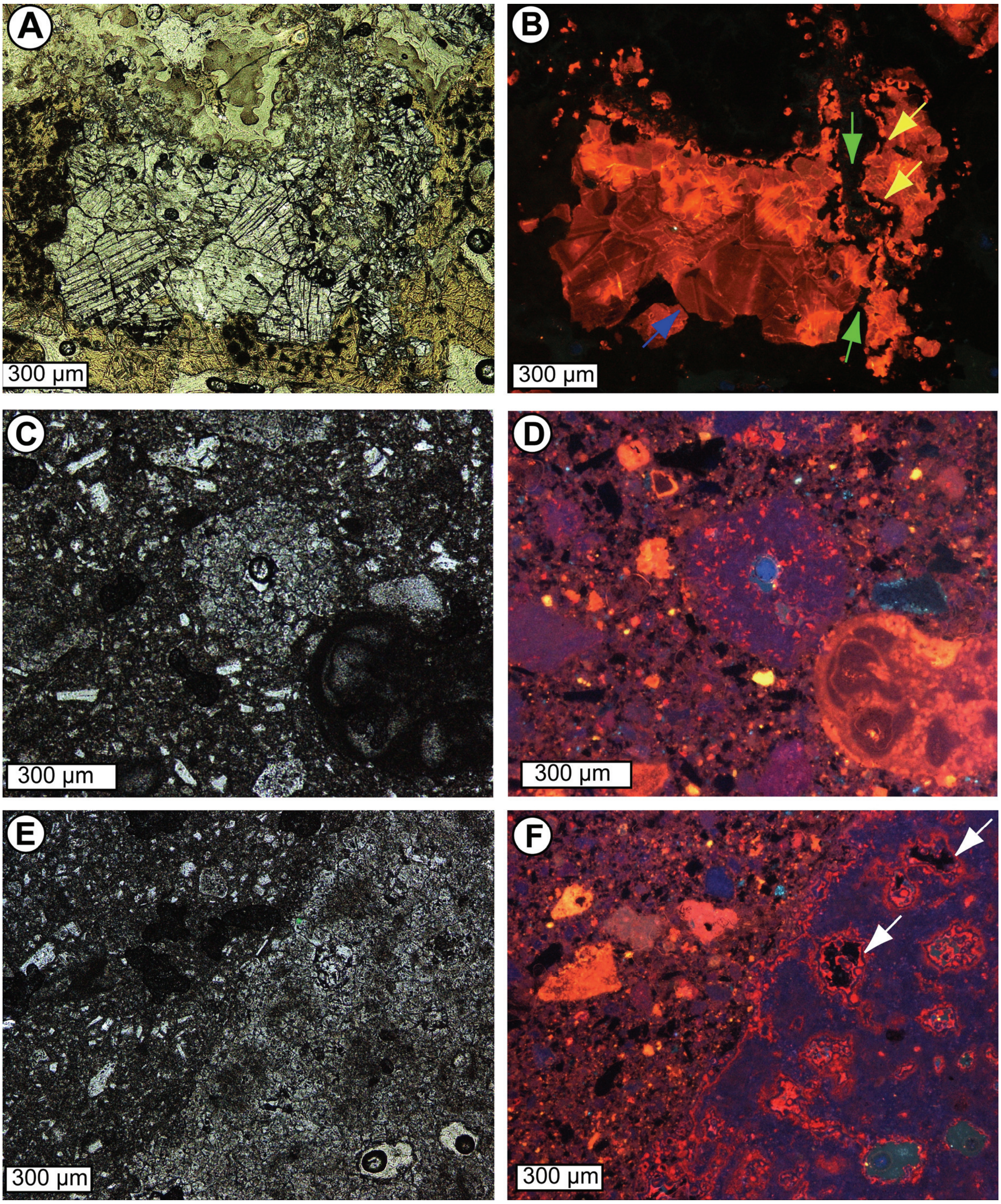

Figure 3-28 Paired PPL (left) and CL (right) micrographs of sample UNAM-7-3-381.40. **(A, B)** Calcite inclusion in silicate melt particle. Silicate melt is intercalating and interfingering into the calcite inclusion (arrows in B). **(C, D)** Calcite spheroid and particles showing a homogenous lilac coloured low luminescence. Note the bright to intermediate luminescent foraminifera. **(E, F)** Large calcite particle with variations in crystal texture. The particle display a lilac coloured low luminescence, which is homogenous despite the varying crystal sizes. Laminations of bright pink colours occur at the rim and inclusions. Inclusions are hollow or contain coarse, bright luminescent calcite with euhedral anhydrite (arrows). Note the tangential alignment of non-luminescent anhydrite crystals in a matrix of microcrystalline calcite. PPL: plane polarised light; CL: cathodoluminescence.

The fine-grained matrix, which is not observed at the El Guayal impactites, is general low-luminescent. Using a long exposure time (>10 s) and high light amplification of the digital camera an adequate contrast can be generated though causing a colour displacement from black to dark lilac. Fossil bearing particles and some tiny particles are intermediate luminescent with red to orange colours (Figs. 3-28C and D). The small anhydrite crystals remain black and elongated crystals show a preferred tangential orientation especially near larger calcite particles (Figs. 3-28E and F). Calcite spheroids and particles with variations in their crystal size and texture (poly- to microcrystalline to micrite-like similar to those observed at El Guayal) display a homogenous low luminescence of lilac colours which indicate cogenetic formation. However, larger particles show thin laminations of bright pink colour at the particle rim and near inclusions and voids (Figs. 3-28E and F). Inclusions are either hollow or contain larger bright luminescent calcite crystals in some cases with euhedral anhydrite crystals (Fig. 3-28F).

In Tab. 3-12, the abundance of clasts, particles and crystals of silicate melt, carbonate and anhydrite with respect to their distinct textures and combinations of UNAM is summarised and compared with the El Guayal section.

Table 3-12 Abundance of different textured phases at the different units of El Guayal and the polymict silicate melt-poor and silicate melt-rich breccia of UNAM-7.

	El Guayal Micro-breccia	El Guayal Accretionary lapilli unit	El Guayal Clay unit	UNAM Silicate melt-poor	UNAM Silicate melt-rich
SILICATES					
Crystalline basement clasts	-	-	-	-	+++
Silicate melt particles	++	+++	(+)	(+)	+++
Quartz clasts	+	+	++	(+)	?
CARBONATES					
Clasts	+++	++	-	-	(+)2)
Spherulitic particles	++	+++	+	+	?
Polygonal/ interlobate particles	-	-	-	+++	?
Microcrystalline particles and crystals	+	++	+++1)	+++1)	?
Combination with silicate melt	++	+++	-	(+)	(+)
ANHYDRITE					
Clasts	-	-	-	+++	+
Microcrystalline crystals	-	-	-	+++	?
Combination with silicate melt	-	-	-	(+)	(+)

+++: abundant; ++: intermediate; +: moderate; (+): rare; -: not observed; ?: not microscopically investigated. 1): as major matrix forming component. 2): only at sample UNAM-5-409.77

4 Discussion

4.1 Interpretation of the petrographic and chemical data of El Guayal and UNAM impactites

The Chicxulub impact event caused the deposition of a ~50 m thick sequence at the K-P site of El Guayal located at ~520 km from the crater centre. This succession documents different phases of arrival of material during the impact process. When interpreting the petrographic and chemical data, sedimentary, impact and postdepositional alteration processes have to be considered. On the other hand, the impactites of the UNAM boreholes give insight into processes for ejecta deposition close to the crater rim and help to interpret processes relevant during ejecta distribution in the ejecta plume.

4.1.1 Basal megabreccia

Stratigraphic and mineralogic studies indicate that the megabreccia at El Guayal was derived from the collapse of the Yucatán platform by impact induced seismic activity (Grajales-Nishimura et al. 2000). The clasts of different microfacies document the diversity of the sampled source regions. The eroded material was transported by gravity flows, and finally deposited at the shelf region of the Yucatán platform. So far, the palaeogeographic position of El Guayal with respect to the shoreline is poorly known. However, the angular morphology of many carbonate clasts in the megabreccia indicates a proximal deposition of the gravity flow.

Distinct spherulitic calcite particles in the uppermost three metres of the megabreccia, which is much finer than the underlying coarse megabreccia, resemble feathery textured carbonate melt particles from the suevite of Y6 borehole core (Jones et al. 2000; Claeys et al. 2003). The radiating spherulitic texture is interpreted as recrystallised carbonate melt, which was quenched at an extremely high cooling rate (see chapter 4.1.2 for detailed discussion). The presence of carbonate melt particles indicates that the uppermost part of the monomict megabreccia formed by incorporation of carbonate impact ejecta to the fine material of the sedimentary gravity flow. The fragmentation of spherulitic calcite particles suggests transport in a turbulent environment. Incomplete melting of calcite is documented by spherulitic textured rims at micritic calcite particles, which indicate a short but intense period of particle heating.

4.1.2 Microbreccia

Implications from silicate ejecta particles

The presence of altered silicate melt particles (now consisting of clay minerals) in the microbreccia indicates the arrival of material from the lower excavation zone of the Chicxulub impact crater. The abundance of silicate melt particles and the lack of crystalline clasts indicate that the silicate basement was shocked up to shock stage IV. Silicate melt particles form by adiabatic pressure release from shock pressures of >60–80 GPa and subsequent cooling from post-shock temperatures of 1300–3000°C during ejection from the impact crater (Stöffler 1971; Engelhardt et al. 1995; French 1998). The transformation temperature from viscous melt to brittle glass is 680°C as shown by viscosity measurements (Wali 1985) and thermal dilation experiments (Fecker 1993) on strain-free synthetic suevite glasses. The elongated vesicles and flow texture in many of the El Guayal silicate melt particles indicate plastic deformation on cooling and argue for temperatures >750°C (Fecker 1993). The sparseness of crystallites (e.g. plagioclase, pyroxene) in the El Guayal melt particles document rapid cooling from temperatures >1100°C (Engelhardt et al. 1995).

The melt particles type 1 with vesicle-rich morphology document exsolution of a gas phase from a vapour-rich melt upon pressure release and cooling. A solid state before deposition in the water column is indicated by the fragmentation of thin-walled particles. They resemble shards derived from volcanic eruptions such as fragments in pyroclastic flow deposits. Volcanic shards are walls of broken bubbles or the junctions of bubbles developed by the vesiculation of magma (Fisher & Schmincke 1984). They originate from rapidly expanding volcanic magma that loses cohesion and breaks into bits when overburden pressures are exceeded. The magmatic expansion creates volcanic glass foam that break into glass shards from broken vesicles (Fisher & Smith 1991; Heiken & Wohletz 1991). The El Guayal melt particles type 1 with an elongated to rounded morphology resemble melt particles described from (1) suevites within the Chicxulub impact structure (e.g. Claeys et al. 2003; Hecht et al. 2004; Tuchscherer et al. 2005), (2) melt injections in impact-related suevitic dikes (Wittmann et al. 2004) and (3) K-P sites outside the crater on the southern Yucatán peninsula (Pope et al. 2005). Additionally, melt particle type 1 of El Guayal resemble suevitic melt particle from the Nördlinger Ries, of which the latter are interpreted as viscous melt lumps transported at high velocities through the atmosphere (Hörz 1965). Contrary to tektites, the melt particle type 1 at El Guayal are not aerodynamically shaped and ballistically emplaced. This indicates a turbulent transport in a high energy environment associated with the ejecta plume. It is inferred that the internal flow texture of the El Guayal melt particle type 1 (Fig. 3-4B) resulted from the collapse and amalgamation of former vesicles during transport.

The relation between heterogeneous altered silicate melts and processes

The chemically heterogeneous clay mineral compositions indicate a complex alteration process of the silicate melt particles. Harker diagrams (Figs. 3-16 and 3-17) show that the melt particle composition with higher SiO_2 content is, when compared with the SiO_2-poor composition, comparable for many elements (MgO, FeO, K_2O) to the composition of impact melt rock from the C1 and Y6 boreholes (Schuraytz et al. 1994). Thus, the SiO_2-rich composition of the montmorillonite/ illite type is interpreted to be less altered than the SiO_2-poor composition of the vermiculite/ chlorite type. It is supported as the vermiculite/ chlorite type is located at rims and associated with fracture surfaces in the altered silicate melt particles indicating a dissolving process. A postdepositional silica release during the montmorillonite/ illite to vermiculite/ chlorite transformation is indicated as silification of calcite is abundant in the presence of silicate melt. This is an important process for the cementing of the ejecta deposits. An analogous scenario though in a different setting is the cementation by precipitation of silica upon dissolving of smectite, which has been reported by studies on the time-dependent alteration behaviour of bentonite (JNC 2000). Furthermore, Pusch (2000) simulated hydrothermal conditions and showed that hot water vapour can initiate dissolution of smectites and precipitation of silica. Additionally, cementation at the microscopic level is reported in natural bentonite deposits (Pusch & Karnland 1988), in-situ tests at Stripa mine (Pusch et al. 1993) and laboratory tests (Pusch et al. 1991; Couture 1985a, b) at elevated temperatures conditions of >100°C.

These processes may be induced by a rather short-term alteration in a similar way as Kieffer & Simonds (1980) proposed that fragmented silicates may react during ejecta transport with hot volatiles to produce hydrated minerals such as clays. The brown coloration of the vermiculite/ chlorite rims resembles the coloration observed in experiments with natural suevite glasses under elevated water pressure (Engelhardt et al. 1995). The experiments by those authors show that water, which invades into natural suevite glass, produces brown-coloured, oxidised marginal zones after annealing for 1h at 600°C with 600 bar H_2O pressure. These observations points towards a short term alteration of silicate melt particles by vapour during distal ejecta transport which resulted to a partial oxidation of the silicate melt particles and induced a postdepositional silica release. The subsequent calcite silification of ejecta particles resulted to a hardening of the deposit and initiated a coherent precipitation of sparitic calcite in the interconnected pore space. These processes including the swelling capacity of clay minerals can be considered as an important mechanism for cementing ejecta deposits which act as a sealing facies on top of the oil producing reservoir facies of the Cantarel oil fields at the Campeche marine platform (Grajales-Nishimura et al. 2000).

Implications from carbonate ejecta particles

Carbonate melts are difficult to identify as they do not quench to glasses (Rankin & Le Bas 1974) but may form aggregates of fine-grained crystals. Liquid immiscibility between silicate and carbonate melt has been demonstrated by high pressure experiments where rounded calcite blebs are found to be surrounded by silicate melt and separated by a smooth meniscus (Minarik 1998). Additionally, Graup (1999) described a wide variety of textural evidence for liquid immiscibility between silicate and carbonate melt in the Ries suevite: Carbonate melt globules within silicate melt and vice versa, deformed and coalesced carbonate spheres within silicate glass, sharp menisci and cusps and budding between silicate melt, fluidal textures and gas vesicles in carbonate schlieren, a quench crystallisation sequence of the carbonate, spinifex textured quenched carbonate, separate carbonate globules in the suevite mineral-fragment matrix, and inclusions of mineral fragments suspended in carbonate blebs. At the Haughton impact structure, a meniscus-like deformable float morphology of calcite embedded in silicate melt is interpreted as former carbonate melts (Osinski & Spray 2001). Experimental investigations showed that the development of carbonate melt textures depends on the degree of undercooling (Jones et al. 2000): Slight cooling rates of several 10's°C per second result in euhedral to elongated textures, at intermediate cooling rates a spindle to needle-like texture forms and at high cooling rates of several 100's°C per second a radiating, spherulitic texture is observed (Fig. 4-1).

The interpretation of carbonate melt is complex as calcite can easily be formed by biogenetic and secondary processes. The following example shows, that a purely morphological identification of carbonate melt can be misleading: At El Guayal the texture of calcite hosted in silicate melt particles is in some cases similar to carbonate-silicate immiscibility textures (Fig. 3-4F). However, at El Guayal, most of the calcite embedded in melt particles lacks a distinctive crystallisation sequence but display coarse crystals and bright yellow cathodoluminescence similar to secondary sparitic calcite veins. These observations indicate that subsequent filling of plastically deformed vesicles by secondary calcite can result in pseudo liquid immiscibility textures. Therefore, the crystallisation textures must be taken into account in order to identify former carbonate melts.

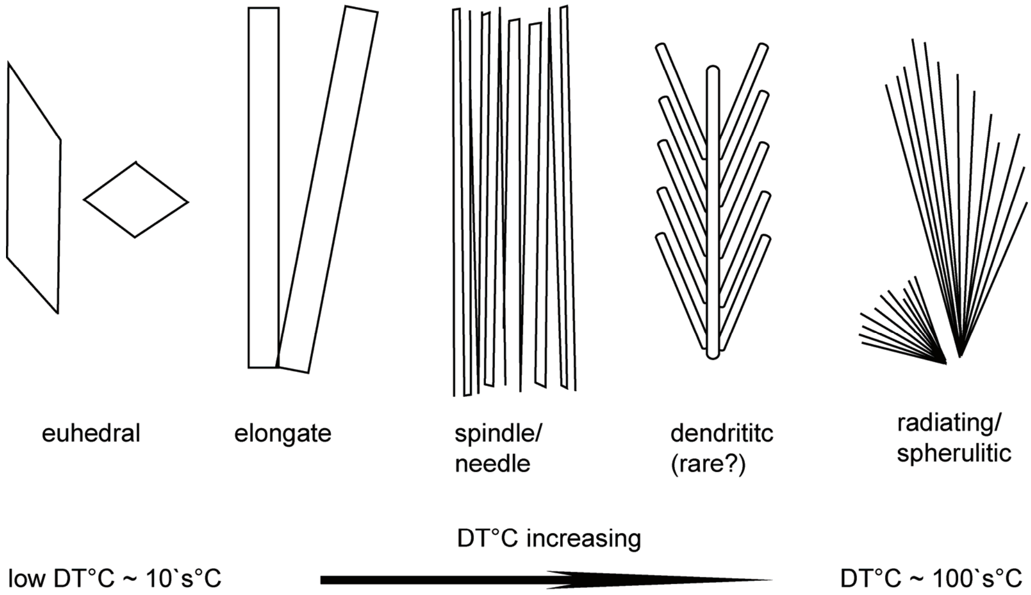

Figure 4-1 Carbonate crystallisation textures as a function of cooling rate/ degree of undercooling (after Jones et al. 2000).

The spherulitic (feathery to needle-like) calcite particles are significantly different from fibrous textured carbonates formed at biogenetic and abiogenetic conditions (e.g. fossil algae, molluscs, ooids, microcodium). The spherulitic calcite particles of El Guayal strongly resemble the radiating spherulitic quench crystallisation texture of Jones et al. (2000) (Fig. 4-1) and carbonate melt particles of the Y6 suevite (Claeys et al. 2003). Thus, the spherulitic calcite spheroids and elongated rounded particles at El Guayal are interpreted as unbroken recrystallised carbonate melt particles rapidly quenched in the air, whereas the angular spherulitic particles represent broken fragments. The lack in luminescence observed for the spherulitic calcite particles of El Guayal is similar to those observed at feathery textured calcite from the Y6 suevite (Heuschkel et al. 1998) and at radially arranged blocky calcite crystals with a typical "cauliflower"-texture in ejecta deposits in northeastern Mexico (Schulte & Kontny 2005). The perfect circular morphology of the spherulitic carbonate melt spheroids at El Guayal may derive from the low viscosity, the high interfacial energy and surface tension forces of carbonate melts. The knowledge about CO_2 solubility in carbonate melts is limited, but high pressure experiments indicate that up to 11.5 wt.% CO_2 can be dissolved at 27 kbar in molten $CaCO_3$ (Huang & Wyllie 1976). With decreasing pressure or increasing temperature above the liquidus carbonate melt coexists with increasing amount of vapour (Tyburczy & Ahrens 1986). This suggests that the small vesicles in spherulitic calcite particles represent exsolution of CO_2 from a carbonate melt upon rapid decompression and cooling.

Interaction of silicate melt with carbonate ejecta

The silicate melt rims around carbonate particles of melt particle type 2b resemble the multiple melt layering at shocked gneiss bombs from the Popigai impact structure (Masaitis & Deutsch 1999), which are interpreted as evidence for a short but intense heating in the ejecta plume. Additionally, similar single or multiple layers of accretionary melt were observed around basement clasts at the Manson impact structure (Witzke & Anderson 1996). The consolidated accumulation of silicate melt at dents of larger carbonate particles at El Guayal show that accretionary silicate melt coating is a special form of aggregation. The petrographic observations show that radially arranged blocky calcite aggregates, which are embedded in silicate melt contain vesicles and a cauliflower morphology resembling quenched carbonate melts from ejecta deposits in northeastern Mexico (Schulte & Kontny 2005). These observations indicate a former liquid state. The central needle-like texture (Fig. 3-3C) indicates intermediate cooling rate (Jones et al. 2000, Fig. 4-1), whereas the thin layer of microcrystalline calcite at the contact to silicate melt indicates a formation at lower cooling rates. Thus, the heat transfer from the silicate melt lowers the cooling rate of enclosed carbonate melts. This process explains that a feathery carbonate melt texture is only observed at particles without silicate melt indicating that association with silicate melt inhibits high cooling rates. The moderate red to orange luminescence for former carbonate melt particles associated with silicate melt points to an exchange of activator cations from the silicate to the coexisting carbonate melt.

The presence of fossils in micritic calcite, which are coated by silicate melt prove a solid state of calcite during accretion with silicate melt. It indicates that aggregation of those two phases occurred in an environment with a temperature below the decomposition temperature of calcite. However, the elevated temperatures of the silicate melts are able to induce complex fusion reactions including recrystallisation of calcite accompanied by decomposition and subsequent reformation of calcite (Eq. 4-1):

Calcination: $CaCO_3 \Leftrightarrow CaO + CO_2$ $\Delta H° = 178\ \text{kJ} / \text{mol}$ **Eq. 4-1**

Silicate melt rimming is able to modify the enclosed calcite, as the silicate melt to glass transformation temperature (680–750°C; Wali 1985; Fecker 1993) is in the similar range than the calcite decomposition temperature. The optimum calcination temperature is 900°C (Moropoulou et al. 2001) which is the temperature of traditional industrial limekilns. Free-surface and powder bed calcite decomposition experiments show that this reaction can already be observed between 660–740°C (Beruto et al. 2004). Degassing and back-reaction experiments show that residual CaO is highly reactive in the interval of 300–700°C and the presence of CO_2 (Agrinier et al. 2001). These authors pointed out that 40 to 80 % of CaO quickly back-reacts to $CaCO_3$ within less than 200 seconds and that the back-reaction is enhanced by a porous structure of residual CaO.

The arrangements of silicate melt of melt particle type 2b as rounded areas or elongated intercalations show that most of the calcite in those particles must have been in a plastic deformable state. This is supported by accreted (shocked) quartz particles which preferably occur within the rim of melt particle type 2b. The change from a micritic to a micrite-like or microcrystalline texture in calcite particles, which are associated with altered silicate melt, indicates a recrystallisation at a low cooling rate due to the heat transfer from accreted silicate melt. This process caused formation of calcite microcrystals within a silicate melt matrix at the carbonate and silicate melt interface. In this zone, the presence of voids in silicate melt (which are pseudomorphs of calcite) could be explained by secondary dissolution processes. However, the temperature of silicate melt is in the similar range or above the calcite decomposition temperature, which gives evidence for CO_2 degassing. Thus, the subhedral calcite particles in larger voids (pseudomorphs of calcite) are interpreted as a product of the progressive consumption of calcite. The former filling of the voids may have been the decomposition product calcium oxide (quicklime) which was subsequentially removed as calcium hydroxide suspension from the particle. The thermal decomposition of calcite is most effective where the proportion of silicate melt and, thus, the energy release is high. Additionally, the subsequent transport of the particle into a hot environment can result in amplified calcite decomposition at the rim. These two processes explain the zonation of decreasing microcrystalline calcite and increasing voids towards the rim of silicate melt coated carbonate particles (Fig. A1-4). The differences in silicate melt, calcite and void abundances at the silicate melt/ carbonate transition zone reflect variations in the amount of microcrystalline calcite observed at melt particle type 2a. These observations provide strong evidence that melt particles type 2a represent the fusion of hot silicate melt with carbonates. This interpretation is further supported by large degassing voids which are restricted to melt particles type 2a. Voids are rare and much smaller at melt particles type 1 which do not contain any microcrystalline calcite. It is suggested that the different content of microcrystalline calcite and voids is depending on the proportion of the different phases and the role of subsequent thermal alteration. A large calcite and small silicate melt proportion results in calcite recrystallisation as documented by polycrystalline subareas of microcrystalline calcite at melt particle type 2b. A small calcite and large proportion of silicate melt results in complete calcite dissolution followed by its recrystallisation and (partial) decomposition. It is notable that microfossils seem to be more resistant to decomposition by hot impact melt than micritic calcite. Similar observations were made from historical lime mortars mostly derived from lime with impurities in the form of incompletely burned fossil fragments or particles (Hale et al. 2003). It can be concluded that apatite, iron and titanium oxide and sulphides in melt particle type 2b are of primary, impact-induced origin. This interpretation is supported by volcanic carbonatites, where sub-prismatic (formerly molten) calcite with melillite contains similar minerals like magnetite and apatite (Stoppa et al. 2000).

The role of thermal alteration of carbonates

Similarly to the calcite recrystallisation, which was caused by heat transfer from hot silicate melt, the texture of calcite particles can be modified during transport into a hot environment. At unbroken spherulitic carbonate particles, the differently textured rims (including coarse, elongated, euhedral, radially arranged or microcrystalline to micrite-like calcite crystals) suggest a complex thermal history. The radial crystal growth and the lack of luminescence in the predominant part of these rims is similar to those observed at the completely quenched melt particles and, thus, also indicates a former molten state of those rims. The variations in crystal size indicate differences in the cooling rate. The larger sized, radially arranged, euhedral elongated crystals are indicative for a low cooling rate with a longer crystallisation time (Jones et al. 2000, Fig. 4-1), whereas a microcrystalline to micrite-like crystallisation suggests a slightly higher cooling rates and a shorter crystallisation time. The lack of vesicles at the rim, which are present in the rapidly quenched spheroids, supports crystallisation at moderate cooling rates, whereby the vesicles of the degassing carbonate had time during crystal growths to liberate from the carbonate melt. The presence of similar partially non-luminescent spikes in their (sometimes radially arranged) microcrystalline calcite rims at micrite-like calcite particles (Figs. 3.2F and H) gives strong evidence for the interpretation that the rims of these particles experienced short but intense thermal alteration. These observations point to a partial remelting at the rim of solidified, formerly molten spherulitic and solid micritic calcite particles during travel to an environment with high temperatures. The subsequent recrystallisation at low cooling rates, which is indicated by the texture at the rim, gives evidence for a prolonged residence time and cooling of the particle at elevated temperatures. Additionally, the varying luminescence of micrite-like calcite particles is interpreted as the beginning of recrystallisation due to thermal alteration at elevated temperatures since an enlargement of crystal size is associated with a reduction in luminescence. The change of luminescence at the elongated euhedral crystals from radial non-luminescent spikes near the interface of the spherulitic and micrite-like calcite particles towards an intense yellow luminescence at the outer single crystal margin points to a different process, which may be related to the fast back-reaction of partially decomposed calcite (Agrinier et al. 2001).

The allochthonous polymict microbreccia represents a suevite (proximal impactite comprising an allochthonous breccia with shocked target rocks and cogenetic melt particles; Stöffler & Grieve 1996) as it is composed of silicate and carbonate melt and shocked particles. The aggregation and fusion of silicate melt with surface carbonates indicates a strong mixing of a hot suevitic component with unshocked material from the upper sedimentary lithologies during distal transport from the crater centre to El Guayal.

4.1.3 The accretionary lapilli unit

The accretionary lapilli unit contains similar components than the underlying microbreccia and, thus, also represents a suevite. However the following macroscopic differences are observed in the accretionary lapilli unit: (1) Much larger silicate melt particles at the base of the accretionary lapilli unit, (2) abundant spheroids and (3) the presence of accretionary lapilli. The accretionary lapilli deposited on top of the microbreccia account for impact material derived from a later stage of the impact process. When compared to the underlying microbreccia, a sudden increase of Barium (Ba) is observed (Fig. 3-21A). As Ba-bearing minerals like baryte are absent in the bulk-rock, this suggests additional incorporation of feldspars, as the latter are the major carrier for Ba (Puchelt 1972). However, feldspars are not abundantly observed, though increasing amounts of silicate melt. This suggests that feldspar-rich rocks were molten, possibly vaporised and condensed as part of the silicate melt.

As shown in the previous section, the association of microcrystalline calcite crystals with spherulitic carbonate melt particles including the recrystallisation from micritic-sized crystals towards larger microcrystalline crystal sizes is a result of thermal alteration. In the upper accretionary lapilli unit, carbonate particles are much smaller and completely recrystallised to microcrystalline calcite particles indicating a prolonged thermal alteration process. The elongated voids in between the radially needle-like aligned calcite crystals (Figs. 3-3F) are, similar to those at MP2 of the bulk rock, pseudomorphs of calcite. As argued in the previous section, these voids are interpreted to have formed during decomposition by the high temperature of the silicate melt and/ or ejecta plume and not by secondary dissolution processes. Thus, the voids display a volume loss upon thermal decomposition of $CaCO_3$, which is comparable to observations of Kloprogge et al. (2004) during decomposition experiments. Thus, at the overlying layer, which is in contact with the clay unit, the lack of microcrystalline calcite is interpreted as complete carbonate decomposition due to thermal alteration which is most effective at small particle sizes, as those have a prolonged residence time in the hot ejecta plume.

The petrographic observations including the higher abundance of melt particle type 2, and the occurrence of carbonate spheroids with silicate melt nuclei near the clay unit and within accretionary lapilli indicate pronounced intermixing of the carbonate and silicate target lithologies in the ejecta plume. Those latter carbonate spheroids are interpreted as accretionary carbonate melts, whereas the vesicular shard-like nuclei indicate their solid state upon coating with carbonate melt. A former liquid state of the coating calcite is indicated as previously argued by a (1) non-luminescent behaviour, (2) radially arranged needle-like recrystallisation texture, (3) cauliflower texture of the former carbonate melt at the contact to the silicate melt and (4) spherical inclusions between radiating calcite crystals, which might either derive from immiscible silicate melts or exsolution of CO_2.

4.1.4 Accretionary lapilli

Aggregation at specific conditions

The word lapilli (plural)/ lapillus (singular) is a volcanologic granulometric classification of commonly angular subround pyroclasts with a size from 2 to 64 mm. Accretionary lapilli is a special type formed as an aggregate in a volcanic eruption cloud (Sparks et al. 1997). Volcanic accretionary lapilli are common in phreatomagmatic eruptions forming within a turbulent, steam-rich ash plume (Moore & Peck 1962). They are associated with deposits of eruption plumes, pyroclastic flows and surge flows (Schumacher & Schmincke 1995). Experimental investigations of formation mechanisms (Gilbert & Lane 1994; Schumacher & Schminke 1995) demonstrated that accretionary lapilli growth is controlled by collision of liquid-coated, solid or molten ash sized particles in a turbulent environment. Particle binding occurs as a result of surface tension forces of condensing liquids and by secondary mineral growth. These mechanisms and conditions allow accretion of a large number of individual particles in the form of concentric layers in a plume-like environment. When the aggregate becomes too heavy to remain in the turbulent environment or is transported to a less energetic region, it is deposited in the accumulating volcaniclastic rock.

The El Guayal accretionary lapilli are similar to volcanic accretionary lapilli, because they show (1) an accreted particle size of <150 µm and in rare cases <300 µm with few nuclei of ~1 mm, (2) a tangential alignment of elongated particles and (3) multiple laminations due to grain size sorting. They resemble impact induced accretionary lapilli found in the Nördlinger Ries crater (Graup 1981) with respect to tangential particle alignment and decreasing particle size near the rim. A similar tangential alignment of shard-like particles has been reported in accretionary coatings around glass and lithic cores at the Sudbury impact structure (Muir & Peredery 1984). The presence of shocked minerals within the El Guayal accretionary lapilli is also observed at accretionary lapilli from the upper Devonian Alamo breccia (Warme 2002) and those related to the Sudbury impact event (Addison et al. 2005). It unequivocally links the El Guayal accretionary lapilli to the Chicxulub ejecta plume.

Accretionary lapilli form under different physical conditions than melt coated particles. The latter are a result of accretion of one melt phase on another (solid or molten) phase. The molten state of the coating phase implies a high temperature which is above the transition point of brittle glass in the case of silicate melt. The formation of accretionary lapilli is a complex aggregation process as documented by the presence of accretionary melt spheroids (consisting of carbonate melt coatings around silicate melt shards) within these lapilli. Thus, accretionary lapilli form by aggregation of several thousands individual ash to dust sized particles in a steam condensing environment (Moore & Peck 1962; Gilbert & Lane 1994; Schumacher & Schmincke 1995). These formation conditions indicate atmospheric interactions and a prolonged residence time within a turbulent plume. The steam condensing environment implies moderate formation conditions (~100°C), which is consistent with the observation that all of the silicate melt particles are in form of solidified, mostly fractured shards at the time of accretion.

Implications from accreted particles

The ternary composition of some feldspar particles is evidence for a formation at elevated temperatures and rapid cooling with no time for chemical equilibration. This assumption is supported by elevated FeO, MgO and TiO_2 values in those ternary feldspars compositions.

The $BaSO_4$ exsolution in one ternary composed feldspar particles documents the exchange with a sulphate saturated environment. At the Yax-1 borehole, baryte crystallisation is observed in vugs and is associated with post-hydrothermal diagenesis or ocean and/or meteoritic water circulation (Zürcher & Kring 2004). At Guayal, baryte crystallisation is observed neither in the accretionary lapilli nor in the bulk rock. Here, the occurrence of baryte as needle-like lamellas and the association with rapidly quenched feldspars possibly indicate a short-term crystallisation process. These observations support that the increasing Ba content in the accretionary lapilli unit is related to feldspar-rich target rocks. The heterogeneously composed areas of some feldspar particles indicate incomplete melting of feldspars and/ or the beginning separation of immiscible melt. These chemical heterogeneities of shock metamorphosed feldspars of El Guayal are similar to observations on feldspars in impact melt rocks from the Lappajärvi crater (Bischoff & Stöffler 1984). Those authors demonstrated that the increase of shock loading on feldspars prior to their incorporation into the melt results in increasing thermal alteration by the superheated melt. Similar to the study from the Lappajärvi crater this work demonstrates that the thermal annealing of (1) shocked plagioclase in impact melt rock results in an increase of K_2O and loss of Na_2O, whereas (2) shocked alkali feldspar show an increase in Na_2O, CaO and significant loss of K_2O. Consequently, the heterogeneous feldspar compositions document a post-shock melting between solidus and liquidus temperatures, where the K-feldspar areas represent the high-temperature phase sanidine.

At altered silicate melt particles, the transformation from montmorillonite/ illite to the vermiculite/ chlorite type would also contribute to the mobilisation of potassium as the vermiculite/ chlorite type has a much lower K_2O content. Laboratory experiments on the steam-induced alteration of kaolinitic, siderite-bearing sandstones have shown that potassium feldspars (in assemblages with magnetite, analcime, chlorite, illite) can be formed at temperatures >175°C (Keith et al. 1994). The strong variation of potassium in the altered silicate melt particles of El Guayal and the preferred association of potassium feldspar with altered silicate melt may indicate that silicate melt alteration is the source for potassium precipitation. Long-term hydrothermal processes did not played a major role at El Guayal (see section 4.2). Thus, the potassium feldspar may be similar to the secondary minerals observed in nuclei of accretionary lapilli formed by a rather short-term process during the prolonged transport at elevated temperatures in the steam-rich ejecta plume.

The laths-shaped texture of clay minerals (Figs. 3-8C and D) is similar to those observed for heavily altered melt particles from the Yax-1 borehole. At Yax-1, laths-shaped holes in melt particles, which are replaced by secondary potassium feldspar, were interpreted as altered or dissolved clinopyroxenes (Hecht et al. 2004).

Silification has obliterated the outlines of many calcite particles as commonly observed at volcanic accretionary lapilli (Boulter 1987). In analogy to volcanic lapilli (Boulter 1987), calcite precipitated subsequentially in the accretionary lapilli of El Guayal. This is indicated by calcite filling of vesicles in silicate melt shards. This calcite filling is of secondary origin as it displays a similar yellow cathodoluminescence like the secondary sparitic calcite veins. However, the non-luminescent melt particles and spherulitic calcite spheroids document that certain amounts of primary carbonate melt particles were accreted. The cores of (non-luminescent) spherulitic calcite spheroids, which consist of altered, vesicular silicate melt, indicate that carbonate melt was accreted on solidified silicate melt. The elevated SiO_2 and Al_2O_3 content of some calcite particles accreted in the lapilli has also been reported from carbonate melts of the Haughton impact structure (Osinski & Spray 2001), the Nördlinger Ries impact structure (Osinski et al. 2004) and from volcanic carbonatites (e.g. Rosatelli et al. 2003). At El Guayal, the positive correlation of the contents of Al_2O_3 and SiO_2 approximately equals the proportion of those elements in altered silicate melt. Thus, the presence of sub-µm up to 3 µm sized spherical silicate melt inclusions in calcite particles can be attributed to the presence of two cogenetic melts. However, the occurrence of angular inclusions in the rim of the carbonate melt particle with a, compared to the spherical inclusions, slightly different composition indicate that solid fragments were incorporated into the carbonate melt. Thus, it is likely, that the spherical silicate melt inclusions were incorporated by similar processes and have not formed by the exsolution of immiscible silicate melt out of one melt. The close association of those carbonate areas, which are rich in silicate melt inclusions, with glomeroblastic microcrystalline calcite argues for a cogenetic formation. This conclusion advocates the interpretation that microcrystalline calcite crystals are either primary carbonate melts which formed at low cooling rates or represent a fast back-reaction of calcite. This assumption is supported by electron-spin-resonance studies of Mn^{2+} and SO_3 of the El Guayal accretionary lapilli which suggest that these and lapilli from other K-P sites on the southern Yucatán peninsula include a component formed in the ejecta plume, either from condensation in the presence of CO_2/SO_3-rich vapours, or reactions between CaO and CO_2/SO_3-rich vapours (Griscom et al. 2003) Thus, much of the original accretionary lapilli matrix was formed by carbonate, which was easily replaced by silica released upon alteration of silicate melt particles due to its small crystal size.

The Ca-rich dolomite type resembles saddle dolomite in chemical composition and shape. Saddle dolomite is a common product of late-stage diagenesis and hydrothermal activity. It normally occurs as pore-filling cement and veins and is reported as a replacement product in some dolomitised limestones. Barber et al. (1985) propose precipitation from a Ca-rich solution. Radke & Mathis (1980) suggest that it forms at temperatures between 60–150°C. Such temperatures are in excellent agreement with those derived from fluid inclusions studies of saddle dolomites from the dolomitised carbonate breccias of the nearby oil reservoir at the Cantarel oil field (80–120°C, Martinez-Ibarra et al. 2003). The calcite overgrowth at the El Guayal saddle dolomites resembles those from the Haughton impact crater (Osinski et al. 2001, 2005a). It can be speculated, that those dolomites have been formed by a short-term precipitation process within the ejecta plume, but a formation by secondary processes cannot be excluded at this point. However, a post-depositional formation of saddle dolomite during carbonate silification seems to be more likely since (1) some of the euhedral saddle dolomites in the accretionary lapilli contain bright luminescent amoeboid calcite similar to amoeboid matrix calcite which was replaced by silica and (2) there is a general association of saddle dolomite with diagenetic processes.

The importance of multiple concentric layering

The multiple concentric layering of the El Guayal accretionary lapilli is of special interest as changing environmental conditions in the ejecta plume are recorded. For volcanic accretionary lapilli, the concentric grain-size zones build up due to differences in the supply of particle sizes related to a progressive increase in formation temperature in the ash plume (Gilbert & Lane 1994). This temperature increase reduces the humidity and the amount of condensed liquid layers on particles, so that accretion is biased towards smaller grain sizes (Moore & Peck 1962). In regions where temperatures exceed the condensation point (without the presence of a liquid phase) particles may accrete to form ash clusters by much weaker electrostatic attraction between charged ash particles (James et al. 2002). Another possible mechanism responsible for concentric laminations can be similar to the formation of hailstone where a chilling environment at high altitudes causes the conversion of liquid water to ice as shown in recent volcanic eruption plumes (Rose et al. 1995). At El Guayal, a formation of the laminations in relation to hot temperatures appears more likely due to (1) the high amount of accreted melt particles, (2) the smaller size of accreted particles in the vicinity of silicate melt nuclei which indicates an elevated temperature of the nuclei, and (3) the coherent deposition of accretionary lapilli together with melt particles. The petrographic and chemical results including (1) the comparable trace element concentrations of the accretionary lapilli and their suevitic host rock (Ba, Cr, V, Ti, Zr), and (2) the presence of (non-luminescent) accretionary carbonate melt spheroids within the lapilli as well at the uppermost accretionary lapilli unit gives strong evidence for a coherent formation of the accretionary lapilli and the upper suevitic deposits. Thus, multiple laminations of the El Guayal accretionary lapilli recorded a recurring heat increase by circulation in a vigorously turbulent plume-like environment. This is because the formation of accretionary lapilli requires a steam enriched condensing environment with moderate plume temperature (~100°C), where solidified melt particles arrive from hotter areas of the ejecta plume.

Veitch & Woods (2001) developed a theoretical model for an eruption column that accounts for the re-entrainment of particles as they fall-out of the laterally spreading umbrella cloud. However, the recurring heat increase needed for the multiple laminations of the El Guayal accretionary lapilli and their very distal deposition require more complex formation conditions as offered by a simple umbrella shaped ash cloud model. In volcanic events the collapse of a vertical eruption column can form hot, gaseous, particulate density currents known as pyroclastic flows (Fischer & Schmincke 1984). Volcanic accretionary lapilli with multiple laminations are reported from ignimbrite flow units and their co-ignimbrite ash cloud deposits (e.g. Riley & Leat 1999; Brown & Branney 2004). The latter forms by elutriation of fine ash from the moving pyroclastic flow. Brown & Branney (2004) proposed the following scenario for multiple laminated accretionary lapilli: The cores formed in a co-ignmibrite ash cloud by aggregation due to hydrostatic attraction similar to smaller, internally homogeneous ash pellets. With ongoing growths, the pellets became too heavy, dropping to a lower more turbulent and hotter level of the ash plume, where they accreted fine rims and evolve into accretionary lapilli. Ongoing circulation between the turbulent plume and hot density currents can form multiple laminations.

Comparison with impact induced accretionary lapilli from other craters shows a deposition at stratigraphic levels comparable to El Guayal. In the case of the Sudbury impact structure accretionary lapilli are at a distance of 650–875 km in the middle of a 25–75 cm thick ejecta layer (Addison et al. 2005). Preliminary investigations of the Bosumtwi impact structure show an accretionary lapilli unit, which was interpreted to represent the final impact fallout layer, at the interface between impact breccias and post-impact lake sediments (Koeberl et al. 2006). This indicates a prolonged formation and atmospheric residence time during late stage plume evolution.

4.1.5 The K-P boundary clay

The clay unit of El Guayal shows a PGE anomaly which indicates an extraterrestrial component. This is due to incorporation of impact debris from a globally distributed plume. Shocked quartz particles, which are present at many K-P boundary sites around the world (Claeys et al. 2002), are enriched in the clay unit of El Guayal compared to the underlying impactites. The shocked quartz particles in the clay unit show less decoration of their PDFs when compared to shocked quartz in the underlying accretionary lapilli unit and the microbreccia. This indicates a less intense thermal alteration of shocked quartz. The occurrences of spherulitic carbonate melt spheroids in the clay unit, which are similar to the larger spherulitic spheroids in the underlying suevite, suggest a cogenetic relationship of those units. Thus, the clay unit represents the finest fraction of Chicxulub ejecta mixed with an extraterrestrial component. This provides strong evidence for linking the Chicxulub impact with the global K-P boundary.

The sedimentary, petrological and chemical data suggest that the entire impactite sequence was deposited in a short time. The settling time in the water column can be calculated by assuming a maximum water depth of 200 m at the Yucatán shelf and applying the settling velocity of the largest particles present in the clay unit. In the clay unit, particles with maximum size of ~64 µm are observed, which corresponds to a settling velocity of 19 m/h (Smit et al. 1996) and settling time of ~10 hours. To this time the atmospheric residence time of supposedly several weeks to years has to be added. This time is short compared to marine sedimentation rates, and consequently few marine carbonates are incorporated into the clay unit. These observations indicate that much of the microcrystalline calcite matrix possibly represent calcite dust, which back-reacted quickly from decomposed carbonates with atmospheric CO_2 (Agrinier et al. 2001).

The calculated modal content of 4 % CaO cannot be explained be the presence of quicklime due to its high reactivity with water (see section 4.1.6). At the Nördlinger Ries suevite, Horn et al. (1999) demonstrated that immiscible carbonate melts and the fine-grained contact zones with silicate melt display extremely heterogeneous compositions. Horn et al. (1999) suggested that the presence of calcium silicate hydrate (CSH) phases, similar to reaction products at the interface between silicates and carbonates in concretes for building materials, are responsible for high CaO concentrations. Therefore, at El Guayal, a specific amount of decomposed carbonates has possibly reacted in the atmosphere with the small fraction of silicates to form CSH-phases. This interpretation is supported as the suevite of the Nördlinger Ries (also named “Bavarian Trass”) is a natural pozzolana, where the phases of the suevite are in a reactive stage and readily form with $Ca(OH)_2$ and H_2O Ca-silicate and -aluminate hydrates (Liebig & Althaus 1998).

4.1.6 UNAM borehole impactites

The UNAM-5 and UNAM-7 boreholes are located 105 and 126 km, respectively, from the crater centre. UNAM-5 is located near the crater rim directly on the outside flank of the outer ring visible on images generated by seismic data (Morgan & Warner 1999). Thus, the impactites of UNAM-5 and UNAM-7 represent the proximal ejecta blanket deposited outside the crater. In the UNAM-5 borehole, at a depth from 332.0 m to 504.0 m and at UNAM-7 from 222.2 to 348.4 m the polymict silicate melt-rich breccias contain highly shocked crystalline (basement) clasts and, thus, can be regarded as a suevite (Stöffler & Grieve 1996). In the UNAM-7 borehole at 348.4 m, the suevite overlies an evaporite-rich polymict silicate melt-poor breccia, of which the latter may be compared to the Bunte breccia from the Nördlinger Ries crater due to the low abundance of silicate melt particles (Urrutia-Fucugauchi et al. 1996b; Sharpton et al. 1999; Schönian et al. 2003, 2006). Sample UNAM-7-381.40 is intercalated in between anhydrite megablocks, whereas the underlying megablocks range in size from 10 to 35 m and those overlying from 5 to 23 m (Schönian et al. 2006).

The polymict silicate melt-rich breccia of UNAM-5 and UNAM-7

The angular and vesicular morphology of the greenish silicate melt particles contained in sample UNAM-5-357.40 document a deposition in solid state. This observation indicates that the upper allochthonous polymict breccia with shocked crystalline target rock and abundant silicate melt particles represents an air-borne suevite. The presence of sedimentary cores in silicate melt particles of samples UNAM-5-357.40 and UNAM-5-409.77 point to a progressive replacement of the sedimentary target by the hot silicate melt. This suggests that the lack of sedimentary clasts in the upper suevites could be due to decomposition during a prolonged residence time in the hot ejecta plume.

The low amount of silicate melt, the presence of sedimentary particles and different pale yellow white, vesicular melt particles in the lower samples UNAM-5-480.37 and UNAM-5-500.55 point to a different transport process during the early stage of ejecta distribution. In the case of sample UNAM-5-480.37, the reaction rims at the different melt particles in contact with the matrix indicate a liquid state during deposition. In the Yax-1 borehole, the carbonates in the lower portion of the suevite sequence are interpreted to potentially represent melt (Dressler et al. 2004; Stöffler et al. 2004; Tuchscherer et al. 2004a). Furthermore, some of those particles develop subhedral shapes (sample UNAM-5-500.55) indicating that the pale yellow white melt particles possibly represent slowly cooled carbonate liquids.

At UNAM-7-267.40 and UNAM-7-307.85, the silicate melt particles with a rounded or amoeboid morphology show reaction rims with the matrix, supporting the interpretation that these melt particle were deposited in a molten state. A hydrothermal overprint is documented in the UNAM-7-267.40 silicate melt particles by a strong enrichment of elements like Br, Cl, S and Sr, elements which are common in seawater. Due to the farther distance of UNAM-7 from the crater centre compared to UNAM-5, the altered, brittle state of the silicate melt particles at UNAM-7 indicate a more susceptible hydrothermal interaction with invading seawater.

The polymict silicate melt-poor, carbonate melt-rich breccia of UNAM-7-381.40

In the polymict silicate melt-poor breccia of UNAM-7-381.40, carbonate melt is documented by the occurrence of spherulitic calcite particles, which are comparable to the feathery textured calcite particles of El Guayal. The high cooling rate and the angular fragmented morphology of those particles suggest quenching and transport in the air. Consequently, the overlying megablocks could have been transported by a similar process. The abundant polygonal spheroids in the polymict breccia are interpreted as recrystallised carbonate melts since those particles contain small vesicles and lack cathodoluminescence which is similar to the spherulitic calcite particles. The glomeroblastic to interlobate texture of these particles resembles those of volcanic carbonate melts in volcanic lapilli (Rosatelli et al. 2003). A rather low cooling rate is affirmed by the relatively large crystal sizes at the rim of carbonate melt spheroids. Furthermore, the large vesicles in the centre of single crystals and polygonal crystals document exsolution of CO_2 from the carbonate melt at moderate cooling rates. Thus, a low cooling rate maximises the size of the inclusions and also the crystal size, whereas higher cooling rates result in smaller inclusions as seen in spherulitic calcite particles. These arguments account -contrary to the spherulitic calcite particles- for a deposition in molten state and slow cooling of the polygonal spheroids when enclosed by a hot matrix.

The heterogeneous textures in the larger carbonate melt particles document the coherent relationship of the different (polygonal, interlobate, microcrystalline and micrite-like) calcite textures. These different textures are caused by differences in the temperature gradient and, hence, different cooling rates which are particularly pronounced at large particles. This observation is important as it supports the assumption, that much of the microcrystalline calcite particles at El Guayal result from impact related processes. The microcrystalline carbonates can thus be explained as carbonate recrystallisation which was induced by thermal alteration.

Additional carbonate melts are observed at UNAM-7-381.40 as carbonate inclusions in an unusual silicate melt particle. These carbonate inclusions experienced a crystallisation sequence similar to the carbonate silicate liquid immiscibility textures from the Nördlinger Ries crater (Graup 1999). The non-luminescent patterns in the carbonate inclusions are also similar to those observed in carbonate melt inclusions inside silicate melt particles of the Yax-1 drill core (Schulte 2006, pers. comm.). Here, the silicate melt schlieren, which interfinger into the carbonate inclusions, clearly support the former liquid state of both phases. Calcium sulphate melts are generally indicated by their coherent occurrence with carbonate melt inclusions. The crystallisation sequence of the large anhydrite core embedded in the silicate melt particle is of special interest as it displays the complex response of anhydrite to heat transfer from the hot silicate melt. The vesicles in the large columnar, euhedral to subhedral anhydrite crystals in the centre indicate SO_X degassing during partial decomposition. The associated smaller subhedral to interlobate crystals near the silicate melt do not contain vesicles and, thus, are interpreted as liquids of which vapour could escape. These observations show that anhydrite displays partial melting features at the silicate melt contact and partial decomposition in the centre. Interestingly, the melting temperature of anhydrite at atmospheric pressures (~1465°C) is close to its decomposition temperature (Ivanov et al. 2004). The partial melting and decomposition indicate that the anhydrite particle was embedded into the silicate melt in solid state. Therefore, the immiscible sulphate melt and also the carbonate melt inclusions may result from particle incorporation into silicate melt rather than separation of two immiscible phases from one melt.

The matrix components of sample UNAM-7-381.40

The heterogeneous flow texture of calcite and anhydrite schlieren at UNAM-7-381.40 clearly demonstrate the ductile behaviour of the matrix. The angular feathery and vesicular carbonate melt particles would not be preserved in a molten carbonate matrix, which was suggested for the suevite matrix of the Nördlinger Ries impact structure (Osinski et al. 2004) and the Haughton impact crater (Osinski et al. 2005a). However, the microcrystalline calcite intercalations within large anhydrite particles are associated with abundant large vesicles, which indicate degassing during decomposition of carbonates accompanied by subsequent fast back-reaction. It can be argued, that a significant amount of the microcrystalline calcite in the matrix formed in a similar way, but liberated vapour could be released more easily from the deposit. Intense interaction with water is documented by the chemistry of the highly altered silicate melt particles deposited above the polymict silicate melt-poor breccia. Thus, the following explanation for matrix formation is plausible: Similar to building processes the reaction of decomposed calcite (quicklime) with water (Eq. 4-2) causes in an exothermic reaction the hydration to calcium hydroxide (portlandite, “slaked lime”):

Slaking: $CaO + H_2O \Rightarrow Ca(OH)_2$ $\Delta H° = -65\ kJ / mol$ **Eq. 4-2**

When calcium hydroxide reacts with carbon dioxide the reformation of calcium carbonate (Eq. 4-3) leads to hardness and strengths of the cement:

Carbonation: $Ca(OH)_2 + CO_2 \Rightarrow CaCO_3 + H_2O$ **Eq. 4-3**

This scenario is supported since the texture of the UNAM-7 matrix is similar to microstructures of ancient lime mortars, relict particles of burnt lime stone in lime mortars or recent carbonated cement (St. John et al. 1998) that is composed of reformed microcrystalline to micritic calcite.

The fluidal texture of anhydrite observed in sample UNAM-7-381.40 resembles those observed at Yax-1-1314.80 (Tuchscherer et al. 2005). These authors agree with Stinnesbeck et al. (2004) that the fluidal anhydrite was formed by dissolution processes. They note that (1) monomict breccias with sharp contacts to the footwall could be indicative for high strain rates unique to a single slip event typical for impacts as described by Kenkmann et al. (2002) and, thus, (2) not all anhydrite dissolution features postdate the pervasive deformation event. However, those assumptions cannot be applied to UNAM-7 as these impactites were ejected out of the crater, while the examples of Tuchscherer et al. (2005) belong to brecciated rocks underlying the suevite. At UNAM-7, the fluidal anhydrite texture must be related to the impact event as (1) anhydrite schlieren in the matrix interfere with embedded carbonate melt particles and (2) a comparable fluidal anhydrite texture, which follows the direction of calcite intercalations with degassing vesicles, is observed within >3 cm sized anhydrite particles and interpreted as plastic deformation induced by heating in the ejecta plume.

Anhydrite crystallisation is indicated by the presence of euhedral anhydrite crystals in the matrix. Crystallisation from an impact generated melt was suggested for samples from the Haughton impact crater (Osinski & Spray 2003b; Osinski et al. 2005a). However, as shown above, a former complete molten state of the matrix is not likely, but rather calcite reformation was the dominant process. Generally, the following alternative processes are attributed to anhydrite formation: (1) Evaporation of seawater forms gypsum, which subsequently dewaters during diagenesis. This process cannot be applied to UNAM-7-381.40, as this sample is overlain by more than one hundred metres of impact breccia and, thus, does not represent an arid to semiarid environment with a high evaporation rate. (2) Primary airborne anhydrite crystals were observed by Buseck & Pósfai (1999). However, those minerals precipitated from aerosols are rounded and much smaller (<1µm) than the anhydrite crystals observed at UNAM-7. (3) A scenario analogous to volcanic-hosted massive sulphide (VHMS) deposits at black smokers may explain the anhydrite crystallisation observed in the matrix of sample UNAM-7-381.40. The initial structure of a black smoker chimney is formed by the precipitation of anhydrite at temperatures around 350°C, where cooler, sulphate-rich seawater mixes with the hot venting plume and the retrograde solubility of anhydrite results in crystallisation at that boundary layer (Haymon 1983).

Thus, a possible scenario is that anhydrite target rock was thermally decomposed and solved as sulphates in the water. The energy release from calcite reformation and heat from melt particles heated the deposit resulting in anhydrite precipitation. This interpretation is supported since precipitation of euhedral anhydrite is observed with luminescent, secondary calcite in (mostly hollow) vesicles of large non-luminescent carbonate melt particles. Additionally, the enrichment of heavy metals in the melt particles of the overlying polymict silicate melt-rich breccia supports a hydrothermal anhydrite origin, as the same elements are enriched at VHMS deposits (e.g. Large 1992).

In summary, the polymict melt-rich breccia at UNAM-5 and UNAM-7 include silicate melt particles and shocked basement clasts and represent a suevite deposited outside of the crater. The suevite decreases in thickness from UNAM-5 to UNAM-7 with increasing distance from the crater rim. The underlying polymict breccia at UNAM-7 contains only few silicate melt particles and is similar to the Bunte breccia of Nördlinger Ries, since it is composed mainly of rock from the upper target lithologies. However, the traditional suevite–Bunte breccia classification cannot be applied in this case since carbonate melt particles are present in the Bunte breccia equivalent of UNAM-7. The presence of carbonate melt and reformed calcite indicate a much hotter ejecta deposit compared to the Bunte breccia from the Nördlinger Ries crater.

It is notable, that carbonate clasts are rarely observed in the impactites of both UNAM-5 and UNAM-7, however, carbonate melt particles and back-reacted carbonate (via hydrothermally slaking or direct reaction of CaO with CO_2) are common. Compared to carbonate, anhydrite occurs much more often, but only as large plastically deformed and, thus, thermally altered particles. Additionally, anhydrite melts are rare and anhydrite reformation occurs only hydrothermally at elevated temperatures. This indicates that anhydrite is less accessible to thermal alteration, compared to carbonates, due to its higher decomposition temperature. Also, anhydrite has a tendency to decompose rather than forming a melt phase or to enter a stage of back-reaction. This may explain the lack of anhydrite at El Guayal. It further indicates that a significant amount of liberated CO_2 may have back-reacted to calcite, whereas SO_X was completely liberated to the atmosphere.

4.2 Genetic relationship of the El Guayal and UNAM impactites to the Chicxulub ejecta blanket and K-P sections

Occurrences of megabreccia in the Gulf of Mexico and Caribbean

The megabreccia of El Guayal is comparable to those in the Gulf of Mexico and the Carribean (Pszczolkowski 1986; Alvarez et al. 1992; Bralower et al. 1998; Grajales-Nishimura et al. 2000; Takayama et al. 2000; Kiyokawa et al. 2002; Dypvik & Jansa 2003). Those megabreccias originate from the collapse of the continental shelf edge which was triggered by impact induced seismic activity.

Seismic waves travel with 8–14 km/s and, thus, are considerable faster compared to suborbital lofted impact ejecta (<8 km/s) (Robertson et al. 2004). Numerical calculations (Collins et al. 2005) demonstrate that at distance of 520 km earthquakes arrive ~100 s after impact, while the arrival time for ejecta travelling on ballistic trajectories (Ahrens & O'Keefe 1978) is ~6 min (Collins et al. 2005). Therefore, the ejecta-rich units are on top of the megabreccia in the stratigraphic section of El Guayal (Grajales-Nishimura et al. 2000).

Comparison of El Guayal suevite with crater suevites

The allochthonous ejecta-rich deposits at El Guayal are petrographically classified as suevite due to the presence of shocked target rock and melt particles. Additionally, the chemical signature of the suevite from El Guayal (Fig. 3-20 and Fig. 3-21) matches the suevite drilled within the crater (Claeys et al. 2003; Schmitt et al. 2004; Tuchscherer et al. 2004b). However, the El Guayal suevite has much lower K_2O and Sr concentrations compared to the crater suevite. The elevated K_2O and Sr concentrations in the crater suevites are attributed to hydrothermal alteration and K-metasomatosis (e.g. Ames et al. 2004; Hecht et al. 2004; Zürcher & Kring 2004). The chemical signatures, petrographic observations and modal content indicate that such processes were not effective at El Guayal due to rapid quenching during transport to a distal site and the deposition in a marine environment, whereas crater suevites are heavily affected by hydrothermal fluids associated to the underlying hot melt pool.

The cooling history can be inferred from petrological observations at the different sites. Spherulitic recrystallised carbonate melts are absent at the Yax-1 drill core, and at the Y6 drill core the feathery textured calcite is only observed in upper part of the suevite (Claeys et al. 2003). Apparently, spherulitic textured carbonate melts are only preserved in air-fall suevites, where the conditions for the required high cooling rates exist. Contrary, the deposition in ground surged suevite deposited near to high temperature melt layers may exclude rapid quenching in the lower crater suevite.

The diversity of accretionary processes related to Chicxulub and other impact events on Earth and terrestrial planets

The presence of accretionary lapilli-like spheroids in ejecta deposits from the Chicxulub crater has been documented on the southern Yucatán peninsula (Pope et al. 1999, 2005) and as far as northeastern Mexico (Schulte et al. 2003, 2005) and Cuba (Alegret et al. 2005). However, these occurrences lack the clear association with accreted shocked particles commonly observed at El Guayal and accreted clay fragments (interpreted as altered silicate melt) are rare. The interpretation of accretionary lapilli is often based on concentric laminations or the presence of a core within circular spheroids. It has to be noted that concentric structures may also result from alternative secondary (diagenetic) alteration processes. This uncertainty is at the centre of the ongoing discussion whether iron-rich spherules on Mars might have formed as concretions in an aqueous environment (Squyres et al. 2004) or represent impact induced accretionary lapilli (Knauth et al 2005). Historically, Lyons & Officer (1992) have wrongly interpreted the K-P boundary at Haiti as a *"sequence of probable volcanic events"* and questioned the presence of volcanic "*accretionary lapilli(?)"*. Thereupon, Smit et al. (1996) note that at this K-P boundary *"99 % of tektites contain abundant bubble cavities, which are diagenetically infilled with clay minerals, or calcite. The bubble-cavity infillings may weather out, leading to interpretation as separate spherules, and the illusion of "accretionary lapilli", whereas they are actually bubble-cavity infillings enclosed in a spherule* *of clay minerals"*. However, Pope et al. (2005) wrongly refers to Smit et al. (1996) stating that *"calcite accretionary lapilli found in Chicxulub ejecta deposits at sites more distal than El Guayal in northeastern Mexico"*. This work shows that concentric structures can also be formed by primary impact-related processes such as accretionary melt coatings or carbonate recrystallisation at the rim of quickly heated carbonate particles. These examples show that the direct transfer of volcanic classifications to impact processes can be misleading. For these reasons the following detailed classification of ejecta is suggested, where the words bomb, lapilli, ash can be added, but only to address the particle size: (1) "ejecta particles" for solid and/ or (partially) molten bodies, (2) "accretionary melt particles" for those with accretionary melt coatings, (3) "accretionary spherule-like aggregates" for particles comprising many individually accreted (tangentially aligned, possible shocked or molten) ash-sized particles with a concentric layering due to grain size sorting. However, in the case of a sedimentary target the identification of primary particles is difficult due to the complex behaviour of carbonates during thermal alteration and the accessibility to secondary alteration processes. Thus, the suggested accretionary lapilli of Witzke & Anderson (1996) from the Manson impact structure are rather accretionary melt particles like those described from the Popigai impact structure (Masaitis & Deutsch 1999). Furthermore, the proposed extraterrestrial accretionary lapilli in lunar microbreccias (McKay et al. 1970; Richardson et al. 1970; Duncan et al. 1975; Grieve et al. 1975; Lindsay 1976) and the howardite Kapoeta (Pedroni 1991) probably formed under different conditions since water is absent in nearly all extraterrestrial environments. In those cases the aggregation process may be driven by electrostatic charges naturally imparted to the particles during the fracturing process (James et al. 2002).

On the southern Yucatán peninsula, the ejecta blanket of the Chicxulub impact crater is present in several localities in southern Quintana Roo and central Belize at ~280–470 km from the crater centre (Pope et al. 2005; Kenkmann & Schönian 2006). The deposits were exposed at subaerial level during the Late Cretaceous. Due to karstification, weathering, and erosion, measurements of the maximum thickness of the ejecta blanket are inhibited (Kenkmann & Schönian 2006) and suevite-like or PGE enriched deposits are not observed. However, those ejecta deposits are of special importance since they give insight into processes during the early stage of ejecta deposition, and link the suevites in or near the Chicxulub crater with the suevite deposits of El Guayal. At the Albion Island quarry (Fig. 4-2) at ~365 km from Chicxulub, a ~1 m thick spheroid bed is overlain by ~15 m thick diamictite bed (Ocampo et al. 1996; Pope et al. 1999). The upper diamictite bed contains rare shocked quartz particles. Large dolomite blocks up to 7.5 m in size are present, and a 3 m sized dolomite block is

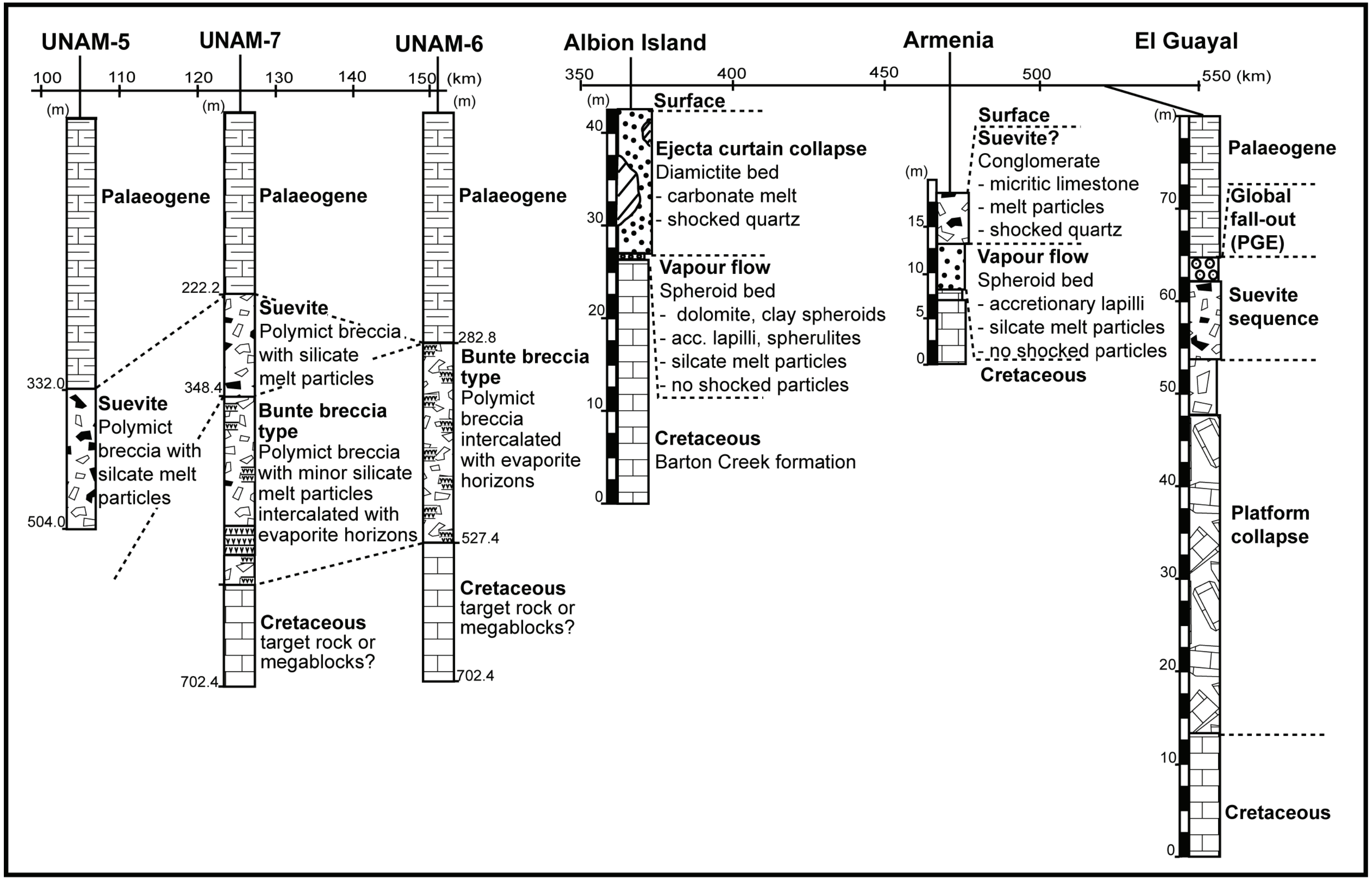

Figure 4-2 Stratigraphic comparison of the of the marine K-P site El Guayal with subaearial exposed ejecta deposits of Albion Island and Armenia (modified after Pope et al. 1999, 2005) on the southern Yucatán peninsula and UNAM boreholes near the outer crater rim (modified after Urrutia-Fucugauchi et al. 1996a, b) in relation to the radial distance to the Chicxulub crater centre. Different horizontal and vertical scales are used for ejecta sites and boreholes.

coated by 7 cm of dolomitic mud. This unit has been interpreted to originate from the collapse of the ejecta curtain (Pope et al. 2005). However, the radially fibrous calcite spherules (termed "pisiods") (Ocampo et al. 1996) are not *"one form of accretionary lapilli"* as assumed by Pope et al. (1999). The spherulitic radial crystal growths resemble the spherulitic carbonate melt spheroids of El Guayal and, thus, support the interpretation of Ocampo et al. (1996) that these spheroids have formed by "*quench crystallisation from carbonate melt"*.

Within the underlying spheroid bed at Albion Island no shocked quartz particles are observed. However, there are dolomite spheroids up to 2.5 cm in diameter which can be either homogenous, while some show an internal structure with an angularly dented core and laminations. Different formation mechanisms were suggested for those dolomite spheroids: (1) Ocampo et al. (1996) noted, that laminated spheroids resemble accretionary lapilli. They propose that decomposition of shock-heated carbonates and sulphates released CaO (quicklime) and possible MgO to form spheroids. Then the unstable oxides reacted with CO_2 to dolomite. The crystallisation of dolomite may either be a primary precipitation from a vapour plume or a secondary diagenetic process after deposition. (2) Pope et al. (1999) observed no differences in the matrix composition between the dolomite spheroids with or without core. They argue that volcanic pyroclastic flows contain lapilli with or without cores, so that both types are accretionary lapilli. Furthermore, they note that mud coated boulders of the diamictite bed are of similar structure and composition as the accretionary lapilli-like spheroids. Mud-coated boulders have not been recognised from volcanic debris-flows so far, and it was concluded that these boulders represent accretionary blocks which were transported in a volatile-rich plume. (3) Fouke et al. (2002) agree with Ocampo et al. (1996) that those spheroids may have generated by quicklime formation. Additionally, it is suggested that the homogenous dolomite spheroids may be altered impact glass, which was replaced by dolomite. Furthermore, Fouke et al. (2002) mention that mechanisms like the formation of lunar and meteoritic chondrules may be an explanation for the genesis of the dolomite spheroids. (4) Smit (1999) remarked that *"the dolomite spheroids may have obtained their concentric banding by accretion within the layer, which is heated, and may be even partially melted through friction between the sliding ejecta curtain and authochtonous dolomite rather than from accretion in a turbulent, volatile-rich plume"*. Thus, it is not clear, whether the altered spheroids from Albion Island are accretionary lapilli or not. However, it has to be noted that some concentric dolomite spheroids have a texture similar to volcanic lithophysae commonly known as "thunder eggs" (Kile 2002). Lithophysae are volcanic spherulites which form by high temperature vapour phase exsolution and crystallisation from the vapour phase, where the central void is subsequentially filled with secondary products such as silica. Thus, even to interpret the dolomite spheroids as accretionary lapilli may not be strictly appropriate, a formation by aggregation of back-reacted carbonates from upper surface target lithologies in a vapour plume, which predates the ejecta curtain (Pope et al. 2005), seems plausible. This process could be attributed to jetting as proposed by Gault et al. (1966), whereby the high-pressure zone between the impactor and the target is free to expand at high velocity into the planet's atmosphere (McKinnon 1997). Furthermore, jetting has also been proposed as a mechanism responsible for the formation of chondrules during asteroid collisions and tektites in terrestrial impacts (McKinnon 1997).

A less altered and less dolomitised spheroid bed, compared to Albion Island, is exposed in the ejecta deposits of Armenia (Fig. 4-2) at ~470 km from the crater centre (Pope et al. 2005). Spheroids of coarse detrital calcite grains with a rim of fine calcite particles and in some cases with an altered silicate melt nucleus resemble accretionary lapilli. Compared to the much larger El Guayal accretionary lapilli, the spheroids of Armenia contain no shocked quartz and silicate melt particles are rare. This indicates a formation during an early stage of the impact process when (in analogy to the Bunte breccia from the Nördlinger Ries) silicates from the lower excavation zone are not abundant. The diamictite bed is missing at Armenia. Therefore, Pope et al. (2005) concluded, that a volatile enriched vapour plume extended >470 km, while the subsequent deposited continuous ejecta blanket was restricted to 330–470 km. The overlying reworked conglomerate present at Armenia (composed of micritic limestone, melt particles and shocked quartz; Pope et al. 2005) is only briefly described. However, due to the similar components compared to the El Guayal suevite, both units could have been deposited by similar processes.

Heating of carbonate particles in the ejecta plume is indicated by microcrystalline limestone ejecta particles ("Pook's Pebbles") from the Cayo district (~475 km southeast of the Chicxulub crater) showing penetrations of rock chips (Ocampo et al. 1997a). Their surface is composed of ~1 μm sized fused calcite grains which were interpreted during thermal annealing which resulted in an incomplete melting of plastically deformed limestones. This structure is somehow similar to the microcrystalline calcite texture at El Guayal ejecta particles (e.g. melt particles type 2b). Experiments have confirmed that nominally brittle limestone can be plastically deformed in low-stress collision interactions under high temperatures of ~175–625°C and low pressures (Ocampo et al. 1997b). This is consistent with the observation that accreted shocked quartz particles occur in the rim of silicate melt particles type 2b which indicates that melt particles type 2 a has been formed by aggregation and fusion of silicate melt with (plastic deformable) carbonate particles rather than separation of two immiscible phases.

Guillemette & Yancey (2006) reported microaccretionary and accretionary spherules at K-P sites at Brazos River, Texas and Bass River, New Jersey located at distances ~1000 km and ~2500 km, respectively from the crater. These ~50 µm up to 2.5 mm sized carbonate spherules are composed of micron sized calcite crystals and contain varying concentrations of larger clay masses with heterogeneous compositions. Guillemette & Yancey (2006) interpreted the spheroids as products from shattered surface carbonate rocks which formed in the ejecta plume. This interpretation is supported by the close similarity of the texture to silicate melt coated calcite particles (melt particle type 2) of El Guayal. The intermixing of silicate melt with calcite is only observed at El Guayal and at more distant K-P sites of Brazos River and Bass River, but not at K-P sites on the southern Yucatán peninsula. This point towards a later stage of the impact process, when the ejecta plume is increasingly enriched in silicate melt and possible better mixed during distal transport. These observations support formation of microcrystalline calcite by primary impact related processes. Thus, much of the microcrystalline calcite at El Guayal and the UNAM boreholes may have originated from dust dispersed by the impact event, which derived from back-reaction of CO_2 and solid CaO (Agrinier et al. 2001; Schulte et al. 2005).

Comparison of the K-P boundary clay at El Guayal with other K-P sites

The link of the global K-P boundary with the Chicxulub impactites is marked by the projectile component (chemically identified by the PGE enrichment) together with Chicxulub ejecta (shocked quartz, silicate melt particles and carbonate melt spheroids) in the clay unit. The enrichment of shocked quartz observed in the clay unit of El Guayal is similar to the presence of shocked quartz in the upper part of a 6 cm spherule layer at Bass River (pers. comm. of Izett in Olsson et al. 1997). The presence of a projectile component in the El Guayal clay unit, but not in the underlying accretionary lapilli unit and microbreccia, is similar to (1) the dual-layer stratigraphy at terrestrial K-P sections in the USA and Canada 2000–4000 km away from Chicxulub (Bohor et al. 1984; Bohor et al. 1987; Izett 1990) and (2) impact layers interrupted by tsunami deposits at K-P sites in shelf regions <800 km from Chicxulub. The dual-layer stratigraphy was explained by differences in the arrival time. A lower layer was deposited by fast ejecta on ballistic trajectories, while a PGE-enriched upper fireball layer was formed by globally distributed ejecta introduced in the stratosphere (Kring & Durda 2002).

In contrast to the dual layer ejecta deposits in the Golf of Mexico, which are separated by tsunami deposits, El Guayal represents a coherent sequence of impactites. This distinct behaviour can be explained by the different palaeogeographic location. The K-P sites with tsunami deposits were in the shallow sea of the North American continental shelf. Thus, broad waves which travelled across the deep sea of the Gulf of Mexico steepened up as the water depths decreases near the shore line of the continental shelf forming tsunami waves. However, El Guayal was at the shelf of the Yucatán carbonate platform. There, the seismic energy lead to fracturing of the Yucatán platform, possibly initiating the travel of waves away from the Yucatán platform, but the surf of tsunami waves could not reach El Guayal. As only back-reflected tsunami waves within Gulf of Mexico palaeogeography would reach El Guayal, the effects of tsunami waves were of minor importance.

4.3 Processes in the ejecta plume of Chicxulub – inferred from textural and petrographic observations

The deposition of the Chicxulub ejecta blanket can be compared to the succession at the Nördlinger Ries crater, where suevite is deposited on top of the Bunte breccia. This represents an inverse stratigraphy as suevite contains material (silicate melt particles and crystalline clasts) excavated from the lower target lithologies, whereas the Bunte breccia contains material from the upper target lithologies. At the UNAM-7 borehole, a similar inverse stratigraphy is observed: A silicate melt-bearing suevite breccia overlies a polymict silicate melt-poor breccia (intercalated with evaporite horizons), where the latter represents the Bunte breccia equivalent. At El Guayal, an inverse but more gradual stratigraphy is exposed within the suevite sequence, which contains mainly calcite particles and minor silicate melt particles at the base, but silicate melt material particles become more abundant towards the top.

However, the following observations are inconsistent with the classical emplacement model of a ballistically emplaced Bunte breccia followed by turbulent deposition of highly shocked suevite from lower excavated target lithologies. For instance, the presence of suevite (defined as ejecta plume deposit) at ~520 km is not expected since numerical simulations indicate a maximum fireball diameter of 10–15 times of the impactor size (Melosh et al. 1993). Thus, a projectile of 10–20 km diameter, such as the Chicxulub impactor, forms a fireball with a maximum diameter of 150–300 km. Furthermore, the traditional definition of Bunte breccia excludes the presence of melt particles, which are rare but present in the case of Chicxulub within the continuous ejecta blanket on the southern Yucatán peninsula (Pope et al. 2005; Kenkmann & Schönian 2006) and also within the Bunte breccia equivalent of the UNAM-7 bore hole (Sharpton 1999; Schönian et al. 2003, 2006; this work). In addition, the presence of molten, decomposed and back-reacted carbonate and plastically deformed anhydrite particles in the Bunte breccia analogue of UNAM-7 suggests a high emplacement temperature which was not recorded in the Nördlinger Ries Bunte breccia inferred to be deposited at relatively cool conditions. These differences between the deposits of the Chicxulub and Nördlinger Ries ejecta can not be explained solely by the 10 fold difference of the size of the impact crater. Rather, it is important to consider additional factors such as the larger proportion of sediments, which contain a high amount of free water due to their porosity, and atmospheric interactions during the impact process. Thus, the response of sediments upon hypervelocity impact and their behaviour in the ejecta plume are important processes during plume evolution.

The role of melting, decomposition and back-reaction of sedimentary target rock

Vaporisation of silicates occurs upon shock pressures reaching >100 GPa, whereas decarbonation occurs at pressures of >40 GPa and vaporisation of H_2O takes place at >10 GPa (Kieffer & Simonds 1980). Thus, an impact event in a water-saturated sedimentary target will produce several orders of magnitude more vapour compared to impacts into dry crystalline target lithologies. Modelling suggests that sediments will melt to a greater extent than crystalline rocks, which is, however, inconsistent with field observation which show that melt sheets are generally not present at craters formed in carbonate rocks, but only at craters formed in crystalline rocks (Kieffer & Simonds 1980). This paradox was addressed by Kieffer & Simonds (1980) who concluded that (1) the resulting melt may not be recognisable in craters formed in sedimentary rocks, and (2) the melt sheets are not found immediately outside of the crater since steam from pore water and CO_2 expand enormously and widely disperses the impact debris by a gas driven transport. These authors suggest that much of the molten and decarbonised sediments become fine ash easily dispersed over a wide range which is also readily eroded or reworked. This is supported by the general problem of identifying a distinct PGE-enriched deposit within (e.g. Tagle et al. 2004; Arz et al. 2004; Smit et al. 2004) and near the Chicxulub impact crater (Pope et al. 2005; Kenkmann & Schönian 2006).

The following occurrences of impact derived carbonate melts indicate that they are a common product of hypervelocity impact into sedimentary target rock: (1) Solidified immiscible carbonate melt is associated with silicate melt in suevites from the Nördlinger Ries impact structure (Graup 1999; Osinski et al. 2004) and the Haughton impact structure (Osinski & Spray 2001), (2) quench textured calcite is abundant in ejecta particles in northeastern Mexico (Schulte et al. 2003), (3) carbonate melt spheroids are present in the diamicite bed of Albion Island (Ocampo et al. 1996), (4) feathery textured carbonate melt particles are recognised in the Chicxulub suevite from the Y6 bore hole (Jones et al. 2000; Claeys et al. 2003), (5) the carbonate in the lower portion of the impactite sequence of Yax-1 may represent melt (Dressler et al. 2004; Stöffler et al. 2004; Tuchscherer et al. 2004a), and (6) the abundant presence of carbonate melt particles at El Guayal and in the UNAM-7 borehole. Field evidence for back-reactions of highly reactive residual oxides with CO_2 is provided by carbonate microstructures at the Haughton impact crater (Martinez et al. 1994). In contrast, Osinski et al. (2005a, b) found no evidence for a back-reaction of the Haughton impactites, but, instead, for carbonate melting. They concluded that melting and not decomposition is the dominant process and reinterpreted the suevites as impact melt rock. However, this work has shown that both melting and decomposition including the subsequent back-reactions are important processes and, thus, have to be considered during ejecta distribution.

The quantification of CO_2 and SO_X release during the Chicxulub impact is difficult since the contribution of the different target lithologies is unknown and experimental results (see Arginier et al. 2001; Skála et al. 2002 for recent compilation) are inconsistent regarding this matter. The response of anhydrite when exposed to a hypervelocity impact is poorly known. Shock experiments indicate that anhydrite is stable over a wide pressure range up to 64 GPa (Skála et al. 2005). However, at high temperature and atmospheric pressure anhydrite reveals a complex behaviour as the melting point for anhydrite at 1465°C is very close to the temperature of the decomposition reaction (Ivanov et al. 2004). This is a significantly higher temperature range than observed for calcite decomposition and melting. The melting point for $CaCO_3$ is at an invariant point of $p = 40$ bars and $T = 1240$ °C (Irving & Wyllie 1973) at which $CaCO_3(s)$, $CaO(s)$, $CO_2(g)$ and liquid coexist. The refined phase diagram of Ivanov & Deutsch (2002) shows that the liquid field of $CaCO_3$ is more extensive than previously considered (Fig. 4-3). Additionally, numerical modelling of shock recovery experiments show that the dominant effect of pressure release is melting and not degassing (Ivanov et al. 2002). Thus, at burial pressures equivalent to depths of a few hundred meters most of the carbonates should be ejected in a liquid state (Jones et al. 2000). However, at atmospheric pressures with increasing temperatures calcite never reaches the melting point, but is vaporised prior to melting (e.g. Pierazzo et al. 1998). Thus, in a vapour plume environment with atmospheric

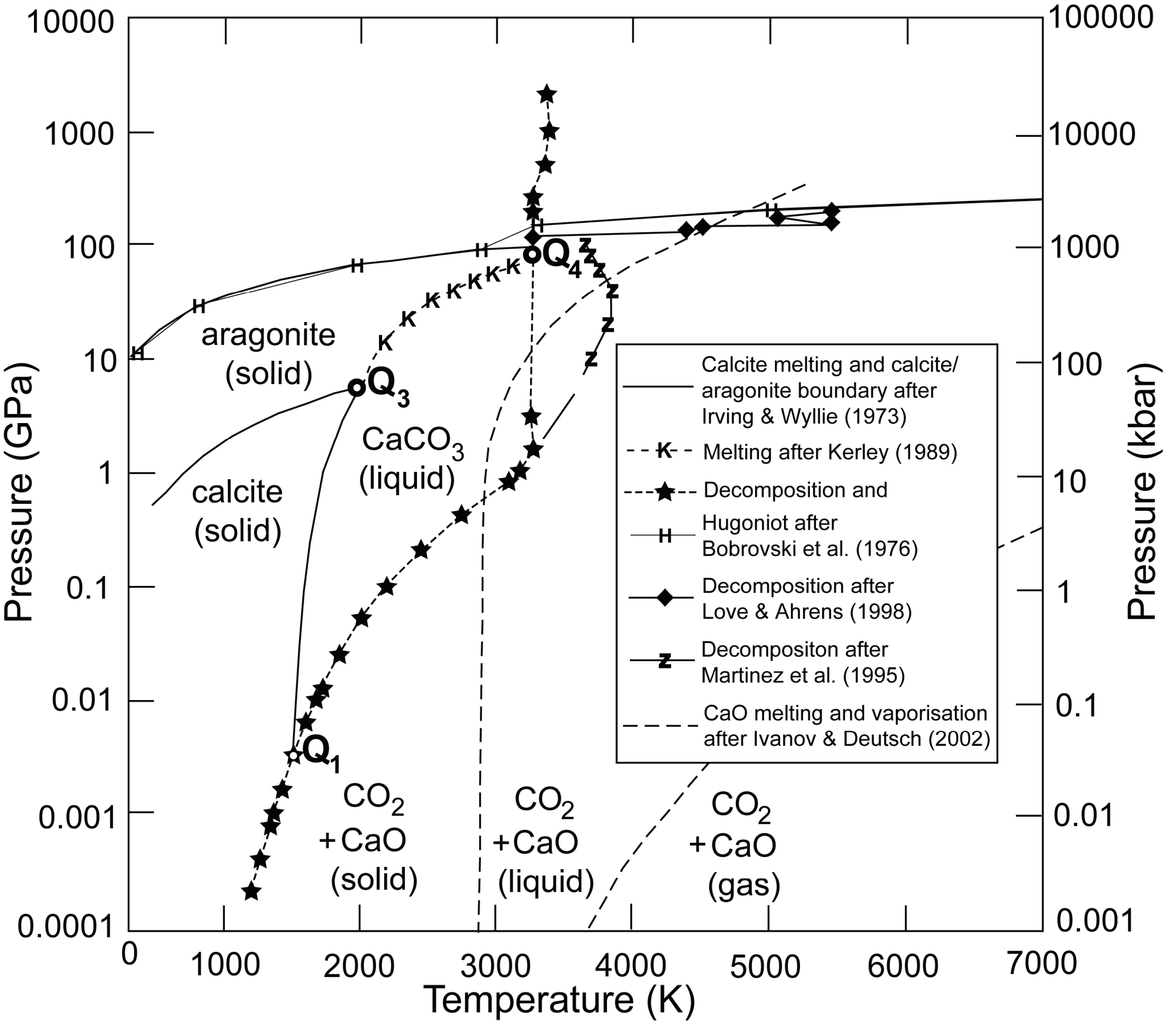

Figure 4-3 Expanded phase diagram of $CaCO_3$ modified after Ivanov & Deutsch (2002). Experimental data by Irving & Wyllie (1973) show the calcite melting curve and calcite/ aragonite transition. The melting curve of $CaCO_3$ at high pressures is after theoretical equation of state (EOS) by Kerley et al. (1989). The decomposition boundary derived from EOS of Bobrovski et al. (1976) intersects the melting curve twice, at the invariant points Q_1 and Q_4: At those points solid, liquid and decomposed $CaCO_3$ coexist in equilibrium. At the invariant point Q_3 calcite, aragonite and liquid $CaCO_3$ coexist. Decomposition curve of Martinez et al. (1995) is based on shock experiments and temperature calculations, the data of Love & Ahrens (1998) is obtained by shock experiments. CaO melting and vaporisation curve after Ivanov & Deutsch (2002) calculated by EOS.

pressures dissociation is expected during post-shock cooling (Agrinier et al. 2001). Additionally, the decomposition during admixing of silicate melt with carbonates (as seen at silicate melt type 2 of El Guayal) is accompanied by the production of a vast amount of vapour. The volume expansion of these gases during pressure release is the major mechanism by which the suevite forms and disperses around the crater (Kieffer & Simonds 1980). These authors also argued that during this process a massive amount of energy is transferred from the ground to the atmosphere: By ingestion of wet sediments into the melt, thermal energy is transferred into the volatile phases and this energy can be removed from the ground if the gas escapes into the atmosphere and space. However, the back-reaction of calcite rebinds vapour and inhibits a loss of energy and may therefore be responsible for a prolonged energy release and transport of the ejecta curtain at elevated temperatures.

The influence of volatiles, atmospheric interactions and distinct temperature environments

The presence of water vapour in the ejecta plume is of special importance for the ejecta distribution. Experiments by Wohletz & Sheridan (1983) showed that water, explosively vaporised from the target lithologies during impact, influences the initial ballistic trajectories of ejecta and produces a surging flow emplacement. Pope et al. (2005) suggested that initial Chicxulub ejecta were emplaced by at least two distinct flows: A volatile-rich flow of fine debris extended >470 km due to explosive vapour expansion, and (2) a later flow of coarse debris was related to the collapse of the ejecta curtain and was deposited not much beyond 360 km. This study proposes a hot transport of ejecta in both the initial vapour flow and the succeeding ejecta curtain due to a prolonged energy release during fast back-reaction of CaO with CO_2. Thus, some of the accretionary lapilli deposited at Albion Island 360 km from the crater centre (Pope et al. 1999) are reinterpreted as lithophysae-like spheroids, which represent spherulites formed due to vapour phase exsolution and crystallisation at high temperatures. During lateral expansion, cooling of the vapour flow resulted in steam condensation and formation of (almost pure) carbonate accretionary lapilli at a distance >470 km (Pope et al. 2005).

At El Guayal, the mixing of hot silicate melt with sediment components and the occurrence of accretionary lapilli both indicate the ejecta transport during a later stage was highly complex and required turbulent formation conditions. This is consistent with the previously inferred extensive turbulent interactions between the plume and atmosphere (Schultz 1992; Barnouin-Jha & Schultz 1996, 1998; Barnouin-Jha et al. 1999a, b). The transport and emplacement of the El Guayal accretionary lapilli was related to two different temperature regimes with close spatial association and intense exchange:

(1) A hot regime, where relative cold surface carbonate particles are strongly heated by the thermal energy of the superheated hot silicate melt. The lower temperature range of this regime is below the calcite decomposition temperature due to the presence of solid, fossil-bearing calcite particles at El Guayal. This is consistent with the deposition temperature of ~500–550°C for the hot, fluidised suevite of the Nördlinger Ries, which has been determined by fission track, ^{40}Ar-^{39}Ar and palaeomagnetic studies (Newsom et al. 1986a, b). The upper

temperature limit of this regime is represented by the suevite glass transformation around 680–750°C (Wali 1985; Fecker 1993). The lack of crystallites in the silicate melt at El Guayal indicates that temperatures exceed locally 1100°C (Engelhardt et al. 1995). (2) A cooler region with steam condensing temperature conditions (~100°C) is required for the formation of the accretionary lapilli.

Models on the Chicxulub expansion plume formation predict the occurrence of a plume doublet (Alvarez et al. 1995; Pope et al. 1997) consisting of (1) an inner hot plume with vaporised projectile material lofted to the stratosphere and globally distributed within several weeks to years and, (2) an outer warm plume with only little impactor contribution. Processes relevant for the formation of the accretionary lapilli including condensation and coagulation should only occur in the highly turbulent, warm region of the ejecta plume (Pope et al. 1997). There, steam, which is essential for the lapilli genesis, and material mainly from the upper portion of the target rock succession such as carbonate volatiles and particles and shocked quartz are expected (Alvarez et al. 1995). The lack of a significant impactor component (PGE enrichment) in the El Guayal accretionary lapilli and its surrounding rock corroborates this interpretation. In contrast, some numerical model calculations suggest that vaporised sediments and water were entrained in the entire plume, though they were not well mixed (Pierazzo et al. 1998; Pierazzo & Melosh 1999). According to numerical models of an oblique impact (30° and 45°) on the Chicxulub target sequence the following temperature and downrange material distribution may be expected after 5 s since first contact (Pierazzo & Melosh 1999): (1) A hot basal region with atmospheric temperatures of >7000°C. (2) On top a water enriched zone with much lower temperatures in the range of ~600–1300°C. (3) At a higher level a calcite dominated zone of ~1500–3300°C. (4) A topmost zone with >7000°C which is enriched in projectile material. Similar calculations for an obliqueness of 45° resulted in a comparable temperature profile at 8 s after impact (Artemieva 2006).

The Chicxulub suevites were deposited during a later stage, but the current knowledge regarding the late stage of ejecta plume behaviour is limited, especially because existing numerical models are restricted to the first several seconds after impact. Studies of the suevite from the Yax-1 drill core show that mm-sized particles are expected to have precipitated in a time interval of 1 to 3 hours after crater modification (Stöffler et al. 2004). Additionally, ash to dust sized particles and a turbulent environment were required for the genesis of El Guayal accretionary lapilli and, thus, indicate atmospheric residence times of more than a few hours. The well-preserved sequence of impactites at El Guayal offers new insights regarding the late stage of plume evolution. At this point the expanding suevitic plume probably reached an unstable state and collapsed due to gravitational forces. A hot, laterally spreading flow was formed, which is somewhat similar to those observed in volcanic surges, pyroclastic flows, or eruption features associated with nuclear and chemical explosions (Carlson & Roberts 1962; Glasstone & Dolan 1977). These processes likely increased the run-out distance due to the expanding vapours and the flow-like ejecta transport so that the suevite could be transported over a distance of >6 crater radii (see also Schulte & Kontny 2005 with data from northeastern Mexico >900 km from the impact that supports such a model). Thus, ejecta do not necessarily had to be carried above the Earth's atmosphere as predicted by Kring & Durda (2002) for debris deposited >400 km.

5 Conclusions

The specific behaviour of the sedimentary, volatile-rich target as well as atmospheric interactions were important for ejecta transport and plume evolution during the Chicxulub impact. Based on the results obtained in this study five distinct stages can be reconstructed for the deposition and alteration of the Chicxulub ejecta blanket as observed at El Guayal, UNAM-7, and UNAM-5:

(1) Seismic activity caused by the shock waves of the impact resulted in fracturing and collapse of the slopes of the Yucatan platform (Fig. 4-4, upper image). During the first minutes after the impact, a monomict carbonate megabreccia was deposited at El Guayal near the shelf region of the Yucatán platform before the arrival of ejecta from the Chicxulub crater. In the high-pressure zone between the impactor and the sedimentary target, jetting resulted in a transport of decomposition products (CaO, CO_2, SO_X) at high velocity in the atmosphere. Steam explosions from instantly vaporised target water led to flow-like transport processes as suggested by Pope et al. (2005). The fast back-reaction of CaO with CO_2 resulted in calcite reformation and a prolonged energy release in the vapour flow.

(2) Anhydrite and carbonate megablocks were excavated out of the impact crater and initiated a lateral extending, ground hugging surface flow (Pope et al. 2005; Kenkmann & Schönian 2006). Thereby, carbonates buried at depths larger than a few hundred meters were ejected out of the impact crater in a liquid state (Jones et al. 2000). Close to the impact crater, the carbonate components show complete melting and reformation suggesting an intense thermal alteration. Continuous decomposition of carbonates and sulphates and calcite reformation resulted in a hot ejecta transport. The presence of water vapour sustained the transformation from ballistic transport to a lateral flow regime. Thereby, small amounts of silicate melts from lower target lithologies were injected to the outwards expanding, calcite-dominated ejecta curtain. Close to the impact crater at UNAM-7, a small fraction of carbonate melt particles were rapidly quenched during airborne transport. Here, the majority of carbonate and silicate melts were deposited in the liquid state together with decomposed sedimentary target components, back-reacted calcite and anhydrite megablocks.

(3) A turbulent expanding ejecta plume was formed above the impact crater. With increasing excavation depths, the ejecta plume was enriched in shocked and molten components of the crystalline silicate basement. About 10 to several tens of minutes after the impact, the ejecta plume collapsed partially (Fig. 4-4, lower image). While the vaporised and condensed material

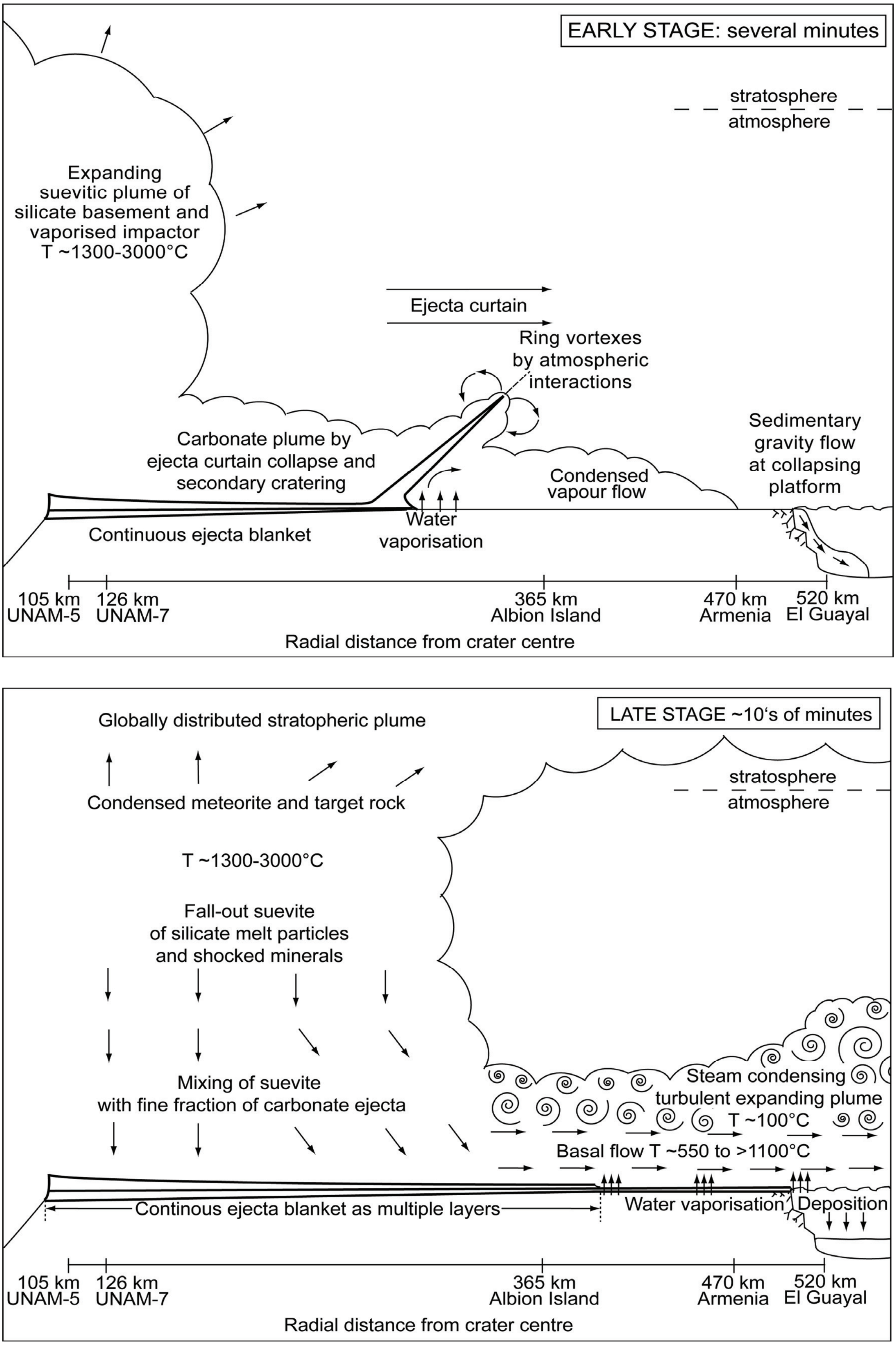

Figure 4-4 Model of Chicxulub ejecta plume behaviour at an early stage and during late stage. A final crater diameter of ~200 km is assumed and crater modification processes are not shown. Not to vertical scale.

derived from the projectile was lifted to the stratosphere for global distribution, the molten and solid target rock was falling back to the surface. Thereby, hot silicate components mixed with the fine fraction of locally surface-derived sediments of which the latter were displaced by the preceding ejecta curtain. The fusion of porous, water-saturated carbonates and sulphates with hot silicate melt resulted in additional vapour release and sustained a gas-driven, lateral basal transport comparable to a volcanic pyroclastic flow with locally varying temperatures of ~550 to >1100°C.

At a higher level, this basal flow was accompanied by a highly turbulent plume comparable to volcanic co-ignimbrite ash clouds. This zone is inferred to have had a moderate temperature (~100°C) due to admixing of ambient air. Thus, steam condensed and accretionary lapilli were formed from carbonate and silicate material which emerged from the basal flow, a process referred to as elutriation in a volcanicclastic environment. Due to the close association of the hot basal flow with a turbulent ash plume of moderate temperature, the accretionary lapilli and the fine fraction of ejecta particles circulated several times between the moderate and hot temperature regime. Progressive lapilli growth ultimately led to aggregates that became too heavy to be held in suspension by the flow. Consequently, the accretionary lapilli settled and sank through the water column in the area now represented by the El Guayal site. This scenario is comparable to co-ignimbrite ash clouds associated with volcanic pyroclastic flows, which are commonly rich in accretionary lapilli.

At El Guayal, the occurrence of predominantly spherulitic textured calcite melt particles may be explained by rapid cooling during distal airborne transport. However, the cogenetic association of carbonate melts with variably textured calcite crystals reflects variations in the cooling rates during transport in an ejecta plume with a heterogeneous temperature distribution. The distal transport at elevated temperatures caused, compared to the proximal ejecta deposits, greater variations in thermal alteration. Additionally, the finer fraction of ejecta particles resided for a longer time in the flow and was more strongly affected by thermal alteration.

Whereas carbonates responded upon thermal alteration by recrystallisation, melting, decomposition and back-reaction, anhydrite showed a different behaviour. The partial melting and partial decomposition of anhydrite observed at UNAM-7 is consistent with the melting temperature of anhydrite at ~1465° for atmospheric pressures which is close to its decomposition temperature (Ivanov et al. 2004). Therefore, similar to calcite, anhydrite decomposition was caused by elevated temperatures in the hot ejecta plume and related to interaction with hot silicate melt. The higher decomposition temperature for anhydrite compared to calcite suggests that, in contrast to calcite, larger anhydrite clasts and megablocks were able to withstand decomposition, while smaller anhydrite particles are fully decomposed. This process explains both the lack of individual anhydrite particles in the upper air-fall suevites of UNAM-5 in the immediate vicinity of the crater, and the absence of anhydrite at the distal K-P site of El Guayal.

(4) For a period of presumably weeks to years, the impactor component was deposited from suspension in the stratosphere together with the finest fraction of ejecta material –mainly ash-sized (partially fragmented) carbonate melt particles, temperature resistant shocked quartz particles– forming the K-P boundary clay. During this time, reactive CaO recombined with atmospheric CO_2 forming microcrystalline calcite dust. A certain amount of CaO may have interacted with the finest fraction of silicate components to form CSH-phases. The presence of Chicxulub impact ejecta like shocked quartz and spherulitic carbonate melt spheroids together with the PGE-enriched impactor component (Tagle, unpublished data) in the clay unit of El Guayal unequivocally links the global K-P boundary with the Chicxulub impact. Hence, the presumption that the Chicxulub event predates the K-P boundary by 300 ka (Keller et al. 2004) is inconsistent with the mineralogical, lithological and biostratigraphical evidence provided by the El Guayal depositional sequence (see also Arenillas et al. 2006).

(5) The prolonged transport of impact debris in the ejecta plume and reaction with hot volatiles induced the particular style of post-sedimentary alteration of the ejecta deposits. At El Guayal, silica was released during the alteration of silicate melt particles. This resulted in an intense silification of recrystallised calcite particles and coherent formation of minor secondary sparitic calcite. These processes including the swelling capacity of clay minerals may have enhanced the sealing properties at ejecta deposits on top of the oil producing reservoir facies of the Cantarel oil fields at the Campeche marine platform (Grajales-Nishimura et al. 2000). At UNAM-7, formation of the calcite matrix by reaction of CaO with condensed target water and invading seawater and subsequent reaction of calcium hydroxide with CO_2 (of which the latter is solved in the water) is a likely scenario. Thereby, anhydrite could have precipitated from sulphate-rich fluids, which were heated during calcite reformation and by melt particles to temperatures >350°C.

In summary, contrary to calcite, anhydrite reformation could only have happened at specific postdepositional conditions. Thus, a certain amount of the degassed CO_2 has back-reacted to calcite, whereas SO_X gases were completely liberated into the atmosphere. These observations including the abundant presence of carbonate melts collectively support the conclusion that the amount of CO_2 released to the atmosphere during the Chicxulub impact was significantly overestimated previously (Agrinier et al. 2001; Ivanov & Deutsch 2002). The presence of accretionary melt particles and accretionary spherule-like aggregates at different K-P boundary deposits indicate that aggregation reduced the amount of particles and ash from the atmosphere, which possibly lowered the duration of global darkening.

6 References

Addison, W.D.; Brumpton, G.R.; Vallini, D.A.; MacNaughton, N.J.; Davis, D.W.; Kissin, S.A.; Fralick, P.W. and Hammond, A (2005): Discovery of distal ejecta from the 1850 Ma Sudbury impact event, Geology 33, pp. 193-196.

Agrinier, P.; Deutsch, A.; Schärer, U. and Martinez, I. (2001): Fast back-reactions of shock released CO_2 from cabonates: An experimental approach, Geochemica et Cosmochimica Acta 65, pp. 2615-2632.

Ahrens, T. J. and O'Keefe, J. A. (1978): Energy and mass distributions of impact ejecta blankets on the moon and Mercury, Proceedings of the Lunar Science Conference 9, pp. 3787-3802.

Alegret, L.; Arenillas, I.; Arz, J. A.; Grajales-Nishimura, J. M. and Soria, A. R. (2005): Cretaceous-Paleogene boundary deposits at Loma Capiro, central Cuba: Evidence for the Chicxulub impact, Geology 33, pp. 721-724.

Alvarez, L. W.; Alvarez, W.; Asaro, F. and Michel, H. V. (1980): Extraterrestrial cause for the Cretaceous Tertiary extinction, Science 208, p. 1095.

Alvarez, W. ; Smit, J.; Lowrie, W.; Asaro, F.; Margolis, S. V.; Claeys, P.; Kastner, M. and Hildebrand, A. R. (1992): Proximal impact deposits at the Cretaceous-Tertiary boundary in the Gulf of Mexico: A restudy of DSDP Leg 77 Sites 536 and 540, Geology 20, pp. 697-700.

Alvarez, W.; Claeys, P. and Kieffer, S. W. (1995): Emplacement of KT boundary shocked quartz from Chicxulub crater, Science 269, pp. 930-935.

Ames, D. E.; Kjarsgaard, I. M.; Pope, K. O.; Dressler, B. and Pilkington, M. (2004): Secondary alteration of the impactite and mineralization in the basal Tertiary sequence, Yaxcopoil-1, Chicxulub impact crater, Mexico., Meteoritics & Planetary Science 39, pp. 1145-1167.

Arenillas, I.; Arz, J. A.; Grajales-Nishimura, J. M.; Murillo-Muñetón, G.; Alvarez, W.; Camargo-Zanoguera, A.; Molina, E. and Rosales-Domínguez, C. (2006): Chicxulub impact event is Cretaceous/Paleogene boundary in age: New micropaleontological evidence, Earth and Planetary Science Letters 249, pp. 241-257.

Artemieva, N. A. (2006): Fluidized impact ejecta and volcanic blast surge - numerical modelling, Lunar and Planetary Science Conference XXXVII, p. #1525 (abstract).

Arz, J. A.; Alegret, L. and Arenillas, I. (2004): Foraminiferal biostratigraphy and paleoenvironmental reconstruction at the Yaxcopoil-1 drill hole, Chicxulub crater, Yucatán Peninsula, Meteoritcs & Planetary Science 39, pp. 1099–1111.

Barber, D. J.; Reeder, R. J. and Smith, D. J. (1985): A TEM microstructural study of dolomite with curved faces (saddle dolomite), Contributions to Mineralogy and Petrology 91, pp. 82-92.

Barnouin-Jha, O. S. and Schultz, P. H. (1996): Ejecta entrainment by impact-generated ring vortices: Theory and experiments, Journal of Geophysical Research 101, pp. 210099-21115.

Barnouin-Jha, O. S. and Schultz, P. H. (1998): Lobateness of impact ejecta deposits from atmospheric interactions, Journal of Geophysical Research 103, pp. 25739-25756.

Barnouin-Jha, O. S.; Schultz, P.H. and Lever, J. H. (1999a): Investigating the interactions between an atmosphere and an ejecta curtain. I. Wind tunnel tests, Journal of Geophysical Research 104, pp. 27105-27116.

Barnouin-Jha, O. S.; Schultz, P.H. and Lever, J. H. (1999b): Investigating the interactions between an atmosphere and an ejecta curtain. II. Numerical Experiments, Journal of Geophysical Research 104, pp. 27117-27131.

Beruto, D. T.; Searcy, A. W. and Kim, M. G. (2004): Microstructure, kinetic, structure, thermodynamic analysis for calcite decomposition: free-surface and powder bed experiments, Thermochimica Acta 424, pp. 99-109.

Bischoff, A. and Stöffler , D. (1984): Chemical and structural changes induced by thermal annealing of shocked feldspar inclusions in impact melt rocks from Lappajärvi crater, Finland, Journal of Geophysical Research (Supplement) 89, pp. B645-B656.

Bobrovsky, S. V.; Gogolev, V. M.; Zamyshlyaev, B. V.; Lozhkina, V. P. and Rasskazov, V. V. (1976): The study of thermal decomposition influence on the spallation velocity for strong shock waves in solids, Fiziko-Technicheskie Problemy Razrabotki Poleznykh Iskopaemyh 3, pp. 49–57 (in Russian, see English translation in Soviet Mining Science).

Bohor, B. F.; Foord, E. E.; Modreski, P. J. and Triplehorn, D. M. (1984): Mineralogic evidence for an impact event at the Cretaceous-Tertiary boundary, Science 224, pp. 867-869.

Bohor, B. F.; Triplehorn, D. M.; Nichols, D. J. and Millard Jr., H. T. (1987): Dinosaurs, spherules, and the "magic" layer: A new K-T boundary clay site in Wyoming, Geology 15, pp. 896-899.

Boulter, C. A. (1987): Subaqueous deposition of accretionary lapilli: Significance for palaeoenvironmental interpretations in Archaean greenstone belts, Precambrian Research 34, pp. 231-246.

Bralower, T. J.; Paull, C. K. and Leckie, R. M. (1998): The Cretaceous-Tertiary boundary cocktail: Chicxulub impact triggers margin collapse and extensive sediment gravity flows, Geology 26, pp. 331-334.

Brown, R. J. and Branney, M. J. (2004): Accretionary lapilli in ignimbrites and the evolution of ash aggregates within pyroclastic density currents: Examples from the Poris Ignimbrite, Tenerife, Canary Islands, International Association of Volcanology and Chemistry of The Earth Interior, General Assembly, Pucón, Chile, p. (abstract).

Burns, E.; Sigurdsson, H.; Carey, S. and D'Hondt, S. (2003): Geochemistry of accretionary lapilli from a Cretaceous-Tertiary impact breccia, Guayal, Mexico, Third International Conference on Large Meteorite Impacts, Nördlingen, Germany, Lunar and Planetary Institute LPI Contribution No. 1167, p. #4132 (abstract).

Buseck, P. R. and Pósfai, M. (1999): Airborne minerals and related aerosol particles: Effects on climate and the environment, Proceedings of the National Academy of Sciences of the United States of America 96, pp. 3372-3379.

Carlson, R. H. and Roberts, W. A. (1962): Ejecta Studies, Project Sedan PNE-217P, University of California Lawrence Radiation Laboratory, Livermore, California.

Carr, M. H.; Crumpler, L. S.; Cutts, J. A.; Greeley, R.; Guest, J. E. and Masursky, H. (1977): Martian impact craters and emplacement by surface flow, Journal of Geophysical Research 82, pp. 4055-4065.

Claeys, P.; Heuschkel, S.; Lounejeva-Baturina, E.; Sanchez-Rubio, G. and Stöffler, D. (2003): The suevite of the drill hole Yucatàn 6 in the Chicxulub impact structure, Meteoritics & Planetary Science 38, pp. 1299-1317.

Claeys, P.; Kiessling, W. and Alvarez, W. (2002): Distribution of Chicxulub ejecta at the Cretaceous-Tertiary boundary, Koerberl, C. and MacLeod, K. G., Catastrophic Events and Mass Extinctions Impacts and Beyond Special Paper 356 pp. 55-68, Geological Society of America, Boulder, Colorado.

Collins, G. S.; Melosh , H. J. and Marcus, R. A. (2005): Earth impact effects program: A web-based computer program for calculating the regional environmental consequences of a meteoroid impact on Earth, Meteoritics & Planetary Science 40, pp. 817-840.

Couture, R. A (1985a): Rapid increase in permeability and porosity of bentonite-sand mixtures due to alteration by water vapor, Materials Research Society Symposium Proceedings 44, pp. 515-522.

Couture, R. A. (1985b): Steam rapidly reduces the swelling capacity of bentonite, Nature 318, pp. 50-52.

Davis, J. (1973): Statistics and data analysis in geology, John Wiley & Sons, New York.

Deer, W. A.; Howie, R. A. and Zussman, J. (1992): An introduction to the rock-forming minerals, 2nd. ed., John Wiley & Sons, New York.

Dressler, B. O.; Sharpton , V. L.; Schwandt, C.S. and Ames, D. (2004): Impactites of the Yaxcopoil-1 drilling site, Chicxulub impact structure: Petrography, geochemistry, and depositional environment, Meteoritics & Planetary Science 39, pp. 857-878.

Duncan, A. R.; Grieve, R. A. F. and Weill, D. F. (1975): The life and times of Big Bertha: Lunar breccia 14321, Geochimica et Cosmochimica Acta 39, pp. 265-273.

Dypvik, H. and Jansa, L. F. (2003): Sedimentary signatures and processes during marine bolide impacts: A review, Sedimentary Geology 161, pp. 309-337.

Engelhardt, W. v. (1990): Distribution, petrography and shock metamorphismof the ejecta of the Ries crater in Germany - A review, Tectonophysics 171, pp. 259-273.

Engelhardt, W. v.; Andt, J.; Fecker, B. and Pankau, H. G. (1995): Suevite breccia from the Ries crater, Germany: Origin, cooling history and devitrification of impact glasses, Meteoritics 30, pp. 279-293.

Fecker, B. (1993): Kristallisationsexperimente an natürlichen Suevitgläsern und Modellrechnungen zur Abkühlungsgeschichte des Fall-out Suevits im Nördlinger Ries, Ph.D. thesis, Mineralogical Institute, Freie Universität Berlin.

Fisher, R. V. and Schmincke, H.-U. (1984): Pyroclastic rocks, Springer, Berlin.

Fisher, R. V. and Smith, G. A. (1991): Volcanism, tectonocs and sedimentation, Sedimentation in volcanic settings, Society for Sedimentary Geology, Tulsa, Oklahoma, Special Publication 45, pp. 1-5.

Fouke, B. W.; Zerkle, A. L.; Alvarez, W.; Pope, K. O.; Ocampo, A. C.; Wachtmann, R. J.; Nishimura, J. M. Grajales; Claeys, P. and Fischer, A. G. (2002): Cathodoluminescence petrography and isotope geochemistry of KT impact ejecta deposited 360 km from the Chicxulub crater, at Albion Island, Belize, Sedimentology 49, pp. 117-138.

French, B. M. (1998): Traces of catastrophe: A handbook of shock-metamorphic effects in terrestrial meteorite impact structures, LPI Contribution 954, Lunar and Planetary Institute, Houston, Texas.

Gault, D.E.; Quaide, W. L. and Oberbeck, V.R. (1966): Impact cratering mechanics and structures, French, B. M. and Short, N. M., Shock metamorphism of natural materials, Mono Book Corp., Baltimore, NASA, Goddard Space Fight Center, Greenbelt, Maryland.

Gilbert, J. S. and Lane, S. J. (1994): The origin of accretionary lapilli, Bulletin of Volcanology 56, pp. 398-411.

Glasstone, S. and Dolan, P. J. (1977): The Effects of Nuclear Weapons 3rd edition, US Department of Defense and Energy Research and Development Administration, Washington DC.

Gomes, R.; Levison, H. F.; Tsiganis, K. and A., Morbidelli (2005): Origin of the cataclysmic Late Heavy Bombardment period of the terrestrial planets, Nature 435, pp. 466-469.

Grajales-Nishimura, J. M.; Esteban, C.-P.; Rosales-Domínguez, C.; Morán-Zenteno, D. J.; Alvarez, W.; Claeys, P.; Ruíz-Morales, J.; García-Hernández, J.; Padilla-Avila, P. and Sánchez-Ríos, A. (2000): Chicxulub impact: The origin of reservoir and seal facies in the southeastern Mexico oil fields, Geology 28, pp. 307-310.

Grajales, J. M.; Moran, D.; Padilla, P. ; Sanchez, M. A.; Cedillo, E. and Alvarez, W. (1996): The Lomas Tristes breccia : A KT impact-related breccia from Southern Mexico, Geological Society of America, Abstracts with Programs 28, p. 183 (abstract).

Graup, G. (1981): Terrestrial chondrules, glass spherules and accretionary lapilli from the suevite, Ries crater, Germany, Earth and Planetary Science Letters 55, pp. 407-418.

Graup, G. (1999): Carbonate-silicate liquid immiscibility upon impact melting: Ries crater, Germany, Meteoritics & Planetary Science 34, pp. 425-438.

Grieve, R. A. F. (1987): Terrestrial impact structures, Annual Reviews Earth Planetary Science 15, pp. 245-270.

Grieve, R. A. F.; McKay, H. D.; Smith, D. and Weill, D. F. (1975): Lunar polimict breccia 14321: A petrographic study, Geochimica et Cosmochimica Acta 39, pp. 229-245.

Griscom, D.; Beltrán-López, V.; Pope, K.O. and Ocampo, A.C. (2003): New geochemical insights from electron-spin-resonance studies of Mn^{2+} and SO_3^- in calcites: Quantitative analyses of Chicxulub crater ejecta from Belize and southern Mexico with comparison to limestones from distal Cretaceous-Tertiary boundary sites, Koeberl, C. and Martínez-Ruiz, F., Impact markers in the stratigraphic record pp. 229-270, Springer, Heidelberg, Germany.

Griscom, D. L. ; Beltrán-López, V.; Merzbacher, C. I. and Bolden, E. (1999): Electron spin resonance of 65-million-year-old glasses and rocks from the Cretaceous-Tertiary boundary, Journal of Non-Crystalline Solids 253, pp. 1-22.

Guillemette, R. N. and Yancey, T. E. (2006): Microaccretionary and accretionary carbonate spherules of the Chicxulub impact event from Brazos River, Texas and Bass River, New Jersey, Lunar and Planetary Science Conference XXXVII, p. #1779 (abstract).

Hale, John; Heinemeier, Jan; Lancaster, Lynne; Lindroos, Alf and Ringbom, Åsa (2003): Dating ancient mortar, American Scientist 91, pp. 130-137.

Haymon, Rachel M. (1983): Growth history of hydrothermal black smoker chimneys, Nature 301, pp. 695 - 698.

Hecht, L.; Wittmann, A.; Schmitt, R.-T. and Stöffler, D. (2004): Composition of impact melt particles and the effects of post-impact alteration in suevitic rocks at the Yaxcopoil-1 drill core, Chicxulub crater, Mexico, Meteoritics & Planetary Science 39, pp. 1169–1186.

Heiken, G. and Wohletz, K. (1991): Fragmentation processes in explosive volcanic eruptions, Fischer, R. V. and Smith, G. A., Sedimentation in volcanic settings Special Publication 45 pp. 19-36, Society for Sedimentary Geology, Tulsa, Oklahoma.

Heuschkel, S.; Lounejeva Baturina, E.; Jones, A. P.; Sanchez-Rubio, G.; Claeys, P. and Stöffler, D. (1998): Carbonate melt in the suevite breccia of the Chicxulub crater, Eos Transaction, AGU Fall Meeting Supplement 79, p. F554 (abstract).

Hildebrand, A. R.; Penfield, G. T.; Kring, D. A.; Pilkington, M.; Camargo Z., A.; Jacobsen, S. B. and Boynton, W. V. (1991): Chicxulub crater: A possible Cretaceous/Tertiary boundary impact crater on the Yucatán peninsula, Mexico, Geology 19, pp. 867-871.

Horn, P.; Hölzl, S. and Fehr, T. (1999): Nichtmischbarkeit von Karbonat/Silikat-Schmelzen: Element- und Sr-Isotopenverhältnisse in Suevit des Ries-Kraters, Bayern, Schriften des Staatlichen Museums für Mineralogie und Geologie zu Dresden 10, pp. 39-43.

Hörz, F. (1965): Untersuchungen an Riesgläsern, Beitäge zur Mineralogie und Petrographie 11, pp. 621-661.

Hörz, F.; Ostertag, R. and Rainey, D. A. (1983): Bunte Breccia of the Ries - Continuous deposits of large impact craters, Reviews of Geophysics and Space Physics 21, pp. 1667-1725.

Huang, W.-L. and Wyllie, P. J. (1976): Melting relationships in the systems CaO-CO_2 and MgO-CO_2 to 33 kilobars, Geochimica et Cosmochimica Acta 40, pp. 129-132.

Irving, A. J. and Wyllie, P. J. (1973): Melting relationships in CaO-CO_2 and MgO-CO_2 to 36 kilobars with comments on CO_2 in the mantle, Earth and Planetary Science Letters 20, pp. 220-225.

Ivanov, B. A.; Badukov, D. D.; Yakovlev, O. I.; Gerasimov, M. V.; Dikov, Y. P.; Pope, K. O. and Ocampo, A. C. (1996): Degassing of sedimentary rocks due to the Chicxulub impact: Hydrocode and physical simulations, Ryder, G.; Fastovsky, D. and Gartner, S., The Cretaceous-Tertairy event and other catastrophes in Earth history Special Paper 307 pp. 125-140, Geological Society of America, Boulder, Colorado.

Ivanov, B. A. and Deutsch, A. (2002): The phase diagram of $CaCO_3$ in relation to shock compression and decomposition, Physics of the Earth and Planetary Interiors 129, pp. 131-143.

Ivanov, B. A.; Langenhorst, F.; Deutsch, A. and Hornemann, U. (2002): How strong was impact-induced CO_2 degassing in the Cretaceous-Tertiary event? Numerical modelling of shock recovery experiments, Koeberl, C. and MacLeod, K. G., Catastrophic events and mass extinctions: Impacts and beyond Special Paper 356 pp. 587–594., Geological Society of America, Boulder, Colorado.

Ivanov, B. A.; Langenhorst, F.; Deutsch, A. and Hornemann, U. (2004): Anhydrite EOS and phase diagram in relation to shock decomposition, Lunar and Planetary Science Conference XXXV, p. #1489 (abstract).

Izett, G. A (1990): The Cretaceous-Tertiary boundary interval, Raton Basin, Colorado and New Mexico, and its content of shock-metamorphosed minerals; Evidence relevant to the K/T boundary impact-extinction theory Special Paper 249, Geological Society of America, Denver, Colorado.

James, M. R. ; Gilbert, J. S. and Lane, S. J. (2002): Experimental investigation of volcanic particle aggregation in the absence of a liquid phase, Journal of Geophysical Research 107, pp. 2191, doi:10.1029/2001JB000950.

Jarosewich, E.; Gooley, R. and Husler, J. (1987): Chromium augite - A new microprobe reference sample, Geostandard Newsletter 11, pp. 197-198.

Jarosewich, E.; Nelen, J. A. and Norberg, J. A. (1980): Reference samples for electron microprobe analysis, Geostandard Newsletter 4, pp. 43-47.

JNC (2000): H12 project to establish technical basis for HLW disposal in Japan, Supporting report 2, Repository design and engineering technology, JNC TN1410 2000-003, Japan Nuclear Cycle Development Institute (JNC),, Tokai, Japan.

Jones, A. P.; Claeys, P. and Heuschkel, S. (2000): Impact melting of carbonates from the Chicxulub crater, Gilmour, I. and Koeberl, C., Impacts and the early earth: Proceedings of the first workshop of the European Science Foundation Scientific Program on the Response of the Earth System to Impact Processes/ ESF IMPACT 91 pp. 343-361, Springer, Berlin.

Keith, D. C.; Wendy, J.H. and Wendlandt, R. F. (1994): Steam-induced alteration of mineralogy and permeability in kaolinitic, siderite-bearing sandstones, AAPG Annual Convention Abstracts, p. 95.

Keller, G.; Adatte, T.; Stinnesbeck, W.; Stüben, D.; Berner, Z.; Kramar, U. and Harting, M. (2004): More evidence that the Chicxulub impact predates the K/T mass extinction, Meteoritics & Planetary Science 39, pp. 1127–1144.

Keller, G.; Stinnesbeck, W.; Adatte, T.; Holland, B.; Stüben, D.; Harting, M.; de Leon, C. and de la Cruz, J. (2003): Spherule deposits in Cretaceous-Tertiary boundary sediments in Belize and Guatemala, Journal of the Geologic Society London 160, pp. 783-795.

Kenkmann, T. (2002): Folding within seconds, Geology 30, pp. 231-234.

Kenkmann, T. and Schönian, F. (2006): Ries and Chicxulub: Impact craters on Earth provide insights for Martian ejecta blankets., Meteoritcs & Planetary Science 41, pp. 1587-1603.

Kerley, G. I. (1989): Equation of state for calcite minerals. I. Theoretical model for dry calcium carbonate, High Pressure Research 2, pp. 29–47.

Kieffer, S. W. and Simonds, C. H. (1980): The role of volatiles and lithology in the impact cratering process, Reviews of Geophysics and Space Physics 18, pp. 143-181.

Kile, D. E. (2002): Occurrence and genesis of thunder eggs containing plume and moss agate from the Del Norte Area, Saguache County, Colorado, Rocks & Minerals July-August, pp. 252-268.

Kiyokawa, S.; Tada, R.; Iturralde-Vinent, M.; Tajika, E.; Yamamoto, S.; Oji, T.; Nakano, Y.; Goto, K.; Takayama, H.; Delgado, D. G.; Otera, C. D.; Rojas-Consuegra, R. and Matsui, T. (2002): Cretaceous-Tertiary boundary sequence in the Cacarajicara formation, western Cuba: An impact-related, high energy, gravity-flow deposit, Koerberl, C. and MacLeod, K. G., Catastrophic Events and Mass Extinctions Impacts and Beyond Special Paper 356 pp. 125-144, Geological Society of America, Boulder Colorado.

Klockenkämper, R. (1997): Total-reflections X-ray fluorescence analysis 140, Winefordenr, J.D., Ed, Chemical analysis: A series of monographs on analytical chemistry and its applications, Wiley-Interscience, John Wiley & Sons, Inc, New York.

Kloprogge, J. T.; Boström, T.E. and Weier, Matt L. (2004): In situ observations of the thermal decomposition of weddelite by heating stage environmental scanning electron microscopy, American Mineralogist 89, pp. 245-248.

Knauth, L. P.; Burt, D. M. and Wohletz, K. H. (2005): Impact origin of sediments at the Opportunity landing site on Mars, Nature 438, p. doi:10.1038/nature04383.

Koeberl, C.; Brandstätter, F.; Hecht, L.; Reimold, W. U.; Peck, J. and King, J. (2006): Uppermost impact fallout layer in a drillcore at the Bosumtwi impact crater (Ghana): A preliminary study, Lunar and Planetary Science Conference XXVII, p. #1552 (abstract).

Kring, D. A. (2005): Hypervelocity collisions into continental crust composed of sediments and an underlying crystalline basement: Comparing the Ries (~24 km) and Chicxulub (~180 km) impact craters, Chemie der Erde 65, pp. 1-46.

Kring, D. A. and Durda, D. D. (2002): Trajectories and distribution of material ejected from the Chicxulub impact crater: Implications for postimpact wildfires, Journal of Geophysical Research 107, pp. 1-22.

Kring, D. A.; Hörz, F.; Zurcher, L. and Urrutia Fucugauchi, J. (2004): Impact lithologies and their emplacement in the Chicxulub impact crater: Initial results from the Chicxulub Scientific Drilling Project, Yaxcopoil, Mexico, Meteoritics & Planetary Science 39, pp. 879–897.

Kring, D.A.; Hildebrand, A.R. and Boynton, W.V. (1991): The petrology of an andesitic melt rock and a polymict breccia from the interior of the Chicxulub structure, Yucatán, Mexico, Lunar and Planetary Science Conference XXII, pp. 755-756 (abstract).

Krogh, T. E.; Kamo, S. L.; Sharpton, V. L.; Marin, L. E. and Hildebrand, Alan R. (1993): U-Pb ages of single shocked zircons linking distal K/T ejecta to the Chicxulub crater, Nature 366, pp. 731–734.

Large, R. (1992): Australian volcanic-hosted massive sulfide deposits: Features, styles, and genetic models, Economic Geology 87, pp. 471-510.

Le Maitre, R. W. (1979): A new generalised petrological mixing system, Contributions to Mineralogy and Petrology 71, pp. 133-137.

Liebig, E. and Althaus, E. (1998): Pozzolanic activity of volcanic tuff and suevite: Effects of calcination, Cement and Concrete Research 28, pp. 567-575.

Lindsay, J. F. (1976): Lunar stratigraphy and sedimentology 3, Developments in Solar System- and Space Science, Elsevier Scientific Publishing Co., Amsterdam.

Lopez-Ramos, E. (1975): Geological summary of the Yucatàn Peninsula., Nairn, A. E. M. and Stehli, F. G, The ocean basins and margins, Vol. 3: The Gulf of Mexico and the Caribbean pp. 257–282, Plenum, New York.

Love, S. G. and Ahrens, T. J. (1998): Measured shock temperatures in calcite and their relation to impact-melting and devolatilization, Lunar and Planetary Science Conference XXIX, p. #1206 (abstract).

Lyons, J. B. and Officer, C. B. (1992): Mineralogy and petrology of the Haiti Cretaceous/Tertiary section, Earth and Planetary Science Letters 109, pp. 205-224.

Machel, H. G.; Mason, R. A.; Mariano, A. N. and Mucci, A. (1991): Causes and emission of luminescence in calcite and dolomite, Barker, C.E. and Kopp, O.C., Luminescence microscopy and spectroscopy- Qualitative and quantitative applications. 25 pp. 9-25, Society for Sedimentary Geology.

Martinez-Ibarra, R.; Tritlla, J.; Cedillo-Pardo, E.; Grajales-Nishimura, J. M. and Murillo-Muñetón, G. (2003): Brine and hydrocarbon evolution during the filling of the Cantarell Oil Field (Gulf of Mexico), Journal of Geochemical Exploration 78–79, pp. 399– 403.

Martinez, I.; Agrinier, P.; Schärer, U. and Javoy, M. (1994): A SEM-ATEM and stable isotope study of carbonates from the Haughton impact crater, Canada, Earth and Planetary Science Letters 121, pp. 559-574.

Martinez, I.; Deutsch, A.; Schärer, U.; Ildephonse, P.; Guyot, F. and Agrinier, P. (1995): Shock recovery experiments on dolomite and thermodynamical modeling of impact induced decarbonatation., Journal of Geophysical Research 100, pp. 15465–15476.

Masaitis, V. L. and Deutsch, A. (1999): Popigai: Gneiss bombs coated with impact melt - Heating in the fireball?, Lunar and Planetary Science Conference XXX, p. #1237 (abstract).

McKay, D. S.; Greenwood, W. R. and Morrison, D. A. (1970): Morphology and related chemistry of small lunar particles from Tranquility Base, Science 167, pp. 654-656.

McKinnon, W. B. (1997): Planetary geology: Extreme cratering, Science 276, pp. 1346-1348.

Melosh, H. J. (1989): Impact cratering: A geologic process, Charnock, H.; Dewey, J.F.; Morris, S. Conway; Navrotsky, A.; Oxburgh, E.R.; Price, R.A. and Skinner, B.J., Eds, Oxford Monographs on Geology and Geophysics 11, Oxford University Press, New York.

Melosh, H. J. (2001): Geophysics: Deep down at Chicxulub, Nature 414, pp. 861-862.

Melosh, H. J.; Artemjeva, N. A.; Golub, A. P; Nemchinov, I. V.; Shuvalov, V. V. and Trubetskaya, I. A. (1993): Remote visual detection of impacts on the lunar surface, Lunar and Planetary Science Conference XXVI, pp. 975-976 (abstract).

Minarik, W. G. (1998): Complications to carbonate melt mobility due to the presence of an immiscible silicate melt, Journal of Petrology 39, pp. 1965-1973.

Montanari, A.; Claeys, P.; Asaro, F.; Bermudez, J. and Smit, J. (1994): Preliminary stratigraphy and iridium and other geochemical anomalies across the KT boundary in the Bochil section (Chiapas, Southeastern Mexico), Papers presented to — New developments regarding the KT event and other catastrophes in Earth history: Lunar and Planetary Contribution 825, pp. 84-85 (abstract).

Moore, J. G. and Peck, D. L. (1962): Accretionary lapill in volcanic rocks of the western continental United States, Journal of Geology 70, pp. 182-193.

Morgan, J. V.; Christeson, G. L. and Zelt, C. A. (2002): Testing the resolution of a 3D velocity tomogram across the Chicxulb crater, Tectonophysics 355, pp. 215-226.

Morgan, J. V.; Warner, M. R.; Collins, G. S.; Melosh, H. J. and Christeson, G. L. (2000): Peak-ring formation in large impact craters: Geophysical constraints from Chicxulub, Earth and Planetary Science Letters 183, pp. 347–354.

Morgan, J. and Warner, M. (1999): Chicxulub; the third dimension of a multi-ring impact basin, Geology 27, pp. 407-410.

Morgan, J.; Warner, M.; Brittan, J.; Buffler, R.; Camargo, A.; Christeson, G.; Dentons, P.; Hildebrand, A.; Hobbs, R.; MacIntyre, H.; Mackenzie, G.; Maguires, P.; Marin, L.; Nakamura, Y.; Pilkington, M.; Sharpton, V. and Snyders, D. (1997): Size and morphology of the Chicxulub impact crater, Nature 390, pp. 472-476.

Moropoulou, A.; Bakolas, A. and Aggelakopoulou, E. (2001): The effects of limestone characteristics and calcination temperature to the reactivity of the quicklime, Cement and Concrete Research 31, pp. 633-639.

Muir, T. L. and Peredery, W. V. (1984): The Onaping Formation, Pye, E.G.; Naldrett, A.J. and Giblin, P.E., The geology and ore deposits of the Sudbury Structure Special Volume 1 pp. 139-210, Ontario Geological Survey, Ontario, Canada.

Neuser, R. D.; Bruhn, F.; Götze, J.; Habermann, D. and Richter, D. K. (1996): Kathodenlumineszenz: Methodik und Anwendung, Zentralblatt Geologie und Paläontologie Teil 1 (1995 1/2), pp. 287-306.

Newsom, H. E.; Graup, G.; Sewards, T. and Keil, K. (1986a): The role of fluidization in the emplacement and alteration of the suevite impact melt deposit at the Ries crater, West Germany, Lunar and Planetary Science Conference XVII, pp. 609-610 (abstract).

Newsom, H. E. and Nelson, M. J. (2004): Major and trace element variations in impact crater clays from Chicxulub, Lonar, and Mistastin, Implications for the Martian soil, Lunar and Planetary Science Conferenc XXXV, p. #1087 (abstract).

Newsom, H.; Graup, G.; Sewards, T. and Keil, K. (1986b): Fluidization and hydrothermal alteration of the suevite deposit at the Ries crater, West Germany, and implications for Mars., Journal of Geophysical Research 91, p. doi: 10.1029/0JGREA000091000B1300E239000001.

Oberbeck, V.R. (1975): The role of ballistic erosion and sedimentation in lunar stratigraphy, Reviews of Geophysics and Space Physics 13, pp. 337-362.

Ocampo, A. C.; Pope, K. O. and Fischer, A.G. (1997a): Carbonate ejecta from the Chicxulub crater: Evidence for ablation and particle interactions under high temperatures and pressures., Lunar and Planetary Science Conference XXVIII, p. #1861 (abstract).

Ocampo, A. C.; Pope, K. O. and Fisher, A. G. (1996): Ejecta blanket deposits of the Chicxulub crater from Albion island, Belize, Ryder, G.; Fastovski, D. and Gartner, S., The Cretaceous-Tertiary event and other catastrophes in Earth history Special Paper 307 pp. 75-88, Geological Society of America, Boulder, Colorado.

Ocampo, A.; Pope, K.; Marshall, J. and Fischer, A. (1997b): Surface textures produced by grain interaction under high temperature: Comparison of Chicxulub ejecta and laboratory experiments, Geological Society of America Annual Meeting, p. #51253 (abstract).

Olsson, R.K.; Miller, K.G.; Browning, J.V.; Habib, D. and Sugarmann, P.J. (1997): Ejecta layer at the Cretaceous-Tertiary boundary, Bass River, New Jersey (Ocean Drilling Program Leg 174AX), Geology 25, pp. 759-762.

Osinski, G. O.; Grieve , R. A. F. and Spray, J. G. (2004): The nature of the groundmass of surficial suevite from the Ries impact structure, Germany, and constraints on its origin, Meteoritics & Planetary Science 39, pp. 1655–1683.

Osinski, G. O.; Lee, P.; Spray, J. G. and Parnell, D. (2005b): Geological overview and cratering model for the Haughton impact structure, Devon Island, Canadian High Arctic, Meteoritics & Planetary Science 40, pp. 1759-1776.

Osinski, G. O.; Spray, J. G. and Lee, P. (2005a): Impactites of the Haughton impact structure, Devon Island, Canadian High Arctic, Meteoritcs & Planetary Science 40, pp. 1789-1812.

Osinski, G. R. and Spray, J. G. (2003b): Evidence for the shock melting of sulfates from the Haughton impact structure, Arctic Canada, Earth and Planetary Science Letters 215, pp. 357-370.

Osinski, G. R. and Spray, J. G. (2001): Impact-generated carbonate melts: Evidence from the Haughton structure, Canada, Earth and Planetary Science Letters 194, pp. 17-29.

Osinski, G. R.; Spray, J. G. and Grieve, R. A. F. (2003a): Impact melting in sedimentary target rocks?, Herrick, R. and Pierrazzo, E., Impact cratering; bridging the gap between modeling and observations p. 59 (abstract), Lunar and Planetary Institute, Houston, Texas.

Pedroni, A. (1991): Accretionary lapilli and other sedimentary textures of the Howardite Kapoeta, Lunar and Planetary Science Conference XXII, pp. 1045-1046 (abstract).

Peucker-Ehrenbrink, B. and Jahn, B. (2001): Rhenium-osmium isotope systematics and platinum group element concentrations: Loess and the upper continental crust, Geochemistry, Geophysics, Geosystems 2, p. # 2001GC000172.

Pierazzo, E and Melosh, H. J. (2000): Understanding oblique impacts from experiments, observations, and modelling, Annual Review of Earth and Planetary Sciences 28, pp. 141-167.

Pierazzo , E.; Hahmann, A. N. and Sloan, L. C. (2003): Chicxulub and Climate: Radiative Perturbations of Impact-Produced S-Bearing Gases, Astrobiology 3, pp. 99-118.

Pierazzo, E.; Kring, D. A. and Melosh, H. J. (1998): Hydrocode simulation of the Chicxulub impact event and the production of climatically active gases, Journal of Geophysical Research 103, pp. 28607-28625.

Pierazzo, E. and Melosh, H. J. (1999): Hydrocode modeling of Chicxulub as an oblique impact event, Earth and Planetary Scienes Letters 165, pp. 163-176.

Pope, K. O.; Baines, H. K.; Ocampo, A. C. and Ivanov, B. (1997): Energy, volatile production, and climate effects of the Chicxulub Cretaceous/Tertiary boundary impact, Journal of Geophysical Research 102, pp. 21645-21664.

Pope, K. O.; Ocampo, A. C.; Fischer, A. G.; Vega, F. J.; Ames, D. E.; King, D. T.; Fouke, B. W.; Wachtmann, R. J. and Kletetschka, G. (2005): Chicxulub impact ejecta in southern Quintana Roo, México and central Belize, Kenkmann, T.; Hörz, F. and Deutsch, A., Large meteorite impacts III Special Paper 384 pp. 171-190, Geological Society of America, Boulder, Colorado.

Pope, K. O.; Ocampo, A. C.; Fisher, A. G.; Alvarez, W.; Fouke, B. W.; Webster, C. L.; Vega, F. J.; Smit, J.; Fritsche, A. E. and Claeys, P. (1999): Chicxulub impact ejecta from Albion Island, Belize, Earth and Planetary Science Letters 170, pp. 351-364.

Pszczolkowski, A. (1986): Megacapas del Maestrichtiano en Cuba occidental y central, Bulletin of the Polish Academy of Sciences. Earth Science 34, pp. 81–94.

Puchelt, H. (1972): Barium, Springer, Handbook of geochemistry 56D pp. 1-16, Wedepohl, K.H., Berlin.

Pusch, R. and Karnland, O. (1988): Geological Evidence of Smectite Longevity. The Sardinian and Gotland Cases, SKB Technical Report 88-26, Stockholm, Sweden.

Pusch, R.; Karnland, O.; Hökmark, H.; Sandén, T. and Börgesson, L. (1991): Final report of the rock sealing project- Sealing properties and longevity of smectitic clay grouts, Stripa Project Technical Report 91-30, SKB, Stockholm, Sweden.

Pusch, R.; Karnland, O.; Lajudie, A.; Lechelle, J. and Bouchet, A. (1993): Hydrothermal field test with french candidate clay embedding steel heater in the Stripa Mine, SKB Technical Report 93-02, Stockholm, Sweden.

Pusch, Roland (2000): On the effect of hot water vapor an MX-80 clay p. 41, SKB Technical Report 00-16, Stockholm, Sweden.

Radke, B. M. and Mathis, R. L. (1980): On the formation and occurence of saddle dolomite, Journal of Sedimentary Petrology 50, pp. 1149-1168.

Rankin, A. H. and Le Bas, M. J. (1974): Liquid immiscibility between silicate and carbonate melts in naturally occurring ijolite magma, Nature 250, pp. 206 –209.

Reiss, D.; Hauber, E.; Michael, G.; Jaumann, R.; Neukum, G. and Team, HRSC Co-Investigator (2005): Small rampart craters in an equatorial region on Mars: Implications for near-surface water or ice, Geopysical Research Letters 32, p. L10202.

Remane, J.; Keller, G.; Hardenbol, J. and Ben Haj Ali, M. (1999): International workshop on Cretaceous-Paleogene transitions in Tunisia: The El Kef stratotype for the Cretaceous-Paleogene boundary reconfirmed, Episodes 22, pp. 47-48.

Richardson, K. A.; McKay, D. S.; Greenwood, W. R. and Foss, T. H. (1970): Alpha-particle activity of Apollo 11 samples, Science 167, pp. 516-517.

Riley, T. R. and Leat, P. T. (1999): Large volume silicic volcanism along the proto-Pacific margin of Gondwana: Lithological and stratigraphical investigations from the Antarctic Peninsula, Geological Magazine 136, pp. 1-16.

Robertson, D. S; McKenna, M. C; Toon, O. B.; Hope, S. and Lillegraven, J. A. (2004): Survival in the first hours of the Cenozoic, Geological Society of America Bulletin 116, pp. 760–768.

Rosatelli, G; Wall, F. and Le Bas, M. J. (2003): Potassic glass and calcite carbonatite in lapilli from extrusive carbonatites at Rangwa caldera complex, Kenya, Mineralogical Magazine 67, pp. 931-955.

Rose, W. I.; Delene, D. J.; Schneider, D. J.; Bluth, G. J. S.; Krueger, A. J.; Sprod, I.; McKee, C.; Davies, H. L. and Ernst, G. G. J. (1995): Ice in the 1994 Rabaul eruption cloud: implications for volcano hazard and atmospheric effects, Nature 375, pp. 477-479.

Schmitt, R. T.; Wittmann, A. and Stöffler, D. (2004): Geochemistry of drill core samples from Yaxcopoil-1 Chicxulub impact crater, Mexico, Meteoritics & Planetary Science 39, pp. 979-1001.

Schönian, F.; Salge, T.; Kenkmann, T.; Stöffler, D.; Arechald, A. M. Soler and Urrutia-Fucugauchi, J. (2006): Chicxulub ejecta blanket: the suevites of the UNAM 5 and 7 drill cores., Lunar and Planetary Science Conference XXXVII, p. #2229 (abstract).

Schönian, F.; Salge, T.; Stöffler, D. and Urrutia-Fucugauchi, J. (2003): Additional observations on the impact breccias of the Chicxulub ejecta blanket from the UNAM-7 drill core, Yucatán, Mexico., Third International Conference on Large Meteorite Impacts LPI Contribution No. 1167 p. #4132 (abstract), Lunar and Planetary Institute, Nördlingen, Germany.

Schulte, P. and Kontny, A. (2005): Chicxulub impact ejecta from the Cretaceous-Paleogene (K-P) boundary in northeastern México, Kenkmann, T.; Hörz, F. and Deutsch, A., Large meteorite impacts III Special Paper 384 pp. 191–221, Geological Society of America, Boulder, Colorado.

Schulte, P.; Stinnesbeck, W.; Stüben, D.; Kramar, U.; Berner, Z.; Keller, G. and Adatte, T. (2003): Fe-rich and K-rich mafic spherules from slumped and channelized Chicxulub ejecta deposits in the northern La Sierrita area, NE Mexico, International Journal of Earth Sciences 92, pp. 114-142.

Schultz, P. H. (1992): Atmospheric effects on ejecta emplacement, Journal of Geophysical Research 97, pp. 11623-11662.

Schumacher, R. and Schmincke, H.U. (1995): Models for the origin of accretionary lapilli, Bulletin of Volcanology 56, pp. 626-639.

Schuraytz, B. C.; Sharpton , V. L. and Marín, L. (1994): Petrology of impact-melt rocks at the Chicxulub multiring basin, Yucatan, Mexico, Geology 22, pp. 868-872.

Sharpton, V. L.; Corrigan, C. M.; Marin, L. E.; Urrutia-Fucugauchi, J. and Vogel, T. A. (1999): Characterization of impact breccias from the Chicxulub impact basin: Implications for excavation and ejecta emplacement, Lunar and Planetary Science Conference XXX, p. #1515 (abstract).

Sharpton, V. L.; Marin, L. E.; Carney, J. L.; Lee, S.; Ryder, G.; Schuraytz, B. C.; Sikora, P. and Spudis, P. D. (1996): A model of the Chicxulub impact bassin based on evaluation of geophysical data, well logs and drill core samples, Ryder, G.; Fastovski, D. and Gartner, S., The Cretaceous-Tertiary Event and Other Catastrophes in Earth History Special Paper 307 pp. 55-74, Geological Society of America, Boulder, Colorado.

Sharpton, Virgil L.; Burke, K.; Camargo-Zanoguera, A.; Hall, Stuart A.; Lee, D. Scott; Marin, Luis E.; Suarez-Reynoso, G.; Quezada-Muneton, J. M.; Spudis, P. D. and Urrutia-Fucugauchi, J. (1993): Chicxulub multiring impact basin: Size and other characteristics derived from gravity analysis, Science 261, pp. 1564-1567.

Sigurdsson, H.; D'Hondt, S. and Carey, S. (1995): Geochemistry of the Cretaceous/Tertiary impact ejecta deposit in Mexico and Belize, Lunar and Planetary Science Conference XXII, pp. 1301-1302 (abstract).

Skála, R; Ederová, J; Matjka, P. and Hörz, F. (2002): Mineralogical investigations of experimentally shocked dolomite: Implications for the outgassing of carbonates, Koeberl, C. and MacLeod, K. G., Catastrophic events and mass extinctions: Impacts and beyond Special Paper 356 pp. 571–585, Geological Society of America, Boulder, Colorado.

Skála, R.; Hörz, F. P. and Langenhorst, F. (2005): Experimentally shock-loaded anhydrite: Unit-cell dimensions, microstrain and domain size from X-ray powder diffraction, Kenkmann, T.; Hörz, F. and Deutsch, A., Large meteorite impacts III Special Paper 384 pp. 413-425, Geological Society of America, Boulder, Colorado.

Smit, J. (1999): The global stratigraphy of the Cretaceous-Tertiary boundary impact ejecta, Annual Review of Earth and Planetary Sciences 27, pp. 75–113.

Smit, J.; van der Gaast, S. and Lustenhouwer, W. (2004): Is the transition impact to post-impact rock complete? Some remarks based on XRF scanning, electron microprobe, and thin section analyses of the Yaxcopoil-1 core in the Chicxulub crater, Meteoritcs & Planetary Science 39, pp. 1113–1126.

Smit, Jan; Roep, T. B.; Alvarez, Walter; Montanari, Alessandro; Claeys, Philippe; Grajales Nishimura, J. M. and Bermudez, J. (1996): Coarse-grained, clastic sandstone complex at the KT boundary around the Gulf of Mexico: Deposition by tsunami waves induced by the Chicxulub impact, Ryder, G.; Fastovsky, D. and Gartner, S., The Cretaceous-Tertairy event and other catastrophes in Earth history Special Paper 307 pp. 151-182, Geological Society of America, Boulder, Colorado.

Sparks, R. S. J.; Bursik, M. I. ; Carey, S. N.; Gilbert, J. S.; Glaze, L. S.; Sigurdsson, H. and Woods, A. W. (1997): Volcanic Plumes, John Wiley & Sons, New York, ISBN: 0-471-93901-3.

Squyres, S. W.; Grotzinger, J. P.; Arvidson, R. E.; Bell, J. F.; Calvin, W.; Christensen, P. R.; Clark, B. C.; Crisp, J. A.; Farrand, W. H.; Herkenhoff, K. E.; Johnson, J. R.; Klingelhöfer, G.; Knoll, A. H.; McLennan, S. M.; H. Y. McSween, Jr.; Morris, R. V.; J. W. Rice, Jr.; Rieder, R. and Soderblom, L. A. (2004): In situ evidence for an ancient aqueous environment at Meridiani Planum, Mars, Science 306, pp. 1709 - 1714.

St. John, D. A.; Poole, A. B. and Sims, I. (1998): Concrete petrography: A handbook of investigative techniques, Arnold, London, Sydney, Auckland.

Stevenson, D. J. (1987): Origin of the Moon. The collision hypothesis, Annual Reviews Earth Planetary Science 15, pp. 271-315.

Stinnesbeck, W.; Keller, G.; Adatte, T.; Harting, M.; Stüben, D.; Istrate, G. and Kramar, U. (2004): Yaxcopoil-1 and the Chicxulub impact, International Journal of Earth Sciences 93, pp. 1042-1065.

Stöffler, D. (1971): Progressive metamorphism and classification of shocked and brecciated crystalline rocks at impact craters, Journal of Geophysical Research 76, pp. 5541–5551.

Stöffler, D.; Artemieva, N. A.; Ivanov, B. A.; Hecht, L.; Kenkmann, T.; Schmitt, R. T.; Tagle, R. A and Wittmann, A. (2004): Origin and emplacement of the impact formations at Chicxulub, Mexico, as revealed by the ICDP deep drilling at Yaxcopoil-1 and by numerical modeling, Meteoritcs & Planetary Science 39, pp. 1035–1067.

Stöffler, D.; Gault, D. E.; Wedekind, J. and Polowski, G. (1975): Experimental hypervelocity impact into quartz sand: Distribution and shock metamorphism of ejecta, Journal of Geophysical Research 80, pp. 4062-4077.

Stöffler, D. and Grieve, R. A. F. (1996): IUGS classification and nomenclature of impact metamorphic rocks: Towards a final proposal, International symposium on the role of impact processes in the geological and biological evolution of planet Earth p. (abstract), Postojna, Slovenia.

Stöffler, D. and Ryder, G. (2001): Stratigraphy and isotope ages of Lunar geologic units: Chronological standard for the inner solar system, Space Science Reviews 96, pp. 9-54.

Stoppa, F.; Woolley, A. R.; Lloyd, F. E. and Eby, N. (2000): Carbonatite lapilli-bearing tuff and a dolomite carbonatite bomb from Murumuli crater, Katwe volcanic field, Uganda, Mineralogical Magazine 64, pp. 641-650.

Stosnach, H. (2005): Trace element analysis using a benchtop total X-ray fluorescence spectrometer, Powder Diffraction 20, pp. 141-145.

Swisher, C. C., III; Grajales-Nishimura, J. M.; Montanari, A.; Margolis, S. V.; Claeys, P.; Alvarez, W.; Renne, P.; Cedillo-Pardo, E.; Maurrasse, F. J.-M. R.; Curtis, G. H.; Smit, J. and McWilliams, M. O. (1992): Coeval ^{40}Ar/^{39}Ar ages of 65.0 million years ago from Chicxulub crater melt rock and Cretaceous-Tertiary boundary tektites, Science 257, pp. 954-958.

Tagle, R.; Erzinger, J.; Hecht, L.; Schmitt, R. T.; Stöffler, D. and Claeys, P. (2004): Platinum group elements in impactites of the ICDP Chicxulub drill core Yaxcopoil-1: Are there traces of the projectile?, Meteoritcs & Planetary Science 39, pp. 1009-1016.

Takayama, H.; Tada, R.; Matsui, T.; Iturralde-Vinent, M. A.; Oji, T.; Tajika, E.; Kiyokawa, S.; Garcia, D.; Okada, H.; Hasegawa, T. and Toyoda, K. (2000): Origin of the Peñalver formation in northwestern Cuba and its relation to K/T boundary impact event, Sedimentary Geology 135, pp. 295–320.

Tuchscherer, M. G.; Reimold, W. U.; Koeberl, C. and Gibson, R. L. (2004b): Major and trace element characteristics of impactites from the Yaxcopoil-1 borehole, Chicxulub structure, Mexico, Meteoritics & Planetary Science 39, pp. 955-978.

Tuchscherer, M. G.; Reimold, W. U.; Koeberl, C.; Gibson, R. L. and Bruin, D. de (2004a): First petrographic results on impactites from the Yaxcopoil-1 borehole, Chicxulub structure, Mexico, Meteoritics & Planetary Science 39, pp. 899–930.

Tuchscherer, M.G.; Reimold, W. U.; Koeberl, C. and Gibson, R. L. (2005): Geochemical and petrographic characteristics of impactites and Cretaceous target rocks form the Yaxcopoil-1 borehole, Chicxulub impact structure, Mexico: Implications for target compositions, Meteoritcs & Planetary Science 40, pp. 1513-1536.

Tyburczy, J. A. and Ahrens, T. J. (1986): Dynamic compression and volatile release of carbonates, Journal of Geophysical Research 91, pp. 4730-4744.

Urrutia-Fucugauchi, J.; Marin, L. and Trejo-Garcia, A. (1996a): UNAM Scientific drilling program of Chicxulub impact structure - Evidence for a 300 kilometer crater diameter, Geophysical Research Letters 23, pp. 1565-1568.

Urrutia-Fucugauchi, J.; Marín, L. and Trejo-García, A. (1996b): Initial results of the UNAM scientific drilling program on the Chicxulub impact structure: rock magnetic properties of UNAM-7 Tekax borehole, Geofisica Internacional 35, pp. 125-133.

Veitch, G. and Woods, A. W. (2001): Particle aggregation in volcanic eruption columns, Journal of Geophysical Research 106, pp. 26405-26442.

Wali, A. (1985): Abkühlung der Suevite im Nördlinger Ries, Diploma thesis, Universität Tübingen.

Warme, J. E.; Morgan, M. and Kuehner, H.-C. (2002): Impact-generated carbonate accretionary lapilli in the Late Devonian Alamo Breccia, Koerberl, C. and MacLeod, K. G., Catastrophic Events and Mass Extinctions Impacts and Beyond Special Paper 356 pp. 489-504, Geological Society of America, Boulder, Colorado.

Wasson, J. T. and Kallemeyn, G. W. (1988): Compositin of chondrites, Philosophical Transactions of the Royal Society of London. Series A, Mathematical and Physical Sciences 235, pp. 535-544.

Wedepohl, K. H. (1995): The composition of the continental crust, Geochimica et Cosmochimica Acta 59, pp. 1217-1232.

Wittmann, A.; Kenkmann, T.; Schmitt, R. T.; Hecht, L. and Stöffler, D. (2004): Impact related breccia lithologies in the ICDP drill core Yaxcopoil-1, Chicxulub impact structure, Mexico, Meteoritcs & Planetary Science 39, pp. 931-954.

Witzke, B. J. and Anderson, R. R. (1996): Sedimentary-clast breccias of the Manson impact structure, Koeberl, C. and Anderson, R.R., The Manson impact structure, Iowa: Anatomy of an impact crater 302 pp. Special Paper 115–144, Geological Society of America, Boulder, Colorado.

Wohletz, K. H. and Sheridan, M. F. (1983): Martian rampart crater ejecta: Experiments and analysis of melt-water interaction, Icarus 56, pp. 15-37.

Zürcher, L. and Kring, D. A. (2004): Hydrothermal alteration in the core of the Yaxcopoil-1 borhole, Chicxulub impact strucure, Mexico, Meteoritcs & Planetary Science 39, pp. 1199–1221.

APPENDIX

A1 Additional images

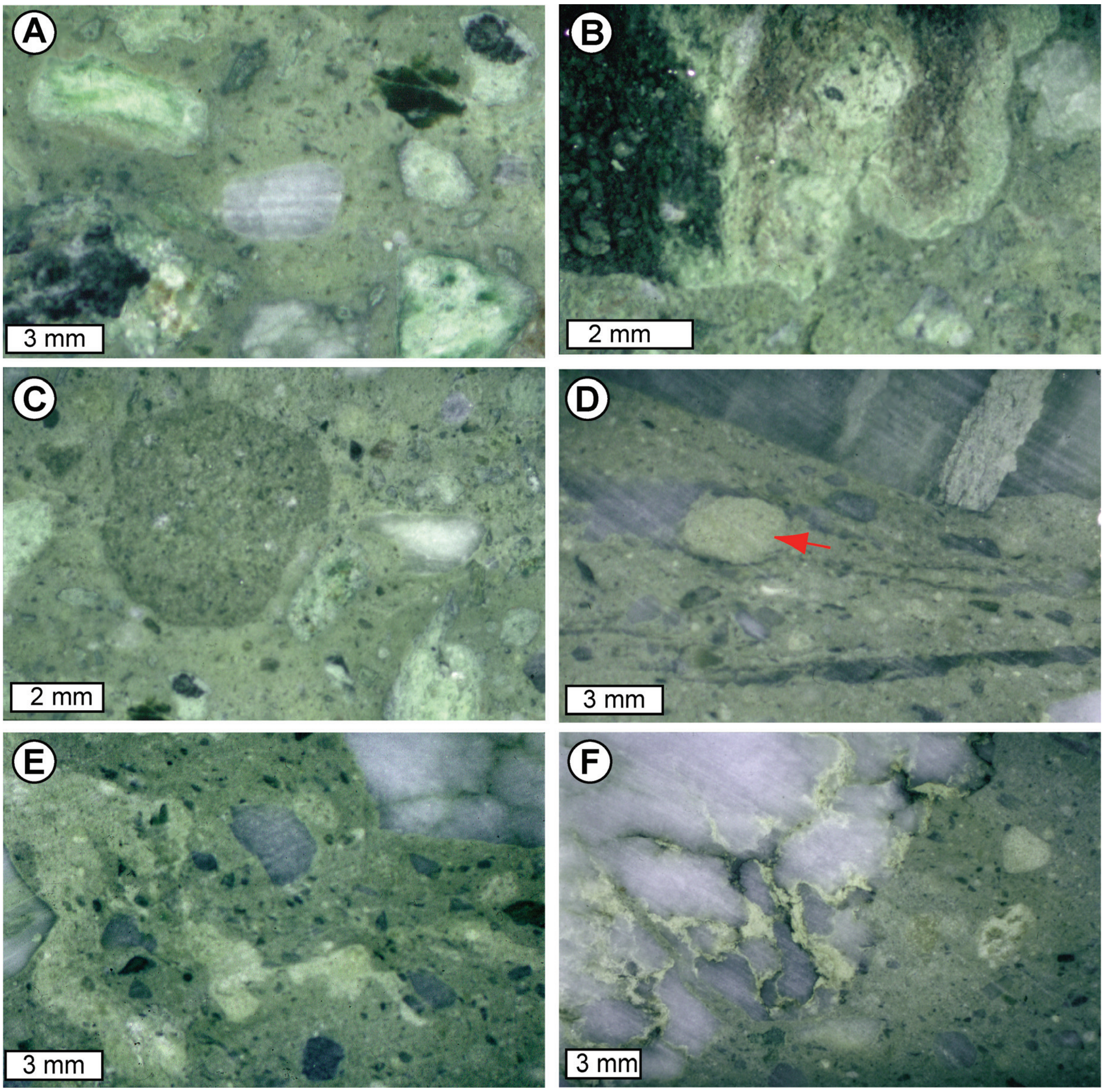

Figure A1-1 UNAM-7 binocular micrographs. (A–C): Sample UNAM-7-307.85, (D–F): SampleUNAM-7-381.40. **(A)** Evaporite particles (grey) in a fine grained carbonate matrix with light green altered melt particles often hosting a core of dark green silicate melt. **(B)** Heterogeneous amoeboid textured melt particle with dark green, light green and grey brown areas. **(C)** Porous, grey brown carbonate particle (presumable carbonate melt), light green and dark green melt particles and anhydrite particles (grey) in a fine grained matrix. **(D)** Anhydrite veins and schlieren interfering with calcite particle (arrow) (compare with Fig. 3-27B) and stratified anhydrite clast at upper margin. **(E)** Light grey carbonate schlieren (compare with Fig. 3-27A). **(F)** Evaporite particle with intercalations of (vesicle-rich) calcite (compare with Fig. 3-27C).

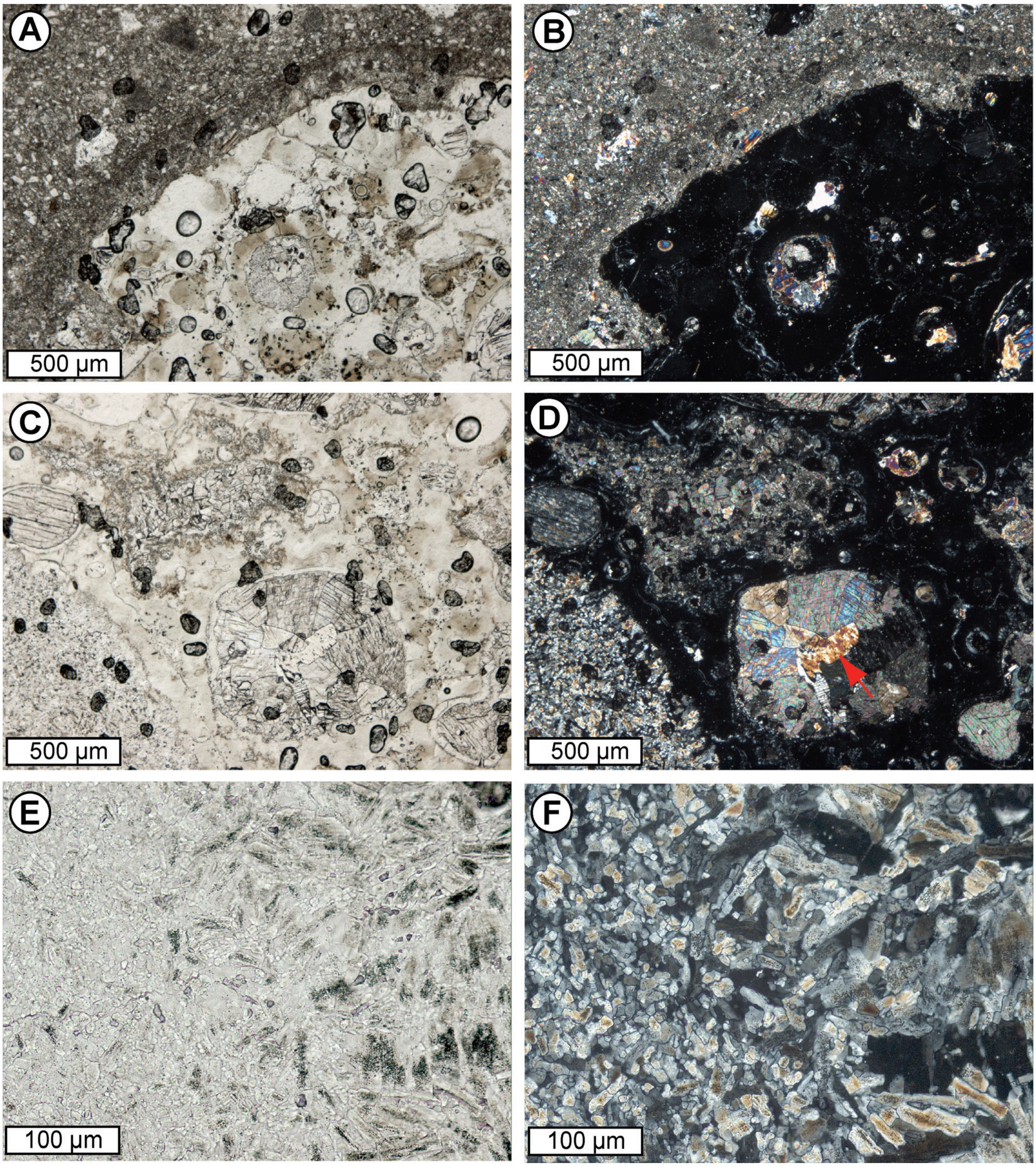

Figure A1-2 Paired micrographs (left: PPL, right XPL) of rare silicate melt particle with carbonate and sulphate inclusions of sample UNAM-7-381.40 (compare with Fig. 3-26C). **(A, B)** The silicate melt particle has a reaction rim in contact with the carbonate matrix. Note the tangential alignment of euhedral anhydrite towards the rim of the melt particle. **(C, D)** Carbonate melt inclusions showing variations in crystal texture. The large rounded inclusion contains coarse sparitic calcite and anhydrite (arrow, confirmed by CL studies). The inclusion left above shows a crystallisation sequence with coarse sparitic crystals in the centre and microcrystalline calcite, where the inclusions thins out. Note the dumbbell shape of the carbonate inclusion in lower right corner. The inclusion at lower left corner consists of anhydrite. **(E, F)** Crystallisation sequence of anhydrite core showing abundant degassing vesicles in large columnar crystals which are missing at smaller subhedral to interlobate crystals indicative for partial melting and partial decomposition (compare with Fig. 3-26D). PPL: plane polarised light; XPL: cross polarised light.

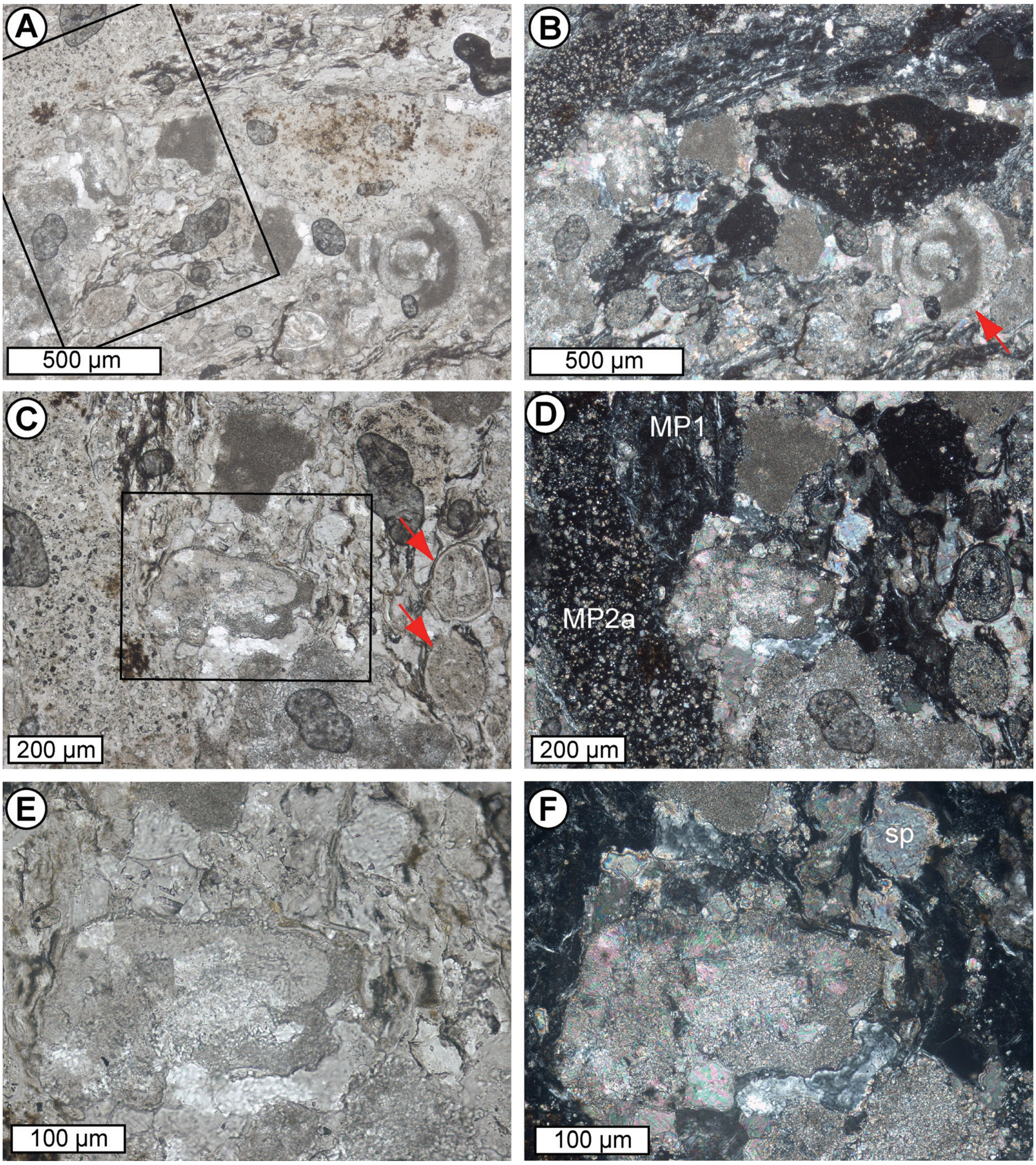

Figure A1-3 Paired micrographs (left: PPL, right: XPL) of the upper microbreccia showing carbonate and silicate ejecta particles (sample Ir11). **(A, B)** Overview showing different melt particles, carbonate particles and foraminifera fragment (arrow). **(C, D)** Close up of (A). Note the oval melt particles (arrows), (MP1: flow textured melt particles type 1, MP2a: melt particle 2a containing voids and microcrystalline calcite). **(E, F)** Close up of (C) showing calcite particle with a spherulitic and needle-like texture grading into microcrystalline calcite. Most calcite particles are microcrystalline, but sparitic calcite occurs in between particles and vesicles of silicate melt particles (sp). PPL: plane polarised light; XPL: cross polarised light.

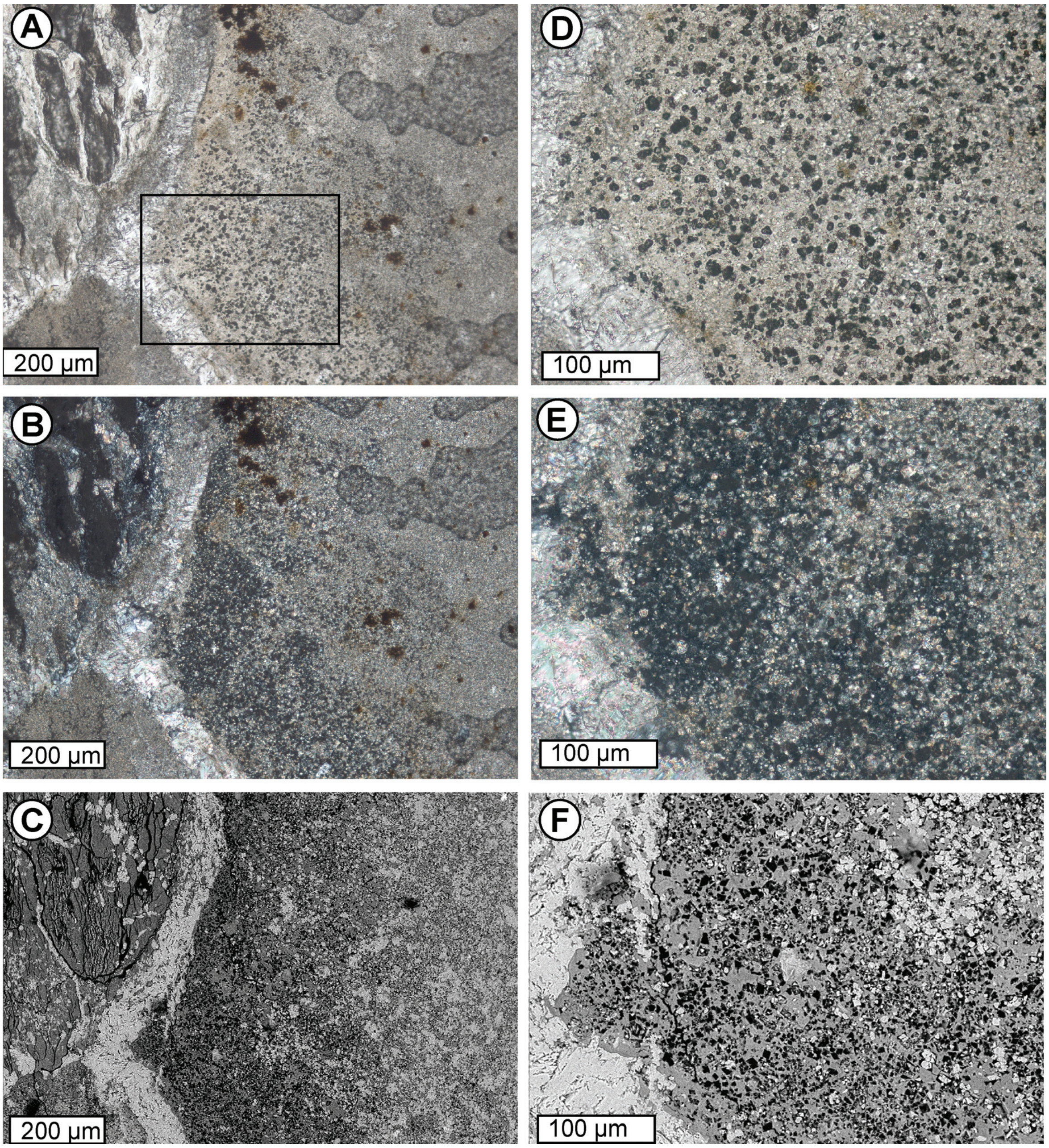

Figure A1-4 Paired micrographs of the transition zone of a carbonate ejecta particle (1x2 cm) with a rim of altered silicate melt from the lowermost accretionary lapilli unit. (A, D): PPL, (B, E): XPL, (C, F): BSE. (D–F) is the close up of (A). The carbonate particle consists of recrystallised microcrystalline calcite which is progressively replaced by altered silicate melt towards the rim. There, the altered silicate melt is vesicle-rich, contains varying amounts of microcrystalline calcite and resembles melt particles type 2. Note the different textured melt particle type 1 in upper left corner at (A–C). Bubbles in (A, B) are artefacts from preparation.

A2 Chemical analyses

A2.1 XRF analyses

Table A2-1 XRF analyses of El Guayal bulk rock and accretionary lapilli.

Sample	G4	G5	G5	G5	G6	G6	G6	G7	G7	G7	G8	G8	G8
No.	1	1	2a	2b	1	2a	2b	1	2a	2b	1	2a	2b
Unit[1]	uMB	uMB	uMB	uMB	lμB	lμB	lμB	mμB	mμB	mμB	uμB	uμB	uμB
(wt.%)													
SiO_2	3.6	5.1	4.5	4.8	11.6	11.6	11.7	13.9	14.2	14.0	20.3	20.2	20.4
TiO_2	0.05	0.07	0.06	0.07	0.13	0.13	0.12	0.13	0.14	0.14	0.19	0.18	0.18
Al_2O_3	1.1	1.7	1.4	1.5	2.9	2.8	2.9	3.1	3.4	3.4	4.7	4.4	4.5
Fe_2O_3[2]	0.31	0.45	0.45	0.50	0.99	0.98	0.99	1.21	1.31	1.28	2.02	1.97	1.99
MnO	0.02	0.02	0.02	0.02	0.03	0.03	0.03	0.03	0.05	0.05	0.08	0.06	0.06
MgO	4.93	4.56	4.02	3.99	4.33	4.73	4.73	4.67	4.85	4.82	5.48	5.52	5.58
CaO	47.3	46.5	47.5	47.0	43.2	42.7	42.2	41.2	40.5	40.7	35.7	35.8	36.0
Na_2O	0.03	<0.02	0.04	<0.02	<0.02	<0.02	0.03	<0.02	<0.02	<0.02	<0.02	<0.02	<0.02
K_2O	0.12	0.25	0.22	0.23	0.3	0.28	0.28	0.24	0.28	0.27	0.39	0.35	0.35
P_2O_5	0.02	0.02	0.02	0.02	0.01	0.02	0.02	0.02	0.02	0.02	0.01	0.02	0.02
SO_3	0.1	0.1	0.1	0.1	0.1	0.1	0.1	0.1	0.1	0.1	0.1	0.1	0.2
LOI	42.3	41.0	41.6	41.6	36.4	36.7	36.7	35.2	35.1	35.1	30.7	30.9	30.8
Total	100.0	99.8	99.9	99.8	100.0	100.1	99.8	99.8	100.0	99.9	99.7	99.5	100.1
CO_2	42.3	40.9	n.d.	n.d.	35.2	n.d.	n.d.	33.3	n.d.	n.d.	27.9	n.d.	n.d.
(μg/g)													
Ba	<30	31	<30	<30	<30	43	51	<30	35	36	<30	36	51
Ce	<30	<30	<30	<30	<30	<30	<30	<30	<30	<30	<30	<30	<30
Co	<15	<15	<15	<15	<15	15	15	<15	<15	<15	18	16	<15
Cr	15	15	<15	15	19	18	17	22	21	22	26	21	22
Cu	<30	<30	<30	<30	<30	<30	<30	<30	<30	<30	<30	<30	<30
Mo	<10	<10	10	11	<10	<10	<10	<10	<10	<10	<10	<10	<10
Nb	<10	<10	<10	<10	<10	<10	<10	<10	<10	<10	<10	<10	<10
Ni	<15	<15	<15	<15	<15	<15	<15	<15	<15	<15	<15	<15	<15
Pb	<15	<15	<15	<15	<15	<15	<15	<15	<15	<15	<15	<15	<15
Rb	<15	<15	<15	<15	<15	<15	<15	<15	<15	<15	<15	<15	<15
Sr	347	334	331	331	318	314	318	312	308	310	271	263	265
Th	<10	<10	<10	<10	<10	<10	<10	<10	<10	<10	<10	<10	<10
U	<10	<10	<10	<10	<10	<10	<10	<10	<10	<10	<10	<10	<10
V	30	35	33	32	34	39	42	38	42	45	47	53	50
Y	<10	<10	<10	<10	<10	<10	<10	<10	<10	<10	<10	<10	<10
Zn	<30	<30	<30	<30	<30	<30	<30	<30	<30	<30	<30	<30	<30
Zr	30	31	31	31	38	37	38	38	40	40	45	43	44

[1] MB: megabreccia; μB: microbreccia (affix shows the stratigraphic level, l: lower; m: middle; u: upper); [2] Total Fe calculated as Fe_2O_3. No. 1 corresponds to samples grinded in a metal mortar and No. 2 in a corundum mortar; n.d.: not determined.

Table A2-1 continued.

Sample	G9	G9	G9	G10	G10	G10	G11	G11	G11	G12	G12	G12
No.	1	2a	2b	1	2a	2b	1	2a	2b	1	2a	2b
Unit[1]	lALU	lALU	lALU	lALU	lALU	lALU	mALU	mALU	mALU	mALU	mALU	mALU
(wt.%)												
SiO_2	19.0	22.6	22.7	20.6	24.1	23.8	23.5	24.1	24.3	30.0	31.7	31.2
TiO_2	0.19	0.27	0.27	0.21	0.29	0.29	0.20	0.21	0.21	0.30	0.32	0.31
Al_2O_3	4.7	6.4	6.5	5.3	6.9	6.9	5.3	5.4	5.5	7.9	8.4	8.3
Fe_2O_3[2]	1.93	2.56	2.63	2.14	2.81	2.83	2.49	2.63	2.51	3.15	3.33	3.27
MnO	0.06	0.06	0.06	0.04	0.05	0.05	0.05	0.05	0.05	0.05	0.05	0.05
MgO	4.82	6.20	6.24	5.63	7.05	7.12	5.14	5.07	5.06	5.42	5.53	5.48
CaO	36.5	32.1	31.6	35.1	30.1	29.7	33.7	32.7	32.5	27.6	25.2	25.2
Na_2O	<0.02	<0.02	0.03	0.02	0.02	0.02	<0.02	<0.02	<0.02	<0.02	<0.02	0.03
K_2O	0.49	0.65	0.66	0.51	0.66	0.66	0.39	0.41	0.43	0.73	0.81	0.80
P_2O_5	0.03	0.04	0.04	0.01	0.02	0.03	0.03	0.03	0.04	0.07	0.07	0.06
SO_3	0.1	<0.10	0.1	0.1	0.1	0.2	0.1	0.1	0.1	0.1	<0.10	<0.10
LOI	31.6	28.8	28.9	30.1	27.6	28	28.8	28.9	28.8	24.4	24.4	25.0
Total	99.4	99.7	99.7	99.8	99.7	99.6	99.7	99.6	99.5	99.8	99.8	99.7
CO_2	28.4	n.d.	n.d.	26.3	n.d.	n.d.	25.7	n.d.	n.d.	20.1	n.d.	n.d.
(μg/g)												
Ba	133	157	146	128	190	179	100	135	115	118	174	168
Ce	<30	<30	<30	<30	<30	<30	<30	<30	<30	<30	<30	<30
Co	<15	18	18	17	18	17	<15	<15	15	17	20	17
Cr	23	32	30	26	42	42	24	29	31	28	46	46
Cu	<30	<30	<30	<30	<30	<30	<30	<30	<30	<30	<30	<30
Mo	<10	<10	<10	<10	<10	<10	<10	<10	<10	<10	<10	<10
Nb	<10	<10	<10	<10	<10	<10	<10	<10	<10	<10	<10	<10
Ni	<15	<15	<15	<15	<15	<15	<15	<15	<15	<15	<15	<15
Pb	<15	<15	<15	<15	<15	<15	<15	<15	<15	<15	<15	<15
Rb	19	<15	<15	<15	<15	<15	<15	<15	<15	17	26	17
Sr	283	241	239	287	226	230	210	209	213	165	153	157
Th	<10	<10	<10	<10	12	11	<10	<10	<10	<10	<10	<10
U	<10	<10	<10	<10	<10	<10	<10	<10	<10	<10	<10	<10
V	47	58	58	48	63	60	50	51	54	62	78	74
Y	<10	<10	<10	<10	<10	<10	<10	<10	<10	<10	<10	<10
Zn	<30	<30	<30	<30	<30	<30	<30	<30	<30	35	32	33
Zr	45	55	55	49	62	60	47	49	50	58	65	65

[1]ALU: accretionary lapilli unit (affix shows the stratigraphic level, l: lower, m: middle); [2]Total Fe calculated as Fe_2O_3. No. 1 corresponds to samples grinded in a metal mortar, No. 2 in a corundum mortar.

Table A2-1 continued.

Sample	G14	G14	14	G13	G13	G13	G15	G15	G15	G9L	G10L
No.	1	2a	2b	1	2a	2b	1	2a	2b	1	1
Unit[1]	uALU	uALU	uALU	uALU	uALU	uALU	CU	CU	CU	AcL	AcL
(wt.%)											
SiO_2	41.7	42.8	42.7	36.5	39.8	39.3	55.1	51.5	52.1	71.3	70.4
TiO_2	0.35	0.34	0.33	0.33	0.29	0.28	0.34	0.31	0.31	0.18	0.20
Al_2O_3	11.4	11.7	11.7	9.5	10.5	10.4	10.1	10.3	10.3	3.3	3.5
Fe_2O_3[2]	4.58	4.98	4.90	3.89	5.16	5.20	4.62	4.92	4.99	1.18	1.10
MnO	0.07	0.08	0.07	0.03	0.05	0.05	0.14	0.1	0.1	0.03	0.03
MgO	7.22	7.57	7.48	6.42	6.54	6.54	5.84	5.76	5.78	4.63	4.94
CaO	17.0	14.4	14.3	21.8	17.9	17.9	11.5	12.9	12.4	8.4	8.4
Na_2O	0.04	0.03	<0.02	<0.02	0.03	0.06	0.05	0.11	0.11	<0.01	<0.01
K_2O	0.96	0.97	0.95	0.91	1.01	1.02	1.07	1.33	1.35	0.28	0.31
P_2O_5	0.06	0.06	0.06	0.04	0.05	0.05	0.06	0.08	0.08	0.07	0.05
SO_3	<0.10	<0.10	<0.10	<0.10	<0.10	<0.10	<0.10	<0.10	<0.10	<0.10	<0.10
LOI	16.3	16.2	17.0	20.0	18.4	18.8	10.6	12.2	12.1	10.1	10.5
Total	99.7	99.1	99.5	99.4	99.7	99.6	99.4	99.5	99.6	99.5	99.4
CO_2	10.5	n.d.	n.d.	14.9	n.d.	n.d.	5.5	n.d.	n.d.	7.8	7.5
(μg/g)											
Ba	165	167	168	119	171	173	197	203	230	141	134
Ce	<30	<30	<30	<30	<30	<30	<30	<30	37	34	31
Co	18	23	23	19	26	24	33	23	22	<15	<15
Cr	50	46	50	41	45	45	61	58	63	27	30
Cu	<30	<30	<30	<30	<30	<30	<30	<30	<30	<30	<30
Mo	<10	<10	<10	<10	<10	<10	<10	<10	<10	<10	<10
Nb	<10	<10	<10	<10	<10	<10	<10	<10	<10	10	10
Ni	<15	16	16	<15	19	17	40	16	47	<15	<15
Pb	<15	<15	<15	<15	<15	<15	<15	<15	<15	17	<15
Rb	22	22	21	18	21	22	33	22	42	<15	<15
Sr	120	125	102	151	126	125	111	119	131	70	74
Th	<10	14	<10	<10	11	10	<10	14	<10	<10	14
U	<10	<10	<10	<10	<10	<10	<10	<10	<10	15	16
V	95	95	100	72	81	79	100	95	93	44	47
Y	<10	<10	<10	<10	<10	<10	<10	<10	<10	<10	<10
Zn	45	54	50	43	<30	52	73	54	71	<30	<30
Zr	76	87	83	70	76	76	77	84	75	59	62

[1] uALU: upper accretionary lapilli unit; AcL.: accretionary lapilli; CU: clay unit; [2] Total Fe calculated as Fe_2O_3. No. 1 corresponds to samples grinded in a metal mortar, No. 2 in a corundum mortar.

A2.2 TXRF analyses

Table A2-2 TXRF analyses of bulk rock and accretionary lapilli of El Guayal compared with two analyses of heterogeneous silicate melt particle of UNAM-7-307.85. G14-2b is an analysis of heterogeneous particles probably with a higher proportion of silicate melt or feldspars, but included for comparison. Both analyses of UNAM-7-2 are from the same but heterogeneous silicate melt particle.

Sample		G5-2	G6-2	G7-2	G8-2	G9-2	G10-2	G11-2	G12-2
		Bulk rock	Bulk rock	Bulk rock	Bulk rock	Bulk rock	Bulk rock	Bulk rock	Bulk rock
Unit		uMB	lμB	mμB	uμB	lALU	lALU	mALU	mALU
(wt.%)									
TiO_2	K	0.028	0.044	0.047	0.068	0.12	0.12	0.085	0.12
Fe_2O_3	K	0.47	0.98	1.29	1.98	2.82	2.82	2.57	3.30
MnO	K	0.0087	0.012	0.018	0.016	0.015	0.013	0.012	0.0086
CaO	K	21.5	12.5	13.4	10.9	9.39	8.33	11.1	6.28
K_2O	K	0.075	0.085	0.081	0.085	0.18	0.14	0.10	0.20
P_2O_5	K	0.053	0.041	0.037	0.033	0.027	0.011	0.025	0.0012
SO_3	K	0.0066	0.0054	0.0053	0.0074	<0.00092	<0.0011	<0.0011	<0.00088
(μg/g)									
Ba	L	50	<1.3	37	8	60	26	32	82
Br	K	0.8	0.5	0.4	<0.086	0.6	0.6	<0.11	0.8
Cl	K	n.d.	n.d.	n.d.	n.d.	n.d.	n.d.	n.d.	n.d.
Co	K	10	24	36	396	71	139	60	89
Cr	K	9	4	3	7	12	15	10	39
Cu	K	2	2	3	3	5	5	3	7
Hf	L	6	<0.25	<0.23	4	4	4	2	4
Ni	K	12	<0.22	<0.20	<0.17	<0.17	<0.22	<0.22	<0.17
Pb	L	6	4	3	5	5	5	4	7
Rb	K	3	3	3	5	9	9	5	10
Sr	K	211	119	119	95	99	90	80	55
V	K	9	8	8	8	19	24	12	25
Yb	L	26	17	22	30	32	28	23	26
Zn	K	3	4	4	5	9	11	9	14

Sample		G14-2b	G13-2	G15-2	G9L	G10L	UNAM-7-2a	UNAM-7-2b	G14-2a
		Bulk rock	Bulk rock	Bulk rock	Acc. lapilli	Acc. lapilli	SMP1	SMP2	Bulk rock
Unit		uALU	uALU	CU	lALU	lALU	307.85 m	307.85 m	heterog.
(wt.%)									
TiO_2	K	0.15	0.13	0.16	0.064	0.079	0.27	0.21	0.24
Fe_2O_3	K	4.78	5.18	4.95	1.18	1.10	6.59	7.21	7.52
MnO	K	0.020	0.0073	0.031	0.0031	0.0033	0.0090	0.021	0.032
CaO	K	3.08	4.26	2.96	3.28	3.66	2.94	24.2	4.69
K_2O	K	0.23	0.23	0.38	0.059	0.077	0.40	0.31	0.39
P_2O_5	K	0.0011	0.0013	0.0015	0.0021	0.0020	n.d.	n.d.	<0.0022
SO_3	K	<0.00085	<0.00096	<0.0011	0.010	0.015	0.68	3.18	<0.0017
(μg/g)									
Ba	L	15	25	345	10	21	n.d.	3	480
Br	K	0.7	1.5	1.1	<0.16	0.6	32	37	0.8
Cl	K	n.d.	n.d.	n.d.	n.d.	n.d.	1541	2120	n.d.
Co	K	121	159	142	28	25	123	277	204
Cr	K	11	24	21	4	8	201	408	17
Cu	K	10	11	15	4	7	330	891	16
Hf	L	3	3	3	5	4	n.d.	n.d.	8
Ni	K	<0.16	<0.18	24	2	2	47	135	2
Pb	L	10	20	10	4	4	25	50	13
Rb	K	12	12	22	1	1	25	2	18
Sr	K	49	50	68	70	68	751	3376	67
V	K	31	22	31	15	14	58	60	50
Yb	L	27	43	22	<0.41	2	n.d.	n.d.	37
Zn	K	21	23	35	3	4	69	164	35

MB: megabreccia; μB: microbreccia; ALU: accretionary lapilli unit; CU: clay unit, (l: lower; m: middle; u: upper); Acc. lapilli: accretionary lapilli; SMP1: heterogeneous silicate melt particle (greyish, compact); SMP2: heterogeneous silicate melt particle (greenish, fine grained); heterog: heterogeneous analyses. K or L is element line; n. d.: not detected.

A2.3 Electron microprobe phase analyses

A2.3.1 Detection limits and standard compositions

Following standards were used to determine the detection limit and to control the stability of the EPMA calibration:

United States National Museum (Jaroswich et al. 1980, 1987):

- Glass, basaltic, Juan de Fuca Ridge, USNM 111240/52 VG-2
- Glass, tektite, synthetic, USNM 2213, Microcline, location unknown, USNM 143966
- Microcline, location unknown, USNM 143966
- Plagioclase (Labradorite), Lake Country, OR, USNM 115900
- Anorthoclase, Kakanui, New Zealand, USNM 133868

Astimex Scientific Limited MINM25-53:

- Chlorite, calcite, dolomite

Table A2-3 Detection limits of chemical elements for EMP analyses. Values in brackets are discarded values due too low element concentration in given standards. The highest value for each element is the assumed detection limit (bold values).

	Glass, basaltic	Glass, Tektite	Microcline	Plagioclase	Anorthoclase
(wt.%)					
SiO_2	0.09	0.09	**0.12**	0.11	**0.12**
TiO_2	**0.09**	(0.13)	-	-	-
Al_2O_3	**0.07**	**0.07**	0.06	**0.07**	0.06
FeO	**0.11**	0.09	(0.26)	(0.08)	(0.08)
MgO	0.05	**0.06**	-	-	-
MnO	**0.08**	(0.10)	-	-	-
CaO	**0.05**	0.04	(0.04)	**0.05**	**0.05**
Na_2O	0.05	0.04	0.04	0.04	**0.06**
K_2O	**0.03**	**0.03**	**0.03**	**0.03**	**0.03**
(µg/g)					
Si	561	517	580	525	569
Ti	438	623	-	-	-
Al	361	356	315	382	298
Fe	844	730	(2092)	642	640
Mg	323	366	-	307	-
Mn	619	740	-	-	-
Ca	387	304	(312)	335	325
Na	352	276	267	293	413
K	286	260	237	238	242

Table A2-4 Comparison of the chemical composition of standards used for EMP analyses.

	Basalt glass				Tektite				Chlorite			
	Prov.	Meas. (N=131)	s (± wt.%)	s (± %)	Prov.	Meas. (N=128)	s (± wt.%)	s (± %)	Prov.	Meas. (N=12)	s (± wt.%)	s (± %)
(wt.%)												
SiO_2	50.81	50.4	0.36	0.7	75.75	75.2	0.48	0.6	30.04	30.0	0.17	0.6
TiO_2	1.85	1.72	0.10	5.9	0.50	0.48	0.04	9.1	-	<0.09	-	-
Al_2O_3	14.06	14.0	0.18	1.3	11.34	11.2	0.16	1.4	18.08	18.8	0.29	1.5
FeO	11.84	11.3	0.55	4.9	4.90	4.74	0.24	5.1	3.31	3.28	0.16	5.0
MgO	6.71	6.73	0.14	2.1	1.51	1.46	0.06	3.9	33.51	31.2	0.33	1.1
MnO	0.22	0.21	0.04	18.0	0.11	0.10	0.04	35.4	-	<0.08	-	-
CaO	11.12	11.1	0.36	3.3	2.66	2.69	0.10	3.7	0.03	<0.05	-	-
Na_2O	2.62	2.49	0.09	3.5	1.06	0.83	0.10	12.3	-	<0.04	0.02	94.4
K_2O	0.19	0.19	0.02	12.9	1.88	1.75	0.17	10.0	-	<0.03	0.01	114.6
Total	99.42	98.2	0.82	0.8	99.71	98.4	0.61	0.6	84.97	83.3	0.56	0.7

	Plagioclase				Microcline				Anorthoclase			
	Prov.	Meas. (N=43)	s (± wt.%)	s (± %)	Prov.	Meas. (N=41)	s (± wt.%)	s (± %)	Prov.	Meas. (N=33)	s (± wt.%)	s (± %)
(wt.%)												
SiO_2	51.25	51.2	0.57	1.1	64.24	65.0	0.44	0.7	66.44	66.5	0.45	0.7
TiO_2	0.05	<0.09	-		0.01	<0.09	-	-	-	<0.09	-	-
Al_2O_3	30.91	30.5	0.25	0.8	18.30	18.7	0.17	0.9	20.12	20.0	0.21	1.0
FeO	0.46	0.39	0.06	16.3	0.04	<0.11	-	-	0.20	0.13	0.03	24.6
MgO	0.14	0.12	0.03	21.7	0.03	<0.06	-	-	-	<0.06	-	-
MnO	0.01	<0.09	-	-	0.04	<0.09	-	-	-	<0.09	-	-
CaO	13.64	13.5	0.40	3.0	0.02	<0.05	-	-	0.87	0.57	0.04	6.3
Na_2O	3.45	3.41	0.09	2.8	1.30	1.26	0.05	3.9	9.31	8.55	0.17	2.0
K_2O	0.18	0.13	0.02	12.6	15.14	15.7	0.44	2.8	2.35	2.54	0.07	2.8
Total	100.09	99.3	0.65	0.7	99.12	100.6	0.67	0.7	99.29	98.3	0.51	0.5
Number of cations on the basis of 24O												
Si		7.032	0.041	0.6		8.950	0.027	0.3		8.920	0.025	0.3
Ti		-	-	-		0.002	0.002	123.6		-	-	-
Al		4.939	0.048	1.0		-	-	-		3.153	0.026	0.8
Fe		0.045	0.007	16.4		0.002	0.003	122.6		0.015	0.004	24.7
Mg		0.025	0.005	21.6		-	-	-		-	-	-
Mn		-	-	-		-	-	-		-	-	-
Ca		1.982	0.058	2.9		-	-	-		0.082	0.005	6.3
Na		0.908	0.026	2.8		0.337	0.013	3.9		2.222	0.050	2.2
K		0.023	0.003	12.5		2.749	0.075	2.7		0.435	0.012	2.7
Total		14.953	0.039	0.3		15.076	0.054	0.4		14.830	0.041	0.3

	Calcite				Dolomite			
	Prov.	Meas. (N=12)	s (wt.%)	s (%)	Prov.	Meas. (N=17)	s (± wt.%)	s (± %)
(wt.%)								
SiO_2	-	<0.12	-	-	-	<0.12	-	-
Al_2O_3	-	<0.07	-	-	-	<0.07	-	-
FeO	-	<0.11	-	-	0.03	<0.11	-	-
MgO	0.02	<0.06	-	-	21.86	21.7	1.08	0.23
MnO	0.01	<0.08	-	0.05	0.03	<0.08	-	0.03
CaO	55.94	55.9	1.8	0.06	30.41	30.5	0.93	0.28
Total	55.97	55.9	1.8	0.02	52.33	52.2	0.08	0.04

N: number of analyses; Prov.: Provided; Meas.: Measured.

A2.3.2 Chemical compositions of melt particles (altered to clay minerals) from El Guayal

The analyses of melt particles with compositional heterogeneities were grouped according to their SiO_2 concentration and named with an affix (L: low; M: intermediate; H: high).

Average compositions

Table A2-5a Average composition (wt.%) of melt particle type 1.

Sample	Dia	N	SiO_2	TiO_2	Al_2O_3	FeO	MgO	MnO	CaO	Na_2O	K_2O	Total
Ir07A-15	3	10	35.7	0.52	14.7	7.80	18.1	<0.08	0.81	0.08	0.22	77.9
s			2.3	0.49	0.8	1.69	1.5	-	0.19	0.02	0.15	2.5
Ir11-17	3	2	43.5	2.27	17.2	4.05	14.7	<0.08	1.33	0.15	2.07	85.2
s			0.7	0.77	0.1	0.85	1.8	-	0.59	0.02	0.03	3.4
Ir11-245	3	3	43.4	1.16	16.6	4.74	17.9	<0.08	1.33	0.16	1.21	86.5
s			4.0	0.93	1.4	1.08	4.8	-	0.25	0.04	0.76	1.7
Ir11-24b	3	3	36.4	<0.09	15.8	6.43	26.9	<0.08	0.51	0.15	0.10	86.3
s			0.3		0.1	0.18	0.2	-	0.04	0.00	0.02	0.7
Ir15aB	3	2	43.1	<0.09	17.0	5.80	19.0	<0.08	1.33	0.10	1.05	87.5
s			3.7		0.6	0.55	3.8	-	0.19	0.03	1.03	0.8
Ir18-3bA	3	5	50.6	0.95	16.3	3.78	12.0	<0.08	2.20	0.51	1.29	87.4
s			2.3	0.90	1.0	1.09	1.3	-	0.22	0.05	0.27	1.2
Ir18-4	3	3	47.6	0.11	16.3	3.42	11.3	<0.08	2.35	0.34	1.14	82.5
s			0.8	0.02	0.8	0.99	2.1	-	0.28	0.08	0.16	3.2
Ir22-1-1-10	3	4	54.0	0.28	18.3	4.04	9.22	<0.08	2.66	0.35	2.97	91.7
s			0.5	0.02	0.2	0.66	0.50	-	0.11	0.06	0.88	1.5
Ir22-3-0-3	3	3	52.8	0.13	17.7	3.38	9.84	<0.08	3.10	0.38	1.03	88.4
s			1.4	0.03	1.4	0.28	1.14	-	0.11	0.05	0.19	1.7

N: Number of analyses; Dia.: beam diameter.

Table A2-5b Average composition (wt.%) of melt particle type 1 with compositional heterogeneities.

Sample	Dia	N	SiO_2	TiO_2	Al_2O_3	FeO	MgO	MnO	CaO	Na_2O	K_2O	Total
Ir07-01M	3	4	40.9	0.58	16.3	5.85	17.4	<0.08	1.38	0.06	0.47	82.9
s			1.3	0.41	0.3	0.88	1.3	-	0.02	0.01	0.11	2.4
Ir07-01L	3	9	35.0	0.33	14.4	8.12	19.8	<0.08	1.12	0.07	0.18	79.1
s			1.0	0.10	0.4	0.61	1.0	-	0.26	0.01	0.06	2.0
Ir11-12H	3	2	49.1	0.14	18.3	3.52	10.8	<0.08	1.03	0.16	3.03	86.1
s			0.8	0.06	0.3	0.24	0.1	-	0.22	0.04	0.32	1.8
Ir11-12M	3	3	43.6	0.22	17.2	5.45	16.3	<0.08	1.37	0.17	1.28	85.5
s			1.6	0.15	0.6	0.64	1.2	-	0.24	0.02	0.50	2.6
Ir11-12L	3	4	37.9	0.23	15.0	7.10	20.5	<0.08	1.02	0.18	0.33	82.3
s			1.0	0.18	0.6	0.60	1.4	-	0.22	0.05	0.09	1.9
Ir11-17H	3	2	46.2	<0.09	18.1	4.04	13.8	<0.08	0.97	0.15	1.88	85.1
s			1.0	-	0.3	0.33	0.5	-	0.03	0.03	0.20	0.6
Ir11-17L	3	3	40.3	<0.09	15.5	5.95	21.0	<0.08	1.17	0.21	0.51	84.6
s			0.5		0.5	0.29	0.6	-	0.22	0.04	0.14	1.1
Ir11-24bH	3	2	45.4	1.44	17.0	5.18	14.7	<0.08	1.36	0.22	2.06	87.4
s			1.7	1.10	0.8	0.82	2.5		0.08	0.00	0.90	1.0
Ir11-24bL	3	2	39.2	0.57	15.3	5.78	20.1	<0.08	1.25	0.14	0.46	82.9
s			1.1	0.62	0.2	0.78	0.5	-	0.69	0.04	0.17	2.5
Ir15aK	3	5	52.0	<0.09	18.7	3.08	4.90	<0.08	0.68	<0.06	5.16	84.6
s			1.2	-	0.6	0.05	0.13	-	0.10	-	0.43	1.8
Ir15aH	3	7	51.5	<0.09	17.0	3.11	5.99	<0.08	1.30	0.08	1.82	80.8
s			1.2	-	0.5	0.29	0.89	-	0.15	0.01	0.31	2.1
Ir15aL	3	8	39.9	0.22	15.4	7.13	22.9	<0.08	1.35	0.09	0.20	87.1
s			1.3	0.12	0.8	0.90	1.0		0.13	0.02	0.06	1.2
Ir18-6H	3	4	51.8	0.11	17.7	3.25	10.9	<0.08	1.97	0.49	1.29	87.5
s			2.1	0.02	0.5	0.16	0.7	-	0.28	0.11	0.13	2.1
Ir18-6L	3	2	40.7	0.37	14.3	8.02	18.4	<0.08	2.05	0.32	0.28	84.5
s			0.0	0.10	0.1	0.09	1.8	-	0.03	0.00	0.04	1.7

N: Number of analyses; Dia.: beam diameter.

Table A2-6a Average composition (wt.%) of melt particle type 2a.

Sample	Dia	N	SiO_2	TiO_2	Al_2O_3	FeO	MgO	MnO	CaO	Na_2O	K_2O	Total
Ir07A-15	3	11	39.3	<0.09	17.1	4.30	14.9	<0.08	0.96	0.08	0.79	77.7
s			3.1	-	0.6	1.00	2.5	-	0.25	0.02	0.38	2.6
Ir11-24	3	5	39.4	<0.09	16.4	5.23	22.3	<0.08	1.35	0.07	0.46	85.4
s			0.7	-	0.4	0.24	0.5	-	0.17	0.00	0.13	1.6
Ir11-06	3	6	38.7	0.18	16.1	5.60	22.1	<0.08	2.45	0.08	0.36	85.5
s			1.7	0.09	1.2	0.24	1.1		1.37	0.03	0.24	2.4
Ir11-21	3	5	39.5	<0.09	16.3	5.45	22.4	<0.08	0.95	0.15	0.64	85.4
s			2.6	-	0.7	0.79	3.5	-	0.08	0.03	0.61	1.2
Ir11-24b	3	3	40.8	0.51	16.7	4.97	20.3	<0.08	2.15	0.16	0.78	86.3
s			1.9	0.16	0.2	0.22	1.3	-	0.77	0.05	0.32	1.3
Ir18-2-1	3	7	49.4	<0.09	14.4	3.18	13.6	<0.08	2.49	0.20	0.60	83.9
s			2.6	-	1.8	0.70	2.2	-	0.49	0.04	0.27	1.8
Ir18-3a	3	6	50.3	0.16	16.1	4.46	13.2	<0.08	2.55	0.46	1.03	88.3
s			2.6	0.06	0.8	1.63	2.1	-	0.36	0.15	0.33	1.4
Ir18-3b	3	3	47.9	0.12	16.0	4.65	15.5	<0.08	2.45	0.48	1.03	88.0
s			4.8	0.04	1.4	1.65	4.2	-	0.13	0.05	0.41	1.2
Ir18-3cA	3	5	51.4	<0.09	16.3	3.18	11.9	<0.08	2.34	0.47	1.03	86.7
s			3.0	-	0.8	0.64	1.6	-	0.21	0.06	0.31	2.2
Ir18-4a	3	3	48.7	<0.09	15.7	3.58	12.4	<0.08	2.83	0.22	1.00	84.4
s			6.2	-	1.3	1.36	2.6	-	0.39	0.11	0.17	4.2
Ir22-1-2	3	5	46.6	<0.09	14.3	6.18	14.6	<0.08	3.49	0.35	0.46	86.1
s			2.7	-	1.9	1.12	1.9	-	0.12	0.12	0.36	2.4

N: Number of analyses; Dia.: beam diameter.

Table A2-6b Average composition (wt.%) of melt particle type 2a with compositional heterogeneities.

Sample	Dia	N	SiO_2	TiO_2	Al_2O_3	FeO	MgO	MnO	CaO	Na_2O	K_2O	Total
Ir07A-01H	3	5	52.3	<0.09	17.9	1.77	9.24	<0.08	2.36	0.14	1.11	84.8
s			2.0	-	0.6	0.26	0.77	-	0.35	0.09	0.18	2.3
Ir07A-01M	3	4	41.8	0.11	17.0	3.82	14.9	<0.08	1.31	<0.06	0.76	79.8
s			2.4	0.01	0.4	0.82	3.0	-	0.11	-	0.31	3.6
Ir07A-01L	3	28	35.5	<0.09	15.3	7.03	26.1	<0.08	0.63	0.06	<0.03	84.6
s			0.5	-	0.7	0.49	1.0	-	0.12	0.00	-	1.2
Ir15a1H	3	4	45.1	0.13	16.0	5.59	18.9	<0.08	1.55	0.11	0.63	87.9
s			5.6	0.05	1.9	1.09	2.9	-	0.16	0.02	0.59	2.4
Ir15a1L	3	4	54.1	0.11	18.7	3.21	6.1	<0.08	1.23	0.09	3.57	87.0
s			1.4	0.02	0.4	0.16	1.1	-	0.20	0.01	0.31	2.0
Ir18-2-2H	3	3	51.3	0.11	16.8	2.62	10.2	<0.08	2.33	0.21	1.08	84.7
s			0.9	0.02	0.4	0.22	0.4		0.12	0.06	0.11	0.9
Ir18-2-2L	3	4	46.4	0.17	16.4	4.46	15.7	<0.08	2.27	0.20	0.67	86.2
s			2.4	0.05	0.6	0.79	1.7	-	0.16	0.05	0.15	2.2
Ir18-2-3H	3	5	52.0	0.10	17.2	2.76	10.7	<0.08	2.29	0.26	1.07	86.4
s			1.0	0.00	0.1	0.15	0.7	-	0.18	0.01	0.06	0.8
Ir18-2-3L	3	2	45.7	<0.09	16.1	5.12	16.3	<0.08	2.69	0.23	0.49	86.8
s			0.2	-	0.1	0.10	0.5	-	0.76	0.03	0.03	1.0
Ir22-2H	3	4	54.1	0.11	17.9	3.37	8.80	<0.08	2.82	0.36	1.43	88.9
s			1.2	0.01	0.4	0.27	0.55	-	0.26	0.02	0.26	0.9
Ir22-2L	3	2	46.0	<0.09	15.0	7.33	16.3	<0.08	4.01	0.19	0.22	89.0
s			0.0	-	0.0	0.04	0.0	-	0.15	0.02	0.04	0.2

N: Number of analyses; Dia.: beam diameter.

Table A2-7 Average composition (wt.%) of melt particle type 2b.

Sample	Dia	N	SiO_2	TiO_2	Al_2O_3	FeO	MgO	MnO	CaO	Na_2O	K_2O	Total
Ir07A-07	3	10	35.8	<0.09	15.4	7.13	26.5	<0.08	0.72	<0.06	0.03	85.6
s			1.2	-	0.9	0.86	3.6	-	0.24	-	0.11	3.9
Ir18-1	3	9	43.3	<0.09	10.6	5.14	21.2	<0.08	2.21	0.23	0.28	83.0
s			1.5	-	2.2	0.77	2.6	-	0.47	0.04	0.15	2.6
Ir07A-17H	3	5	43.9	<0.09	16.3	2.84	12.4	<0.08	1.34	0.13	0.57	77.4
s			3.0	-	0.4	0.61	1.9	-	0.51	0.05	0.23	2.1
Ir07A-17L	3	14	35.8	<0.09	15.0	7.12	26.3	<0.08	0.67	<0.06	0.02	84.9
s			0.4	-	0.3	0.30	0.9	-	0.08	-	0.01	1.3
Ir18-1bH	3	3	44.7	<0.09	10.5	4.45	17.3	<0.08	2.06	0.27	0.49	79.8
s			0.5	-	0.8	0.25	1.4	-	0.17	0.04	0.12	1.1
Ir18-1aL	3	3	39.6	<0.09	12.0	6.61	25.5	<0.08	1.77	0.28	0.11	85.8
s			0.8	-	0.8	0.89	1.1	-	0.42	0.05	0.04	1.8

N: Number of analyses; Dia.: beam diameter.

Individual and average compositions of melt particles (altered to clay minerals)

Table A2-8a Individual and average compositions (wt.%) of melt particle type 1.

Sample	Dia	N	SiO_2	TiO_2	Al_2O_3	FeO	MgO	MnO	CaO	Na_2O	K_2O	Total
Ir07A-151-1	3		35.3	0.57	14.7	7.45	17.7	<0.08	0.79	0.09	0.18	76.7
Ir07A-151-2	3		38.7	0.22	15.9	5.00	15.7	<0.08	0.86	0.07	0.50	77.0
Ir07A-151-3	3		33.8	0.18	13.9	8.63	17.5	<0.08	0.79	0.06	0.12	75.0
Ir07A-151-4	3		38.5	0.12	15.6	6.76	17.9	<0.08	1.11	0.12	0.33	80.6
Ir07A-152-2	3		38.1	0.76	15.0	6.15	15.7	<0.08	0.87	0.09	0.41	77.1
Ir07A-152-3	3		37.7	1.70	15.3	7.88	19.0	<0.08	1.11	0.08	0.27	83.0
Ir07A-153-1	3		34.2	0.17	13.7	11.17	20.2	<0.08	0.70	<0.06	0.09	80.3
Ir07A-153-2	3		33.6	<0.09	14.0	9.11	19.0	<0.08	0.60	0.07	0.07	76.6
Ir07A-154-1	3		33.5	0.52	14.9	7.95	18.5	<0.08	0.69	<0.06	0.12	76.3
Ir07A-154-2	3		33.7	0.46	14.1	7.89	19.4	<0.08	0.54	<0.06	0.08	76.3
Ir07A-15	**3**	**10**	**35.7**	**0.52**	**14.7**	**7.80**	**18.1**	**<0.08**	**0.81**	**0.08**	**0.22**	**77.9**
s			**2.3**	**0.49**	**0.8**	**1.69**	**1.5**	**-**	**0.19**	**0.02**	**0.15**	**2.5**
Ir11-171	3		44.0	1.72	17.1	3.45	13.5	<0.08	0.91	0.14	2.09	82.9
Ir11-173	3		43.0	2.82	17.2	4.65	16.0	<0.08	1.74	0.17	2.05	87.7
Ir11-17	**3**	**2**	**43.5**	**2.27**	**17.2**	**4.05**	**14.7**	**<0.08**	**1.33**	**0.15**	**2.07**	**85.2**
s			**0.7**	**0.77**	**0.1**	**0.85**	**1.8**	**-**	**0.59**	**0.02**	**0.03**	**3.4**
Ir11-245-1	3		47.6	1.85	17.9	3.76	13.1	<0.08	1.16	0.10	2.06	87.6
Ir11-245-2	3		42.9	0.10	16.7	4.58	17.9	<0.08	1.21	0.19	0.98	84.5
Ir11-245-3	3		39.6	1.53	15.2	5.90	22.7	<0.08	1.62	0.18	0.59	87.3
Ir11-245	**3**	**3**	**43.4**	**1.16**	**16.6**	**4.74**	**17.9**	**<0.08**	**1.33**	**0.16**	**1.21**	**86.5**
s			**4.0**	**0.93**	**1.4**	**1.08**	**4.8**	**-**	**0.25**	**0.04**	**0.76**	**1.7**
Ir11-24b-8	3		36.3	<0.09	15.8	6.22	26.7	<0.08	0.52	0.15	0.07	85.7
Ir11-24b-9	3		36.2	<0.09	15.7	6.53	27.1	<0.08	0.46	0.15	0.12	86.3
Ir11-24b-10	3		36.7	<0.09	15.9	6.54	27.1	<0.08	0.54	0.15	0.11	87.0
Ir11-24b	**3**	**3**	**36.4**	**<0.09**	**15.8**	**6.43**	**26.9**	**<0.08**	**0.51**	**0.15**	**0.10**	**86.3**
s			**0.3**	**-**	**0.1**	**0.18**	**0.2**	**-**	**0.04**	**0.00**	**0.02**	**0.7**
Ir15a1-9	3		40.5	<0.09	16.6	6.19	21.7	<0.08	1.47	0.07	0.32	86.9
Ir15a1-10	3		45.7	<0.09	17.5	5.41	16.3	<0.08	1.20	0.12	1.77	88.0
Ir15aB	**3**	**2**	**43.1**	**<0.09**	**17.0**	**5.80**	**19.0**	**<0.08**	**1.33**	**0.10**	**1.05**	**87.5**
s			**3.7**	**-**	**0.6**	**0.55**	**3.8**	**-**	**0.19**	**0.03**	**1.03**	**0.8**
Ir18-3b5	3		52.8	<0.09	17.1	3.04	10.5	<0.08	2.30	0.47	1.53	87.7
Ir18-3b6	3		51.7	0.12	16.5	2.73	11.0	<0.08	2.49	0.45	1.36	86.3
Ir18-3b7	3		50.3	0.49	16.6	4.32	12.8	<0.08	1.93	0.52	1.31	88.3
Ir18-3b8	3		46.7	2.19	14.5	5.42	13.5	<0.08	2.21	0.55	0.82	85.9
Ir18-3b9	3		51.3	1.02	16.8	3.39	12.0	<0.08	2.06	0.56	1.44	88.6
Ir18-3bA	**3**	**5**	**50.6**	**0.95**	**16.3**	**3.78**	**12.0**	**<0.08**	**2.20**	**0.51**	**1.29**	**87.4**
s			**2.3**	**0.90**	**1.0**	**1.09**	**1.3**	**-**	**0.22**	**0.05**	**0.27**	**1.2**

N: Number of analyses; Dia.: beam diameter.

Table A2-8a continued.

Sample	Dia	N	SiO_2	TiO_2	Al_2O_3	FeO	MgO	MnO	CaO	Na_2O	K_2O	Total
Ir18-44	3		46.8	0.10	16.8	4.52	13.6	<0.08	2.51	0.25	1.17	85.7
Ir18-45	3		48.2	0.12	16.7	3.13	10.8	<0.08	2.03	0.38	1.29	82.6
Ir18-46	3		48.0	<0.09	15.3	2.60	9.4	<0.08	2.53	0.40	0.97	79.2
Ir18-4	**3**	**3**	**47.6**	**0.11**	**16.3**	**3.42**	**11.3**	**<0.08**	**2.35**	**0.34**	**1.14**	**82.5**
s			**0.8**	**0.02**	**0.8**	**0.99**	**2.1**	**-**	**0.28**	**0.08**	**0.16**	**3.2**
Ir22-1-1-101	3		53.6	0.29	18.2	4.42	9.7	<0.08	2.76	0.32	3.37	92.7
Ir22-1-1-102	3		53.9	0.29	18.3	4.42	9.0	<0.08	2.60	0.35	3.29	92.1
Ir22-1-1-104	3		54.0	0.26	18.1	4.28	9.5	<0.08	2.76	0.29	3.58	92.7
Ir22-1-1-103	3		54.7	<0.09	18.5	3.05	8.6	<0.08	2.53	0.43	1.67	89.5
Ir22-1-1-10	**3**	**4**	**54.0**	**0.28**	**18.3**	**4.04**	**9.2**	**<0.08**	**2.66**	**0.35**	**2.97**	**91.7**
s			**0.5**	**0.02**	**0.2**	**0.66**	**0.5**	**-**	**0.11**	**0.06**	**0.88**	**1.5**
Ir22-3-0-31	3		51.3	<0.09	16.2	3.70	11.1	<0.08	3.02	0.39	0.81	86.6
Ir22-3-0-32	3		53.2	0.11	18.1	3.24	9.4	<0.08	3.05	0.33	1.13	88.5
Ir22-3-0-33	3		54.0	0.15	18.9	3.19	9.0	<0.08	3.22	0.42	1.15	90.0
Ir22-3-0-3	**3**	**3**	**52.8**	**0.13**	**17.7**	**3.38**	**9.8**	**<0.08**	**3.10**	**0.38**	**1.03**	**88.4**
s			**1.4**	**0.03**	**1.4**	**0.28**	**1.1**	**-**	**0.11**	**0.05**	**0.19**	**1.7**

N: Number of analyses; Dia.: beam diameter.

Table A2-8b Individual and average compositions (wt.%) of melt particle type 1 with compositional heterogeneities.

Sample	Dia	N	SiO_2	TiO_2	Al_2O_3	FeO	MgO	MnO	CaO	Na_2O	K_2O	Total
Ir07-01-5-1	3		39.6	0.94	16.4	6.72	17.9	<0.08	1.38	<0.06	0.44	83.4
Ir07-01-5-2	3		42.7	0.65	16.8	5.16	16.5	<0.08	1.38	<0.06	0.62	83.8
Ir07-01-5-3	3		41.0	0.14	16.2	6.50	19.0	<0.08	1.35	0.06	0.43	84.6
Ir07-01-5-6	3		40.3	<0.09	16.0	5.02	16.1	<0.08	1.40	0.07	0.38	79.3
Ir07-01M	**3**	**4**	**40.9**	**0.58**	**16.3**	**5.85**	**17.4**	**<0.08**	**1.38**	**0.06**	**0.47**	**82.9**
s			**1.3**	**0.41**	**0.3**	**0.88**	**1.3**	**-**	**0.02**	**0.01**	**0.11**	**2.4**
Ir07-01-4-1	3		34.7	<0.09	14.7	7.51	20.8	0.10	0.96	<0.06	0.13	79.1
Ir07-01-4-2	3		34.6	0.24	14.6	8.14	20.0	<0.08	0.95	0.09	0.16	78.9
Ir07-01-4-3	3		34.7	0.30	14.4	8.90	20.5	<0.08	0.99	0.06	0.17	80.0
Ir07-01-4-4	3		35.2	0.31	14.5	7.72	19.5	<0.08	0.86	<0.06	0.17	78.4
Ir07-01-4-5	3		33.0	0.45	13.6	8.21	17.9	<0.08	1.04	0.06	0.19	74.4
Ir07-01-5-4	3		35.4	<0.09	14.0	8.72	19.9	<0.08	1.21	<0.06	0.11	79.5
Ir07-01-5-5	3		35.7	0.46	14.8	8.36	18.6	<0.08	1.35	0.07	0.22	79.5
Ir07-01-5-7	3		35.8	0.19	14.7	8.54	20.4	<0.08	1.00	<0.06	0.14	80.9
Ir07-01-5-8	3		36.4	0.33	14.6	7.01	20.7	<0.08	1.70	0.06	0.32	81.1
Ir07-01L	**3**	**9**	**35.0**	**0.33**	**14.4**	**8.12**	**19.8**	**<0.08**	**1.12**	**0.07**	**0.18**	**79.1**
s			**1.0**	**0.10**	**0.4**	**0.61**	**1.0**	**-**	**0.26**	**0.01**	**0.06**	**2.0**
Ir11-125	3		49.6	0.18	18.6	3.70	10.7	<0.08	1.19	0.20	3.25	87.4
Ir11-129	3		48.6	0.10	18.1	3.35	10.9	<0.08	0.87	0.13	2.81	84.9
Ir11-12H	**3**	**2**	**49.1**	**0.14**	**18.3**	**3.52**	**10.8**	**<0.08**	**1.03**	**0.16**	**3.03**	**86.1**
s			**0.8**	**0.06**	**0.3**	**0.24**	**0.1**	**-**	**0.22**	**0.04**	**0.32**	**1.8**
Ir11-124	3		41.9	0.14	16.8	5.40	16.0	<0.08	1.10	0.16	1.12	82.6
Ir11-127	3		43.8	0.39	16.9	6.11	17.6	<0.08	1.55	0.19	0.89	87.5
Ir11-122	3		45.0	0.13	17.8	4.84	15.2	<0.08	1.48	0.16	1.84	86.6
Ir11-12M	**3**	**3**	**43.6**	**0.22**	**17.2**	**5.45**	**16.3**	**<0.08**	**1.37**	**0.17**	**1.28**	**85.5**
s			**1.6**	**0.15**	**0.6**	**0.64**	**1.2**	**-**	**0.24**	**0.02**	**0.50**	**2.6**
Ir11-121	3		38.9	<0.09	15.9	6.28	21.4	<0.08	1.13	0.19	0.43	84.3
Ir11-123	3		38.4	0.36	14.7	7.66	19.0	<0.08	1.28	0.24	0.36	82.1
Ir11-126	3		36.7	<0.09	14.7	7.38	19.6	<0.08	0.83	0.15	0.22	79.6
Ir11-128	3		37.6	0.11	14.9	7.07	21.9	<0.08	0.83	0.14	0.33	82.9
Ir11-12L	**3**	**4**	**37.9**	**0.23**	**15.0**	**7.10**	**20.5**	**<0.08**	**1.02**	**0.18**	**0.33**	**82.3**
s			**1.0**	**0.18**	**0.6**	**0.60**	**1.4**	**-**	**0.22**	**0.05**	**0.09**	**1.9**
Ir11-174	3		46.9	<0.09	18.3	3.81	13.5	<0.08	0.95	0.17	2.02	85.7
Ir11-177	3		45.5	0.13	17.9	4.27	14.1	<0.08	0.99	0.13	1.74	84.8
Ir11-17H	**3**	**2**	**46.2**	**<0.09**	**18.1**	**4.04**	**13.8**	**<0.08**	**0.97**	**0.15**	**1.88**	**85.1**
s			**1.0**	**-**	**0.3**	**0.33**	**0.5**	**-**	**0.03**	**0.03**	**0.20**	**0.6**
Ir11-172	3		39.7	<0.09	15.2	5.95	21.1	<0.08	1.42	0.16	0.39	83.9
Ir11-175	3		40.4	<0.09	16.0	5.66	20.3	<0.08	1.03	0.22	0.48	84.2
Ir11-176	3		40.7	<0.09	15.3	6.24	21.6	<0.08	1.05	0.24	0.67	85.9
Ir11-17L	**3**	**3**	**40.3**	**<0.09**	**15.5**	**5.95**	**21.0**	**<0.08**	**1.17**	**0.21**	**0.51**	**84.6**
s			**0.5**	**<0.09**	**0.5**	**0.29**	**0.6**	**-**	**0.22**	**0.04**	**0.14**	**1.1**

N: Number of analyses; Dia.: beam diameter.

Table A2-8b Continued.

Sample	Dia	N	SiO_2	TiO_2	Al_2O_3	FeO	MgO	MnO	CaO	Na_2O	K_2O	Total
Ir11-24b-6	3		46.6	2.22	17.5	4.60	12.9	<0.08	1.31	0.22	2.69	88.1
Ir11-24b-7	3		44.2	0.66	16.4	5.77	16.5	<0.08	1.42	0.22	1.42	86.6
Ir11-24bH	**3**	**2**	**45.4**	**1.44**	**17.0**	**5.18**	**14.7**	**<0.08**	**1.36**	**0.22**	**2.06**	**87.4**
s			**1.7**	**1.10**	**0.8**	**0.82**	**2.5**	**-**	**0.08**	**0.00**	**0.90**	**1.0**
Ir11-24b-4	3		38.4	0.13	15.2	6.34	19.8	<0.08	0.76	0.11	0.34	81.1
Ir11-24b-5	3		39.9	1.01	15.5	5.23	20.5	<0.08	1.73	0.16	0.59	84.6
Ir11-24bL	**3**	**2**	**39.2**	**0.57**	**15.3**	**5.78**	**20.1**	**<0.08**	**1.25**	**0.14**	**0.46**	**82.9**
s			**1.1**	**0.62**	**0.2**	**0.78**	**0.5**	**-**	**0.69**	**0.04**	**0.17**	**2.5**
Ir15a16	3		51.8	<0.09	19.5	3.07	4.9	<0.08	0.57	<0.06	5.55	85.4
Ir15a17	3		52.0	<0.09	19.1	3.16	4.8	<0.08	0.62	<0.06	5.48	85.1
Ir15a18	3		51.5	0.12	17.9	3.04	4.8	<0.08	0.64	<0.06	5.26	83.3
Ir15a19	3		50.7	<0.09	18.3	3.11	4.9	<0.08	0.77	<0.06	4.48	82.2
Ir15a20	3		54.0	0.11	18.9	3.03	5.1	<0.08	0.78	<0.06	5.00	86.9
Ir15aK	**3**	**5**	**52.0**	**<0.09**	**18.7**	**3.08**	**4.9**	**<0.08**	**0.68**	**<0.06**	**5.16**	**84.6**
s			**1.2**	**-**	**0.6**	**0.05**	**0.1**	**-**	**0.10**	**-**	**0.43**	**1.8**
Ir15a1	3		50.9	<0.09	16.9	3.28	7.2	<0.08	1.37	0.07	1.38	81.1
Ir15a2	3		51.0	<0.09	16.4	3.25	5.9	<0.08	1.23	0.09	1.53	79.4
Ir15a3	3		53.0	<0.09	17.6	2.77	6.1	<0.08	1.54	0.07	1.63	82.6
Ir15a4	3		50.6	<0.09	17.1	3.55	7.2	<0.08	1.37	0.07	2.19	82.1
Ir15a5	3		53.5	<0.09	17.9	3.18	5.5	<0.08	1.31	0.09	2.01	83.5
Ir15a6	3		50.9	<0.09	16.8	2.77	5.2	<0.08	1.22	0.08	1.86	78.8
Ir15a7	3		50.4	<0.09	16.6	2.96	5.0	<0.08	1.06	<0.06	2.14	78.1
Ir15aH	**3**	**7**	**51.5**	**<0.09**	**17.0**	**3.11**	**6.0**	**<0.08**	**1.30**	**0.08**	**1.82**	**80.8**
s			**1.2**	**-**	**0.5**	**0.29**	**0.9**	**-**	**0.15**	**0.01**	**0.31**	**2.1**
Ir15a8	3		40.9	0.12	16.6	5.91	21.8	<0.08	1.35	0.11	0.31	87.1
Ir15a9	3		39.6	<0.09	15.8	6.36	23.2	<0.08	1.36	0.08	0.15	86.5
Ir15a10	3		39.6	<0.09	16.3	6.90	23.7	<0.08	1.45	0.07	0.14	88.1
Ir15a11	3		39.0	0.17	15.0	7.67	23.5	<0.08	1.31	0.11	0.17	86.9
Ir15a12	3		40.8	0.44	14.7	6.47	21.5	<0.08	1.41	0.08	0.29	85.7
Ir15a13	3		41.6	0.20	14.4	7.25	21.7	<0.08	1.21	0.11	0.19	86.6
Ir15a14	3		40.3	0.28	14.8	8.68	23.8	<0.08	1.53	0.10	0.18	89.6
Ir15a15	3		37.5	0.14	15.4	7.80	24.1	<0.08	1.14	0.06	0.21	86.4
Ir15aL	**3**	**8**	**39.9**	**0.22**	**15.4**	**7.13**	**22.9**	**<0.08**	**1.35**	**0.09**	**0.20**	**87.1**
s			**1.3**	**0.12**	**0.8**	**0.90**	**1.0**	**-**	**0.13**	**0.02**	**0.06**	**1.2**
Ir18-61	3		51.2	0.13	16.9	3.19	10.4	<0.08	1.69	0.56	1.15	85.3
Ir18-63	3		49.1	<0.09	18.0	3.50	11.8	<0.08	1.78	0.59	1.45	86.3
Ir18-64	3		53.5	<0.09	17.9	3.16	10.4	<0.08	2.25	0.37	1.26	88.9
Ir18-65	3		53.5	0.09	18.1	3.18	11.0	<0.08	2.17	0.43	1.29	89.7
Ir18-6H	**3**	**4**	**51.8**	**0.11**	**17.7**	**3.25**	**10.9**	**<0.08**	**1.97**	**0.49**	**1.29**	**87.5**
s			**2.1**	**0.02**	**0.5**	**0.16**	**0.7**	**-**	**0.28**	**0.11**	**0.13**	**2.1**
Ir18-66	3		40.8	0.44	14.3	8.08	17.2	<0.08	2.03	0.33	0.30	83.4
Ir18-67	3		40.7	0.30	14.4	7.95	19.7	<0.08	2.07	0.32	0.25	85.7
Ir18-6L	**3**	**2**	**40.7**	**0.37**	**14.3**	**8.02**	**18.4**	**<0.08**	**2.05**	**0.32**	**0.28**	**84.5**
s			**0.0**	**0.10**	**0.1**	**0.09**	**1.8**	**-**	**0.03**	**0.00**	**0.04**	**1.7**

N: Number of analyses; Dia.: beam diameter.

Table A2-9a Individual and average compositions (wt.%) of melt particle type 2a.

Sample	Dia	N	SiO_2	TiO_2	Al_2O_3	FeO	MgO	MnO	CaO	Na_2O	K_2O	Total
Ir07A-155-1	3		34.5	0.17	16.6	4.91	15.8	<0.08	1.08	0.08	0.46	73.6
Ir07A-155-2	3		34.7	<0.09	16.6	5.23	16.8	<0.08	0.95	0.06	0.25	74.7
Ir07A-155-3	3		40.2	<0.09	17.8	4.37	15.8	0.10	0.96	0.06	0.73	80.1
Ir07A-155-5	3		43.5	<0.09	17.3	3.45	13.0	<0.08	1.42	0.12	0.81	79.7
Ir07A-155-6	3		37.2	0.91	16.9	4.78	17.0	<0.08	0.71	0.06	0.62	78.2
Ir07A-155-7	3		42.1	0.10	17.7	3.10	12.1	<0.08	0.87	0.09	1.33	77.4
Ir07A-155-8	3		39.5	<0.09	16.2	4.17	15.9	<0.08	1.29	0.06	0.51	77.6
Ir07A-155-9	3		39.9	<0.09	16.7	4.39	14.5	<0.08	1.08	0.10	1.16	77.9
Ir07A-155-10	3		41.2	<0.09	17.4	4.92	16.8	<0.08	0.80	0.07	0.89	82.1
Ir07A-155-11	3		36.6	<0.09	16.7	5.72	17.1	<0.08	0.88	0.09	0.55	77.8
Ir07A-155-12	3		42.8	0.09	17.8	2.29	9.2	<0.08	0.53	<0.06	1.44	74.1
Ir07A-15	**3**	**11**	**39.3**	**<0.09**	**17.1**	**4.30**	**14.9**	**<0.08**	**0.96**	**0.08**	**0.79**	**77.7**
s			**3.1**	**-**	**0.6**	**1.00**	**2.5**	**-**	**0.25**	**0.02**	**0.38**	**2.6**
Ir11-241-1	3		39.3	<0.09	16.4	5.22	22.3	<0.08	1.43	0.06	0.44	85.2
Ir11-241-2	3		39.0	<0.09	16.0	4.97	22.2	<0.08	1.43	0.07	0.38	84.1
Ir11-242-1	3		38.8	<0.09	16.2	5.13	22.6	<0.08	1.11	0.07	0.31	84.3
Ir11-243-1	3		40.5	0.21	16.6	5.62	22.9	<0.08	1.54	0.07	0.53	88.1
Ir11-244-1	3		39.2	0.19	16.9	5.20	21.5	<0.08	1.24	0.07	0.63	85.0
Ir11-24	**3**	**5**	**39.4**	**<0.09**	**16.4**	**5.23**	**22.3**	**<0.08**	**1.35**	**0.07**	**0.46**	**85.4**
s			**0.7**	**-**	**0.4**	**0.24**	**0.5**	**-**	**0.17**	**0.00**	**0.13**	**1.6**
Ir11-06-2	3		36.6	<0.09	15.1	5.48	22.1	<0.08	2.38	0.10	0.13	81.9
Ir11-06-3	3		38.6	<0.09	15.6	5.59	21.8	<0.08	2.39	0.06	0.16	84.3
Ir11-06-4	3		40.5	<0.09	18.0	5.66	22.3	<0.08	1.50	0.07	0.79	88.9
Ir11-06-6	3		40.6	0.09	17.0	5.47	21.8	<0.08	1.75	0.11	0.45	87.3
Ir11-06-8	3		36.8	0.26	15.9	6.04	24.0	<0.08	1.56	0.04	0.25	84.9
Ir11-06-7	3		38.9	0.19	15.0	5.38	20.7	<0.08	5.14	<0.06	0.40	85.7
Ir11-06	**3**	**6**	**38.7**	**0.18**	**16.1**	**5.60**	**22.1**	**<0.08**	**2.45**	**0.08**	**0.36**	**85.5**
s			**1.7**	**0.09**	**1.2**	**0.24**	**1.1**	**-**	**1.37**	**0.03**	**0.24**	**2.4**
Ir11-211	3		36.5	0.09	15.5	6.16	24.9	<0.08	1.08	0.11	0.13	84.5
Ir11-212	3		40.3	<0.09	16.9	5.20	21.2	<0.08	0.91	0.14	0.75	85.5
Ir11-213	3		38.0	<0.09	15.9	5.95	24.9	<0.08	0.98	0.13	0.27	86.2
Ir11-214	3		39.3	<0.09	16.2	5.77	24.3	<0.08	0.92	0.19	0.39	87.1
Ir11-215	3		43.2	<0.09	17.2	4.19	16.9	<0.08	0.88	0.15	1.64	84.2
Ir11-21	**3**	**5**	**39.5**	**<0.09**	**16.3**	**5.45**	**22.4**	**<0.08**	**0.95**	**0.15**	**0.64**	**85.4**
s			**2.6**	**-**	**0.7**	**0.79**	**3.5**	**-**	**0.08**	**0.03**	**0.61**	**1.2**
Ir11-24b-1	3		43.0	<0.09	16.8	4.76	20.3	<0.08	1.82	0.21	0.63	87.6
Ir11-24b-2	3		39.3	0.62	16.9	4.95	19.0	<0.08	3.03	0.12	1.14	85.1
Ir11-24b-3	3		40.0	0.40	16.5	5.19	21.5	<0.08	1.59	0.15	0.56	86.0
Ir11-24b	**3**	**3**	**40.8**	**0.51**	**16.7**	**4.97**	**20.3**	**<0.08**	**2.15**	**0.16**	**0.78**	**86.3**
s			**1.9**	**0.16**	**0.2**	**0.22**	**1.3**	**-**	**0.77**	**0.05**	**0.32**	**1.28**

N: Number of analyses; Dia.: beam diameter.

Table A2-9a Continued.

Sample	Dia	N	SiO_2	TiO_2	Al_2O_3	FeO	MgO	MnO	CaO	Na_2O	K_2O	Total
Ir18-2-11	3		47.4	<0.09	12.1	3.48	16.0	<0.08	2.31	0.20	0.46	82.0
Ir18-2-12	3		52.4	0.13	17.1	2.29	10.5	<0.08	2.14	0.20	1.17	85.9
Ir18-2-13	3		48.7	<0.09	13.3	3.05	14.6	<0.08	2.17	0.25	0.55	82.7
Ir18-2-14	3		51.7	<0.09	15.5	2.88	12.8	<0.08	2.51	0.20	0.54	86.2
Ir18-2-15	3		51.0	<0.09	15.7	3.17	12.6	<0.08	2.37	0.22	0.57	85.6
Ir18-2-16	3		49.5	<0.09	14.9	2.86	12.3	<0.08	2.39	0.23	0.59	82.8
Ir18-2-17	3		44.8	<0.09	12.4	4.54	16.7	<0.08	3.57	0.11	0.31	82.6
Ir18-2-1	**3**	**7**	**49.4**	**<0.09**	**14.4**	**3.18**	**13.6**	**<0.08**	**2.49**	**0.20**	**0.60**	**83.9**
s			**2.6**	**-**	**1.8**	**0.70**	**2.2**	**-**	**0.49**	**0.04**	**0.27**	**1.8**
Ir18-3a1	3		51.3	0.14	17.1	3.25	12.0	<0.08	2.77	0.30	1.51	88.3
Ir18-3a2	3		47.0	0.09	15.9	5.30	17.2	<0.08	3.09	0.27	0.61	89.5
Ir18-3a3	3		47.1	0.23	15.4	7.38	13.8	<0.08	2.54	0.53	0.91	87.8
Ir18-3a4	3		52.8	<0.09	15.9	3.53	12.4	<0.08	2.18	0.46	0.87	88.1
Ir18-3a6	3		51.5	<0.09	15.3	3.18	12.4	<0.08	2.16	0.61	0.96	86.0
Ir18-3a5	3		52.1	0.17	17.2	4.15	11.7	<0.08	2.54	0.62	1.33	89.9
Ir18-3a	**3**	**6**	**50.3**	**0.16**	**16.1**	**4.46**	**13.2**	**<0.08**	**2.55**	**0.46**	**1.03**	**88.3**
s			**2.6**	**0.06**	**0.8**	**1.63**	**2.1**	**-**	**0.36**	**0.15**	**0.33**	**1.4**
Ir18-3b2	3		47.1	0.09	16.1	5.28	16.5	<0.08	2.33	0.53	0.92	88.9
Ir18-3b3	3		43.4	0.16	14.5	5.90	19.1	<0.08	2.44	0.43	0.68	86.7
Ir18-3b4	3		53.0	0.12	17.3	2.77	10.8	<0.08	2.58	0.47	1.49	88.5
Ir18-3b	**3**	**3**	**47.9**	**0.12**	**16.0**	**4.65**	**15.5**	**<0.08**	**2.45**	**0.48**	**1.03**	**88.0**
s			**4.8**	**0.04**	**1.4**	**1.65**	**4.2**	**-**	**0.13**	**0.05**	**0.41**	**1.2**
Ir18-3c1	3		51.3	<0.09	16.0	2.93	11.7	<0.08	2.26	0.56	0.97	85.8
Ir18-3c4	3		52.5	<0.09	16.5	2.70	11.2	<0.08	2.50	0.48	1.11	86.9
Ir18-3c5	3		52.9	<0.09	16.7	2.96	11.1	<0.08	2.62	0.43	1.13	87.8
Ir18-3c6	3		54.1	0.12	17.0	3.01	11.1	<0.08	2.20	0.45	1.39	89.4
Ir18-3c3	3		46.3	<0.09	15.1	4.30	14.7	<0.08	2.13	0.42	0.55	83.5
Ir18-3cA	**3**	**5**	**51.4**	**<0.09**	**16.3**	**3.18**	**11.9**	**<0.08**	**2.34**	**0.47**	**1.03**	**86.7**
s			**3.0**	**-**	**0.8**	**0.64**	**1.6**	**-**	**0.21**	**0.06**	**0.31**	**2.2**
Ir18-41	3		52.9	<0.09	16.8	2.92	10.7	<0.08	3.21	0.32	1.13	88.0
Ir18-42	3		51.6	<0.09	16.0	2.67	11.0	<0.08	2.86	0.23	1.06	85.4
Ir18-43	3		41.5	0.12	14.2	5.14	15.4	<0.08	2.43	0.11	0.81	79.8
Ir18-4a	**3**	**3**	**48.7**	**<0.09**	**15.7**	**3.58**	**12.4**	**<0.08**	**2.83**	**0.22**	**1.00**	**84.4**
s			**6.2**	**-**	**1.3**	**1.36**	**2.6**	**-**	**0.39**	**0.11**	**0.17**	**4.2**
Ir22-1-21	3		45.9	<0.09	13.2	6.45	15.6	<0.08	3.36	0.30	0.22	85.0
Ir22-1-22	3		44.8	<0.09	12.6	6.46	16.3	<0.08	3.36	0.31	0.21	84.1
Ir22-1-23	3		45.3	<0.09	13.4	6.11	15.6	<0.08	3.53	0.23	0.19	84.4
Ir22-1-24	3		45.9	<0.09	15.2	7.50	14.0	<0.08	3.60	0.37	0.67	87.2
Ir22-1-26	3		51.3	0.09	17.3	4.40	11.6	<0.08	3.60	0.54	0.99	89.8
Ir22-1-2	**3**	**5**	**46.6**	**<0.09**	**14.3**	**6.18**	**14.6**	**<0.08**	**3.49**	**0.35**	**0.46**	**86.1**
s			**2.7**	**-**	**1.9**	**1.12**	**1.9**	**-**	**0.12**	**0.12**	**0.36**	**2.40**

N: Number of analyses; Dia.: beam diameter.

Table A2-9b Individual and average compositions (wt.%) of melt particle type 2a with compositional heterogeneities.

Sample	Dia	N	SiO_2	TiO_2	Al_2O_3	FeO	MgO	MnO	CaO	Na_2O	K_2O	Total
Ir07A-016-5	3		54.2	<0.09	18.5	1.58	8.6	<0.08	2.55	0.10	1.34	86.8
Ir07A-016-6	3		53.8	<0.09	17.8	1.51	8.3	<0.08	2.18	0.07	1.11	84.8
Ir07A-016-7	3		52.9	<0.09	18.4	2.11	10.2	<0.08	2.46	0.11	1.18	87.4
Ir07A-016-8	3		49.3	<0.09	17.1	2.00	9.5	<0.08	2.76	0.27	0.86	81.9
Ir07A-016-9	3		51.2	0.10	17.8	1.67	9.6	<0.08	1.85	<0.06	1.04	83.2
Ir07A-01H	**3**	**5**	**52.3**	**<0.09**	**17.9**	**1.77**	**9.2**	**<0.08**	**2.36**	**0.14**	**1.11**	**84.8**
s			**2.0**	**-**	**0.6**	**0.26**	**0.8**	**-**	**0.35**	**0.09**	**0.18**	**2.3**
Ir07A-016-10	3		43.7	0.12	17.3	3.98	16.5	<0.08	1.23	0.06	0.76	83.7
Ir07A-012-9	3		41.2	0.10	17.0	4.42	17.3	<0.08	1.40	<0.06	0.49	81.9
Ir07A-012-10	3		43.6	0.10	17.3	2.61	10.5	<0.08	1.40	<0.06	1.20	76.8
Ir07A-012-8	3		38.7	0.12	16.5	4.25	15.3	<0.08	1.20	<0.06	0.60	76.6
Ir07A-01M		**4**	**41.8**	**0.11**	**17.0**	**3.82**	**14.9**	**<0.08**	**1.31**	**<0.06**	**0.76**	**79.8**
s			**2.4**	**0.01**	**0.4**	**0.82**	**3.0**	**-**	**0.11**	**-**	**0.31**	**3.6**
Ir07A-011-1	3		36.0	<0.09	15.1	7.39	26.4	<0.08	0.60	<0.06	<0.03	85.6
Ir07A-011-2	3		35.3	<0.09	15.2	7.31	26.7	<0.08	0.51	<0.06	<0.03	85.0
Ir07A-011-3	3		35.7	<0.09	14.6	7.61	25.7	<0.08	0.57	<0.06	<0.03	84.2
Ir07A-011-4	3		35.6	<0.09	14.6	7.36	28.5	<0.08	0.44	<0.06	0.04	86.5
Ir07A-011-5	3		35.5	<0.09	14.7	7.42	26.9	<0.08	0.47	<0.06	<0.03	85.2
Ir07A-011-6	3		35.5	<0.09	14.4	7.61	27.1	<0.08	0.48	<0.06	<0.03	85.1
Ir07A-011-7	3		35.4	<0.09	14.8	7.15	26.4	<0.08	0.54	<0.06	0.04	84.4
Ir07A-011-8	3		34.5	<0.09	14.1	7.58	26.3	<0.08	0.56	<0.06	<0.03	83.1
Ir07A-011-9	3		35.3	<0.09	13.9	6.20	26.7	<0.08	0.39	<0.06	<0.03	82.6
Ir07A-011-10	3		35.7	<0.09	15.0	6.78	26.4	<0.08	0.52	<0.06	<0.03	84.5
Ir07A-011-11	3		35.9	<0.09	15.5	6.59	26.8	<0.08	0.59	<0.06	0.03	85.6
Ir07A-011-12	3		34.7	<0.09	15.0	7.81	23.7	<0.08	0.55	<0.06	0.03	81.9
Ir07A-013-1	3		36.1	<0.09	15.4	7.60	26.3	<0.08	0.63	<0.06	<0.03	86.2
Ir07A-013-2	3		35.3	<0.09	15.4	6.62	26.0	<0.08	0.74	<0.06	<0.03	84.1
Ir07A-013-3	3		36.1	<0.09	15.5	6.64	26.5	<0.08	0.63	<0.06	0.03	85.5
Ir07A-013-4	3		35.6	<0.09	15.1	6.81	26.4	<0.08	0.63	<0.06	<0.03	84.7
Ir07A-013-5	3		35.0	<0.09	15.4	6.91	25.2	<0.08	0.67	<0.06	<0.03	83.3
Ir07A-012-1	3		35.9	<0.09	16.1	6.42	25.3	<0.08	0.76	0.06	0.05	84.6
Ir07A-012-2	3		34.9	<0.09	15.0	7.37	25.9	<0.08	0.81	0.06	<0.03	84.0
Ir07A-012-3	3		35.3	<0.09	15.9	7.00	25.6	<0.08	0.69	<0.06	0.04	84.7
Ir07A-012-4	3		35.5	<0.09	15.3	7.12	26.7	<0.08	0.73	<0.06	<0.03	85.5
Ir07A-012-5	3		35.6	<0.09	15.4	7.31	27.1	<0.08	0.62	0.06	<0.03	86.1
Ir07A-012-6	3		34.0	<0.09	15.4	7.08	25.2	<0.08	0.67	<0.06	<0.03	82.4
Ir07A-012-7	3		35.3	<0.09	15.8	7.06	24.8	<0.08	0.80	<0.06	0.03	83.9
Ir07A-016-1	3		35.1	<0.09	15.5	5.79	26.8	<0.08	0.77	<0.06	<0.03	84.1
Ir07A-016-2	3		35.5	<0.09	15.8	7.09	26.9	<0.08	0.70	<0.06	<0.03	86.1
Ir07A-016-3	3		36.8	<0.09	17.2	6.19	23.9	<0.08	0.85	<0.06	0.15	85.1
Ir07A-016-4	3		35.4	<0.09	16.6	6.96	25.9	<0.08	0.75	<0.06	0.06	85.8
Ir07A-01L	**3**	**28**	**35.5**	**<0.09**	**15.3**	**7.03**	**26.1**	**<0.08**	**0.63**	**<0.06**	**<0.03**	**84.6**
s			**0.5**	**<0.09**	**0.7**	**0.49**	**1.0**	**-**	**0.12**	**-**	**-**	**1.2**

N: Number of analyses; Dia.: beam diameter.

Table A2-9b Continued.

Sample	Dia	N	SiO_2	TiO_2	Al_2O_3	FeO	MgO	MnO	CaO	Na_2O	K_2O	Total
Ir15a1-2	3		46.0	0.09	17.5	4.19	14.9	<0.08	1.54	0.09	1.48	85.9
Ir15a1-3	3		52.7	0.16	13.2	5.26	18.6	<0.08	1.32	<0.06	0.17	91.4
Ir15a1-4	3		40.9	<0.09	16.3	6.41	21.6	<0.08	1.70	0.11	0.33	87.3
Ir15a1-5	3		41.0	<0.09	16.9	6.50	20.6	<0.08	1.63	0.12	0.54	87.2
Ir15a1H	**3**	**4**	**45.1**	**0.13**	**16.0**	**5.59**	**18.9**	**<0.08**	**1.55**	**0.11**	**0.63**	**87.9**
s			**5.6**	**0.05**	**1.9**	**1.09**	**2.9**	**-**	**0.16**	**0.02**	**0.59**	**2.4**
Ir15a1-1	3		53.3	<0.09	18.1	3.03	5.1	<0.08	1.06	0.10	3.55	84.3
Ir15a1-6	3		55.7	0.11	18.9	3.24	6.2	<0.08	1.45	0.10	3.53	89.1
Ir15a1-7	3		54.7	0.09	18.7	3.15	5.7	<0.08	1.35	0.08	3.21	86.9
Ir15a1-8	3		52.7	0.14	18.9	3.42	7.6	<0.08	1.07	0.09	3.97	87.9
Ir15a1L	**3**	**4**	**54.1**	**0.11**	**18.7**	**3.21**	**6.1**	**<0.08**	**1.23**	**0.09**	**3.57**	**87.0**
s			**1.4**	**0.02**	**0.4**	**0.16**	**1.1**	**-**	**0.20**	**0.01**	**0.31**	**2.0**
Ir18-2-24	3		50.3	0.10	16.3	2.81	10.7	<0.08	2.28	0.19	0.96	83.7
Ir18-2-26	3		51.5	0.11	17.1	2.68	10.0	<0.08	2.24	0.17	1.08	84.9
Ir18-2-27	3		52.0	0.13	17.0	2.38	10.0	<0.08	2.47	0.28	1.19	85.5
Ir18-2-2H	**3**	**3**	**51.3**	**0.11**	**16.8**	**2.62**	**10.2**	**<0.08**	**2.33**	**0.21**	**1.08**	**84.7**
s			**0.9**	**0.02**	**0.4**	**0.22**	**0.4**	**-**	**0.12**	**0.06**	**0.11**	**0.9**
Ir18-2-21	3		45.3	0.22	15.9	5.41	18.0	<0.08	2.03	0.16	0.74	87.7
Ir18-2-22	3		43.7	0.15	16.1	4.80	16.0	<0.08	2.41	0.15	0.45	83.8
Ir18-2-23	3		49.3	0.13	17.3	3.69	14.6	<0.08	2.31	0.26	0.80	88.4
Ir18-2-25	3		47.2	<0.09	16.2	3.95	14.2	<0.08	2.31	0.23	0.67	84.8
Ir18-2-2L	**3**	**4**	**46.4**	**0.17**	**16.4**	**4.46**	**15.7**	**<0.08**	**2.27**	**0.20**	**0.67**	**86.2**
s			**2.4**	**0.05**	**0.6**	**0.79**	**1.7**	**-**	**0.16**	**0.05**	**0.15**	**2.2**
Ir18-2-31	3		50.5	0.10	17.0	2.85	11.7	<0.08	2.09	0.28	1.09	85.6
Ir18-2-34	3		52.6	0.10	17.3	2.53	10.1	<0.08	2.15	0.26	1.07	86.1
Ir18-2-35	3		52.2	0.11	17.2	2.69	10.2	<0.08	2.29	0.26	1.02	85.9
Ir18-2-36	3		53.0	<0.09	17.1	2.88	10.7	<0.08	2.54	0.26	1.16	87.8
Ir18-2-37	3		51.9	<0.09	17.2	2.87	11.0	<0.08	2.37	0.26	1.00	86.7
Ir18-2-3H	**3**	**5**	**52.0**	**0.10**	**17.2**	**2.76**	**10.7**	**<0.08**	**2.29**	**0.26**	**1.07**	**86.4**
s			**1.0**	**0.004**	**0.1**	**0.15**	**0.7**	**-**	**0.18**	**0.01**	**0.06**	**0.8**
Ir18-2-32	3		45.5	0.15	16.1	5.05	16.7	<0.08	3.22	0.25	0.47	87.5
Ir18-2-33	3		45.8	<0.09	16.2	5.19	15.9	<0.08	2.15	0.21	0.50	86.1
Ir18-2-3L	**3**	**2**	**45.7**	**<0.09**	**16.1**	**5.12**	**16.3**	**<0.08**	**2.69**	**0.23**	**0.49**	**86.8**
s			**0.2**	**-**	**0.1**	**0.10**	**0.5**	**-**	**0.76**	**0.03**	**0.03**	**1.0**
Ir22-21	3		55.0	0.10	18.5	3.16	8.3	<0.08	2.75	0.35	1.69	89.8
Ir22-22	3		54.5	0.11	17.9	3.19	8.8	<0.08	2.50	0.34	1.50	88.7
Ir22-23	3		54.6	0.12	17.9	3.41	8.6	<0.08	2.90	0.39	1.44	89.3
Ir22-25	3		52.4	<0.09	17.4	3.75	9.6	<0.08	3.12	0.35	1.08	87.6
Ir22-2H	**3**	**4**	**54.1**	**0.11**	**17.9**	**3.37**	**8.8**	**<0.08**	**2.82**	**0.36**	**1.43**	**88.9**
s			**1.2**	**0.01**	**0.4**	**0.27**	**0.5**	**-**	**0.26**	**0.02**	**0.26**	**0.9**
Ir22-24	3		46.0	<0.09	15.0	7.31	16.3	<0.08	4.12	0.18	0.25	89.2
Ir22-26	3		46.0	<0.09	15.0	7.36	16.3	<0.08	3.91	0.21	0.19	88.9
Ir22-2L	**3**	**2**	**46.0**	**<0.09**	**15.0**	**7.33**	**16.3**	**<0.08**	**4.01**	**0.19**	**0.22**	**89.0**
s			**0.0**	**-**	**0.0**	**0.04**	**0.0**	**-**	**0.15**	**0.02**	**0.04**	**0.2**

N: Number of analyses; Dia.: beam diameter.

Table A2-10 Individual and average compositions (wt.%) of melt particle type 2b.

Sample	Dia	N	SiO_2	TiO_2	Al_2O_3	FeO	MgO	MnO	CaO	Na_2O	K_2O	Total
Ir07-073-1	3		38.9	<0.09	15.8	5.45	19.9	<0.08	1.27	0.09	0.27	81.8
Ir07-073-2	3		35.6	<0.09	15.4	5.29	16.7	<0.08	1.15	0.09	0.27	74.5
Ir07-071-1	3		35.5	<0.09	15.1	7.24	27.2	<0.08	0.76	<0.06	0.03	86.0
Ir07-071-2	3		35.9	<0.09	15.4	7.93	27.9	<0.08	0.71	<0.06	0.00	87.9
Ir07-071-3	3		34.6	<0.09	14.5	6.94	25.8	<0.08	0.84	<0.06	0.01	82.8
Ir07-072-3	3		37.2	<0.09	17.8	6.21	25.1	<0.08	0.99	<0.06	0.10	87.5
Ir07-074	3		35.6	<0.09	15.3	7.10	26.8	<0.08	0.64	<0.06	0.02	85.5
Ir07-075-1	3		36.2	<0.09	15.1	7.27	26.6	<0.08	0.57	<0.06	0.02	85.8
Ir07-075-2	3		35.5	<0.09	14.8	7.34	26.3	<0.08	0.62	<0.06	0.01	84.6
Ir07-075-3	3		36.3	<0.09	14.9	7.05	26.3	<0.08	0.62	0.06	0.02	85.3
Ir07A-07	**3**	**10**	**35.8**	**<0.09**	**15.4**	**7.13**	**26.5**	**<0.08**	**0.72**	**<0.06**	**0.03**	**85.6**
s			**1.2**	**-**	**0.9**	**0.86**	**3.6**	**-**	**0.24**	**-**	**0.11**	**3.9**
Ir18-11	3		44.5	<0.09	10.7	4.35	17.9	<0.08	2.38	0.30	0.50	80.6
Ir18-12	3		44.4	<0.09	9.7	4.82	21.3	<0.08	2.11	0.24	0.27	82.9
Ir18-13	3		43.9	<0.09	9.7	5.74	23.9	<0.08	2.78	0.27	0.23	86.6
Ir18-14	3		44.4	<0.09	9.1	4.86	20.9	<0.08	2.59	0.22	0.28	82.4
Ir18-15	3		40.7	<0.09	11.5	6.63	25.1	<0.08	1.72	0.21	0.07	85.9
Ir18-16	3		43.3	<0.09	9.1	4.53	19.5	<0.08	1.93	0.22	0.31	78.9
Ir18-17	3		44.2	<0.09	9.2	4.45	21.6	<0.08	1.79	0.21	0.21	81.6
Ir18-19	3		40.7	<0.09	10.4	5.85	23.5	<0.08	1.67	0.18	0.13	82.4
Ir18-110	3		43.5	<0.09	15.9	5.02	17.5	<0.08	2.88	0.23	0.53	85.7
Ir18-1	**3**	**9**	**43.3**	**<0.09**	**10.6**	**5.14**	**21.2**	**<0.08**	**2.21**	**0.23**	**0.28**	**83.0**
s			**1.5**	**-**	**2.2**	**0.77**	**2.6**	**-**	**0.47**	**0.04**	**0.15**	**2.6**

N: Number of analyses; Dia.: beam diameter.

Table A2-10 Continued.

Sample	Dia	N	SiO_2	TiO_2	Al_2O_3	FeO	MgO	MnO	CaO	Na_2O	K_2O	Total
Ir07-171-7	3		40.9	<0.09	15.9	3.41	14.6	<0.08	0.73	0.09	0.42	76.0
Ir07-171-8	3		42.9	<0.09	16.1	3.35	14.0	<0.08	0.92	0.12	0.47	77.9
Ir07-173-5	3		44.7	<0.09	16.5	2.64	11.8	<0.08	1.72	0.13	0.53	78.0
Ir07-173-6	3		42.0	<0.09	16.0	2.88	12.0	<0.08	1.40	0.08	0.47	74.9
Ir07-173-7	3		48.7	<0.09	16.8	1.92	9.7	<0.08	1.91	0.20	0.97	80.3
Ir07A-17H	**3**	**5**	**43.9**	**<0.09**	**16.3**	**2.84**	**12.4**	**<0.08**	**1.34**	**0.13**	**0.57**	**77.4**
s			**3.0**	**-**	**0.4**	**0.61**	**1.9**	**-**	**0.51**	**0.05**	**0.23**	**2.1**
Ir07-171-1	3		36.4	<0.09	15.0	6.87	26.9	<0.08	0.67	0.07	0.03	85.9
Ir07-171-2	3		36.3	<0.09	15.2	7.50	27.7	<0.08	0.67	<0.06	0.02	87.5
Ir07-171-3	3		35.3	<0.09	14.7	7.35	26.4	<0.08	0.55	0.06	0.02	84.4
Ir07-171-4	3		35.6	<0.09	15.2	7.62	26.3	<0.08	0.57	<0.06	0.03	85.4
Ir07-171-5	3		35.9	<0.09	14.8	7.20	26.6	<0.08	0.69	0.06	0.02	85.3
Ir07-171-6	3		35.7	<0.09	14.8	7.16	25.9	<0.08	0.62	<0.06	0.01	84.3
Ir07-172-1	3		36.1	<0.09	14.6	6.93	27.5	<0.08	0.61	0.06	0.00	85.8
Ir07-172-2	3		35.9	<0.09	14.8	7.35	27.6	<0.08	0.78	<0.06	0.04	86.6
Ir07-172-3	3		35.6	<0.09	14.9	7.27	25.4	<0.08	0.67	<0.06	0.01	83.9
Ir07-172-4	3		35.3	<0.09	15.3	7.27	26.0	<0.08	0.64	<0.06	0.03	84.7
Ir07-173-1	3		35.2	<0.09	14.8	6.64	25.0	<0.08	0.74	0.07	0.01	82.6
Ir07-173-2	3		35.7	<0.09	14.5	6.67	25.7	<0.08	0.59	<0.06	0.02	83.3
Ir07-173-3	3		35.6	<0.09	15.4	6.88	25.2	<0.08	0.76	<0.06	0.00	83.9
Ir07-173-4	3		36.3	<0.09	15.2	7.02	26.4	<0.08	0.79	<0.06	0.03	85.8
Ir07A-17L	**3**	**14**	**35.8**	**<0.09**	**15.0**	**7.12**	**26.3**	**<0.08**	**0.67**	**<0.06**	**0.02**	**84.9**
s			**0.4**	**-**	**0.3**	**0.30**	**0.9**	**-**	**0.08**	**-**	**0.01**	**1.3**
Ir18-14	3		45.2	<0.09	9.6	4.67	18.8	<0.08	1.89	0.30	0.40	80.9
Ir18-15	3		44.8	<0.09	10.7	4.49	17.1	<0.08	2.06	0.23	0.44	79.9
Ir18-16	3		44.2	<0.09	11.1	4.17	16.0	<0.08	2.23	0.28	0.62	78.7
Ir18-1bH	**3**	**3**	**44.7**	**<0.09**	**10.5**	**4.45**	**17.3**	**<0.08**	**2.06**	**0.27**	**0.49**	**79.8**
s			**0.5**	**-**	**0.8**	**0.25**	**1.4**	**-**	**0.17**	**0.04**	**0.12**	**1.1**
Ir18-11	3		40.4	<0.09	11.9	5.96	24.9	<0.08	1.98	0.32	0.14	85.5
Ir18-12	3		39.4	<0.09	11.3	6.24	24.9	<0.08	2.04	0.23	0.12	84.3
Ir18-13	3		38.8	<0.09	12.9	7.62	26.8	<0.08	1.29	0.30	0.07	87.7
Ir18-1aL	**3**	**3**	**39.6**	**<0.09**	**12.0**	**6.61**	**25.5**	**<0.08**	**1.77**	**0.28**	**0.11**	**85.8**
s			**0.8**	**-**	**0.8**	**0.89**	**1.1**	**-**	**0.42**	**0.05**	**0.04**	**1.8**

N: Number of analyses; Dia.: beam diameter.

A2.3.2 Chemical composition of particles within accretionary lapilli from El Guayal

A2.3.2.1 Composition of silicate melt particles (altered to clay minerals)

Average compositions

Table A2-11a Average composition (wt.%) of melt particles within accretionary lapilli

Sample	Dia	N	SiO_2	TiO_2	Al_2O_3	FeO	MgO	MnO	CaO	Na_2O	K_2O	Total
L11NT	3	12	51.4	0.34	19.0	3.22	12.7	<0.08	0.96	0.22	3.29	91.1
s			2.7	0.24	0.6	0.96	2.3	-	0.16	0.08	1.18	1.2
L9a11.1A	3	3	49.2	<0.09	14.5	1.57	15.5	<0.08	1.94	0.25	0.94	83.9
s			1.5	-	1.0	0.24	1.5	-	0.27	0.02	0.22	0.6
L9a11.1B	3	3	55.1	<0.09	19.4	0.82	7.87	<0.08	1.00	0.31	4.21	88.7
s			1.0	-	0.4	0.10	0.29	-	0.02	0.03	0.54	1.6
L9a11.1C	3	3	48.3	<0.09	12.3	1.80	18.0	<0.08	2.26	0.27	0.53	83.5
s			0.9	-	0.8	0.09	0.6	-	0.04	0.01	0.12	1.1

N: Number of analyses; Dia.: beam diameter.

Table A2-11b. Average composition (wt.%) of melt particles within accretionary lapilli with compositional heterogeneities.

Sample	Dia	N	SiO_2	TiO_2	Al_2O_3	FeO	MgO	MnO	CaO	Na_2O	K_2O	Total
L4NT2H	3	13	52.3	0.30	17.3	2.99	13.4	<0.08	1.51	0.24	2.69	90.8
s			1.4	0.21	0.8	0.49	1.2	-	0.45	0.13	0.51	1.7
L4NT2L	3	4	37.8	0.13	15.1	7.70	24.2	<0.08	0.80	0.05	0.29	86.0
s			2.2	0.02	0.9	0.83	1.5	-	0.12	0.04	0.17	1.4
L9a2b10-1AH	3	4	52.7	<0.09	16.7	1.92	10.6	<0.08	1.68	0.40	1.48	85.4
s			0.8	-	0.4	0.04	0.1	-	0.07	0.06	0.08	0.7
L9a2b10-1BL	3	2	38.7	0.15	13.9	8.41	21.8	<0.08	1.22	0.20	0.32	84.7
s			3.1	0.05	0.4	1.20	2.7	-	0.12	0.11	0.18	1.0
L9a2b1-1bH	3	2	52.8	<0.09	16.3	1.91	9.94	<0.08	1.49	0.42	1.71	84.6
s			0.5	-	0.5	0.05	0.16	-	0.16	0.06	0.17	0.0
L9a2b1-15L	3	4	38.7	0.22	14.0	7.62	21.1	<0.08	1.34	0.16	0.23	83.3
s			1.4	0.12	1.0	0.73	0.8	-	0.07	0.03	0.16	1.0
L9a2b8-5B	3	4	52.7	<0.09	16.5	1.47	9.9	<0.08	1.64	0.26	1.76	84.4
s			1.6	-	0.6	0.06	0.2	-	0.05	0.03	0.08	2.1
L9a2b8-5Na	3	3	50.2	<0.09	16.0	1.59	10.2	<0.08	1.08	2.07	1.59	82.8
s			0.6	-	0.2	0.06	0.0	-	0.28	0.23	0.14	0.6

N: Number of analyses; Dia.: beam diameter.

Table A2-12 Average composition (wt.%) of clay minerals within accretionary lapilli which are pseudomorphs of a former laths-shaped phase.

Sample	Dia	N	SiO_2	TiO_2	Al_2O_3	FeO	MgO	MnO	CaO	Na_2O	K_2O	Total
L9a2b6-4		6	52.5	<0.09	17.8	0.70	4.56	<0.08	1.46	0.22	5.67	82.9
s			2.4	-	2.9	0.83	2.42	-	0.52	0.06	2.56	1.9
L9a2b5-4		2	55.3	<0.09	19.5	0.09	2.44	<0.08	1.27	0.47	6.22	85.3
s			0.5	-	0.6	0.03	0.18	-	0.08	0.31	1.30	0.6
L4NT3H	3	4	53.9	<0.09	27.1	0.22	3.06	<0.08	1.16	0.77	2.93	89.2
s			2.3	-	2.0	0.14	0.93	-	0.36	0.38	1.29	2.0
L4NT3M	3	2	43.3	<0.09	12.9	5.35	22.8	<0.08	0.79	0.26	2.12	87.5
s			3.1	-	0.9	0.94	1.4	-	0.04	0.13	1.66	3.4
L4Nucl10H		4	55.3	<0.09	25.7	0.31	3.02	<0.08	1.48	0.72	3.51	90.0
s			2.4	-	2.5	0.17	0.63	-	1.07	0.38	2.34	1.6
L4Nucl10M		4	43.6	<0.09	12.4	4.50	19.50	<0.08	0.93	0.17	2.83	83.9
s			3.1	-	1.8	1.00	2.67	-	0.32	0.07	2.20	4.4

N: Number of analyses; Dia.: beam diameter.

Individual and average compositions of melt particles (altered to clay minerals)

Table A2-12a Individual and average compositions (wt.%) of melt particles within accretionary lapilli.

Sample	Dia	N	SiO_2	TiO_2	Al_2O_3	FeO	MgO	MnO	CaO	Na_2O	K_2O	Total
L11NT-1	3		52.6	0.18	19.7	2.33	12.1	<0.08	1.12	0.26	2.50	90.8
L11NT-2	3		54.8	0.22	20.0	1.41	9.8	<0.08	1.16	0.20	3.15	90.7
L11NT-3	3		48.4	0.18	18.8	3.22	15.4	<0.08	1.14	0.16	1.89	89.2
L11NT-4	3		45.8	0.45	18.3	5.36	17.7	<0.08	0.84	0.15	1.63	90.4
L11NT-5	3		52.1	0.32	18.3	2.79	12.1	<0.08	1.13	0.17	3.85	90.8
L11NT-6	3		52.3	0.18	18.6	2.86	12.3	<0.08	1.10	0.20	3.00	90.5
L11NT-7	3		54.7	0.34	18.7	3.36	9.9	<0.08	0.81	0.21	5.12	93.2
L11NT-8	3		53.9	0.39	18.9	3.80	10.3	<0.08	0.76	0.20	5.41	93.6
L11NT-9	3		52.0	0.25	19.4	2.83	11.7	<0.08	0.90	0.38	4.07	91.6
L11NT-10	3		50.6	0.24	19.3	3.45	13.3	<0.08	0.85	0.29	3.47	91.5
L11NT-11	3		50.9	0.28	18.4	3.91	13.1	<0.08	0.78	0.33	3.11	90.8
L11NT-12	3		49.2	1.04	19.1	3.37	14.5	<0.08	0.90	0.13	2.22	90.4
L11NT	**3**	**12**	**51.4**	**0.34**	**19.0**	**3.22**	**12.7**	**<0.08**	**0.96**	**0.22**	**3.29**	**91.1**
s			**2.7**	**0.24**	**0.6**	**0.96**	**2.3**	**-**	**0.16**	**0.08**	**1.18**	**1.2**
9a11.11	3		50.8	0.13	15.2	1.30	13.8	<0.08	1.85	0.27	1.18	84.5
9a11.12	3		47.7	<0.09	15.0	1.77	15.9	<0.08	1.73	0.23	0.86	83.3
9a11.13	3		48.9	<0.09	13.3	1.66	16.7	<0.08	2.24	0.25	0.77	83.8
L9a11.1A	**3**	**3**	**49.2**	**<0.09**	**14.5**	**1.57**	**15.5**	**<0.08**	**1.94**	**0.25**	**0.94**	**83.9**
s			**1.5**	**-**	**1.0**	**0.24**	**1.5**	**-**	**0.27**	**0.02**	**0.22**	**0.6**
9a11.14	3		54.7	<0.09	19.1	0.81	7.8	<0.08	0.99	0.28	3.62	87.4
9a11.15	3		56.2	0.11	19.8	0.73	7.6	<0.08	1.02	0.33	4.70	90.5
9a11.16	3		54.3	<0.09	19.3	0.92	8.2	<0.08	0.98	0.32	4.31	88.4
L9a11.1B	**3**	**3**	**55.1**	**<0.09**	**19.4**	**0.82**	**7.9**	**<0.08**	**1.00**	**0.31**	**4.21**	**88.7**
s			**1.0**	**-**	**0.4**	**0.10**	**0.3**	**-**	**0.02**	**0.03**	**0.54**	**1.6**
9a11.17	3		49.3	<0.09	13.2	1.74	17.3	<0.08	2.31	0.25	0.67	84.7
9a11.18	3		47.6	<0.09	12.2	1.90	18.3	<0.08	2.24	0.28	0.47	83.1
9a11.19	3		48.0	<0.09	11.6	1.76	18.4	<0.08	2.23	0.27	0.45	82.8
L9a11.1C	**3**	**3**	**48.3**	**<0.09**	**12.3**	**1.80**	**18.0**	**<0.08**	**2.26**	**0.27**	**0.53**	**83.5**
s			**0.9**	**-**	**0.8**	**0.09**	**0.6**	**-**	**0.04**	**0.01**	**0.12**	**1.1**

N: Number of analyses; Dia.: beam diameter.

Table A2-12b Individual and average compositions of melt particles within accretionary lapilli with compositional heterogeneities.

Sample	Dia	N	SiO$_2$	TiO$_2$	Al$_2$O$_3$	FeO	MgO	MnO	CaO	Na$_2$O	K$_2$O	Total
L4NT1-2	3		53.7	0.28	18.5	3.24	12.0	<0.08	2.24	0.38	2.88	93.2
L4NT1-3	3		53.5	0.97	17.8	2.99	12.3	<0.08	1.49	0.25	3.20	92.5
L4NT1-4	3		52.3	0.20	17.9	3.27	12.8	<0.08	2.68	0.62	2.31	92.1
L4NT1-5	3		54.9	0.17	18.4	1.78	11.5	<0.08	1.19	0.24	2.35	90.5
L4NT1-6	3		51.2	0.28	16.6	3.11	14.3	<0.08	1.24	0.19	2.87	89.8
L4NT1-8	3		53.0	0.27	17.2	3.37	13.6	<0.08	1.24	0.17	3.44	92.3
L4NT1-9	3		53.7	0.27	17.4	3.35	13.3	<0.08	1.29	0.22	2.87	92.4
L4NT1-10	3		51.4	0.27	16.9	2.93	14.3	<0.08	1.16	0.21	2.98	90.2
L4NT2-4	3		51.4	0.19	18.0	2.52	12.8	<0.08	1.18	0.20	2.39	88.7
L4NT2-6	3		52.8	0.28	16.7	3.74	13.7	<0.08	1.51	0.13	2.81	91.7
L4NT2-7	3		51.8	0.24	17.2	2.71	13.9	<0.08	1.50	0.14	2.46	89.9
L4NT2-9	3		49.7	0.16	15.9	2.76	16.0	<0.08	1.41	0.19	1.40	87.6
L4NT2-10	1		50.9	0.27	16.9	3.16	13.6	<0.08	1.43	0.16	2.97	89.4
L4NT2H	**3**	**13**	**52.3**	**0.30**	**17.3**	**2.99**	**13.4**	**<0.08**	**1.51**	**0.24**	**2.69**	**90.8**
s			**1.4**	**0.21**	**0.8**	**0.49**	**1.2**	**<0.08**	**0.45**	**0.13**	**0.51**	**1.7**
L4NT2-2	3		36.2	0.11	14.7	8.59	25.5	<0.08	0.68	0.01	0.10	85.9
L4NT2-3	3		36.9	0.14	15.0	8.10	24.2	<0.08	0.74	0.06	0.26	85.3
L4NT2-5	3		41.1	0.11	16.4	6.67	22.2	<0.08	0.97	0.10	0.51	88.1
L4NT2-8	3		36.8	0.14	14.2	7.43	25.1	<0.08	0.80	0.04	0.29	84.9
L4NT2L	**3**	**4**	**37.8**	**0.13**	**15.1**	**7.70**	**24.2**	**<0.08**	**0.80**	**0.05**	**0.29**	**86.0**
s			**2.2**	**0.02**	**0.9**	**0.83**	**1.5**	**-**	**0.12**	**0.04**	**0.17**	**1.4**
9a2b10-1A1	3		51.9	<0.09	16.5	1.94	10.7	<0.08	1.67	0.32	1.43	84.5
9a2b10-1A2	3		52.5	<0.09	17.1	1.86	10.4	<0.08	1.78	0.39	1.47	85.5
9a2b10-1B1	3		52.8	<0.09	16.8	1.94	10.6	<0.08	1.64	0.44	1.60	85.8
9a2b10-1B2	3		53.7	<0.09	16.3	1.96	10.5	<0.08	1.63	0.45	1.44	86.0
L9a2b10-1AH	**3**	**4**	**52.7**	**<0.09**	**16.7**	**1.92**	**10.6**	**<0.08**	**1.68**	**0.40**	**1.48**	**85.4**
s			**0.8**	**-**	**0.4**	**0.04**	**0.1**	**-**	**0.07**	**0.06**	**0.08**	**0.7**
9a2b10-1A3	3		40.9	0.18	13.6	7.56	19.9	<0.08	1.14	0.28	0.45	84.0
9a2b10-1B3	3		36.5	0.12	14.3	9.26	23.7	<0.08	1.30	0.12	0.19	85.4
L9a2b10-1BL	**3**	**2**	**38.7**	**0.15**	**13.9**	**8.41**	**21.8**	**<0.08**	**1.22**	**0.20**	**0.32**	**84.7**
s			**3.1**	**0.05**	**0.4**	**1.20**	**2.7**	**-**	**0.12**	**0.11**	**0.18**	**1.0**
9a2b1-15	3		53.2	<0.09	15.9	1.94	10.1	<0.08	1.38	0.46	1.59	84.6
9a2b1-16	3		52.5	<0.09	16.6	1.88	9.8	<0.08	1.60	0.37	1.84	84.6
L9a2b1-1bH	**3**	**2**	**52.8**	**<0.09**	**16.3**	**1.91**	**9.9**	**<0.08**	**1.49**	**0.42**	**1.71**	**84.6**
s			**0.5**	**-**	**0.5**	**0.05**	**0.2**	**-**	**0.16**	**0.06**	**0.17**	**0.0**
9a2b1-11	3		40.4	0.16	14.5	7.17	20.2	<0.08	1.26	0.19	0.46	84.3
9a2b1-12	3		39.2	<0.09	13.1	7.64	20.9	<0.08	1.40	0.15	0.14	82.5
9a2b1-13	3		37.9	0.13	13.1	8.64	21.0	<0.08	1.30	0.12	0.10	82.2
9a2b1-14	3		37.4	0.35	15.2	7.02	22.1	<0.08	1.41	0.18	0.24	83.9
L9a2b1-15L	**3**	**4**	**38.7**	**0.22**	**14.0**	**7.62**	**21.1**	**<0.08**	**1.34**	**0.16**	**0.23**	**83.3**
s			**1.4**	**0.12**	**1.0**	**0.73**	**0.8**	**-**	**0.07**	**0.03**	**0.16**	**1.0**

N: Number of analyses; Dia.: beam diameter.

Table A2-12b Continued.

Sample	Dia	N	SiO_2	TiO_2	Al_2O_3	FeO	MgO	MnO	CaO	Na_2O	K_2O	Total
L9a2b8-54	3		53.8	<0.09	16.9	1.51	9.8	<0.08	1.66	0.29	1.68	85.7
L9a2b8-55	3		54.1	<0.09	17.1	1.46	9.9	<0.08	1.69	0.25	1.87	86.4
L9a2b8-58	3		52.5	0.10	16.4	1.52	9.8	<0.08	1.66	0.23	1.75	83.9
L9a2b8-59	3		50.5	<0.09	15.8	1.38	10.3	<0.08	1.56	0.25	1.74	81.6
L9a2b8-5B	**3**	**4**	**52.7**	**<0.09**	**16.5**	**1.47**	**9.9**	**<0.08**	**1.64**	**0.26**	**1.76**	**84.4**
s			**1.6**	**-**	**0.6**	**0.06**	**0.2**	**-**	**0.05**	**0.03**	**0.08**	**2.1**
L9a2b8-51	3		50.8	<0.09	16.2	1.52	10.2	<0.08	1.41	1.81	1.46	83.5
L9a2b8-52	3		49.6	<0.09	15.8	1.64	10.2	<0.08	0.95	2.16	1.73	82.2
L9a2b8-53	3		50.3	0.09	16.1	1.60	10.2	<0.08	0.90	2.23	1.57	82.9
L9a2b8-5Na	**3**	**3**	**50.2**	**<0.09**	**16.0**	**1.59**	**10.2**	**<0.08**	**1.08**	**2.07**	**1.59**	**82.8**
s			**0.6**	**-**	**0.2**	**0.06**	**0.0**	**-**	**0.28**	**0.23**	**0.14**	**0.6**
9a2b5-4B1H	3		51.1	0.12	16.1	1.39	8.6	<0.08	1.40	0.27	2.62	81.6
9a2b5-4A1L	3		41.0	<0.09	15.0	5.93	20.1	<0.08	1.52	0.18	0.45	84.2

N: Number of analyses; Dia.: beam diameter.

Table A2-13 Individual and average composition (wt.%) of clay minerals within accretionary lapilli which are pseudomorphs of a former laths-shaped phase within accretionary lapilli.

Sample	Dia	N	SiO_2	TiO_2	Al_2O_3	FeO	MgO	MnO	CaO	Na_2O	K_2O	Total
9a2b6-4T1	0		49.5	<0.09	13.4	1.98	7.9	<0.08	0.94	0.15	7.42	81.3
9a2b6-4T2	0		53.2	0.09	20.1	0.12	2.9	<0.08	1.38	0.30	4.81	82.9
9a2b6-4T3	0		52.4	<0.09	21.0	0.15	3.4	<0.08	1.90	0.25	4.53	83.6
9a2b6-4T4	0		54.1	<0.09	17.3	0.09	2.1	<0.08	0.89	0.24	10.07	84.8
9a2b6-4T5	0		55.6	<0.09	19.6	0.33	3.9	<0.08	1.48	0.24	3.57	84.8
9a2b6-4T6	0		49.8	<0.09	15.6	1.50	7.3	<0.08	2.20	0.16	3.66	80.2
L9a2b6-4	**0**	**6**	**52.5**	**<0.09**	**17.8**	**0.70**	**4.6**	**<0.08**	**1.46**	**0.22**	**5.67**	**82.9**
s			**2.4**	**-**	**2.9**	**0.83**	**2.4**	**-**	**0.52**	**0.06**	**2.56**	**1.9**
9a2b5-41	0		55.6	<0.09	19.1	0.07	2.3	<0.08	1.22	0.25	7.15	85.7
9a2b5-43	0		54.9	<0.09	19.9	0.11	2.6	<0.08	1.33	0.69	5.30	84.8
L9a2b5-4	**0**	**2**	**55.3**	**<0.09**	**19.5**	**0.09**	**2.4**	**<0.08**	**1.27**	**0.47**	**6.22**	**85.3**
s			**0.5**	**-**	**0.6**	**0.03**	**0.2**	**-**	**0.08**	**0.31**	**1.30**	**0.6**
L4NT3-2	3		53.1	0.24	27.5	0.02	3.7	<0.08	0.84	0.37	1.64	87.4
L4NT3-3	3		54.4	<0.09	26.1	0.35	2.3	<0.08	1.29	1.27	3.98	89.7
L4NT3-5	3		56.9	<0.09	25.0	0.29	4.0	<0.08	0.90	0.59	4.11	91.9
L4NT3-6	3		51.4	<0.09	29.6	0.22	2.3	<0.08	1.60	0.84	2.01	87.9
L4NT3H	3	4	53.9	<0.09	27.1	0.22	3.1	<0.08	1.16	0.77	2.93	89.2
s			2.3	-	2.0	0.14	0.9	<0.08	0.36	0.38	1.29	2.0
L4NT3-4	3		45.5	<0.09	13.5	4.69	21.8	<0.08	0.77	0.35	3.29	89.9
L4NT3-7	3		41.1	<0.09	12.2	6.02	23.8	<0.08	0.82	0.16	0.94	85.1
L4NT3M	**3**	**2**	**43.3**	**<0.09**	**12.9**	**5.35**	**22.8**	**<0.08**	**0.79**	**0.26**	**2.12**	**87.5**
s			**3.1**	**-**	**0.9**	**0.94**	**1.4**	**-**	**0.04**	**0.13**	**1.66**	**3.4**
L4Nucl102	0		57.9	<0.09	23.4	0.18	3.1	<0.08	0.74	0.33	6.02	91.7
L4Nucl103	0		56.8	<0.09	23.8	0.54	3.8	<0.08	0.64	0.63	4.98	91.2
L4Nucl104	0		52.7	<0.09	27.5	0.30	2.3	<0.08	2.95	1.24	1.61	88.7
L4Nucl108	0		53.8	<0.09	28.1	0.21	2.8	<0.08	1.57	0.69	1.43	88.7
L4Nucl10H	**0**	**4**	**55.3**	**<0.09**	**25.7**	**0.31**	**3.0**	**<0.08**	**1.48**	**0.72**	**3.51**	**90.0**
s			**2.4**	**-**	**2.5**	**0.17**	**0.6**	**-**	**1.07**	**0.38**	**2.34**	**1.6**
L4Nucl109	0		48.1	<0.09	13.3	3.67	16.0	<0.08	0.70	0.14	5.97	87.9
L4Nucl105	0		41.2	<0.09	13.3	5.42	21.0	<0.08	0.98	0.23	2.38	84.5
L4Nucl106	0		43.0	<0.09	9.7	3.59	19.0	<0.08	1.37	0.22	0.84	77.7
L4Nucl107	0		42.0	<0.09	13.3	5.31	22.0	<0.08	0.67	0.09	2.14	85.5
L4Nucl10M	**0**	**4**	**43.6**	**<0.09**	**12.4**	**4.50**	**19.5**	**<0.08**	**0.93**	**0.17**	**2.83**	**83.9**
s			**3.1**	**-**	**1.8**	**1.00**	**2.7**	**-**	**0.32**	**0.07**	**2.20**	**4.4**

N: Number of analyses; Dia.: beam diameter.

A2.3.2.2 Selected feldspar particles with compositional heterogeneities within accretionary lapilli

Average composition (wt.%)

Table A2-14 Average composition (wt.%) of feldspar particles with ternary compositions and plagioclase particles associated with compositional heterogeneities.

Sample	L9a1 7.4		9A1 7.1		L9a1 3.16				L9a1 7.23-4			
Label	T1		T2		P3		P3l		P4a		P4b	
Dia.	0-3		3		0-3		0-3		0-3		0-3	
N	7		5		6		5		9		12	
SiO_2	63.5	1.3	62.2	0.9	63.4	0.9	62.8	2.1	64.3	0.3	64.7	1.0
TiO_2	0.15	0.05	0.20	0.06	<0.09	-	<0.09	-	<0.09	-	<0.09	-
Al_2O_3	20.2	0.7	20.1	0.3	23.2	0.3	22.5	0.6	22.3	0.5	22.1	0.3
MgO	0.34	0.34	0.23	0.05	<0.06	-	0.12	0.04	<0.06	-	<0.06	-
FeO	1.01	0.24	1.09	0.27	<0.11	-	<0.11	-	<0.11	-	<0.11	-
MnO	<0.08	-	<0.08	-	<0.08	-	<0.08	-	<0.08	-	<0.08	-
CaO	3.92	0.49	4.05	0.77	5.17	0.05	3.74	0.65	4.05	0.42	3.87	0.15
K_2O	6.74	0.54	7.87	0.83	1.55	0.27	7.25	0.28	1.14	0.31	3.92	0.37
Na_2O	3.50	0.21	3.58	0.30	6.76	0.14	3.23	0.50	7.36	0.57	5.65	0.38
Total	99.3	1.1	99.3	0.6	100.2	0.9	99.8	1.4	99.2	0.9	100.3	0.9
Ab	0.35		0.33		0.64		0.32		0.71		0.54	
An	0.21		0.20		0.27		0.20		0.22		0.21	
Or	0.44		0.47		0.10		0.48		0.07		0.25	
Number of cations on the basis of 24O												
Si	8.65		8.56		8.40		8.49		8.56		8.59	
Ti	0.01		0.02		-		-		-		-	
Al	3.24		3.26		3.63		3.59		3.50		3.46	
Mg	0.07		0.05		-		0.03		-		-	
Fe	0.11		0.13		-		-		-		-	
Mn	-		-		-		-		-			
Ca	0.57		0.60		0.73		0.54		0.58		0.55	
K	1.17		1.38		0.26		1.25		0.19		0.66	
Na	0.93		0.96		1.74		0.85		1.90		1.46	
Total	14.76		14.96		14.78		14.76		14.74		14.70	

T1: Ternary composed angular particle with exsolution of $BaSO_4$, (Fig. 3-13A); T2: Ternary composed particle with calcite rim and two iron sulphide grains in centre; P3: Plagioclase particle with lamella (P3l), (Fig. 3-13C); P4a: Plagioclase area associated with mixed phase composition of heterogeneous feldspar (P4b), (Fig. 3-13B). Labels correspond to Fig. 3-12. N: Number of analyses; Dia.: beam diameter.

Table A2-15 Average composition (wt.%) of alkali feldspar particles associated with potassium-feldspar as rims or lamella within accretionary lapilli.

Sample	L9A1 4-3				L9a1 10-1				L9a2b 6-2			
Label	A1c		A1r		A2c		A2r		A3c		A3l	
Dia.	0		3		0		0		0		0	
N	3	s	2	s	5	s	3	s	5	s	2	s
SiO_2	65.8	0.5	65.4	0.39	66.8	0.4	69.5	0.6	67.5	0.9	67.6	0.1
TiO_2	<0.09	-	<0.09	-	<0.09	-	<0.09	-	<0.09	-	<0.09	-
Al_2O_3	18.9	0.4	17.5	0.17	20.1	0.5	17.6	0.2	19.7	0.2	18.2	0.1
MgO	<0.06	-	<0.06	-	<0.06	-	0.22	0.10	0.29	0.31	0.25	0.22
FeO	<0.11	-	<0.11	-	0.19	0.06	<0.11	-	0.19	0.08	<0.11	-
MnO	<0.08	-	<0.08	-	<0.08	-	<0.08	-	<0.08	-	<0.08	-
CaO	0.16	0.02	0.56	0.07	1.40	0.49	0.08	0.02	0.57	0.06	0.32	0.09
K_2O	12.20	0.10	17.59	0.13	5.57	1.20	15.63	0.69	4.63	1.29	14.56	1.29
Na_2O	3.58	0.07	<0.06	-	6.28	0.65	0.19	0.05	6.91	0.74	0.67	0.72
Total	100.7	0.8	101.0	0.15	100.3	0.3	103.3	0.3	99.8	0.7	101.8	0.8
Ab	0.31		0.00		0.59		0.02		0.67		0.06	
An	0.01		0.03		0.07		0.00		0.03		0.02	
Or	0.69		0.97		0.34		0.98		0.30		0.92	
Number of cations on the basis of 24O												
Si	8.94		9.04		8.88		9.22		8.97		9.11	
Ti	-		-		-		-		-		-	
Al	3.03		2.85		3.15		2.75		3.08		2.89	
Mg	-		-		-		0.04		0.06		0.05	
Fe	-		-		0.02		-		0.01		-	
Mn	0.00		-		-		-		-		-	
Ca	0.02		0.08		0.20		0.01		0.08		0.05	
K	2.12		3.11		0.95		2.65		0.78		2.50	
Na	0.94		0.02		1.62		0.05		1.78		0.17	
Total	15.07		15.09		0.00		14.74		14.77		14.78	

A1c, A2c, A3c: centre of sodium–potassium feldspar particle; A1r, A2r: potassium-rich feldspar rim; A3l: potassium-rich feldspar lamella. Labels correspond to Fig. 3-14A. N: Number of analyses; Dia.: beam diameter.

Table A2-16 Average composition (wt.%) of sodium-potassium feldspar particle with compositional heterogeneities as potassium-rich areas and calcium-sodium-rich areas (Fig. 3-15).

Sample	L9a1 4-2		L9a1 4-2		L9a1 4-2	
Label	A4c		A4K		A4NaCa	
Dia.	0-3		2		0-3	
N	7	s	4	s	6	s
SiO_2	65.3	1.2	66.1	0.7	64.5	1.7
TiO_2	<0.09	-	<0.09	-	<0.09	-
Al_2O_3	18.9	0.2	18.3	0.3	21.2	0.7
MgO	<0.06	0.00	<0.06	-	<0.06	-
FeO	<0.11	-	<0.11	-	<0.11	-
MnO	<0.08	-	<0.08	-	<0.08	-
CaO	0.37	0.21	0.26	0.32	2.64	0.78
K_2O	10.86	0.42	15.81	0.98	5.48	1.62
Na_2O	3.45	0.26	0.58	0.47	5.53	0.92
Total	99.0	1.2	101.0	0.6	99.4	1.1
Ab	0.32		0.04		0.52	
An	0.02		0.01		0.14	
Or	0.66		0.95		0.34	
Number of cations on the basis of 24O						
Si	8.96		9.05		8.68	
Ti	-		-		-	
Al	3.06		2.95		3.37	
Mg	-		-		-	
Fe	-		-		-	
Mn	-		-		-	
Ca	0.05		0.04		0.38	
K	1.90		2.76		0.94	
Na	0.92		0.12		1.45	
Total	14.91		14.92		14.83	

A4c: centre of alkali feldspar particle; A4K: potassium-rich areas at rims, intercalations and flow textured areas; A4NaCa: calcium and sodium rich area. Labels correspond to Fig. 3-14B. N: Number of analyses; Dia.: beam diameter.

Individual analyses (wt.%)

Table A2-18 Individual and average compositions (wt.%) of feldspar particles with ternary composition.

Sample	Dia.	N	SiO_2	TiO_2	Al_2O_3	MgO	FeO	MnO	CaO	K_2O	Na_2O	Total	Ab	An	Or
Angular feldspar particle with exsolution of $BaSO_4$ (T1)															
9A1 7.4-1	3		61.4	0.18	21.7	0.23	0.99	<0.08	4.55	6.75	3.76	99.5	0.35	0.23	0.41
9A1 7.4-2	1		61.7	0.11	20.0	0.20	1.21	<0.08	3.73	7.20	3.50	97.7	0.34	0.20	0.46
9A1 7.4-3	1		64.8	<0.09	20.2	0.16	0.91	<0.08	3.43	7.71	3.78	101.1	0.35	0.18	0.47
9a1 7-4a1	0		63.8	0.17	20.0	1.09	0.61	<0.08	3.23	6.60	3.18	98.6	0.34	0.19	0.47
9a1 7-4a2	0		63.9	0.23	20.2	0.20	0.96	<0.08	4.37	6.22	3.40	99.5	0.34	0.24	0.41
9a1 7-4a4	0		64.5	0.10	19.6	0.16	1.00	<0.08	3.91	6.50	3.38	99.1	0.34	0.22	0.44
9a1 7-4a5	0		64.3	0.12	19.7	0.35	1.37	<0.08	4.21	6.22	3.53	99.8	0.36	0.23	0.41
L9a1 7.4-T	**0-3**	**7**	**63.5**	**0.15**	**20.2**	**0.34**	**1.01**	**<0.08**	**3.92**	**6.74**	**3.50**	**99.3**	**0.35**	**0.21**	**0.44**
s (± wt.%)			**1.3**	**0.05**	**0.7**	**0.34**	**0.24**	**-**	**0.49**	**0.54**	**0.21**	**1.1**			
Feldspar particle with calcite rim and two and iron sulphide grains in centre (T2)															
9A1 7.1-4	3		61.0	0.14	19.9	0.24	1.28	<0.08	5.27	7.26	3.76	98.8	0.33	0.25	0.42
9A1 7.1-1	3		61.8	0.25	19.8	0.27	1.33	<0.08	4.13	7.12	3.89	98.6	0.36	0.21	0.43
9A1 7.1-5	3		61.9	0.28	20.2	0.26	1.27	<0.08	3.95	7.71	3.64	99.2	0.33	0.20	0.47
9A1 7.1-3	3		63.1	0.22	20.3	0.15	0.80	<0.08	3.74	8.06	3.51	99.9	0.32	0.19	0.49
9A1 7.1-2	3		63.0	0.14	20.4	0.24	0.79	<0.08	3.18	9.21	3.12	100.1	0.29	0.16	0.55
9A1 7.1-T	**3**	**5**	**62.2**	**0.20**	**20.1**	**0.23**	**1.09**	**<0.08**	**4.05**	**7.87**	**3.58**	**99.3**	**0.33**	**0.20**	**0.47**
s			**0.9**	**0.06**	**0.3**	**0.05**	**0.27**	**-**	**0.77**	**0.83**	**0.30**	**0.6**			

N: Number of analyses; Dia.: beam diameter.

Table A2-19 Individual and average compositions (wt.%) of plagioclase particles with compositional variations.

Sample	Dia.	N	SiO$_2$	TiO$_2$	Al$_2$O$_3$	MgO	FeO	MnO	CaO	K$_2$O	Na$_2$O	Total	Ab	An	Or
Lamella bearing plagioclase in melt particle															
Plagioclase (P3)															
9a1 3.16a-1	3		62.9	<0.09	23.0	<0.06	<0.11	<0.08	5.17	1.42	6.86	99.4	0.64	0.27	0.09
9a1 3.16a-2	3		62.1	<0.09	23.3	<0.06	<0.11	<0.08	5.23	1.48	6.83	99.1	0.64	0.27	0.09
9a1 3.16a-3	3		62.9	<0.09	22.8	<0.06	<0.11	<0.08	5.10	2.09	6.60	99.7	0.61	0.26	0.13
L9a1 3.16a 1	0		63.8	<0.09	23.0	<0.06	<0.11	<0.08	5.12	1.51	6.87	100.4	0.64	0.26	0.09
L9a1 3.16a 2	0		64.6	<0.09	23.6	<0.06	<0.11	<0.08	5.16	1.32	6.84	101.5	0.65	0.27	0.08
L9a1 3.16a 3	0		64.0	<0.09	23.6	<0.06	<0.11	<0.08	5.23	1.48	6.55	101.0	0.63	0.28	0.09
L9a1 3.16-P	**0-3**	**6**	**63.4**	**<0.09**	**23.2**	**<0.06**	**<0.11**	**<0.08**	**5.17**	**1.55**	**6.76**	**100.2**	**0.64**	**0.27**	**0.10**
s			**0.9**	**-**	**0.3**	**-**	**-**	**-**	**0.05**	**0.27**	**0.14**	**0.9**			
Lamella within plagioclase (P3l)															
9a1 3.16a-4	3		61.5	<0.09	23.1	0.12	0.16	<0.08	4.61	7.05	3.92	100.5	0.35	0.23	0.42
9a1 3.16a-5	3		59.8	<0.09	22.3	0.19	<0.11	<0.08	4.25	7.30	3.46	97.4	0.33	0.22	0.45
L9a1 3.16b 2	0		64.1	<0.09	22.4	0.09	<0.11	<0.08	3.48	7.02	3.15	100.2	0.33	0.20	0.48
L9a1 3.16b 3	0		64.5	<0.09	21.8	0.10	<0.11	<0.08	3.21	7.70	2.59	99.9	0.28	0.19	0.54
L9a1 3.16b	0		64.0	<0.09	23.1	0.12	<0.11	<0.08	3.16	7.19	3.02	100.7	0.32	0.18	0.50
L9a1 3.16-L	**0-3**	**5**	**62.8**	**<0.09**	**22.5**	**0.12**	**<0.11**	**<0.08**	**3.74**	**7.25**	**3.23**	**99.8**	**0.32**	**0.20**	**0.48**
s			**2.1**	**-**	**0.6**	**0.04**	**-**	-	**0.65**	**0.28**	**0.50**	1.4			
Heterogeneous feldspar with round plagioclase area															
Rounded plagioclase area (P4a)															
L9a1 7.2 3-4-3	3		63.9	<0.09	23.0	<0.06	<0.11	<0.08	4.68	0.74	7.79	100.2	0.72	0.24	0.04
L9a1 7.2 3-4-4	3		64.2	<0.09	23.0	<0.06	<0.11	<0.08	4.21	0.88	8.04	100.4	0.73	0.21	0.05
L9a1 7.2 3-4-1	3		64.3	<0.09	21.7	0.09	<0.11	<0.08	3.09	1.16	8.35	98.7	0.77	0.16	0.07
L9a1 7.2 3-4-2	3		64.4	<0.09	22.7	0.16	<0.11	<0.08	3.99	1.59	7.38	100.4	0.69	0.21	0.10
9a1 7.2 3-4 7	0		64.0	<0.09	22.2	<0.06	<0.11	<0.08	4.23	0.85	6.98	98.3	0.71	0.24	0.06
9a1 7.2 3-4 8	0		64.2	<0.09	22.2	<0.06	<0.11	<0.08	4.05	1.09	7.06	98.6	0.70	0.22	0.07
9a1 7.2 3-4 9	0		64.9	<0.09	22.4	<0.06	<0.11	<0.08	4.01	1.11	6.89	99.5	0.70	0.23	0.07
9a1 7.2 3-4 10	0		64.5	<0.09	21.9	0.06	<0.11	<0.08	4.00	1.64	6.68	98.8	0.67	0.22	0.11
9a1 7.2 3-4 11	0		64.0	<0.09	21.5	<0.06	<0.11	<0.08	4.23	1.19	7.11	98.0	0.69	0.23	0.08
L9a1 7.2 3-4P	**0-3**	**9**	**64.3**	**<0.09**	**22.3**	**<0.06**	**<0.11**	**<0.08**	**4.05**	**1.14**	**7.36**	**99.2**	**0.71**	**0.22**	**0.07**
s			**0.3**	**-**	**0.5**	**-**	**-**	**-**	**0.42**	**0.31**	**0.57**	**0.9**			
Heterogeneous area (P4b)															
L9a1 7.2 3-4-6	3		62.8	<0.09	22.0	0.06	<0.11	<0.08	3.76	3.60	6.23	98.4	0.58	0.19	0.22
L9a1 7.2 3-4-7	3		64.3	<0.09	22.4	0.09	<0.11	<0.08	4.04	3.88	6.16	101.0	0.56	0.20	0.23
L9a1 7.2 3-4-5	3		63.2	<0.09	22.2	<0.06	<0.11	<0.08	3.96	3.99	6.05	99.6	0.56	0.20	0.24
L9a1 7.2 3-4-8	3		63.8	<0.09	22.4	0.08	<0.11	<0.08	3.88	4.33	5.69	100.3	0.53	0.20	0.27
L9a1 7.2 3-4-9	3		64.4	<0.09	21.5	<0.06	<0.11	<0.08	3.69	4.45	5.59	99.7	0.53	0.19	0.28
L9a1 7.2 3-4 1	0		65.8	<0.09	22.3	<0.06	<0.11	<0.08	4.01	3.55	5.67	101.4	0.55	0.22	0.23
L9a1 7.2 3-4 2	0		65.8	<0.09	22.4	<0.06	<0.11	<0.08	3.91	3.52	5.71	101.5	0.56	0.21	0.23
L9a1 7.2 3-4 3	0		65.7	<0.09	22.3	0.07	<0.11	<0.08	3.79	3.45	5.76	101.1	0.57	0.21	0.22
9a1 7.2 3-4 4	0		65.8	<0.09	22.0	<0.06	<0.11	<0.08	3.72	3.62	5.51	100.7	0.55	0.21	0.24
9a1 7.2 3-4 5	0		65.1	<0.09	21.7	0.06	<0.11	<0.08	3.68	4.47	5.03	100.2	0.50	0.20	0.29
9a1 7.2 3-4 6	0		64.8	<0.09	22.0	<0.06	<0.11	<0.08	4.12	4.04	5.10	100.1	0.51	0.23	0.27
9a1 7.2 3-4 12	0		64.9	<0.09	21.7	<0.06	<0.11	<0.08	3.93	4.11	5.34	100.1	0.52	0.21	0.26
L9a1 7.2 3-4T	**0-3**	**12**	**64.7**	**<0.09**	**22.1**	**<0.06**	**<0.11**	**<0.08**	**3.87**	**3.92**	**5.65**	**100.3**	**0.54**	**0.21**	**0.25**
s			**1.0**	**-**	**0.3**	**-**	**-**	**-**	**0.15**	**0.37**	**0.38**	**0.9**			

N: Number of analyses; Dia.: beam diameter.

Table A2-20 Individual and average compositions (wt.%) of sodium-potassium feldspar particles associated with potassium feldspar at rims or lamellae.

Sample	Dia.	N	SiO_2	TiO_2	Al_2O_3	MgO	FeO	MnO	CaO	K_2O	Na_2O	Total	Ab	An	Or
Alkali feldspar centre															
9A1 4-3-1	3		65.5	<0.09	18.5	<0.06	0.11	<0.08	0.14	12.1	3.53	99.9	0.31	0.01	0.69
9A1 4-3-2	3		66.3	<0.09	19.1	<0.06	<0.11	<0.08	0.15	12.3	3.66	101.6	0.31	0.01	0.68
9A1 4-3-3	3		65.5	<0.09	19.1	<0.06	<0.11	<0.08	0.18	12.2	3.55	100.6	0.30	0.01	0.69
9A1 4-3		**3**	**65.8**	**<0.09**	**18.9**	**<0.06**	**<0.11**	**<0.08**	**0.16**	**12.2**	**3.58**	**100.7**	**0.31**	**0.01**	**0.69**
s			**0.5**	**-**	**0.4**	**-**	**-**	**-**	**0.02**	**0.10**	**0.07**	**0.8**			
K-feldspar rim															
9A1 4-3-4	3		65.6	<0.09	17.3	<0.06	<0.11	<0.08	0.61	17.50	<0.06	101.1	0.00	0.03	0.97
9A1 4-3-5	3		65.1	<0.09	17.6	<0.06	<0.11	<0.08	0.52	17.69	0.07	100.9	0.01	0.02	0.97
9A1 4-3	**3**	**2**	**65.4**	**<0.09**	**17.5**	**<0.06**	**<0.11**	**<0.08**	**0.56**	**17.59**	**<0.06**	**101.0**	**0.00**	**0.03**	**0.97**
s			**0.4**	**-**	**0.2**	**-**	**-**	**-**	**0.07**	**0.13**	**-**	**0.1**			
Alkali feldspar centre															
9a1 10-1 1	0		66.3	<0.09	20.7	<0.06	0.27	<0.08	1.99	4.40	6.71	100.4	0.63	0.10	0.27
9a1 10-1 2	0		67.2	<0.09	19.4	<0.06	<0.11	<0.08	0.69	7.43	5.25	100.0	0.50	0.04	0.46
9a1 10-1 3	0		67.0	<0.09	20.4	<0.06	0.14	<0.08	1.61	4.62	6.93	100.7	0.64	0.08	0.28
9a1 10-1 4	0		66.9	<0.09	20.0	<0.06	0.17	<0.08	1.22	5.66	6.24	100.2	0.59	0.06	0.35
9a1 10-1 5	0		66.5	<0.09	20.1	<0.06	0.20	<0.08	1.51	5.72	6.27	100.3	0.58	0.08	0.35
L9a1 10-1	**0**	**5**	**66.8**	**<0.09**	**20.1**	**<0.06**	**0.19**	**<0.08**	**1.40**	**5.57**	**6.28**	**100.3**	**0.59**	**0.07**	**0.34**
s			0.4	-	0.5	-	0.06	-	0.49	1.20	0.65	0.3	0.05	0.02	0.08
K-feldspar rim															
9a1 10-1 6	0		69.3	<0.09	17.6	0.21	<0.11	<0.08	0.06	16.13	0.14	103.6	0.01	0.00	0.98
9a1 10-1 7	0		69.0	<0.09	17.7	0.13	<0.11	<0.08	0.08	15.92	0.19	103.1	0.02	0.00	0.98
9a1 10-1 9	0		70.2	<0.09	17.3	0.33	0.15	<0.08	0.11	14.84	0.23	103.3	0.02	0.01	0.97
L9a1 10-1-K	**0**	**3**	**69.5**	**<0.09**	**17.6**	**0.22**	**<0.11**	**<0.08**	**0.08**	**15.63**	**0.19**	**103.3**	**0.02**	**0.00**	**0.98**
s			**0.6**	**-**	**0.2**	**0.10**	**-**	**-**	**0.02**	**0.69**	**0.05**	**0.3**			
Alkali feldspar particle															
9a2b 6-2 1	0		66.7	<0.09	20.0	0.48	0.28	<0.08	0.66	5.90	6.19	100.2	0.59	0.03	0.37
9a2b 6-2 2	0		66.7	<0.09	19.5	0.75	0.15	<0.08	0.56	4.08	6.78	98.5	0.69	0.03	0.27
9a2b 6-2 3	0		68.6	<0.09	19.6	0.05	<0.11	<0.08	0.51	2.99	7.99	99.8	0.78	0.03	0.19
9a2b 6-2 4	0		67.6	<0.09	19.7	0.07	<0.11	<0.08	0.61	5.98	6.31	100.4	0.60	0.03	0.37
9a2b 6-2 7	0		68.0	<0.09	19.6	0.11	0.15	<0.08	0.53	4.19	7.29	99.9	0.71	0.03	0.27
L9a2b 6-2-NaK	**0**	**5**	**67.5**	**<0.09**	**19.7**	**0.29**	**0.19**	**<0.08**	**0.57**	**4.63**	**6.91**	**99.8**	**0.67**	**0.03**	**0.30**
s			**0.9**	**-**	**0.2**	**0.31**	**0.08**	**-**	**0.06**	**1.29**	**0.74**	**0.7**	**0.08**	**0.00**	**0.08**
K-feldspar lamella															
9a2b 6-2 6	0		67.7	<0.09	18.2	0.41	0.14	<0.08	0.25	15.48	0.16	102.3	0.02	0.01	0.97
9a2b 6-2 5	0		67.5	<0.09	18.3	0.09	<0.11	<0.08	0.38	13.65	1.18	101.2	0.11	0.02	0.87
L9a2b 6-2-K	**0**	**2**	**67.6**	**<0.09**	**18.2**	**0.25**	**<0.11**	**<0.08**	**0.32**	**14.56**	**0.67**	**101.8**	**0.06**	**0.02**	**0.92**
s			**0.1**	**-**	**0.1**	**0.22**	**-**	**-**	**0.09**	**1.29**	**0.72**	**0.8**			

N: Number of analyses; Dia.: beam diameter.

Table A2-21 Alkali feldspar particle with compositional heterogeneities as potassium-rich areas and calcium-sodium-rich areas.

Sample	Dia.	N	SiO_2	TiO_2	Al_2O_3	MgO	FeO	MnO	CaO	K_2O	Na_2O	Total	Ab	An	Or
Alkali feldspar centre															
L9a 4-2 7.7-9	3		63.9	<0.09	18.7	<0.06	<0.11	<0.08	0.14	11.10	3.42	97.3	0.32	0.01	0.68
L9a 4-2 7.7-10	3		64.4	<0.09	19.1	<0.06	<0.11	<0.08	0.20	11.02	3.49	98.2	0.32	0.01	0.67
L9a 4-2 7.7-11	3		64.7	<0.09	18.8	<0.06	<0.11	<0.08	0.23	10.77	3.45	98.0	0.32	0.01	0.66
L9a 4-2 7.7-12	3		66.4	<0.09	19.2	0.08	<0.11	<0.08	0.64	10.61	3.48	100.5	0.32	0.03	0.65
9a1 4-2a10	0		66.1	<0.09	19.2	<0.06	<0.11	<0.08	0.58	10.48	3.96	100.3	0.35	0.03	0.62
9a1 4-2a11	0		67.0	<0.09	18.6	0.07	<0.11	<0.08	0.53	10.43	3.18	99.9	0.31	0.03	0.66
9a1 4-2a12	3		64.9	<0.09	18.9	<0.06	<0.11	<0.08	0.25	11.63	3.16	98.9	0.29	0.01	0.70
L9a1 4-2-KNa	**0-3**	**7**	**65.3**	**<0.09**	**18.9**	**<0.06**	**<0.11**	**<0.08**	**0.37**	**10.86**	**3.45**	**99.0**	**0.32**	**0.02**	**0.66**
s			**1.2**	**-**	**0.2**		**-**	**-**	**0.21**	**0.42**	**0.26**	**1.2**			
K-rich areas at rims, intrusions and flow textured areas															
L9a 4-2 7.7-1	3		65.2	<0.09	18.7	<0.06	<0.11	<0.08	0.72	14.42	1.10	100.2	0.10	0.04	0.86
L9a 4-2 7.7-3	3		66.5	<0.09	18.4	<0.06	<0.11	<0.08	0.22	15.80	0.45	101.4	0.04	0.01	0.95
L9a 4-2 7.7-2	3		66.2	<0.09	18.1	<0.06	<0.11	<0.08	0.05	16.47	0.20	101.1	0.02	0.00	0.98
L9a 4-2 7.7-4	3		66.7	<0.09	18.0	<0.06	<0.11	<0.08	0.05	16.54	<0.06	101.3	0.00	0.00	0.99
L9a 4-2 7.7-K	**2**	**4**	**66.1**	**<0.09**	**18.3**	**<0.06**	**<0.11**	**<0.08**	**0.26**	**15.81**	**0.58**	**101.0**	**0.04**	**0.01**	**0.95**
s			**0.7**	**-**	**0.3**	**-**	**-**	**-**	**0.32**	**0.98**	**0.47**	**0.6**			
Calcium- and sodium-rich areas															
L9a 4-2 7.7-8	3		63.9	<0.09	20.6	0.50	<0.11	<0.08	1.36	7.97	4.92	99.4	0.45	0.07	0.48
L9a 4-2 7.7-7	3		61.9	<0.09	21.9	<0.06	<0.11	<0.08	3.15	4.89	5.72	97.6	0.54	0.16	0.30
L9a 4-2 7.7-6	3		62.8	<0.09	21.8	<0.06	<0.11	<0.08	3.42	4.71	6.14	99.0	0.55	0.17	0.28
L9a 4-2 7.7-5	3		64.2	<0.09	21.3	<0.06	<0.11	<0.08	2.32	3.70	7.10	98.6	0.66	0.12	0.23
9a1 4-2a1	0		66.8	<0.09	20.0	<0.06	<0.11	<0.08	1.56	7.85	4.86	101.1	0.45	0.08	0.47
9a1 4-2a4	0		65.5	<0.09	21.1	<0.06	<0.11	<0.08	2.97	5.38	4.88	99.9	0.48	0.16	0.35
9a1 4-2a6	0		65.9	<0.09	20.9	<0.06	<0.11	<0.08	2.41	6.32	4.50	100.2	0.45	0.13	0.42
L9a 4-2 7.7-NaCa	**0-3**	**6**	**64.5**	**<0.09**	**21.2**	**<0.06**	**<0.11**	**<0.08**	**2.64**	**5.48**	**5.53**	**99.4**	**0.52**	**0.14**	**0.34**
s			**1.7**	**-**	**0.7**	**-**	**-**	**-**	**0.78**	**1.62**	**0.92**	**1.1**			

N: Number of analyses; Dia.: beam diameter.

A2.3.2.3 Calcite composition

Table A2-22 Selected compositions (wt.%) of calcite particles within accretionary lapilli with elevated SiO_2, Al_2O_3, MgO and FeO values. Totals including CO_2 are 100% wt.%.

Sample	SiO_2	Al_2O_3	FeO	MgO	MnO	CaO	Total
1-1	1.08	0.52	0.32	0.86	<0.09	52.5	55.4
1-2	0.60	0.31	0.20	0.87	<0.09	53.5	55.6
1-3	1.31	0.67	0.24	0.89	<0.09	52.0	55.2
1-4	1.69	0.64	0.28	0.79	<0.09	51.6	55.1
2-1	1.30	0.60	0.29	0.92	0.09	52.0	55.3
2-4	1.18	0.63	0.32	1.05	0.09	51.9	55.3
2-5	0.87	0.47	0.23	0.92	<0.09	52.8	55.5
3-1	1.08	0.61	0.30	1.08	<0.09	52.1	55.3
3-2	0.61	0.36	0.27	0.83	<0.09	53.4	55.6
3-3	1.15	0.62	0.31	0.94	0.09	52.1	55.3
3-4	1.80	0.94	0.27	1.00	<0.09	50.8	54.9
3-5	1.13	0.66	0.30	1.02	0.09	52.0	55.3
Ca1a	<0.12	<0.07	<0.11	0.42	<0.09	55.5	56.0
Ca1b	<0.12	<0.07	<0.11	0.40	<0.09	55.6	56.0
Calcite1-1	1.17	0.60	0.20	0.85	<0.09	52.4	55.3
Calcite1-2	<0.12	<0.07	<0.11	0.46	<0.09	55.3	56.0
BigClast2	<0.12	<0.07	<0.11	0.59	<0.09	55.3	55.9
BigClast3	<0.12	<0.07	<0.11	0.55	<0.09	55.2	55.9
2B-1	<0.12	0.06	0.17	0.61	<0.09	55.0	55.9
2B-2	1.07	0.60	0.32	0.91	0.10	52.3	55.3
2B-3	<0.12	<0.07	0.16	0.40	<0.09	55.3	56.0
CaS2-1	0.58	0.31	0.13	0.29	<0.09	54.3	55.7
CaS2-2	<0.12	<0.07	0.18	0.57	<0.09	54.9	55.9
CaS2-3	<0.12	0.08	0.20	0.61	0.09	54.9	55.9
CaS3-1	<0.12	<0.07	0.20	0.45	<0.09	55.1	56.0
CaS3-2	<0.12	<0.07	<0.11	0.16	<0.09	55.7	56.0
CaS4-1	<0.12	<0.07	0.18	0.38	0.11	55.2	56.0
CaS4-3	<0.12	<0.07	0.15	0.30	<0.09	55.4	56.0
CaS4-4	<0.12	<0.07	0.16	0.28	<0.09	55.4	56.0
Ca1-2M	<0.12	0.27	<0.11	0.38	<0.09	55.4	56.0
Ca1-3R	<0.12	0.12	<0.11	0.49	<0.09	55.3	56.0
Ca1-4R	<0.12	0.14	<0.11	0.42	<0.09	55.4	56.0
Ca-1-5R	<0.12	0.08	<0.11	0.49	<0.09	55.3	56.0
Ca2-1	<0.12	0.17	<0.11	0.40	<0.09	55.4	56.0
Ca2-2M	<0.12	<0.07	0.11	1.14	0.14	54.5	55.9
Ca2-3RmS	<0.12	<0.07	<0.11	0.67	0.22	55.0	55.9
Ca2-4R	<0.12	<0.07	0.26	0.56	0.18	54.8	55.9
Ca3-1M	<0.12	<0.07	0.14	1.14	0.17	54.3	55.8
Ca3-2R	<0.12	0.12	<0.11	0.40	<0.09	55.3	55.3
Ca3-3R	0.48	0.11	<0.11	0.51	<0.09	54.6	54.6

N: Number of analyses; Dia.: beam diameter.

A2.3.2.4 Dolomite composition

Table A2-22 Common dolomite composition (wt.%) within accretionary lapilli. Totals including CO_2 are 100% wt.%.

	SiO_2	Al_2O_3	FeO	MgO	MnO	CaO	Total
DolB4-1	<0.12	<0.07	<0.11	21.4	<0.09	30.9	52.3
DolB4-2	<0.12	<0.07	<0.11	21.2	<0.09	31.1	52.4
DolB4-3	<0.12	<0.07	<0.11	21.0	<0.09	31.3	52.4
DolB1-1	<0.12	<0.07	<0.11	18.4	<0.09	34.3	52.9
DolB1-2	<0.12	<0.07	<0.11	20.6	<0.09	31.8	52.5
DolB1-1	<0.12	<0.07	<0.11	21.8	<0.09	30.4	52.3
DolB1-2	<0.12	<0.07	<0.11	22.0	<0.09	30.3	52.2
DolB1-3	<0.12	<0.07	<0.11	21.3	<0.09	31.0	52.4
DolB2-1	<0.12	<0.07	<0.11	21.6	<0.09	30.6	52.3
DolB2-2	<0.12	<0.07	<0.11	21.7	<0.09	30.5	52.3
DolB2-3	<0.12	<0.07	<0.11	21.2	<0.09	31.1	52.4
DolB2-4	<0.12	<0.07	<0.11	20.7	<0.09	31.6	52.5
DolB2-5	<0.12	<0.07	<0.11	21.4	<0.09	30.9	52.3
DolB3-1	<0.12	<0.07	<0.11	*20.4*	<0.09	*32.1*	52.5
DolB3-2	<0.12	<0.07	<0.11	21.4	<0.09	30.9	52.4
DoB4-1	<0.12	<0.07	<0.11	21.6	<0.09	30.7	52.3
DoB4-2	<0.12	<0.07	<0.11	21.7	<0.09	30.5	52.3
Ca28-7-1M	<0.12	<0.07	<0.11	21.0	<0.09	31.3	52.4
DolB1-3M	<0.12	<0.07	<0.11	20.8	<0.09	31.6	52.5
DolB1-4R	<0.12	<0.07	<0.11	21.6	<0.09	30.6	52.3
DolB2-2MR1	<0.12	<0.07	<0.11	21.9	<0.09	30.4	52.3
DolB2-2MR2	<0.12	<0.07	<0.11	21.0	<0.09	31.4	52.4
DolB2-2MR3	<0.12	<0.07	<0.11	21.5	<0.09	30.7	52.3
	<0.12	<0.07	<0.11	21.2	<0.09	31.1	52.4
Mean (N=24)	**<0.12**	**<0.07**	**<0.11**	**21.2**	**<0.09**	**31.1**	**52.4**
s (± wt.%)	**-**	**-**	**-**	**0.7**	**-**	**0.8**	**0.1**

N: Number of analyses; Dia.: beam diameter.

Table A2-23 Ca-rich and Mg-poor dolomite composition (wt.%) within accretionary lapilli.

	SiO_2	Al_2O_3	FeO	MgO	MnO	CaO	Total
DolA5-2	<0.12	<0.07	<0.11	17.0	<0.09	36.0	53.1
DolA5-3	<0.12	<0.07	<0.11	17.8	<0.09	35.0	53.0
DolA5-4	<0.12	<0.07	<0.11	19.0	<0.09	33.7	52.8
DolA6-1	1.51	<0.07	<0.11	17.9	<0.09	32.9	52.4
DolA6-2	<0.12	<0.07	<0.11	18.6	<0.09	34.3	52.8
DolA6-3	<0.12	<0.07	<0.11	19.3	<0.09	33.4	52.7
DolA7-1	<0.12	<0.07	<0.11	18.8	<0.09	34.0	52.8
DolA7-2	<0.12	<0.07	<0.11	18.2	<0.09	34.7	52.9
DolA7-3	<0.12	<0.07	<0.11	18.1	<0.09	34.7	52.9
DolA7-4	<0.12	<0.07	<0.11	18.2	<0.09	34.6	52.9
DolA7-5	<0.12	<0.07	<0.11	17.7	<0.09	35.1	53.0
DolA7-6	<0.12	<0.07	<0.11	17.9	<0.09	35.0	53.0
DolA7-7	<0.12	<0.07	<0.11	18.2	<0.09	34.6	52.9
DolA1-2	<0.12	<0.07	<0.11	19.0	<0.09	33.7	52.8
DolA1-3	<0.12	<0.07	<0.11	18.1	<0.09	34.7	52.9
DolA2-1	<0.12	<0.07	<0.11	18.8	<0.09	33.8	52.8
DolA2-2	<0.12	<0.07	<0.11	18.7	<0.09	34.1	52.8
DolA2-3	<0.12	<0.07	<0.11	18.7	<0.09	34.1	52.8
DoA3-1	<0.12	<0.07	<0.11	19.5	<0.09	35.3	55.0
DoA3-2	<0.12	<0.07	<0.11	15.8	<0.09	37.0	53.0
DoA3-3	<0.12	<0.07	<0.11	15.1	<0.09	34.5	49.8
DoA3-4	<0.12	<0.07	<0.11	15.3	<0.09	35.9	51.4
DolA4-1	<0.12	<0.07	<0.11	18.9	<0.09	33.7	52.8
DolA4-2	<0.12	<0.07	<0.11	18.5	<0.09	34.1	52.8
DolA-2R	<0.12	<0.07	<0.11	18.2	<0.09	34.6	52.9
DolA2-1M	<0.12	<0.07	<0.11	18.6	<0.09	34.1	52.8
DolA2-2R	<0.12	<0.07	<0.11	17.8	<0.09	35.2	53.0
DolA1-1	<0.12	<0.07	<0.11	18.9	<0.09	33.8	52.8
DolA1-2	<0.12	<0.07	<0.11	18.9	<0.09	33.8	52.8
DolA1-3	<0.12	<0.07	<0.11	18.8	<0.09	33.9	52.8
DolA1-4	<0.12	<0.07	<0.11	18.8	<0.09	33.6	52.7
DolA2-1	<0.12	<0.07	<0.11	18.5	<0.09	34.2	52.9
DolA2-2	<0.12	<0.07	<0.11	18.7	<0.09	34.0	52.8
Mean (N=24)	**<0.12**	**<0.07**	**<0.11**	**18.3**	**<0.09**	**34.3**	**52.8**
s (± wt.%)	**-**	**-**	**-**	**1.1**	**-**	**1.0**	**0.7**

N: Number of analyses; Dia.: beam diameter.

A2.3.2.5 Silica matrix

Table A2-24 Composition (wt.%) of silica matrix of accretionary lapilli.

Sample	SiO_2	TiO_2	Al_2O_3	FeO	MgO	CaO	MnO	Na_2O	K_2O	Total
Matrix1	96.4	0.09	0.86	<0.11	0.34	0.73	<0.08	0.07	0.07	98.6
Matrix3	96.0	0.28	1.06	0.22	0.68	0.47	0.08	0.08	0.08	98.9
Matrix7	97.1	0.26	0.95	<0.11	0.32	0.29	<0.08	0.10	0.11	99.2
Matrix8	95.0	0.29	1.15	0.14	0.47	0.25	<0.08	0.12	0.15	97.6
Matrix9	96.0	0.02	0.91	<0.11	0.55	0.49	<0.08	0.06	0.08	98.2
Matrix10	95.9	<0.09	0.87	<0.11	0.57	0.55	<0.08	<0.06	0.09	98.0
Matrix11	96.8	<0.09	0.39	<0.11	0.27	0.52	<0.08	<0.06	0.03	98.1
Matrix12	95.8	0.09	0.88	<0.11	0.54	0.89	<0.08	<0.06	0.08	98.4
Matrix13	97.0	0.43	0.98	<0.11	0.25	0.26	<0.08	0.09	0.13	99.2
Matrix24	96.8	<0.09	1.00	0.16	0.43	0.17	<0.08	0.08	0.12	98.7
Matrix25	95.4	0.23	1.16	0.22	0.86	0.53	<0.08	0.09	0.11	98.6
Matrix26	94.9	0.28	1.40	0.13	0.44	0.37	<0.08	0.10	0.43	98.1
Matrix27	94.9	<0.09	0.63	0.16	0.95	1.17	<0.08	0.07	0.02	97.9
Matrix28	97.0	0.31	1.03	<0.11	0.28	0.24	<0.08	0.12	0.10	99.2
Matrix29	93.2	<0.09	0.74	<0.11	0.21	2.65	<0.08	<0.06	0.10	97.1
Matrix30	97.1	0.33	0.91	0.12	0.24	0.38	<0.08	0.10	0.09	99.2
Matrix42	100.5	0.01	0.07	<0.11	<0.06	0.06	<0.08	<0.06	0.03	100.7
Matrix43	96.2	0.18	1.12	<0.11	0.18	0.76	<0.08	0.09	0.15	98.7
Matrix44	96.8	0.09	0.88	<0.11	0.24	0.45	<0.08	0.09	0.13	98.8
Matrix45	99.4	<0.09	0.21	<0.11	<0.06	0.06	<0.08	<0.06	0.05	99.8
Matrix46	98.2	<0.09	0.50	<0.11	0.12	0.11	<0.08	<0.06	0.09	99.2
Matrix47	99.4	<0.09	0.21	<0.11	<0.06	<0.05	<0.08	<0.06	0.03	99.7
Matrix48	99.5	<0.09	0.18	<0.11	<0.06	<0.05	<0.08	<0.06	0.04	99.9
Matrix48	99.5	<0.09	0.21	<0.11	<0.06	0.05	<0.08	<0.06	0.04	100.0
Matrix49	95.3	0.21	0.96	0.12	0.63	0.78	<0.08	<0.06	0.08	98.2
Matrix51	94.5	0.24	1.35	0.12	0.71	0.75	<0.08	0.09	0.21	98.0
Matrix53	96.5	<0.09	0.92	<0.11	0.30	0.63	<0.08	0.10	0.07	98.6
Matrix54	95.4	0.11	0.83	<0.11	0.24	1.28	<0.08	0.06	0.07	98.0
Matrix55	96.5	0.21	1.05	<0.11	0.45	0.35	<0.08	0.08	0.14	99.0
Matrix56	98.9	<0.09	0.40	<0.11	0.07	0.08	<0.08	<0.06	0.07	99.6
Matrix57	97.5	0.10	0.88	<0.11	0.31	0.30	<0.08	<0.06	0.07	99.2
Matrix59	97.8	<0.09	0.77	<0.11	0.18	0.39	<0.08	0.08	0.07	99.4
Matrix66	94.9	<0.09	1.05	0.16	1.01	1.06	<0.08	<0.06	0.10	98.4
Matrix67	97.2	0.31	1.02	0.15	0.43	0.18	<0.08	0.08	0.11	99.5
Matrix68	99.7	<0.09	0.28	<0.11	<0.06	0.06	<0.08	<0.06	0.06	100.3
Matrix69	99.1	<0.09	0.33	<0.11	<0.06	0.05	<0.08	0.06	0.04	99.6
Matrix70	99.0	<0.09	0.36	<0.11	<0.06	0.05	<0.08	<0.06	0.05	99.6
Matrix71	97.9	<0.09	0.76	<0.11	0.35	0.24	<0.08	<0.06	0.08	99.5
Matrix72	99.4	<0.09	0.67	<0.11	0.11	0.21	<0.08	0.06	0.10	100.5
Matrix 73	99.4	<0.09	0.69	<0.11	0.11	0.21	<0.08	<0.06	0.06	100.6
Mean(N=40)	**97.1**	**0.20**	**0.76**	**<0.11**	**0.40**	**0.48**	**<0.08**	**0.08**	**0.09**	**99.0**
s (± wt.%)	**1.8**	**0.11**	**0.34**	**0.04**	**0.24**	**0.48**	**-**	**0.02**	**0.07**	**0.9**

A3 Modal composition calculations

Table A3-1 Selected results of modelled modal composition (%) of El Guayal samples (mean values of the constrained mixing model of Le Maitre 1979 and the method of the least square Davis 1973). Results with negative values and high error have been neglected. The most certain result with the lowest error are in grey rows.

Sample	Unit	No.	Calc.	Dol.	SMP Si	SMP Mg	Silica	K-feldspar	Haem.	Quickl.	Sum	s	Sum carbonate	Sum SMP
G4	uMB	1	74.5	19.6	5.3	n.m.	0.8	n.m.	n.m.	n.m.	100.1	0.2	94.1	5.3
G4	uMB	2	74.4	19.7	4.9	n.m.	0.6	0.5	n.m.	n.m.	100.2	0.2	94.1	4.9
G5	uMB	1	76.5	14.9	8.2	n.m.	0.4	n.m.	n.m.	n.m.	100.0	0.2	91.4	8.2
G5	uMB	2	76.4	15.0	7.6	n.m.	0.3	0.7	n.m.	n.m.	100.0	0.2	91.4	7.6
G6	lμB	1	76.5	14.9	8.2	n.m.	0.4	n.m.	n.m.	n.m.	100.0	0.2	91.4	8.2
G6	lμB	2	73.4	6.0	6.9	9.2	4.1	0.8	n.m.	n.m.	100.4	0.3	79.4	16.1
G7	mμB	1	76.5	14.9	8.2	n.m.	0.4	n.m.	n.m.	n.m.	100.0	0.2	91.4	8.2
G7	mμB	2	70.9	4.2	7.8	11.4	5.4	0.6	n.m.	n.m.	100.3	0.3	75.2	19.2
G8	uμB	1	58.7	6.5	30.6	n.m.	4.0	n.m.	n.m.	n.m.	99.8	2.1	65.2	30.6
G8	uμB	2	63.8	n.m.	9.5	17.8	8.4	0.7	n.m.	n.m.	100.3	0.4	63.8	27.3
G9	lALU	1	57.5	n.m.	13.6	20.9	6.4	2.6	n.m.	n.m.	100.9	1.4	57.5	34.5
G9	lALU	2	54.8	8.2	26.9	5.7	4.7	0.3	n.m.	n.m.	100.8	1.1	63.1	32.7
G10	lALU	1	57.5	n.m.	13.6	20.9	6.4	2.6	n.m.	n.m.	100.9	1.4	57.5	34.5
G10	lALU	2	53.1	5.6	23.4	12.7	5.3	0.8	n.m.	n.m.	100.8	0.9	58.7	36.1
G11	mALU	1	58.6	n.m.	19.1	13.4	9.0	n.m.	n.m.	n.m.	100.0	0.8	58.6	32.5
G12	mALU	1	45.5	n.m.	39.5	8.0	7.0	n.m.	n.m.	n.m.	100.0	1.3	45.5	47.6
G14	uALU	1	24.6	n.m.	56.6	10.7	8.4	n.m.	n.m.	n.m.	100.2	2.1	24.6	67.3
G14	uALU	2	24.4	n.m.	58.7	7.2	8.5	n.m.	2.1	n.m.	100.9	0.8	24.4	65.8
G13	uALU	1	33.0	n.m.	48.1	10.1	9.2	n.m.	n.m.	n.m.	100.3	2.4	33.0	58.2
G13	uALU	2	32.8	n.m.	50.5	6.2	9.3	n.m.	2.3	n.m.	98.8	0.9	32.8	56.7
G15	CU	1	17.2	n.m.	56.3	5.1	21.1	n.m.	n.m.	n.m.	99.7	3.7	17.2	61.4
G15	CU	2	16.9	n.m.	58.8	0.4	21.3	n.m.	2.7	n.m.	100.2	2.6	16.9	59.2
G15	CU	3	12.5	n.m.	56.4	2.1	22.1	n.m.	2.7	4.1	99.9	0.3	12.5	58.5

MB: megabreccia; μB: microbreccia; ALU: Accretionary lapilli unit; CU: clay unit; (l: lower; m: middle; u: upper); Calc.: calcite; Dol.: dolomite; SMP Si: SiO_2-rich, MgO-poor clay altered silicate melt (montmorillonite/ illite type); SMP Mg: MgO-rich, SiO_2-poor clay altered silcate melt (vermicullite/ chlorite type); Haem.: haematite; Quickl.: quicklime; n.m.: not modelled.

Lebenslauf

Name	Tobias Salge
Geboren	02.03.1970 in Hannover
1990 – 1995	Mineralogiestudium am Institut für Mineralogie, Universität Hannover
1995 – 1998	Mineralogiestudium am Institut für Mineralogie und Mineralische Rohstoffe, Technische Universität Clausthal
SS 1996	Forschungsaufenthalt an der School of Earth Sciences, University of Tasmania, Australien Studie über *Hochdruckexperimente mit einer Piston-Zylinder-Apparatur über die Petrogenese von MOR-Basalten.* Betreuer: Dr. T. Falloon
1998	Diplom-Mineraloge, TU Clausthal Hauptprüfungen: Allgemeine und Angewandte Mineralogie, Petrologie – Geochemie – Lagerstättenkunde Nebenprüfungen: Kristallographie, Anorganische Chemie Diplomarbeit über *Spurenelementverteilungskoeffizienten zwischen Amphibol und basaltischer Schmelze in natürlichen Systemen.* Betreuer: Prof. Dr. K. Mengel Gesamtnote „Sehr gut“
1998 – 2001	Mitarbeiter am Institut für Mineralogie, Museum für Naturkunde im Forschungsprojekt *Stratigraphie, Geochemie, Mineralogie von Impaktejekta an der Grenze Späteozän-Oligozän: Vergleich mit Ejektaformationen der Kreide-Tertiär-Grenze* unter der Leitung von Dr. P. Claeys
2001 – 2006	Promovend am Institut für Mineralogie, Museum für Naturkunde über *The ejecta blanket of the Chicxulub impact crater, Yucatán, Mexico: Petrographic and chemical studies of the K-P section of El Guayal and UNAM boreholes.* Betreuer: Prof. Dr. D. Stöffler, Dr. L. Hecht

Acknowledgement

This work was carried out at the Institute of Mineralogy in the Museum of Natural History of the Humboldt University Berlin.

I am most grateful to Prof. Dr. Dieter Stöffler and PD Dr. Lutz Hecht, who exerted much positive influence on the work and supported me in each regard without limiting thereby my scopes.

I want to express my gratitude to Prof. Dr. Phillipe Claeys for the assignation of the El Guayal rock samples. For making the UNAM drill core samples available, I kindly thank Prof. Jaime Urrutia-Fucugauchi.

All my colleagues at the Museum of Natural History I am very grateful for their helpfulness and for the pleasant working climate. In particular, I thank Dr. Roald Tagle for conducting the PGE analyses and assistance with the EMP carbonate analyses. I am grateful to Dr. Ralf-Thomas Schmitt for the accomplishment of the XRF analyses. Dr. Marcus Apel, Jana Berlin, Daniel Doman, Dr. Ansgar Greshake, Dr. Sabine Heuschkel, PD Dr. Thomas Kenkmann, Prof. Dr. Wolfgang Kiessling, Cornelia Meyer, Prof. Dr. Ulrich Riller, Frank Schönian, Silke Weseler and Axel Wittmann contributed a substantial amount to the success of this work with their specialised knowledge and the constant readiness for discussions.

I acknowledge the technical staff of the mineralogy at the Museum for Natural History, Hans Rudolf Knöffler for the preparation of thin sections, Peter Czaja for support in instrumental microanalysis, Ingrid Felber for making the glass tablets and Hwa Ja Nier not only for the photo work.

Dr. Hagen Stosnach is thanked for the introduction to TXRF analysis.

For the proof reading and fruitful discussions I am very grateful to Dr. Jörg Fritz, Dr. Holger Paulick and Dr. Peter Schulte.

I thank my friends Arne, Lars, Peter, Nils, Eike, Cornelia, Vera, Max and Lisa for the good times.

My special thanks apply to my mother, who supported me in any regard.

Publizierte Konferenzbeiträge

SALGE, T. (2006). Behaviour of sedimentary and silicate target lithologies in the Chicxulub ejecta plume. Beihefte zum European Journal of Mineralogy, v. 18: 113.

SALGE, T. (2006). Chicxulub ejecta plume: Influence of sedimentary target rock, volatiles and atmosphere. European Planetary Science Congress #1, September 18-22, 2006, Berlin, Germany, (CD-ROM).

SALGE, T., HECHT, L. & STÖFFLER, D. (2006). Chicxulub ejecta plume formation and the link with the global K-P boundary. Meteoritics & Planetary Science, v. 41 Supp.: A157.

SCHÖNIAN, F., **SALGE, T.**, KENKMANN, T., STÖFFLER. D., SOLER ARECHALDE, A.M. & URRUTIA FUCUGAUCHI, J. (2006). Chicxulub ejecta blanket: The suevites of the UNAM 5 and 7 drill cores. In: 37th Lunar and Planetary Science Conference, March 2006, League City, USA, Lunar and Planetary Institute, Houston: #2229.

SCHÖNIAN, F., **SALGE, T.**, STÖFFLER, D. & URRUTIA-FUCUGAUCHI, J. (2003). Additional observations on the impact breccias of the Chicxulub ejecta blanket from the UNAM-7 drill core, Yucatán, Mexico. In: Third International Conference on Large Meteorite Impacts, Nördlingen, Germany, Lunar and Planetary Institute, Houston, LPI Contribution No. 1167: #4132.

STÖFFLER, D., IVANOV, B. A., HECHT, L., KENKMANN, T., SCHMITT, R. T., **SALGE, T.**, SCHÖNIAN, F., TAGLE, R., WESELER, S. & WITTMANN, A. (2003). Origin and emplacement of the impact formations at Chicxulub, Mexico, with special emphasis on the Yax-1 deep drilling. In: Third International Conference on Large Meteorite Impacts, Nördlingen, Germany, Lunar and Planetary Institute, Houston, LPI Contribution No. 1167: #4092.

STÖFFLER, D., HECHT, L., IVANOV, B. A., KENKMANN, T., **SALGE, T.**, SCHMITT, R. T., SCHÖNIAN, F., TAGLE, R. & WITTMANN, A. (2003). Characteristics of the multi-ring impact basin of Chicxulub, Mexico, as derived from drill core data and numerical modeling. Meteoritics & Planetary Science, v. 37 Supp.: A126.

SALGE, T., TAGLE, R. & CLAEYS, P. (2000). Accretionary lapilli from the KT boundary site of Guayal, Mexico: Preliminary Insights of expansion plume formation. Meteoritics & Planetary Science, v. 35 Supp.: A140.

SALGE, T., SCHULTE, P., STINNESBECK, W. & CLAEYS, P. (2000). Sedimentology and petrology of the shallow UNAM cores drilled around the Chicxulub impact crater. ICDP/KTB-SPP-Kolloquium, Wissenschaftliches Programm und Abstracts, Bochum: 183-184.

CLAEYS, P., **SALGE, T.**, TAGLE, R., HEUSCHKEL, S. & GRAJALES-NISHIMURA, J. M. (1999). Characterization and distribution of the Chicxulub suevite. Geological Society of America, 31th annual meeting, Abstracts with Programs, v. 31: A-123.

SALGE, T., TAGLE, R. & CLAEYS, P. (1999). Diamonds and PGE in the Late Eocene type section at Massignano: A clue to the source of the ejecta debris? 3rd ESF Impact Programme Workshop on Geological and Biological Evidences for Global Catastrophes Espéraza/Quillan (France), September 26-30, 2006: 63.

SALGE, T., CLAEYS, P. & GRAJALES, M. (1999). The lapilli bed in El Guayal (Tabasco): Fall out suevite from the Cretaceous-Tertiary boundary Chicxulub crater? Journal of Conference Abstracts, v. 4: 268.

Selbständigkeitserklärung

Berlin, den 30. Oktober 2006

Hiermit erkläre ich, dass ich die vorliegende Arbeit selbständig und nur unter Verwendung der angegebenen Literatur und Hilfsmittel angefertigt habe. Die aus fremden Quellen direkt oder indirekt übernommenen Inhalte sind im Text und den Abbildungen entsprechend gekennzeichnet. Die Personen, die mir fachlich beratend und betreuend beiseite gestanden haben und jene, die an der Fertigstellung dieser Arbeit mitgewirkt haben, sind in der Danksagung am Ende der Arbeit erwähnt.

…….………………………..

Tobias Salge